CERN–2005–014
DESY–PROC–2005–001
14 December 2005

HERA AND THE LHC

A workshop on the implications of HERA for LHC physics

March 2004 – March 2005

Parton density functions
Multijet final states and energy flow
Heavy quarks
Diffraction
Monte Carlo tools

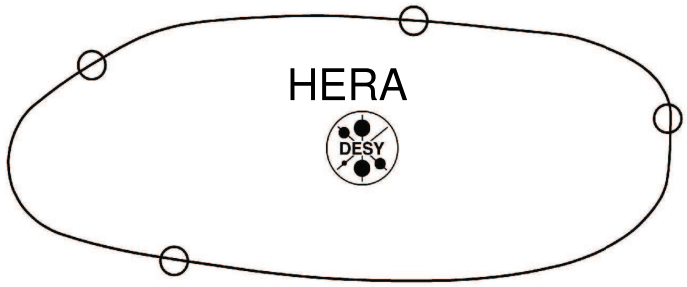

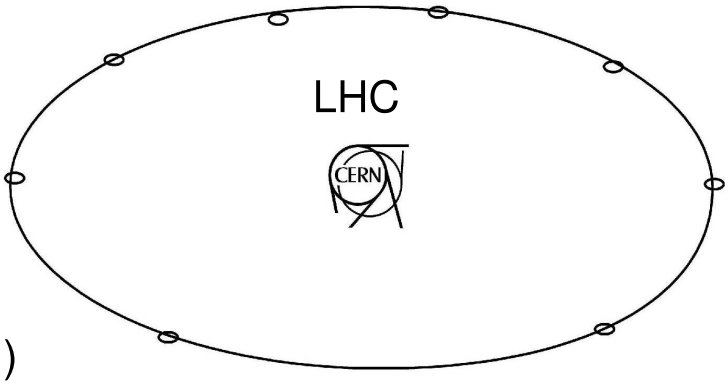

Proceedings
Editors:
A. De Roeck (CERN)
H. Jung (DESY)

Geneva
2005

Organizing Committee:

G. Altarelli (CERN), J. Blümlein (DESY), M. Botje (NIKHEF),
J. Butterworth (UCL), A. De Roeck (CERN) (chair), K. Eggert (CERN),
H. Jung (DESY) (chair), M. Mangano (CERN), A. Morsch (CERN),
P. Newman (Birmingham), G. Polesello (INFN), O. Schneider (EPFL),
R. Yoshida (ANL)

Advisory Committee:

J. Bartels (Hamburg), M. Della Negra (CERN), J. Ellis (CERN),
J. Engelen (CERN), G. Gustafson (Lund), G. Ingelman (Uppsala), P. Jenni (CERN),
R. Klanner (DESY), M. Klein (DESY), L. McLerran (BNL), T. Nakada (CERN),
D. Schlatter (CERN), F. Schrempp (DESY), J. Schukraft (CERN),
J. Stirling (Durham), W.K. Tung (Michigan State), A. Wagner (DESY),
R. Yoshida (ANL)

Contents

Part V

Working Group 4: Diffraction

List of participants

L. Adamczyk, N. Amapane, V. Andreev, M. Arneodo, V. Avati, C. Avila, J. Bartels, R. Bellan, S. Bolognesi, M. Boonekamp, A. Bruni, A. Bunyatyan, G. Cerminara, B. Cox, R. Croft, A. De Roeck, M. Diehl, I. Efthymiopoulos, K. Eggert, F. Ferro, J. Forshaw, E. Gotsman, D. Goulianos, P. Grafström, M. Grothe, M. Groys, C. Hogg, G. Ingelman, X. Janssen, H. Jung, J. Kalliopuska, M. Kapishin, D. Kharzeev, V. Khoze, M. Klasen, H. Kowalski, G. Kramer, J. W. Lämsä, P. V. Landshoff, P. Laycock, E. Levin, A. Levy, L. Lönnblad, M. Lublinsky, L. Lytkin, D. Macina, T. Mäki, U. Maor, C. Mariotti, N. Marola, C. Marquet, A. D. Martin, V. Monaco, J. Monk, L. Motyka, S. Munier, M. Murray, E. Naftali, P. Newman, J. Nystrand, F. Oljemark, R. Orava, K. Österberg, M. Ottela, A. Panagiotou, R. Peschanski, A. Pilkington, K. Piotrzkowski, A. Proskuryakov, A. Prygarin, J. Raufeisen, M. Rijssenbeek, M. Ruspa, M. G. Ryskin, M. Ryynänen, A. Sabio-Vera, R. Sacchi, S. Schätzel, F.-P. Schilling, A. Sobol, M. Strikman, S. Tapprogge, M. Taševský, P. Van Mechelen, R. Venugopalan, K. Vervink, G. Watt, K. Wichmann, G. Wolf.

Introduction to Diffraction

M. Arneodo [a], *J. Bartels* [b], *A. Bruni* [c], *B. E. Cox* [d], *M. Diehl* [e], *J. Forshaw* [d], *M. Grothe* [f], *H. Kowalski* [e], *R. Orava* [g], *K. Piotrzkowski* [h] *and P. Van Mechelen* [i]

[a] Università del Piemonte Orientale, Novara, and INFN-Torino, Italy

[b] II. Institut für Theoretische Physik, Universität Hamburg, Luruper Chaussee 149, 22761 Hamburg, Germany

[c] INFN Bologna, Via Irnerio 46, 40156 Bologna, Italy

[d] School of Physics and Astronomy, The University of Manchester, Manchester M139PL, United Kingdom

[e] Deutsches Elektronen-Synchroton DESY, 22603 Hamburg, Germany

[f] University of Torino and INFN-Torino, Italy; also at University of Wisconsin, Madison, WI, USA

[g] High Energy Physics Division, Department of Physical Sciences, University of Helsinki and Helsinki Institute of Physics, P. O. Box 64, 00014 University of Helsinki, Finland

[h] Institut de Physique Nucléaire, Université Catholique de Louvain, Louvain-la-Neuve, Belgium

[i] Universiteit Antwerpen, Antwerpen, Belgium

Abstract

We summarize the main activities of the Working Group on Diffraction in this workshop, which cover a wide range of experimental, phenomenological and theoretical studies. Central themes are exclusive and inclusive diffraction at HERA and the LHC, multiple interactions and rapidity gap survival, and parton saturation.

1 Forward proton tagging at the LHC as a means to discover new physics

The use of forward proton tagging detectors at CMS and ATLAS as a means to search for and identify the nature of new physics at the LHC was one of the major topics of discussion at the workshop. The process of interest is the so-called 'central exclusive' production process $pp \to p \oplus \phi \oplus p$, where $\oplus$ denotes the absence of hadronic activity (a 'gap') between the outgoing intact protons and the decay products of the central system ϕ. The final state therefore consists of *only* the decay products of the system ϕ, which can be seen in the central detectors, and the two outgoing protons, which must be detected at some point downstream of the interaction point where they emerge far enough from the LHC beams. To this end, the feasibility of installing proton tagging detectors at 420 m from the interaction points of ATLAS and/or CMS, at a suitable time after the initial start-up of the LHC, is currently being assessed [1]. These would complement and increase the acceptance of the detectors already planned in the 220 m/240 m region by CMS / TOTEM and ATLAS. The choice of the 420 m region is set by the central system masses of interest; protons which lose approximately 60 GeV of their longitudinal momentum — the interesting range from the point of view of Higgs boson searches — emerge from the beam in this region.

The motivation for these studies stems from the unique properties of central exclusive production. Firstly, the mass of the central system ϕ can be measured to high accuracy by measuring the four-momenta of the outgoing protons alone, without reference to the central system (the so-called 'missing mass method' [2]). The achievable mass resolution and the acceptance as a function of mass of the 420 m detectors (in combination with the already planned 220 m proton detectors) are discussed in detail in these proceedings [3, 4]. The resolution can be as good as 1 GeV for a Higgs boson of mass 140 GeV. As an example, in the case of a 140 GeV Standard Model Higgs decaying to two W bosons, and the subsequent leptonic decays of one or both of the W's to leptons plus neutrinos, six events are expected with no modification of the level-1 trigger thresholds of ATLAS and CMS for 30 fb^{-1} of delivered luminosity. We discuss the trigger issues in more detail below. This number is expected to double if realistic changes are made to the leptonic trigger thresholds [5].

A second crucial advantage is that, to a good approximation, the central system ϕ is produced in the $J_z = 0$, C and P even state, and an absolute determination of the quantum numbers of any resonance is possible by measuring correlations between the outgoing proton momenta. Observation of any resonance production with associated proton tags, therefore, allows a determination of its quantum numbers, something that is difficult to do in any other process at the LHC. Such a determination could be made with only a few 'gold-plated' events.

Thirdly, states which would otherwise be very difficult to detect in conventional channels can be detected in the central exclusive channel. Perhaps the best-studied example is the high $\tan\beta$ region of the MSSM, where over 100 signal events can be detected with backgrounds lower by an order of magnitude or more, within 30 fb^{-1} of delivered luminosity at the LHC [6]. There are extensions to the MSSM in which central exclusive production becomes in all likelihood the only method at the LHC of isolating the underlying physics. One example [7] is the case where there are non-vanishing CP phases in the gaugino masses and squark couplings. In such scenarios, the neutral Higgs bosons are naturally nearly degenerate for large values of $\tan\beta$ and charged Higgs masses around 150 GeV. In such scenarios, observing the mass spectrum using forward proton tagging may well be the only way to explore such a Higgs sector at the LHC. Explicit CP-violation in the Higgs sector can be observed as an asymmetry in the azimuthal distributions of the tagged protons [8].

From an experimental perspective, the key issue along with the mass resolution and acceptance is the level-1 (L1) trigger efficiency. The problem is that detectors at 420 m from the interaction points of ATLAS or CMS are too far away to participate in a L1 trigger decision without an increase in the trigger latency. This means that the central detectors, or forward detectors up to 220 m, must be relied upon to keep candidate events until the signals from 420 m can be used in higher level trigger decisions. A full description of the work done at the workshop is presented in Refs. [9, 10] in these proceedings. The most difficult case is that of a low-mass (120 GeV) Higgs boson decaying in the b-quark channel (a decay mode that will not be observed in any other measurement at the LHC). The relatively low transverse momenta of the b-jets necessitate L1 jet E_T thresholds as low as 40 GeV. Thresholds that low would result in a L1 trigger rate of more than 50 kHz, because of the QCD background, and thus would essentially saturate the available output bandwidth. The output rate of a 2-jet L1 trigger condition with thresholds of 40 GeV per jet can be kept at an acceptable level of order 1 kHz in the absence of pile-up (i.e. for a single proton–proton interaction per bunch crossing) by either using the TOTEM T1 and T2 detectors (or the ATLAS forward detectors) as vetoes — central exclusive events have no energy in these regions — or by requiring that a proton be seen in the TOTEM (or ATLAS) detectors at 220 m on one side of the interaction point. This gives a sufficient reduction of the QCD background event rate. At higher luminosities, up to $2 \times 10^{33}\,\mathrm{cm}^{-2}\,\mathrm{s}^{-1}$, where pile-up is present, it is necessary to combine a 220 m tag with additional conditions based on event topology and on H_T, the scalar sum of all L1 jet E_T values. These L1 trigger conditions result in signal efficiencies between 15% and 20%. A further 10% of the Higgs events can be retained by exploiting the muon-rich final state in the $H \to b\bar{b}$ mode, with no requirements on the forward detectors. Other interesting decay channels, such as WW and $\tau\tau$, should be possible at the highest luminosities ($1 \times 10^{34}\,\mathrm{cm}^{-2}\,\mathrm{s}^{-1}$) since both ATLAS and CMS will trigger on such events routinely using only the central detectors.

As well as upgrading the proton tagging capabilities of ATLAS and CMS, there was also discussion of upgrading the very forward region of CMS to extend the pseudo-rapidity coverage up to $|\eta| \sim 11$. This would allow proton x values down to 10^{-8} to be probed, opening up an unexplored region of small-x parton dynamics [11].

In summary, central exclusive production provides an excellent means of measuring the masses of new particles with a precision at the 1 GeV level, irrespective of the decay mode of the particles. It also provides a clean way of unambiguously determining the quantum numbers of any resonances produced in the central exclusive process (including Standard Model and MSSM Higgs bosons) at the LHC.

In certain regions of the MSSM, and indeed for any scenarios in which the new particles couple strongly to gluons, central exclusive production may be the discovery channel[1]. The challenge is to design and build proton tagging detectors with the capability to measure the momentum loss of the outgoing protons at the 1 GeV level.

2 Theory of diffractive Higgs production

It is a fact that the theoretical predictions for central exclusive production suffer from several sources of uncertainty. The theoretical framework is presented and critically assessed in the contribution by Forshaw [13]. The emphasis is on the calculations of the Durham group, which are performed within perturbative QCD. The use of perturbative QCD is shown to be justified, with around 90% of the contribution to the Standard Model Higgs production cross-section ($m_H = 120$ GeV) coming from the region where the gluon virtualities are all above 1 GeV.

One of the main sources of uncertainty in the perturbative calculation arises from a lack of knowledge of the proton's generalized, unintegrated gluon distribution function, and so far estimates are based upon theoretically motivated corrections to the more familiar gluon distribution function. It is hard to make an accurate assessment of the uncertainty arising from this source, but currently a factor of 2 uncertainty on the Higgs production cross-section is probably not unrealistic. Measurements of exclusive diffraction at HERA can help constrain the generalized gluon distribution in kinematics similar to the one relevant for exclusive Higgs production at the LHC [14]. High-quality data are now available for $ep \to e\, J/\Psi\, p$. Exclusive production of Υ mesons and deeply virtual Compton scattering $ep \to e\gamma p$ involve smaller theoretical uncertainties, but are experimentally more demanding and should be explored in more detail with HERA II data.

Since the focus is on exclusive final states such as $p \oplus H \oplus p$, it is necessary to sum the Sudakov logarithms which arise in perturbation theory. One must go beyond summing the leading double logarithms and sum also the single logarithms. Without the single logs, one vastly underestimates the production rate. Unfortunately, perturbative emissions are not the only way to spoil the exclusive nature of the final state: extra particles can also be produced as a result of soft interactions between the colliding protons. To account for such soft interactions is clearly outside of the scope of perturbation theory and one is forced to resort to non-perturbative models. It is universally assumed that one can estimate the effect of forbidding additional particle production by simply multiplying the perturbative cross-section by an overall 'gap survival' factor [15]. The two most sophisticated models of this factor are discussed in some detail and compared with each other in the contribution of Gotsman et al. [16]. It turns out that, although the approaches are different in many respects, they tend to predict very similar values for the gap survival factor. Nevertheless, both models are essentially multi-channel eikonal models and one would like to test them against data. Fortunately that is possible: data from HERA and the Tevatron already tend to support the theoretical models and future measurements at the LHC will allow one to further constrain them.

Uncertainties in the gluon densities and in our knowledge of gap survival can be reduced as we test our ideas against data, both at present colliders and at the LHC itself. Fortunately, these uncertainties essentially factorize (from the hard subprocess which produces the central system) into a universal 'effective gluon luminosity' function. Thus one can hope to extract the important physics associated with the production of the central system by first measuring the luminosity function in a 'standard candle' process. The ideal candidate is $pp \to p + \gamma\gamma + p$ [17] since the hard subprocess is well known ($gg \to \gamma\gamma$) and the effective gluon luminosity can be extracted over a wide kinematic range. In this way one might hope to extract the effective coupling of any centrally produced new physics to two gluons.

[1] For a recent review of the physics case for FP420, see [12] and references therein.

During the period of the workshop, Monte Carlo codes have been developed which simulate the theoretical predictions for both interesting signal processes and also the associated backgrounds. These codes are now routinely used, for example, to help develop the case for the installation of low-angle proton detectors at the LHC, and new processes are being added with time. A review and comparison of the various Monte Carlos is to be found in the contribution of Boonekamp et al. [18].

3 Diffractive structure functions and diffractive parton distributions

The cross-section for the reaction $ep \to eXp$ can be expressed in terms of the diffractive structure functions F_2^D and F_L^D, in analogy to the way in which $d\sigma/dx\,dQ^2$ is related to the structure functions F_2 and F_L for inclusive DIS, $ep \to eX$. The function F_2^D describes the proton structure in processes in which a fast proton is present in the final state; F_L^D corresponds to longitudinal polarization of the virtual photon. Since in diffractive events the proton typically loses a fraction of less than 0.02–0.03 of its initial momentum, the parton participating in a diffractive interaction has a fractional momentum which is also less than 0.02–0.03. Diffractive DIS thus probes the low-x structure of the proton, in a way complementary to that provided by non-diffractive DIS.

Diffractive structure functions, like the usual ones, can be expressed as the convolution of universal partonic cross-sections and a specific type of parton distribution functions, the diffractive PDFs. This is the so-called diffractive factorization theorem. Diffractive PDFs can be determined by means of QCD fits similar to those used for extracting the standard PDFs from the F_2 data.

Several measurements of F_2^D are available from the H1 and ZEUS collaborations. Three alternative approaches have been used to select diffractive events:

1. a fast proton is required in the final state; this can be done only be means of a proton spectrometer able to detect scattered protons which do not leave the beam pipe (see e.g. [19]);
2. a rapidity gap in the forward direction is required;
3. the different shape of the M_X distribution for diffractive and non-diffractive events is exploited.

Method 1 selects the reaction $ep \to eXp$ with a high degree of purity; the acceptance of proton spectrometers is, however, small, yielding comparatively small samples. Methods 2 and 3 select the reaction $ep \to eXY$, as opposed to $ep \to eXp$, with Y a proton or a low-mass system. Samples selected with these two methods may include some contamination from non-diffractive processes. Method 3 suppresses the contribution of subleading exchanges (i.e. Reggeon and pion exchanges, as opposed to Pomeron exchange), which is instead present in the samples selected with methods 1 and 2.

Results obtained with the three methods are presented and compared in these proceedings [20]. Methods 2 and 3 yield results for F_2^D which are higher than those obtained with the LPS by factors as large as 1.4, depending on the degree of forward coverage. This normalization difference is due to the proton-dissociative background (from $ep \to eXY$) and is relatively well understood. Having corrected for this effect, the results of the three methods exhibit, at present, a fair degree of agreement. However, differences in the shapes of the Q^2, β and $x_{I\!P}$ dependences become apparent especially when comparing the results obtained with method 3 and those obtained with methods 1 and 2. The origin of these differences is at present not clear. An urgent task for the HERA community is to understand these discrepancies and provide a consistent set of measurements of F_2^D.

Several NLO fits of the F_2^D data were discussed at the workshop [20–22]. The corresponding parametrizations are available in Ref. [23]. The diffractive PDFs are dominated by gluons, as expected given the low-x region probed, with the density of gluons larger than that of quarks by a factor 5–10. There are significant discrepancies between the results of the fits, reflecting, at least in part, the differences in the fitted data. In addition, Martin, Ryskin and Watt [22] argue that the leading-twist formula used in Refs. [20,21] is inadequate in large parts of the measured kinematics, and use a modified expression which includes an estimate of power-suppressed effects.

The discrepancies between the various diffractive PDFs, while not fully understood, are at the moment the best estimate of their uncertainties. Here as well, it is imperative that the HERA community provide a consistent set of diffractive PDFs. Not only are they important for our understanding of the proton structure, but they are also an essential input for any calculation of the cross-sections for *inclusive* diffractive reactions at the LHC — which are interesting in themselves in addition to being a potentially dangerous background to the central *exclusive* production processes discussed in Sections 1 and 2.

No direct measurement exists of F_L^D. The dominant role played by gluons in the diffractive parton densities implies that the leading-twist F_L^D must also be relatively large. A measurement of F_L^D to even modest precision would provide an independent and theoretically very clean tool to verify our understanding of the underlying dynamics and to test the gluon density extracted indirectly in QCD fits from the scaling violations of F_2^D. This is discussed in Ref. [24].

4 Diffractive charm and dijet production at HERA

As mentioned in Section 2, the possibility to observe central exclusive processes depends critically on the survival probability of large rapidity gaps. This probability is not unity as a consequence of the rescattering between the spectator partons in the colliding hadrons: these interactions generate final-state particles which fill the would-be rapidity gap and slow down the outgoing proton or antiproton [16]. This is why the diffractive factorization theorem [25] is expected to fail for hadron–hadron scattering — and therefore also for resolved photoproduction, where the photon acts as a hadron.

In $p\bar{p}$ collisions at the Tevatron, breaking of diffractive factorization was indeed observed. The fraction of diffractive dijet events at CDF is a factor 3 to 10 smaller than that predicted on the basis of the diffractive parton densities obtained at HERA. Similar suppression factors were observed in all hard diffractive processes in proton–antiproton collisions.

In photoproduction processes, however, the situation is far from clear at the moment. A recent ZEUS result [26] indicates that the cross-section for diffractive photoproduction of D^* mesons, a process dominated by the *direct* photon component, is well described by NLO QCD predictions based on the diffractive PDFs. This lends support to the idea that in direct processes the photon is pointlike and that the diffractive factorization theorem holds in this case. Conversely, diffractive dijet data from H1 and ZEUS are better described by a global suppression of *both* the direct and resolved contribution. A discussion of how this might be understood is given in Refs. [27, 28], where a critical study of the factorization scheme and scale dependence of resolved and direct contributions is presented.

5 Multiple scattering at HERA and the LHC

A thorough analysis of the event structure at the LHC will have to take into account contributions from multiple-parton interactions, i.e. from interactions involving more than one parton in each of the colliding protons. Such multiple interactions are expected to be particularly important in the region of small longitudinal momentum fractions and not too high momentum scales. At HERA there are several pieces of evidence that multiple interactions are present; the strongest one comes from the observation of diffractive final states in deep-inelastic electron–proton scattering. A useful tool for analysing these multiple interactions are the so-called AGK cutting rules. During this workshop several groups have studied their application to HERA and to future LHC scattering processes.

The theoretical basis of the AGK rules in perturbative QCD has been outlined in Ref. [29], and a few first applications to HERA and to LHC scattering processes have been addressed. The contribution by Watt et al. [30] uses the AGK rules for deriving, from the measured *diffractive* structure function, absorptive corrections to the *inclusive* structure function F_2. An iterative scheme is then set up which leads to corrected parton densities: at low Q^2 and small x, they tend to be higher than those without absorptive corrections. In particular, they seem to weaken the trend of the gluon density becoming negative, which has been seen in the global parton analyses of both MRST2004 and CTEQ6.

The study presented in Ref. [31] is based upon a specific saturation model that has been successfully applied both to the total $\gamma^* p$ cross-section and to the diffractive process $\gamma^* p \to J/\Psi\, p$. An analysis of this model, based upon the AGK rules, leads to the conclusion that contributions of multiple interactions to F_2 are quite sizeable, even for Q^2 as large as 40 GeV^2.

6 Parton saturation: from HERA to the LHC

A key experimental finding of HERA is the strong rise of structure functions at small x, which implies a high density of small-x gluons in the proton. From theoretical considerations, it is clear that for sufficiently large parton densities, dynamics beyond what can be described by leading-twist factorization and linear DGLAP evolution must become important. If the associated momentum scale is high enough, the strong coupling is still small enough to serve as an expansion parameter, but at very high gluon densities the gluon potential can be so strong that the non-linear term $g_s f^{abc} A^b_\mu A^c_\nu$ in the gluon field strength is as large as the linear term $\partial_\mu A^a_\nu - \partial_\nu A^a_\mu$. High parton densities thus offer the possibility to study QCD in a strongly non-linear regime, and the effective theory of such a 'colour glass condensate' is reviewed in Ref. [32]. A possible link between the strong gluon fields in this description and QCD instantons is discussed in Ref. [33].

The theory and phenomenology of parton saturation are in rapid development, of which the workshop could only provide a snapshot. Data on both inclusive and diffractive deeply inclusive scattering, in particular their very similar energy dependence at given Q^2, suggest that saturation effects are relevant in HERA kinematics, see Ref. [34] and references therein. When saturation is important, the usual parton densities cease to be the key input quantities for describing physical processes. For many reactions a suitable quantity is instead the colour-dipole cross-section — a concept that has been successfully applied in HERA phenomenology. An important theoretical laboratory to study saturation effects is provided by the non-linear Balitsky–Kovchegov equation. In a contribution to the workshop, this equation has been applied to the colour-dipole cross-section for the proton [35]. To describe saturation in pp collisions in general requires non-perturbative functions that can be written as matrix elements of Wilson line operators; *one* of these functions is the colour-dipole cross-section just mentioned [32]. The formulation of suitable evolution equations for pp scattering is an active area of research [36].

7 Rapidity gaps in electroweak processes

Diffractive processes are characterized by rapidity gaps. Such gaps can also originate from the exchange of a photon, a W or a Z boson (see for example Ref. [15]). Selecting events with large rapidity gaps filters out specific final states and, at the same time, leads to better-constrained event kinematics. However, the event rate is lowered by the gap survival probability, as discussed in the previous sections.

The contribution by Amapane et al. [37] discusses the possibility to study the scattering of longitudinally polarized vector bosons (V_L) in pp collisions with the CMS detector at the LHC. $V_L V_L$ fusion may lead to Higgs production; should the Higgs boson not exist, the cross-section for $V_L V_L$ scattering will deviate from the Standard Model prediction at high invariant masses of the $V_L V_L$ system. In all cases, $V_L V_L$ scattering should shed light on the mechanism behind the electroweak symmetry breaking. Preliminary studies based on Pythia and a fast simulation of the CMS detector are encouraging. It will be interesting to investigate in more detail the potential of the rapidity-gap signature for improved signal extraction and background control.

Large rapidity gaps at hadron colliders can also be due to photon exchange. In this case, a direct tagging of high-energy photon interactions can be achieved by using forward proton detectors [38]. Both photon–photon and photon–proton interactions at the LHC have been studied [39]. Some of these events can be used to scan the gap survival probability in impact parameter space, which would help to constrain models for gap survival. A reference point is given by single W boson photoproduction, which has been studied theoretically in this context [40] and is being investigated at HERA.

Finally, diffractive photoproduction of Υ mesons, currently being studied at HERA, can be accessed at the LHC in an extended range of small x. This will provide a very clean channel to study the generalized gluon distribution (see Section 2) and can be seen as a complement to measurements of the usual gluon distribution at very small x, for instance in forward jet production at the LHC.

Acknowledgements

We wish to thank all participants of the Working Group on Diffraction for their valuable contributions to this Workshop. This work has been supported by PPARC and the Royal Society in the UK, and the Italian Ministry for Education, University and Scientific Research under the programme 'Incentivazione alla mobilità di studiosi stranieri e italiani residenti all'estero'.

References

[1] M. G. Albrow *et al.*, Proposal submitted to the LHCC: CERN-LHCC-2005-025, LHCC-I-015.

[2] M. G. Albrow and A. Rostovtsev, hep-ph/0009336.

[3] J. Kalliopuska *et al.*, these proceedings.

[4] V. Avati and K. Österberg, these proceedings.

[5] B. E. Cox *et al.*, hep-ph/0505240.

[6] A. B. Kaidalov, V. A. Khoze, A. D. Martin and M. G. Ryskin, Eur. Phys. J. C **33** (2004) 261 [hep-ph/0311023].

[7] J. R. Ellis, J. S. Lee and A. Pilaftsis, Phys. Rev. D **71** (2005) 075007 [hep-ph/0502251].

[8] V. A. Khoze, A. D. Martin and M. G. Ryskin, Eur. Phys. J. C **34** (2004) 327 [hep-ph/0401078].

[9] M. Arneodo *et al.*, these proceedings.

[10] G. Bruni, G. Iacobucci, L. Rinaldi and M. Ruspa, these proceedings.

[11] V. Andreev *et al.*, these proceedings.

[12] B. E. Cox, AIP Conf. Proc. **753** (2005) 103 [hep-ph/0409144].

[13] J. R. Forshaw, these proceedings.

[14] J. Collins *et al.*, these proceedings.

[15] J. D. Bjorken, Phys. Rev. D **47** (1993) 101.

[16] E. Gotsman, E. Levin, U. Maor, E. Naftali and A. Prygarin, these proceedings.

[17] V. A. Khoze, A. D. Martin, M. G. Ryskin and W. J. Stirling, Eur. Phys. J. C **38** (2005) 475 [hep-ph/0409037].

[18] M. Boonekamp *et al.*, these proceedings.

[19] R. Sacchi, these proceedings (web version only).

[20] P. Newman and F.-P. Schilling, these proceedings.

[21] M. Groys, A. Levy and A. Proskuryakov, these proceedings.

[22] A. Martin, M. Ryskin and G. Watt, these proceedings.

[23] F.-P. Schilling, these proceedings.

[24] P. Newman, these proceedings.

[25] J. C. Collins, Phys. Rev. D **57** (1998) 3051, Erratum ibid. D **61** (2000) 019902 [hep-ph/9709499].

[26] ZEUS Collaboration, Paper 268 submitted to the XXII International Symposium on Lepton–Photon Interactions at High Energy, Uppsala, Sweden, June 2005, avalaible from http:www-zeus.desy.de ; I. Melzer-Pellman for the ZEUS Collaboration, talk at International Conference on the Structure and Interactions of the Photon (PHOTON 2005), Warsaw, Poland, August 2005.

[27] A. Bruni, M. Klasen, G. Kramer and S. Schätzel, these proceedings.

[28] M. Klasen and G. Kramer, hep-ph/0506121, to appear in J. Phys. G.

[29] J. Bartels, these proceedings.
[30] G. Watt, A. D. Martin and M. G. Ryskin, these proceedings.
[31] H. Kowalski, these proceedings.
[32] R. Venugopalan, these proceedings.
[33] F. Schrempp, these proceedings.
[34] M. Arneodo and M. Diehl, these proceedings.
[35] E. Gotsman, E. Levin, U. Maor and E. Naftali, these proceedings (web version only).
[36] M. Lublinsky, these proceedings (web version only).
[37] N. Amapane et al., these proceedings.
[38] K. Piotrzkowski, Phys. Rev. D **63** (2001) 071502 [hep-ex/0009065].
[39] K. Piotrzkowski, these proceedings (web version only).
[40] V. A. Khoze, A. D. Martin and M. G. Ryskin, Eur. Phys. J. C **24** (2002) 459 [hep-ph/0201301].

Diffraction for non-believers

Michele Arneodo[a] *and Markus Diehl*[b]
[a]Università del Piemonte Orientale, 28100 Novara, Italy
[b]Deutsches Elektronen-Synchroton DESY, 22603 Hamburg, Germany

Abstract
Diffractive reactions involving a hard scale can be understood in terms of quarks and gluons. These reactions have become a valuable tool for investigating the low-x structure of the proton and the behavior of QCD in the high-density regime, and they may provide a clean environment to study or even discover the Higgs boson at the LHC. In this paper we give a brief introduction to the description of diffraction in QCD. We focus on key features studied in ep collisions at HERA and outline challenges for understanding diffractive interactions at the LHC.

1 Introduction

In hadron-hadron scattering a substantial fraction of the total cross section is due to diffractive reactions. Figure 1 shows the different types of diffractive processes in the collision of two hadrons: in elastic scattering both projectiles emerge intact in the final state, whereas single or double diffractive dissociation corresponds to one or both of them being scattered into a low-mass state; the latter has the same quantum numbers as the initial hadron and may be a resonance or continuum state. In all cases, the energy of the outgoing hadrons a, b or the states X, Y is approximately equal to that of the incoming beam particles, to within a few per cent. The two (groups of) final-state particles are well separated in phase space and in particular have a large gap in rapidity between them.

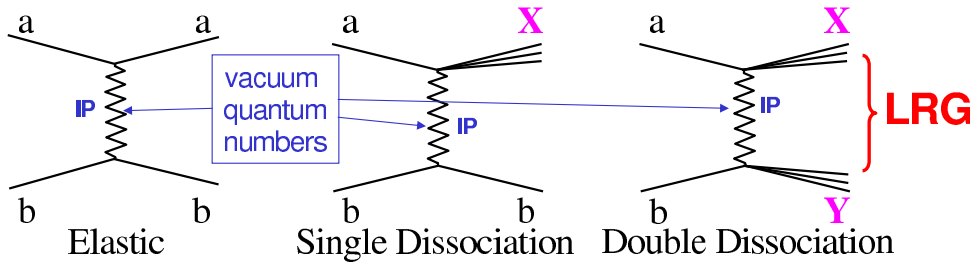

Fig. 1: Elastic scattering, single diffractive dissociation and double diffractive dissociation in the collision of two hadrons a and b. The two (groups of) final-state hadrons are separated by a large rapidity gap (LRG). The zigzag lines denote the exchange of a Pomeron ($I\!P$) in the t-channel. There are further graphs, not shown, with multiple Pomeron exchange.

Diffractive hadron-hadron scattering can be described within Regge theory (see e.g. [1]). In this framework, the exchange of particles in the t-channel is summed coherently to give the exchange of so-called "Regge trajectories". Diffraction is characterized by the exchange of a specific trajectory, the "Pomeron", which has the quantum numbers of the vacuum. Regge theory has spawned a successful phenomenology of soft hadron-hadron scattering at high energies. Developed in the 1960s, it predates the theory of the strong interactions, QCD, and is based on general concepts such as dispersion relations. Subsequently it was found that QCD perturbation theory in the high-energy limit can be organized following the general concepts of Regge theory; this framework is often referred to as BFKL after the authors of the seminal papers [2].

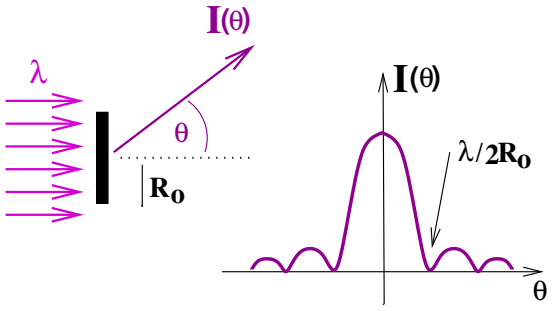

Fig. 2: Distribution of the intensity I in the diffraction of light of wavelength λ from a circular target of size R_0.

It is clear that a t-channel exchange leading to a large rapidity gap in the final state must carry zero net color: if color were exchanged, the color field would lead to the production of further particles filling any would-be rapidity gap. In QCD, Pomeron exchange is described by the exchange of two interacting gluons with the vacuum quantum numbers.

The effort to understand diffraction in QCD has received a great boost from studies of diffractive events in ep collisions at HERA (see e.g. [3] for further reading and references). The essential results of these studies are discussed in the present paper and can be summarized as follows:

- Many aspects of diffraction are well understood in QCD when a hard scale is present, which allows one to use perturbative techniques and thus to formulate the dynamics in terms of quarks and gluons. By studying what happens when the hard scale is reduced towards the non-perturbative region, it may also be possible to shed light on soft diffractive processes.
- Diffraction has become a tool to investigate low-momentum partons in the proton, notably through the study of diffractive parton densities in inclusive processes and of generalized parton distributions in exclusive ones. Diffractive parton densities can be interpreted as conditional probabilities to find a parton in the proton when the final state of the process contains a fast proton of given four-momentum. Generalized parton distributions, through their dependence on both longitudinal and transverse variables, provide a three-dimensional picture of the proton in high-energy reactions.
- A fascinating link has emerged between diffraction and the physics of heavy-ion collisions through the concept of saturation, which offers a new window on QCD dynamics in the regime of high parton densities.

Perhaps unexpectedly, the production of the Higgs boson in diffractive pp collisions is drawing more and more attention as a clean channel to study the properties of a light Higgs boson or even discover it. This is an example of a new theoretical challenge: to adapt and apply the techniques for the QCD description of diffraction in ep collisions to the more complex case of pp scattering at the LHC. A first glimpse of phenomena to be expected there is provided by the studies of hard diffraction in $p\bar{p}$ collisions at the Tevatron.

1.1 A digression on the nomenclature: why "diffraction" ?

Physics students first encounter the term "diffraction" in optics. Light of wavelength λ impinging on a black disk of radius R_0 produces on a distant screen a diffraction pattern, characterized by a large forward peak for scattering angle $\theta = 0$ (the "diffraction peak") and a series of symmetric minima and maxima, with the first minimum at $\theta_{\min} \simeq \pm\lambda/(2R_0)$ (Fig. 2). The intensity I as a function of the scattering angle θ is given by

$$\frac{I(\theta)}{I(\theta=0)} = \frac{[2J_1(x)]^2}{x^2} \simeq 1 - \frac{R_0^2}{4}(k\theta)^2, \tag{1}$$

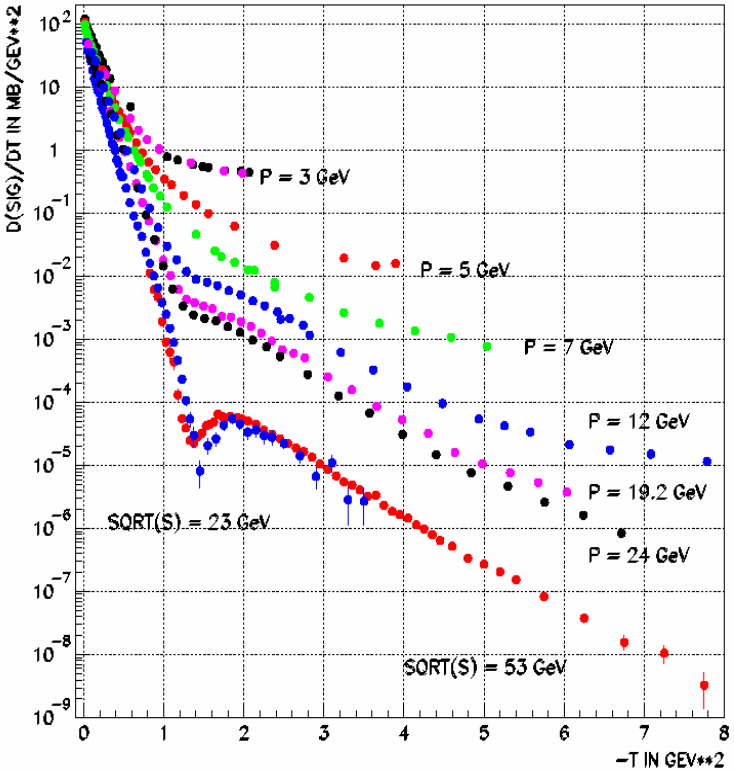

Fig. 3: Compilation of proton-proton elastic cross section data as a function of t. The symbol P indicates the momentum of the incoming proton in a fixed target experiment and $\sqrt{s}$ the center-of-mass energy in a pp collider setup.

where J_1 is the Bessel function of the first order and $x = kR_0 \sin\theta \simeq kR_0\,\theta$ with $k = 2\pi/\lambda$. The diffraction pattern is thus related to the size of the target and to the wavelength of the light beam.

As shown in Fig. 3, the differential cross section $d\sigma/dt$ for elastic proton-proton scattering, $pp \to pp$, bears a remarkable resemblance to the diffraction pattern just described (see e.g. [4]). At low values of $|t|$ one has

$$\frac{\frac{d\sigma}{dt}(t)}{\frac{d\sigma}{dt}(t=0)} \simeq e^{-b|t|} \simeq 1 - b\,(P\theta)^2, \tag{2}$$

where $|t| \simeq (P\theta)^2$ is the absolute value of the squared four-momentum transfer, P is the incident proton momentum and θ is the scattering angle. The t-slope b can be written as $b = R^2/4$, where once again R is related to the target size (or more precisely to the transverse distance between projectile and target). A dip followed by a secondary maximum has also been observed, with the value of $|t|$ at which the dip appears decreasing with increasing proton momentum. It is hence not surprising that the term diffraction is used for elastic pp scattering. Similar t distributions have been observed for the other diffractive reactions mentioned above, leading to the use of the term diffraction for all such processes.

1.2 Diffraction at HERA ?!

Significant progress in understanding diffraction has been made at the ep collider HERA, where 27.5 GeV electrons or positrons collide with 820 or 920 GeV protons. This may sound peculiar: diffraction is a typical hadronic process while ep scattering at HERA is an electro-weak reaction, where the electron

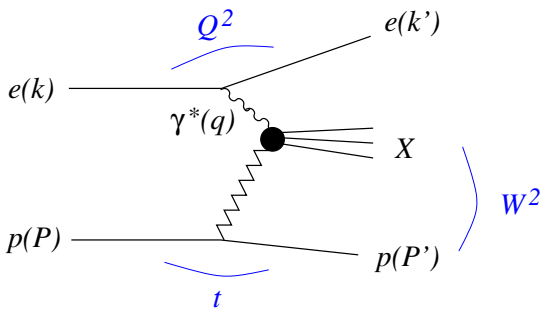

Fig. 4: Schematic diagram of inclusive diffractive DIS, $ep \to eXp$. Four-momenta are indicated in parentheses.

radiates a virtual photon (or a Z or W boson), which then interacts with the proton.[1] To understand this, it is useful to look at ep scattering in a frame where the virtual photon moves very fast (for instance in the proton rest frame, where the γ^* has a momentum of up to about 50 TeV at HERA). The virtual photon can fluctuate into a quark-antiquark pair. Because of its large Lorentz boost, this virtual pair has a lifetime much longer than a typical strong interaction time. In other words, the photon fluctuates into a pair long before the collision, and it is the pair that interacts with the proton. This pair is a small color dipole. Since the interaction between the pair and the proton is mediated by the strong interaction, diffractive events are possible.

An advantage of studying diffraction in ep collisions is that, for sufficiently large photon virtuality Q^2, the typical transverse dimensions of the dipole are small compared to the size of a hadron. Then the interaction between the quark and the antiquark, as well as the interaction of the pair with the proton, can be treated perturbatively. With decreasing Q^2 the color dipole becomes larger, and at very low Q^2 these interactions become so strong that a description in terms of quarks and gluons is no longer justified. We may then regard the photon as fluctuating into a vector meson – this is the basis of the well-known vector meson dominance model – and can therefore expect to see diffractive reactions very similar to those in hadron-hadron scattering.

A different physical picture is obtained in a frame where the incident proton is very fast. Here, the diffractive reaction can be seen as the deep inelastic scattering (DIS) of a virtual photon on the proton target, with a very fast proton in the final state. One can thus expect to probe partons in the proton in a very specific way. For suitable diffractive processes there are in fact different types of QCD factorization theorems, which bear out this expectation (see Sects. 2 and 3).

2 Inclusive diffractive scattering in ep collisions

Figure 4 shows a schematic diagram of inclusive diffractive DIS. The following features are important:

- The proton emerges from the interaction carrying a large fraction x_L of the incoming proton momentum. Diffractive events thus appear as a peak at $x_L \approx 1$, the diffractive peak, which at HERA approximately covers the region $0.98 < x_L < 1$ (see the left panel of Fig. 5). The right panel of Fig. 5 shows that large values of $|t|$ are exponentially suppressed, similarly to the case of elastic pp scattering we discussed in Sect. 1.1. These protons remain in the beam-pipe and can only be measured with detectors located inside the beam-pipe.
- The collision of the virtual photon with the proton produces a hadronic final state X with the photon quantum numbers and invariant mass M_X. A large gap in rapidity (or pseudorapidity) is present between X and the final-state proton. Figure 6 shows a typical diffractive event at HERA.

[1] For simplicity we will speak of a virtual photon in the following, keeping in mind that one can have a weak gauge boson instead.

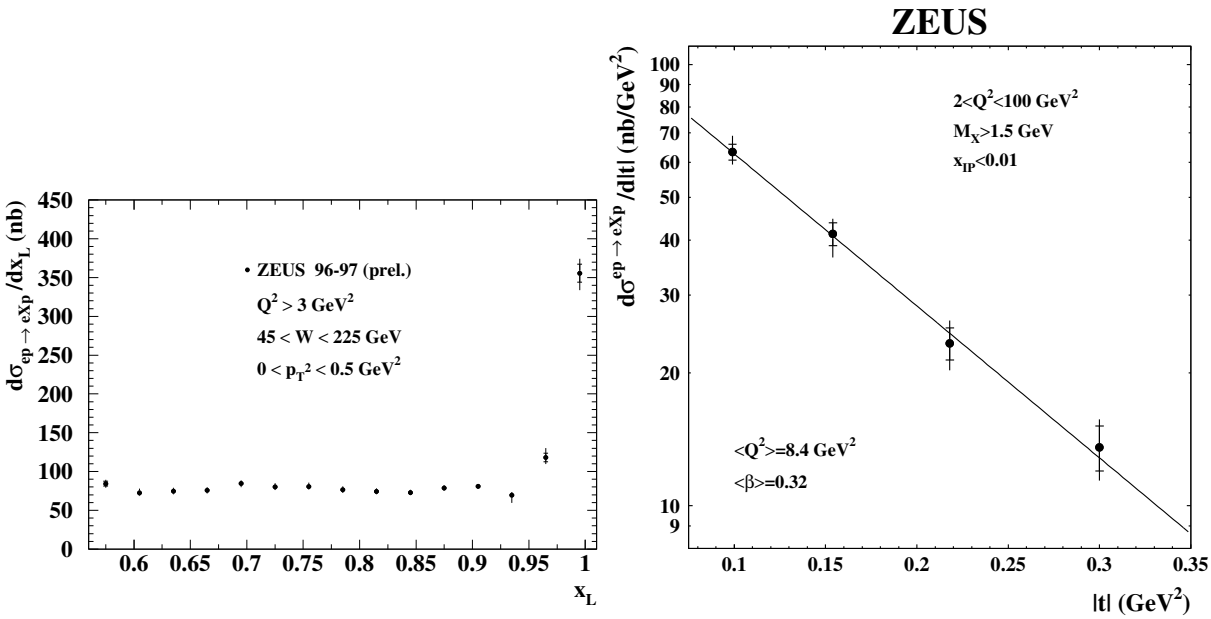

Fig. 5: Left: Differential cross section $d\sigma/dx_L$ for the process $ep \to eXp$ (from [5]). The diffractive peak at $x_L \approx 1$ is clearly visible. Right: Differential cross section $d\sigma/dt$ for the same process for $x_L > 0.99$ (from [6]). The average $|t|$ of this spectrum is $\langle|t|\rangle \approx 0.15$ GeV^2.

Diffractive ep scattering thus combines features of hard and soft scattering. The electron receives a large momentum transfer; in fact Q^2 can be in the hundreds of GeV^2. In contrast, the proton emerges with its momentum barely changed.

2.1 Diffractive structure functions

The kinematics of $\gamma^* p \to Xp$ can be described by the invariants $Q^2 = -q^2$ and $t = (P - P')^2$, and by the scaling variables $x_{I\!P}$ and β given by

$$x_{I\!P} = \frac{(P - P') \cdot q}{P \cdot q} = \frac{Q^2 + M_X^2 - t}{W^2 + Q^2 - M_p^2}, \qquad \beta = \frac{Q^2}{2(P - P') \cdot q} = \frac{Q^2}{Q^2 + M_X^2 - t}, \tag{3}$$

where $W^2 = (P + q)^2$ and the four-momenta are defined in Fig. 4. The variable $x_{I\!P}$ is the fractional momentum loss of the incident proton, related as $x_{I\!P} \simeq 1 - x_L$ to the variable x_L introduced above. The quantity β has the form of a Bjorken variable defined with respect to the momentum $P - P'$ lost by the initial proton instead of the initial proton momentum P. The usual Bjorken variable $x_B = Q^2/(2P \cdot q)$ is related to β and $x_{I\!P}$ as $\beta x_{I\!P} = x_B$.

The cross section for $ep \to eXp$ in the one-photon exchange approximation can be written in terms of diffractive structure functions $F_2^{D(4)}$ and $F_L^{D(4)}$ as

$$\frac{d\sigma^{ep\to eXp}}{d\beta\, dQ^2\, dx_{I\!P}\, dt} = \frac{4\pi\alpha_{\rm em}^2}{\beta Q^4}\left[\left(1 - y + \frac{y^2}{2}\right)F_2^{D(4)}(\beta, Q^2, x_{I\!P}, t) - \frac{y^2}{2}F_L^{D(4)}(\beta, Q^2, x_{I\!P}, t)\right], \tag{4}$$

in analogy with the way $d\sigma^{ep\to eX}/(dx_B\, dQ^2)$ is related to the structure functions F_2 and F_L for inclusive DIS, $ep \to eX$. Here $y = (P \cdot q)/(P \cdot k)$ is the fraction of energy lost by the incident lepton in the proton rest frame. The structure function $F_L^{D(4)}$ corresponds to longitudinal polarization of the virtual photon;

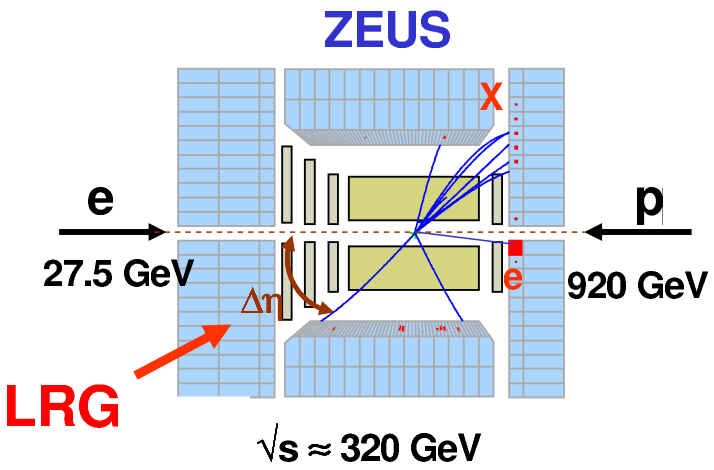

Fig. 6: A DIS event with a large rapidity gap (LRG) observed with the ZEUS detector at HERA. The scattered proton escapes into the beam-pipe. The symbol $\Delta\eta$ denotes the difference in pseudorapidity between the scattered proton and the most forward particle of the observed hadronic system X. Pseudorapidity is defined as $\eta = -\ln\tan(\theta/2)$ in terms of the polar angle θ measured with respect to the incoming proton direction, which is defined as "forward".

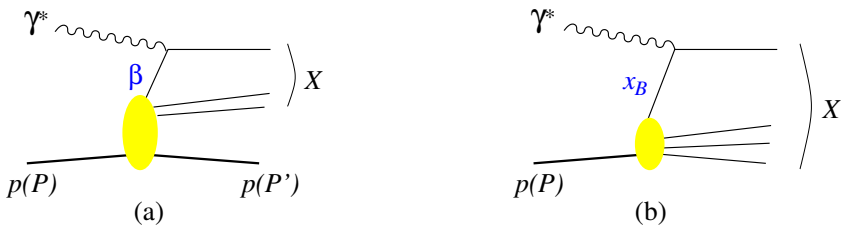

Fig. 7: Parton model diagrams for deep inelastic diffractive (a) and inclusive (b) scattering. The variable β is the momentum fraction of the struck quark with respect to $P - P'$, and x_B its momentum fraction with respect to P.

its contribution to the cross section is small in a wide range of the experimentally accessible kinematic region (in particular at low y). The structure function $F_2^{D(3)}$ is obtained from $F_2^{D(4)}$ by integrating over t:

$$F_2^{D(3)}(\beta, Q^2, x_{I\!P}) = \int dt\, F_2^{D(4)}(\beta, Q^2, x_{I\!P}, t). \tag{5}$$

In a parton model picture, inclusive diffraction $\gamma^* p \to Xp$ proceeds by the virtual photon scattering on a quark, in analogy to inclusive scattering (see Fig. 7). In this picture, β is the momentum fraction of the struck quark with respect to the exchanged momentum $P - P'$ (indeed the allowed kinematical range of β is between 0 and 1). The diffractive structure function describes the proton structure in these specific processes with a fast proton in the final state. F_2^D may also be viewed as describing the structure of whatever is exchanged in the t-channel in diffraction, i.e. of the Pomeron (if multiple Pomeron exchange can be neglected). It is however important to bear in mind that the Pomeron in QCD cannot be interpreted as a particle on which the virtual photon scatters, as we will see in Sect. 2.5.

Figures 8 and 9 show recent H1 data [7] on $F_2^{D(3)}$ at fixed $x_{I\!P}$ as a function of β for different Q^2 bins, and as a function of Q^2 for different bins of β.[2] The data have two remarkable features:

[2]To be precise, the H1 data are for the so-called reduced diffractive cross section, which equals $F_2^{D(3)}$ if F_L^D can be neglected.

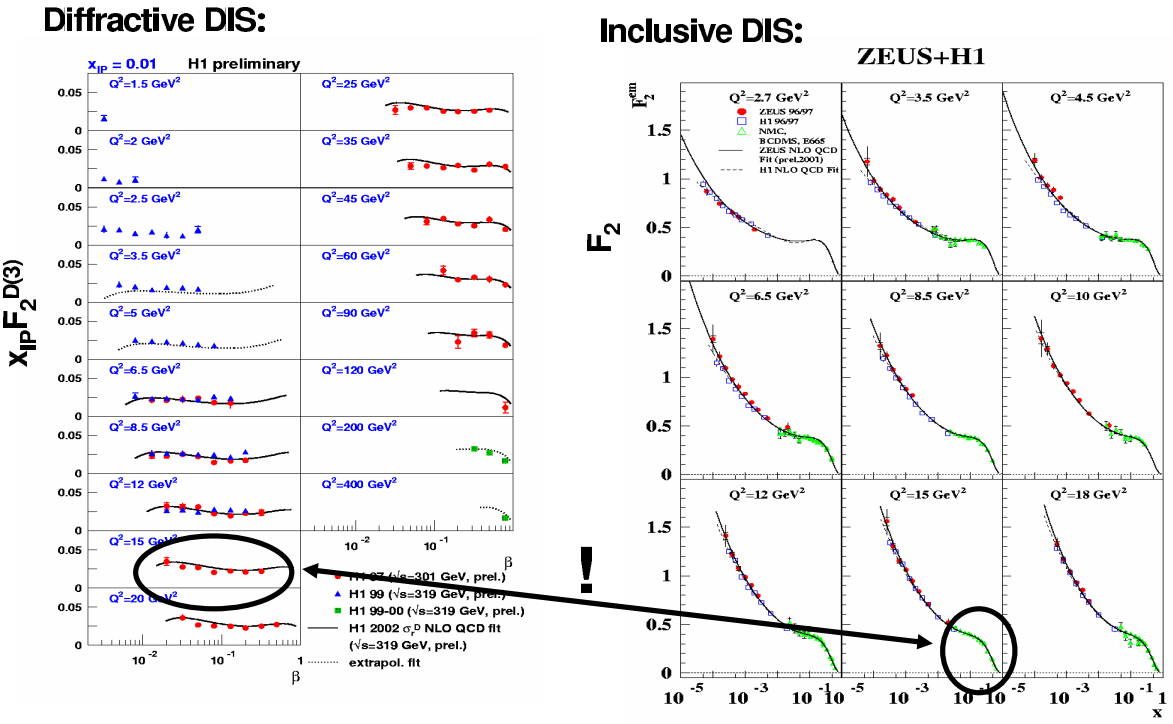

Fig. 8: Left: the diffractive structure function of the proton as a function of β (from [7]). Right: the structure function of the proton as a function of x_B (from [8]). The two highlighted bins show the different shapes of F_2^D and F_2 in corresponding ranges of β and x_B at equal Q^2.

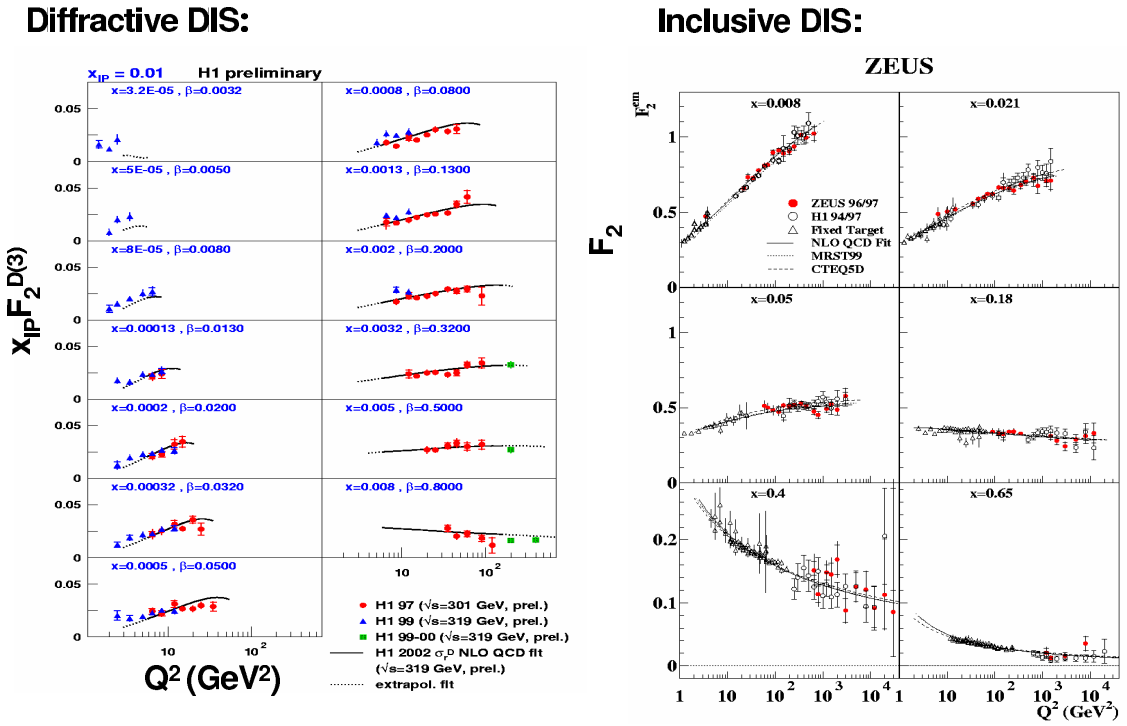

Fig. 9: Left: the diffractive structure function of the proton as a function of Q^2 (from [7]). Right: the structure function of the proton as a function of Q^2 (from [9]).

– F_2^D is largely flat in the measured β range. Keeping in mind the analogy between β in diffractive DIS and x_B in inclusive DIS, this is very different from the behavior of the "usual" structure function F_2, which strongly decreases for $x_B \gtrsim 0.2$ (see Fig. 8).
– The dependence on Q^2 is logarithmic, i.e. one observes approximate Bjorken scaling. This indicates the applicability of the parton model picture to inclusive $\gamma^* p$ diffraction. The structure function F_2^D increases with Q^2 for all β values except the highest. This is reminiscent of the scaling violations of F_2, except that F_2 rises with Q^2 only for $x_B \lesssim 0.2$ and that the scaling violations become negative at higher x_B (see Fig. 9). In the proton, negative scaling violations reflect the presence of the valence quarks radiating gluons, while positive scaling violations are due to the increase of the sea quark and gluon densities as the proton is probed with higher resolution. The F_2^D data thus suggest that the partons resolved in diffractive events are predominantly gluons. This is not too surprising if one bears in mind that these partons carry only a small part of the proton momentum: the struck quark in the diagram of Fig. 7a has a momentum fraction $\beta x_{I\!P} = x_B$ with respect to the incident proton, and $x_{I\!P} \lesssim 0.02 - 0.03$ in diffractive events.

2.2 Diffractive parton distributions

The conclusion just reached can be made quantitative by using the QCD factorization theorem for inclusive diffraction, $\gamma^* p \to Xp$, which formalizes the parton model picture we have already invoked in our discussion. According to this theorem, the diffractive structure function, in the limit of large Q^2 at fixed β, $x_{I\!P}$ and t, can be written as [10–12]

$$F_2^{D(4)}(\beta, Q^2, x_{I\!P}, t) = \sum_i \int_\beta^1 \frac{dz}{z}\, C_i\Big(\frac{\beta}{z}\Big)\, f_i^D(z, x_{I\!P}, t; Q^2), \tag{6}$$

where the sum is over partons of type i. The coefficient functions C_i describe the scattering of the virtual photon on the parton and are exactly the same as in inclusive DIS. In analogy to the usual parton distribution functions (PDFs), the diffractive PDFs $f_i^D(z, x_{I\!P}, t; Q^2)$ can be defined as operator matrix elements in a proton state, and their dependence on the scale Q^2 is given by the DGLAP evolution equations. In parton model language, they can be interpreted as conditional probabilities to find a parton i with fractional momentum $z x_{I\!P}$ in a proton, probed with resolution Q^2 in a process with a fast proton in the final state (whose momentum is specified by $x_{I\!P}$ and t).

During the workshop, several fits of the available F_2^D data were discussed which are based on the factorization formula (6) at next-to-leading order (NLO) in α_s [13,14]. Figure 10 compares the diffractive PDFs from an earlier H1 fit [7] to those from the fit of the ZEUS data [15] by Schilling and Newman [13]. As expected the density of gluons is larger than that of quarks, by about a factor 5–10. Discrepancies between the two sets are evident, and it remains to be clarified to which extent they reflect differences in the fitted data. Martin, Ryskin and Watt [16] have argued that the leading-twist formula (6) is inadequate in large parts of the measured kinematics, and performed a fit to a modified expression which includes an estimate of power-suppressed effects. The discrepancies between the various diffractive PDFs, while not fully understood, may be taken as an estimate of the uncertainties on these functions at this point in time. A precise and consistent determination of the diffractive PDFs and their uncertainties is one of the main tasks the HERA community has to face in the near future. They are a crucial input for predicting cross sections of inclusive diffractive processes at the LHC.

2.3 Diffractive hard-scattering factorization

Like usual parton densities, diffractive PDFs are process-independent functions. They appear not only in inclusive diffraction but also in other processes where diffractive hard-scattering factorization holds. In analogy with Eq. (6), the cross section of such a process can be evaluated as the convolution of the relevant parton-level cross section with the diffractive PDFs. For instance, the cross section for charm

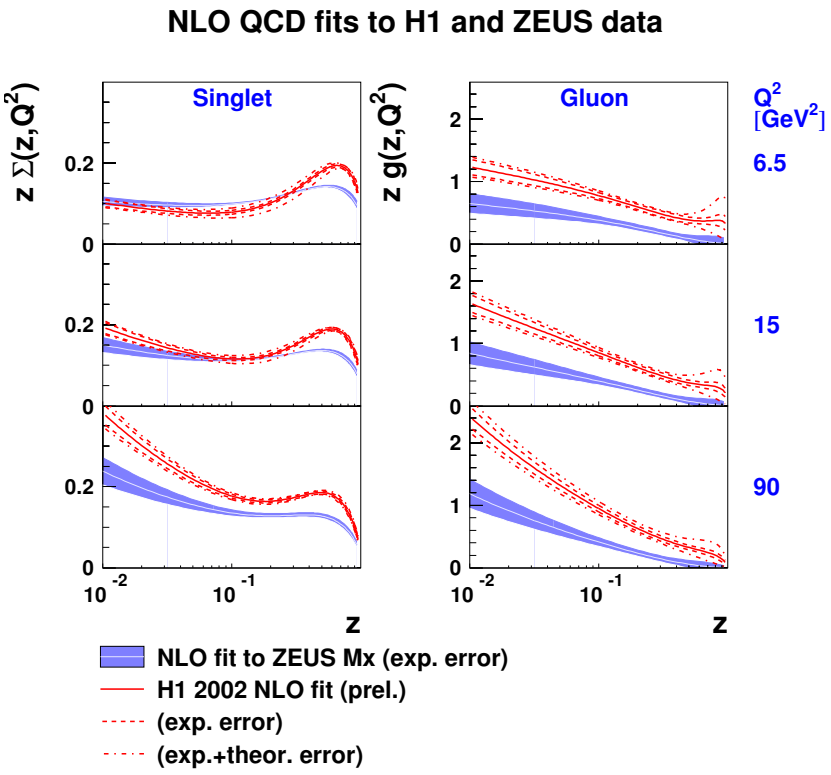

Fig. 10: Diffractive quark singlet and gluon distributions obtained from fits to H1 [7] and ZEUS [15] data (from [13]).

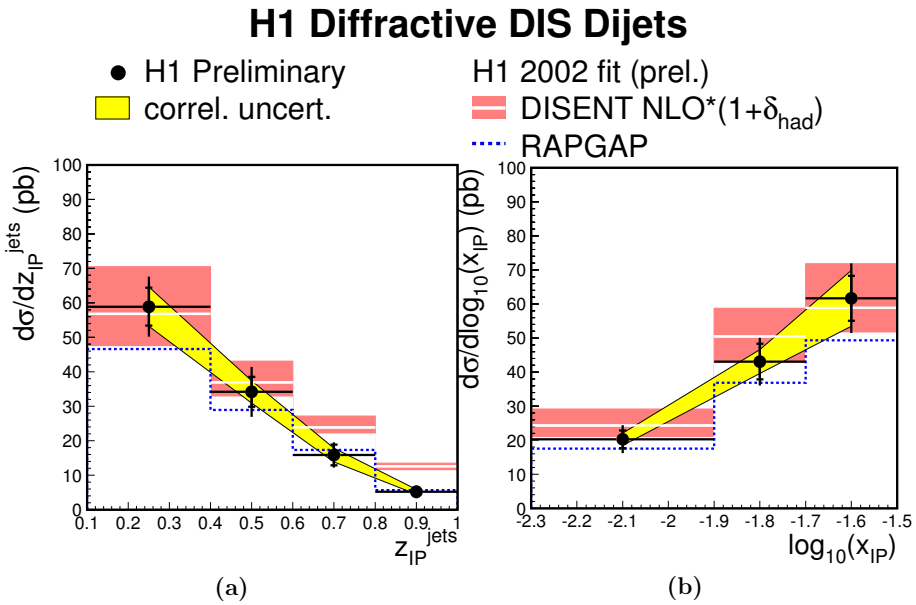

(a) (b)

Fig. 11: Cross section for dijet production in diffractive DIS, compared with the expectations based on the diffractive PDFs [7] (from [17]). The variable $z_{I\!P}^{\rm jets}$ estimates the fractional momentum of the parton entering the hard subprocess.

production in diffractive DIS can be calculated at leading order in α_s from the $\gamma^* g \to c\bar{c}$ cross section and the diffractive gluon distribution. An analogous statement holds for jet production in diffractive DIS. Both processes have been analyzed at next-to-leading order in α_s.

As an example, Fig. 11 shows a comparison between the measured cross sections for diffractive dijet production and the expectations based on diffractive PDFs extracted from a fit to F_2^D. These data lend support to the validity of hard-scattering factorization in diffractive $\gamma^* p$ interactions. For further discussion we refer the reader to [18].

2.4 Limits of diffractive hard-scattering factorization: hadron-hadron collisions

A natural question to ask is whether one can use the diffractive PDFs extracted at HERA to describe hard diffractive processes such as the production of jets, heavy quarks or weak gauge bosons in $p\bar{p}$ collisions at the Tevatron. Figure 12 shows results on diffractive dijet production from the CDF collaboration [19] compared to the expectations based on the diffractive PDFs [6, 7] from HERA. The discrepancy is spectacular: the fraction of diffractive dijet events at CDF is a factor 3 to 10 smaller than would be expected on the basis of the HERA data. The same type of discrepancy is consistently observed in all hard diffractive processes in $p\bar{p}$ events, see e.g. [20]. In general, while at HERA hard diffraction contributes a fraction of order 10% to the total cross section, it contributes only about 1% at the Tevatron.

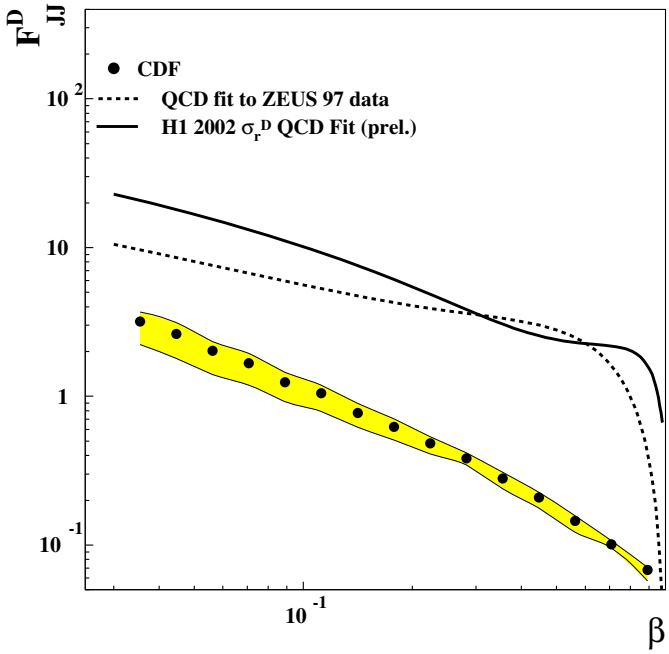

Fig. 12: CDF results for the cross section of diffractive dijet production with a leading antiproton in $p\bar{p}$ collisions (expressed in terms of a structure function F_{JJ}^D), compared with the predictions obtained from the diffractive PDFs [6] and [7] extracted at HERA (from [21]). See also the analogous plot in the original CDF publication [19].

In fact, diffractive hard-scattering factorization does not apply to hadron-hadron collisions [11,12]. Attempts to establish corresponding factorization theorems fail because of interactions between spectator partons of the colliding hadrons. The contribution of these interactions to the cross section does not decrease with the hard scale. Since they are not associated with the hard-scattering subprocess (see Fig. 13), we no longer have factorization into a parton-level cross section and the parton densities of one of the colliding hadrons. These interactions are generally soft, and we have at present to rely on phenomenological models to quantify their effects [22].

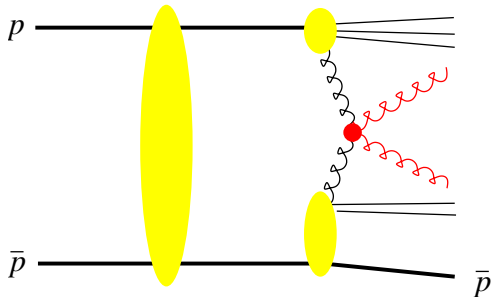

Fig. 13: Example graph for diffractive dijet production with a leading antiproton in a $p\bar{p}$ collision. The interaction indicated by the large vertical blob breaks hard diffractive factorization. It reduces the diffractive cross section, as explained in the text.

The yield of diffractive events in hadron-hadron collisions is lowered precisely because of these soft interactions between spectator partons (often referred to as "reinteractions" or "multiple scatterings"). They can produce additional final-state particles which fill the would-be rapidity gap (hence the often-used term "rapidity gap survival"). When such additional particles are produced, a very fast proton can no longer appear in the final state because of energy conservation. Diffractive factorization breaking is thus intimately related to multiple scattering in hadron-hadron collisions; understanding and describing this phenomenon is a challenge in the high-energy regime that will be reached at the LHC [23].

In pp or $p\bar{p}$ reactions, the collision partners are both composite systems of large transverse size, and it is not too surprising that multiple interactions between their constituents can be substantial. In contrast, the virtual photon in $\gamma^* p$ collisions has small transverse size, which disfavors multiple interactions and enables diffractive factorization to hold. According to our discussion in Sect. 1.2, we may expect that for decreasing virtuality Q^2 the photon behaves more and more like a hadron, and diffractive factorization may again be broken. This aspect of diffractive processes in photoproduction at HERA was intensively discussed during the workshop, and findings are reported in [18].

2.5 Space-time structure: the Pomeron is not a particle

It is tempting to interpret diffractive $\gamma^* p$ processes as the scattering of a virtual photon on a Pomeron which has been radiated off the initial proton. Diffractive DIS would then probe the distribution of partons in a "Pomeron target". This is indeed the picture proposed by Ingelman and Schlein long ago [24].

This picture is however not supported by an analysis in QCD (see e.g. [25]). There, high-energy scattering is dominated by the exchange of two gluons, whose interaction is (in an appropriate gauge) described by ladder diagrams, as shown in Fig. 14. By analyzing these diagrams in time-ordered perturbation theory, one can obtain the dominant space-time ordering in the high-energy limit. The result depends on the reference frame, as illustrated in the figure. In the Breit frame, which is natural for a parton-model interpretation, the photon does *not* scatter off a parton in a pre-existing two-gluon system; in fact some of the interactions in the gluon ladder building up the Pomeron exchange take place long after the virtual photon has been absorbed. The picture in the Breit frame is however compatible with the interpretation of diffractive parton densities given in Sect. 2.2, namely the probability to find a parton under the condition that subsequent interactions will produce a fast proton in the final state.

We note that the Ingelman-Schlein picture suggests that the diffractive structure function takes a factorized form $F_2^{D(4)} = f_{I\!P}(x_{I\!P}, t)\, F_2^{I\!P}(\beta, Q^2)$, where $f_{I\!P}$ is the "Pomeron flux" describing the emission of the Pomeron from the proton and its subsequent propagation, and where $F_2^{I\!P}$ is the "structure function of the Pomeron". Phenomenologically, such a factorizing ansatz works not too badly and is often used, but recent high-precision data have shown its breakdown at small $x_{I\!P}$ [15].

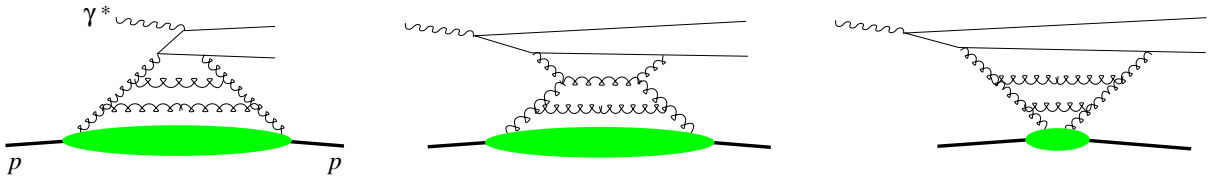

Fig. 14: Dominant time ordering for diffractive dissociation of a virtual photon in (a) the Breit frame, (b) the photon-proton center-of-mass, (c) the proton rest frame. The physical picture in (a) corresponds to the parton-model description of diffraction, and the one in (b) and (c) to the picture of the photon splitting into a quark-antiquark dipole which subsequently interacts with the proton.

3 Exclusive diffractive processes

Let us now discuss diffractive processes where a real or virtual photon dissociates into a single particle. Since diffraction involves the exchange of vacuum quantum numbers, this particle can in particular be a vector meson (which has the same J^{PC} quantum numbers as the photon) – in this case the process is sometimes referred to as "elastic" vector meson production. Another important case is deeply virtual Compton scattering (DVCS), $\gamma^* p \to \gamma p$.[3] A striking feature of the data taken at HERA (Figs. 15 and 16) is that the energy dependence of these processes becomes steep in the presence of a hard scale, which can be either the photon virtuality Q^2 or the mass of the meson in the case of J/Ψ or Υ production. This is similar to the energy dependence of the $\gamma^* p$ total cross section (related by the optical theorem to forward Compton scattering, $\gamma^* p \to \gamma^* p$), which changes from flat to steep when going from real photons to Q^2 of a few GeV^2.

To understand this similarity, let us recall that in perturbative QCD diffraction proceeds by two-gluon exchange. The transition from a virtual photon to a real photon or to a quark-antiquark pair subsequently hadronizing into a meson is a short-distance process involving these gluons, provided that either Q^2 or the quark mass is large. In fact, in an approximation discussed below, the cross sections for DVCS and vector meson production are proportional to the square of the gluon distribution in the proton, evaluated at a scale of order $Q^2 + M_V^2$ and at a momentum fraction $x_{I\!P} = (Q^2 + M_V^2)/(W^2 + Q^2)$, where the vector meson mass M_V now takes the role of M_X in inclusive diffraction [28]. In analogy to the case of the total $\gamma^* p$ cross section, the energy dependence of the cross sections shown in Figs. 15 and 16 thus reflects the x and scale dependence of the gluon density in the proton, which grows with decreasing x with a slope becoming steeper as the scale increases.

There is however an important difference in how the gluon distribution enters the descriptions of inclusive DIS and of exclusive diffractive processes. The inclusive DIS cross section is related via the optical theorem to the imaginary part of the forward virtual Compton amplitude, so that the graphs in Fig. 17 represent the *cross section* of the inclusive process. Hence, the gluon distribution in Fig. 17a gives the *probability* to find *one* gluon in the proton (with any number of unobserved spectator partons going into the final state). In contrast, the corresponding graphs for DVCS and exclusive meson production in Fig. 18 represent the *amplitudes* of exclusive processes, which are proportional to the *probability amplitude* for first extracting a gluon from the initial proton and then returning it to form the proton in the final state. In the approximation discussed below, this probability amplitude is given by the gluon distribution. The cross sections of DVCS and exclusive meson production are then proportional to the *square* of the gluon distribution.

A detailed theoretical analysis of DVCS and exclusive meson production at large Q^2 shows that short-distance factorization holds, in analogy to the case of inclusive DIS. QCD factorization theorems [29] state that in the limit of large Q^2 (at fixed Bjorken variable x_B and fixed t) the Compton

[3] We do not discuss processes with diffractive dissociation of the proton in this paper, but wish to mention interesting studies of vector meson or real photon production at large $|t|$, where the proton predominantly dissociates, see e.g. [26].

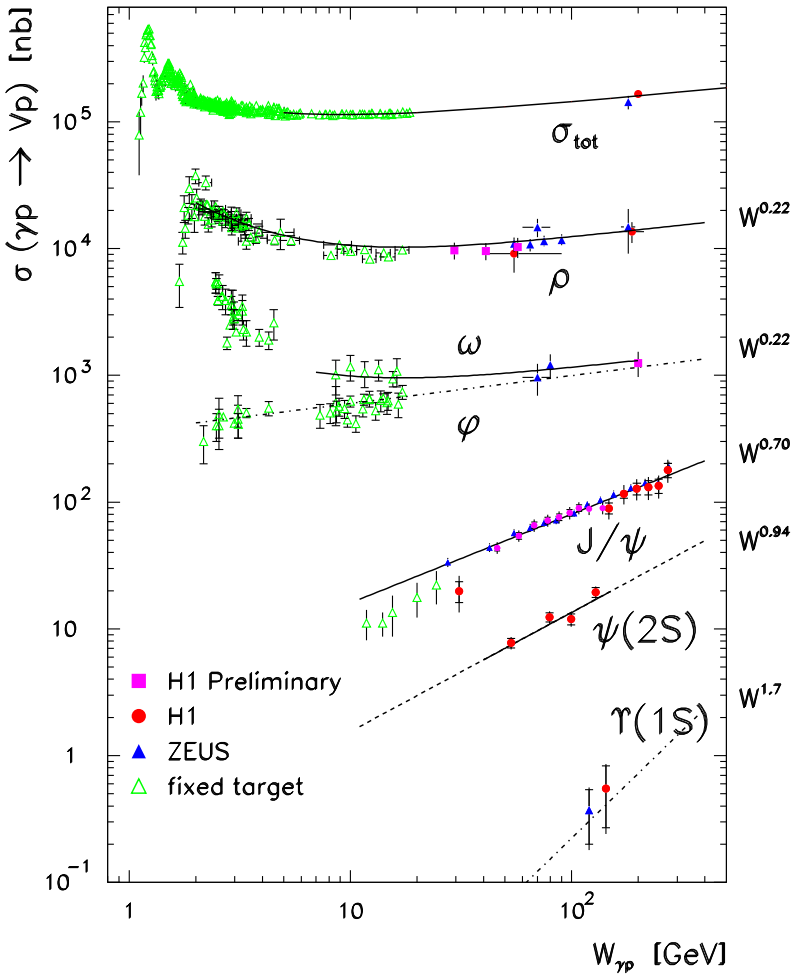

Fig. 15: Compilation of results on the cross section for vector meson photoproduction, $\gamma p \to Vp$, with $V = \rho, \omega, \phi, J/\Psi, \psi', \Upsilon$, as a function W. The total γp cross section $\sigma_{\rm tot}$ is also shown.

amplitude factorizes into a hard-scattering subprocess and a hadronic matrix element describing the emission and reabsorption of a parton by the proton target (see Fig. 18a). As shown in Fig. 18b, the analogous result for exclusive meson production involves in addition the quark-antiquark distribution amplitude of the meson (often termed the meson wave function) and thus a further piece of non-perturbative input.

The hadronic matrix elements appearing in the factorization formulae for exclusive processes would be the usual PDFs if the proton had the same momentum in the initial and final state. Since this is not the case, they are more general functions taking into account the momentum difference between the initial and final state proton (or, equivalently, between the emitted and reabsorbed parton). These "generalized parton distributions" (GPDs) depend on two independent longitudinal momentum fractions instead of a single one (compare Figs. 17a and 18a), on the transverse momentum transferred to the proton (whose square is $-t$ to a good approximation at high energy), and on the scale at which the partons are probed. The scale dependence of the GPDs is governed by a generalization of the DGLAP equations. The dependence on the difference of the longitudinal momenta (often called "skewness") contains information on correlations between parton momenta in the proton wave function. It can be neglected in the approximation of leading $\log x$ (then the GPDs at $t = 0$ reduce to the usual PDFs as anticipated above), but it is numerically important in typical HERA kinematics. The dependence on t allows for a very intuitive interpretation if a Fourier transformation is performed with respect to the transverse momentum transfer. We then obtain distributions depending on the impact parameter of the

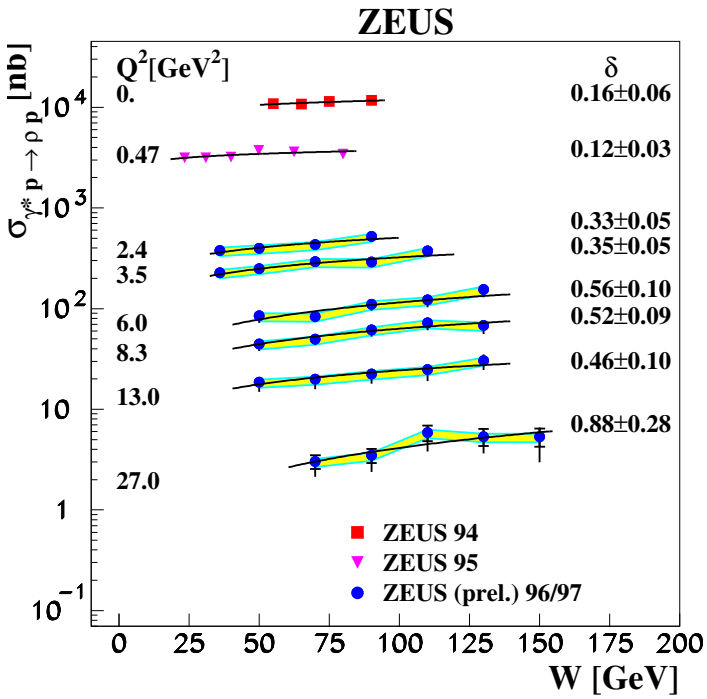

Fig. 16: Cross section for exclusive ρ production as a function of W (from [27]). The lines represent the result of fits to the data with the form $\sigma(\gamma^* p \to \rho p) \propto W^\delta$, yielding the exponents given in the figure.

partons, which describe the two-dimensional distribution of the struck parton in the transverse plane, and on its longitudinal momentum fraction in the proton. The t dependence of exclusive diffractive processes thus provides unique information beyond the longitudinal momentum spectra encoded in the usual parton densities. The study of the generalized parton distributions is a prime reason to measure DVCS and exclusive meson production in ep scattering. Detailed discussions and references can be found in the recent reviews [30, 31].

An observable illustrating the short-distance factorization in meson production at high Q^2 is the ratio of the ϕ and ρ production cross sections, shown in Fig. 19. At large Q^2 the process is described in terms of a light quark coupling to the photon and of the generalized gluon distribution. Using approximate flavor SU(3) symmetry between the ρ and ϕ wave functions, the only difference between the two channels is then due to different quark charge and isospin factors, which result in a cross section ratio of $2/9$.

3.1 High-energy factorization and the dipole picture

So far we have discussed the description of hard exclusive diffraction within short-distance, or collinear factorization. A different type of factorization is high-energy, or k_t factorization, which is based on the BFKL formalism. Here the usual or generalized gluon distribution appearing in the factorization formulae depends explicitly on the transverse momentum k_t of the emitted gluon. In collinear factorization, this k_t is integrated over in the parton distributions and set to zero when calculating the hard-scattering process (the partons are thus approximated as "collinear" with their parent hadron). Likewise, the meson wave functions appearing in k_t factorization explicitly depend on the relative transverse momentum between the quark and antiquark in the meson, whereas this is integrated over in the quark-antiquark distribution amplitudes (cf. Sect. 3) of the collinear factorization formalism. Only gluon distributions appear in k_t factorization, whereas collinear factorization formulae involve both quark and gluon distributions (see e.g. Sects. 8.1 and 8.2 in [30] for a discussion of this difference). We note that other

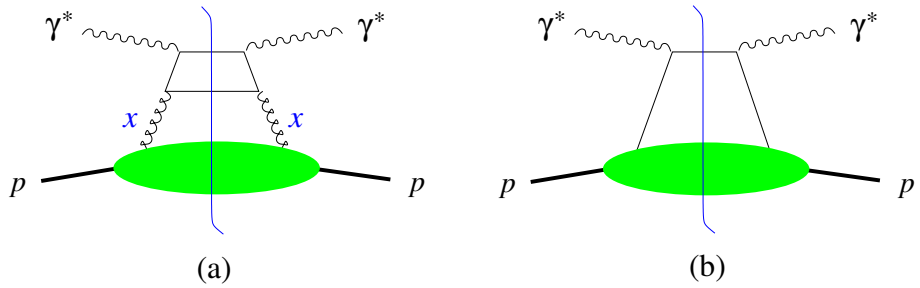

Fig. 17: Factorization of forward Compton scattering, which is related to the total inclusive structure function via the optical theorem, $\mathrm{Im}\,\mathcal{A}(\gamma^* p \to \gamma^* p) = \frac{1}{2}\sum_X |\mathcal{A}(\gamma^* p \to X)|^2 \propto \sigma(\gamma^* p \to X)$. The final state of the inclusive process is obtained by cutting the diagrams along the vertical line. The blobs represent the gluon or quark distribution in the proton. Graph (b) is absent in the k_t factorization formalism (see Sect. 3.1): its role is taken by graph (a) in the "aligned jet configuration", where the quark line joining the two photons carries almost the entire photon momentum.

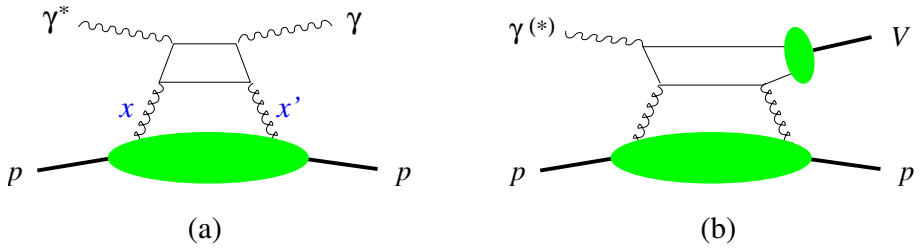

Fig. 18: (a) Factorization of deeply virtual Compton scattering, $\gamma^* p \to \gamma p$, which can be measured in the exclusive process $ep \to ep\gamma$. The blob represents the generalized gluon distribution, with x and x' denoting the momentum fractions of the gluons. (b) Factorization of exclusive meson production. The small blob represents the vector meson wave function. In the collinear factorization formalism, there are further graphs (not shown) involving quark instead of gluon exchange.

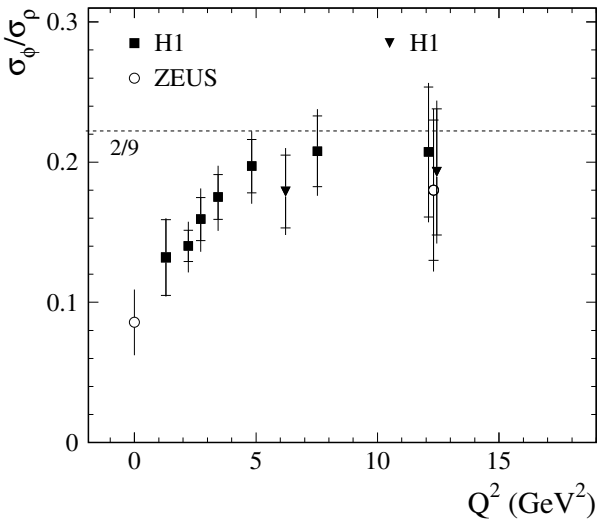

Fig. 19: The ratio of cross sections for $\gamma^* p \to \phi p$ and $\gamma^* p \to \rho p$ as a function of the photon virtuality (from [32]).

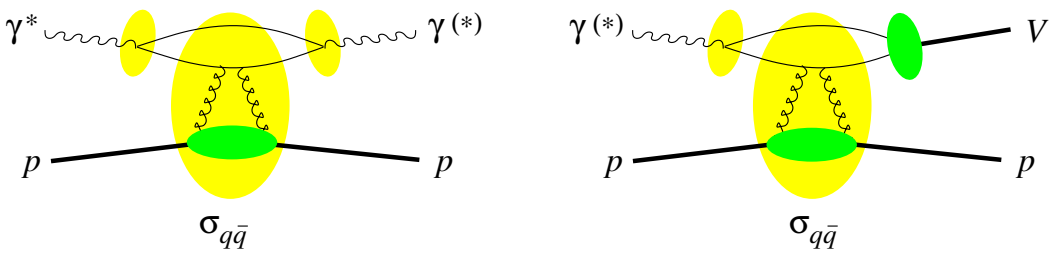

Fig. 20: The dipole representation of the amplitudes for Compton scattering (a) and for meson production (b), corresponding to the graphs in Figs. 17a and 18.

factorization schemes have been developed, which combine features of the collinear and k_t factorization formalisms.

The two different types of factorization implement different ways of separating different parts of the dynamics in a scattering process. The building blocks in a short-distance factorization formula correspond to either small or large particle virtuality (or equivalently to small or large transverse momentum), whereas the separation criterion in high-energy factorization is the particle rapidity. Collinear and k_t factorization are based on taking different limits: in the former case the limit of large Q^2 at fixed x_B and in the latter case the limit of small x_B at fixed Q^2 (which must however be large enough to justify the use of QCD perturbation theory). In the common limit of large Q^2 and small x_B the two schemes give coinciding results. Instead of large Q^2 one can also take a large quark mass in the limits just discussed.

A far-reaching representation of high-energy dynamics can be obtained by casting the results of k_t factorization into a particular form. The different building blocks in the graphs for Compton scattering and meson production in Figs. 17a and 18 can be rearranged as shown in Fig. 20. The result admits a very intuitive interpretation in a reference frame where the photon carries large momentum (this may be the proton rest frame but also a frame where the proton moves fast, see Fig. 14): the initial photon splits into a quark-antiquark pair, which scatters on the proton and finally forms a photon or meson again. This is the picture we have already appealed to in Sect. 1.2.

In addition, one can perform a Fourier transformation and trade the relative transverse momentum between quark and antiquark for their transverse distance r, which is conserved in the scattering on the target. The quark-antiquark pair acts as a color dipole, and its scattering on the proton is described by a "dipole cross section" $\sigma_{q\bar{q}}$ depending on r and on $x_{I\!P}$ (or on x_B in the case of inclusive DIS). The wave functions of the photon and the meson depend on r after Fourier transformation, and at small r the photon wave function is perturbatively calculable. Typical values of r in a scattering process are determined by the inverse of the hard momentum scale, i.e. $r \sim (Q^2 + M_V^2)^{-1/2}$. An important result of high-energy factorization is the relation

$$\sigma_{q\bar{q}}(r, x) \propto r^2 x g(x) \tag{7}$$

at small r, where we have replaced the generalized gluon distribution by the usual one in the spirit of the leading $\log x$ approximation. A more precise version of the relation (7) involves the k_t dependent gluon distribution. The dipole cross section vanishes at $r = 0$ in accordance with the phenomenon of "color transparency": a hadron becomes more and more transparent for a color dipole of decreasing size.

The scope of the dipole picture is wider than we have presented so far. It is tempting to apply it outside the region where it can be derived in perturbation theory, by modeling the dipole cross section and the photon wave function at large distance r. This has been very been fruitful in phenomenology, as we will see in the next section.

The dipole picture is well suited to understand the t dependence of exclusive processes, parameterized as $d\sigma/dt \propto \exp(-b|t|)$ at small t. Figure 21 shows that b decreases with increasing scale $Q^2 + M_V^2$

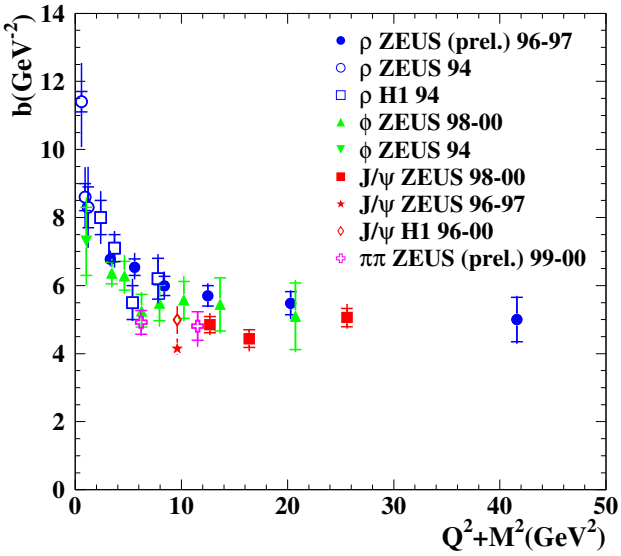

Fig. 21: The logarithmic slope of the t dependence at $t = 0$ for different meson production channels, as well as for non-resonant dipion production.

and at high scales becomes independent of the produced meson. A Fourier transform from momentum to impact parameter space readily shows that b is related to the typical transverse distance between the colliding objects, as anticipated by the analogy with optical diffraction in Sect. 1.1. At high scale, the $q\bar{q}$ dipole is almost pointlike, and the t dependence of the cross section is controlled by the t dependence of the generalized gluon distribution, or in physical terms, by the transverse extension of the proton. As the scale decreases, the dipole acquires a size of its own, and in the case of ρ or ϕ photoproduction, the values of b reflect the fact that the two colliding objects are of typical hadronic dimensions; similar values would be obtained in elastic meson-proton scattering.

3.2 Exclusive diffraction in hadron-hadron collisions

The concepts we have introduced to describe exclusive diffraction can be taken over to pp or $p\bar{p}$ scattering, although further complications appear in these processes. A most notable reaction is exclusive production of a Higgs boson, $pp \to pHp$, sketched in Fig. 22. The generalized gluon distribution is a central input in this description. The physics interest, theory description, and prospects to measure this process at the LHC have been discussed in detail at this workshop [33, 34]. A major challenge in the description of this process is to account for secondary interactions between spectator partons of the two projectiles, which can produce extra particles in the final state and hence destroy the rapidity gaps between the Higgs and final-state protons – the very same mechanism we discussed in Sect. 2.4.

4 Parton saturation

We have seen that diffraction involves scattering on small-x gluons in the proton. Consider the density in the transverse plane of gluons with longitudinal momentum fraction x that are resolved in a process with hard scale Q^2. One can think of $1/Q$ as the "transverse size" of these gluons as seen by the probe. The number density of gluons at given x increases with increasing Q^2, as described by DGLAP evolution (see Fig. 23). According to the BFKL evolution equation it also increases at given Q^2 when x becomes smaller, so that the gluons become more and more densely packed. At some point, they will start to overlap and thus reinteract and screen each other. One then enters a regime where the density of partons

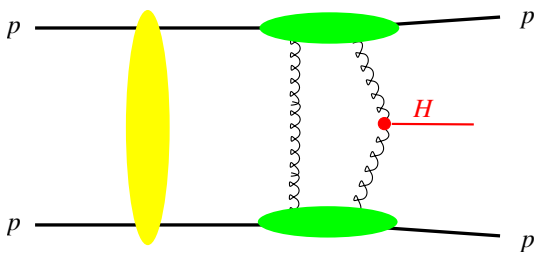

Fig. 22: Graph for the exclusive production of a Higgs boson in pp scattering. The horizontal blobs indicate generalized gluon distributions, and the vertical blob represents secondary interactions between the projectiles (cf. Fig. 13).

saturates and where the linear DGLAP and BFKL evolution equations cease to be valid. If Q^2 is large enough to have a small coupling α_s, we have a theory of this non-linear regime called "color glass condensate", see e.g. [35]. To quantify the onset of non-linear effects, one introduces a saturation scale Q_s^2 depending on x, such that for $Q^2 < Q_s^2(x)$ these effects become important. For smaller values of x, the parton density in the target proton is higher, and saturation sets in at larger values of Q^2 as illustrated in Fig. 23.

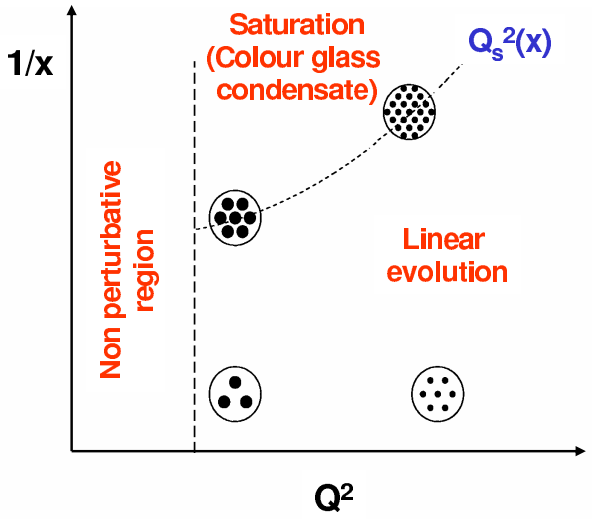

Fig. 23: Schematic view of the density of gluons in the transverse plane, as a function of the momentum fraction x and the resolution scale Q^2. Above the line given by $Q_s^2(x)$, saturation effects set in.

The dipole picture we introduced in Sect. 3.1 is well suited for the theoretical description of saturation effects. When such effects are important, the relation (7) between dipole cross section and gluon distribution ceases to be valid; in fact the gluon distribution itself is then no longer an adequate quantity to describe the dynamics of a scattering process. In a certain approximation, the evolution of the dipole cross section with x is described by the Balitsky-Kovchegov equation [36], which supplements the BFKL equation with a non-linear term taming the growth of the dipole cross section with decreasing x.

Essential features of the saturation phenomenon are captured in a phenomenological model for the dipole cross section, originally proposed by Golec-Biernat and Wüsthoff, see [37, 38]. Figure 24 shows $\sigma_{q\bar{q}}$ as a function of r at given x in this model. The dipole size r now plays the role of $1/Q$ in our discussion above. At small r the cross section rises following the relation $\sigma_{q\bar{q}}(r, x) \propto r^2 x g(x)$. At some value $R_s(x)$ of r, the dipole cross section is so large that this relation ceases to be valid, and $\sigma_{q\bar{q}}$

starts to deviate from the quadratic behavior in r. As r continues to increase, $\sigma_{q\bar{q}}$ eventually saturates at a value typical of a meson-proton cross section. In terms of the saturation scale introduced above, $R_s(x) = 1/Q_s(x)$. For smaller values of x, the initial growth of $\sigma_{q\bar{q}}$ with r is stronger because the gluon distribution is larger. The target is thus more opaque and as a consequence saturation sets in at lower r.

A striking feature found both in this phenomenological model [39] and in the solutions of the Balitsky-Kovchegov equation (see e.g. [40]) is that the total $\gamma^* p$ cross section only depends on Q^2 and x_B through a single variable $\tau = Q^2/Q_s^2(x_B)$. This property, referred to as geometric scaling, is well satisfied by the data at small x_B (see Fig. 25) and is an important piece of evidence that saturation effects are visible in these data. Phenomenological estimates find Q_s^2 of the order 1 GeV^2 for x_B around 10^{-3} to 10^{-4}.

The dipole formulation is suitable to describe not only exclusive processes and inclusive DIS, but also inclusive diffraction $\gamma^* p \to Xp$. For a diffractive final state $X = q\bar{q}$ at parton level, the theory description is very similar to the one for deeply virtual Compton scattering, with the wave function for the final state photon replaced by plane waves for the produced $q\bar{q}$ pair. The inclusion of the case $X = q\bar{q}g$ requires further approximations [37] but is phenomenologically indispensable for moderate to small β. Experimentally, one observes a very similar energy dependence of the inclusive diffractive and the total cross section in $\gamma^* p$ collisions at given Q^2 (see Fig. 26). The saturation mechanism implemented in the Golec-Biernat Wüsthoff model provides a simple explanation of this finding. To explain this aspect of the data is non-trivial. For instance, in the description based on collinear factorization, the energy dependence of the inclusive and diffractive cross sections is controlled by the x dependence of the ordinary and the diffractive parton densities. This x dependence is not predicted by the theory.

The description of saturation effects in pp, pA and AA collisions requires the full theory of the color glass condensate, which contains concepts going beyond the dipole formulation discussed here and is e.g. presented in [35]. We remark however that estimates of the saturation scale $Q_s^2(x)$ from HERA data can be used to describe features of the recent data from RHIC [41].

5 A short summary

Many aspects of diffraction in ep collisions can be successfully described in QCD if a hard scale is present. A key to this success are factorization theorems, which render parts of the dynamics accessible to calculation in perturbation theory. The remaining non-perturbative quantities, namely diffractive PDFs and generalized parton distributions, can be extracted from measurements and contain specific information about small-x partons in the proton that can only be obtained in diffractive processes. To describe hard diffractive hadron-hadron collisions is more challenging since factorization is broken by rescattering between spectator partons. These rescattering effects are of interest in their own right because of their intimate relation with multiple scattering effects, which at LHC energies are expected to be crucial for understanding the structure of events in hard collisions. A combination of data on inclusive and diffractive ep scattering hints at the onset of parton saturation at HERA, and the phenomenology developed there is a helpful step towards understanding high-density effects in hadron-hadron collisions.

Acknowledgements

It is a pleasure to thank our co-convenors and all participants for the fruitful atmosphere in the working group on diffraction, and A. De Roeck and H. Jung for their efforts in organizing this workshop. We are indebted to A. Proskuryakov for Figs. 5 and 12, to P. Fleischmann for Fig. 15, and to A. Bonato, K. Borras, A. Bruni, J. Forshaw, M. Grothe, H. Jung, L. Motyka, M. Ruspa and M. Wing for valuable comments on the manuscript.

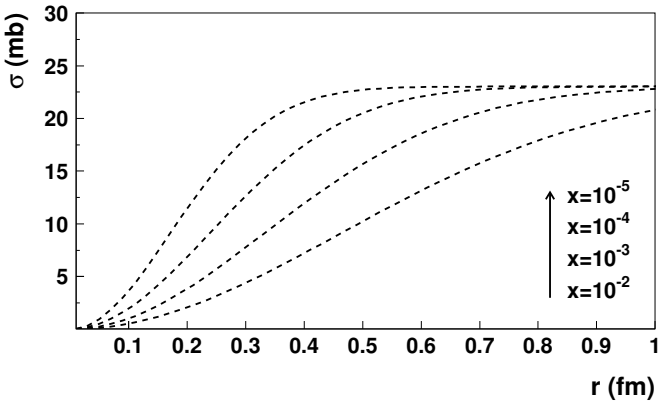

Fig. 24: The dipole cross section $\sigma_{q\bar{q}}$ in the Golec-Biernat Wüsthoff model as a function of dipole size r for different x (from [38]).

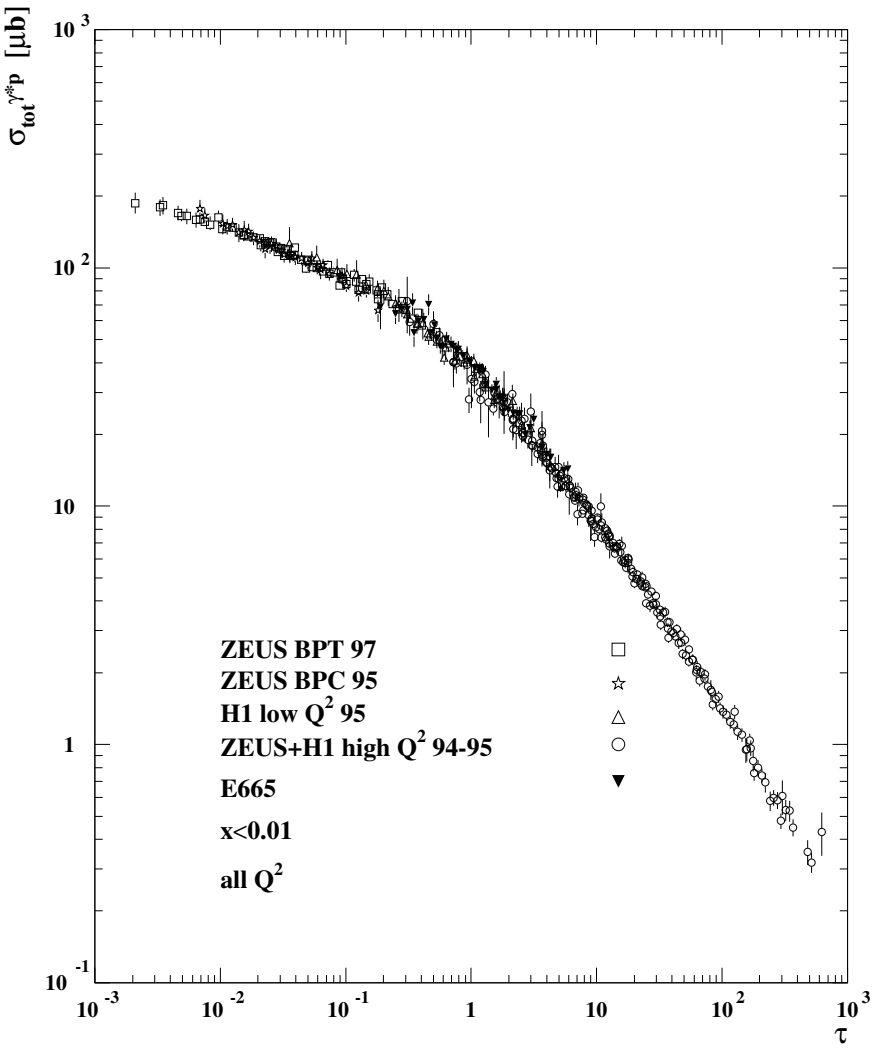

Fig. 25: Geometric scaling of the $\gamma^* p$ cross section in a single variable $\tau = Q^2/Q_s^2(x_B)$, as determined in [39]. The Q^2 of these data ranges from 0.045 to 450 GeV^2.

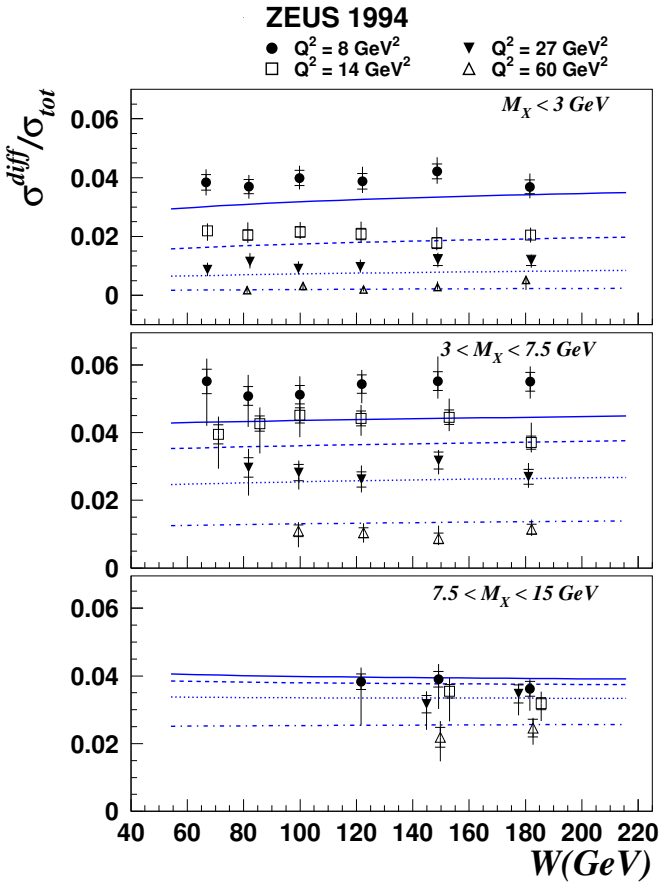

Fig. 26: Data on the ratio of diffractive and total $\gamma^* p$ cross sections compared with the result of the Golec-Biernat Wüsthoff model (from [37]).

References

[1] P. D. B. Collins, *An Introduction to Regge Theory and High-Energy Physics*, Cambridge University Press, Cambridge, 1977.

[2] E. A. Kuraev, L. N. Lipatov and V. S. Fadin, Sov. Phys. JETP **44** (1976) 443; ibid. **45** (1977) 199; I. I. Balitsky and L. N. Lipatov, Sov. J. Nucl. Phys. **28** (1978) 822.

[3] J. R. Forshaw and D. A. Ross, *Quantum chromodynamics and the pomeron*, Cambridge Lect. Notes Phys. **9** (1997) 1;
A. Hebecker, Phys. Rept. **331** (2000) 1 [hep-ph/9905226];
M. Wüsthoff and A. D. Martin, J. Phys. G **25** (1999) R309 [hep-ph/9909362];
V. Barone and E. Predazzi, *High-energy particle diffraction*, Springer, 2002;
I. P. Ivanov, N. N. Nikolaev and A. A. Savin, hep-ph/0501034.

[4] K. Goulianos, Phys. Rept. **101** (1983) 169.

[5] G. Bruni *et al.*, these proceedings.

[6] S. Chekanov *et al.* [ZEUS Collaboration], Eur. Phys. J. C **38** (2004) 43 [hep-ex/0408009].

[7] H1 Collaboration, Paper 89 submitted to the International Europhysics Conference on High Energy Physics (EPS 2003), July 2003, Aachen, Germany, available from http://www-h1.desy.de

[8] ZEUS Collaboration, Paper 1048 submitted to the 30th International Conference on High Energy Physics (ICHEP 2000), July–August 2000, Osaka, Japan, available from http://www-zeus.desy.de

[9] S. Chekanov *et al.* [ZEUS Collaboration], Eur. Phys. J. C **21** (2001) 443 [hep-ex/0105090].

[10] L. Trentadue and G. Veneziano, Phys. Lett. B **323** (1994) 201.

[11] A. Berera and D. E. Soper, Phys. Rev. D **53** (1996) 6162 [hep-ph/9509239].
[12] J. C. Collins, Phys. Rev. D **57** (1998) 3051, Erratum ibid. D **61** (2000) 019902 [hep-ph/9709499].
[13] P. Newman and F.-P. Schilling, these proceedings.
[14] M. Groys, A. Levy and A. Proskuryakov, these proceedings.
[15] S. Chekanov *et al.* [ZEUS Collaboration], Nucl. Phys. B **713** (2005) 3 [hep-ex/0501060].
[16] A. D. Martin, M. G. Ryskin and G. Watt, Eur. Phys. J. C **37** (2004) 285 [hep-ph/0406224];
A. D. Martin, M. G. Ryskin and G. Watt, these proceedings.
[17] H1 Collaboration, Paper 6-0177 submitted to the 32nd International Conference on High Energy Physics (ICHEP 2004), August 2004, Beijing, China, available from http://www-h1.desy.de
[18] A. Bruni *et al.*, these proceedings [hep-ph/0509202].
[19] T. Affolder *et al.* [CDF Collaboration], Phys. Rev. Lett. **84** (2000) 5043.
[20] L. Alvero *et al.*, Phys. Rev. D **59** (1999) 074022 [hep-ph/9805268].
[21] A. Proskuryakov, Y. Yamazaki and M. Arneodo, presented at the HERA-LHC Workshop, 11–13 October 2004, CERN, http://agenda.cern.ch/fullAgenda.php?ida=a044163
[22] E. Gotsman *et al.*, these proceedings.
[23] J. Bartels, M. Salvadore and G. P. Vacca, Eur. Phys. J. C **42** (2005) 53 [hep-ph/0503049];
J. Bartels, these proceedings,
C. Buttar *et al.*, these proceedings.
[24] G. Ingelman and P. E. Schlein, Phys. Lett. B **152** (1985) 256.
[25] J. Bartels and M. G. Ryskin, Z. Phys. C **76** (1997) 241 [hep-ph/9612226].
[26] R. Enberg *et al.*, hep-ph/0407328;
S. Chekanov *et al.* [ZEUS Collaboration], Eur. Phys. J. C **26** (2003) 389 [hep-ex/0205081];
A. Aktas *et al.* [H1 Collaboration], Phys. Lett. B **568** (2003) 205 [hep-ex/0306013].
[27] ZEUS Collaboration, Paper 594 submitted to the International Europhysics Conference on High Energy Physics (EPS 2001), July 2001, Budapest, Hungary, available from http://www-zeus.desy.de
[28] M. G. Ryskin, Z. Phys. C **57** (1993) 89.
[29] J. C. Collins, L. Frankfurt and M. Strikman, Phys. Rev. D **56** (1997) 2982 [hep-ph/9611433];
J. C. Collins and A. Freund, Phys. Rev. D **59** (1999) 074009 [hep-ph/9801262].
[30] M. Diehl, Phys. Rept. **388**, 41 (2003) [hep-ph/0307382].
[31] A. V. Belitsky and A. V. Radyushkin, hep-ph/0504030.
[32] C. Adloff *et al.* [H1 Collaboration], Phys. Lett. B **483** (2000) 360 [hep-ex/0005010].
[33] Contributions to these proceedings by J. Kalliopuska *et al.*; V. Avati and K. Österberg; M. Arneodo *et al.*; V. Andreev *et al.*
[34] J. Forshaw, these proceedings [hep-ph/0508274];
M. Boonekamp *et al.*, these proceedings.
[35] H. Weigert, hep-ph/0501087;
R. Venugopalan, these proceedings.
[36] I. Balitsky, Nucl. Phys. B **463** (1996) 99 [hep-ph/9509348];
Y. V. Kovchegov, Phys. Rev. D **61** (2000) 074018 [hep-ph/9905214].
[37] K. Golec-Biernat and M. Wüsthoff, Phys. Rev. D **60** (1999) 114023 [hep-ph/9903358].
[38] K. Golec-Biernat, Acta Phys. Polon. B **33** (2002) 2771 [hep-ph/0207188].
[39] A. M. Stasto, K. Golec-Biernat and J. Kwiecinski, Phys. Rev. Lett. **86** (2001) 596 [hep-ph/0007192].
[40] K. Golec-Biernat, L. Motyka and A. M. Stasto, Phys. Rev. D **65** (2002) 074037 [hep-ph/0110325];
M. Lublinsky, Eur. Phys. J. C **21** (2001) 513 [hep-ph/0106112];
S. Munier and R. Peschanski, Phys. Rev. Lett. **91** (2003) 232001 [hep-ph/0309177].
[41] D. Kharzeev and E. Levin, Phys. Lett. B **523** (2001) 79 [nucl-th/0108006];
A. Krasnitz, Y. Nara and R. Venugopalan, Nucl. Phys. A **727** (2003) 427 [hep-ph/0305112].

Diffractive Higgs Production: Experiment

Editors: B. E. Cox[a] and M. Grothe[b]
[a] School of Physics and Astronomy, The University of Manchester, Manchester M139PL, UK
[b] University of Torino and INFN-Torino, Italy; also at University of Wisconsin, Madison, WI, USA

TOTEM forward measurements: exclusive central diffraction

J. Kalliopuska, J.W. Lämsä, T. Mäki, N. Marola, R. Orava, K. Österberg, M. Ottela and S. Tapprogge

Abstract
In this contribution, we present a first systematic study of the precision of the momentum measurement of protons produced in the central exclusive diffractive processes, $p\,p \rightarrow p + X + p$, as well as the accuracy of the reconstructed mass for particle state X based on these proton measurements. The scattered protons are traced along the LHC beam line using the nominal LHC optics, accounting for uncertainties related to beam transport and proton detection.
To search for and precisely measure new particle states X with masses below 200 GeV, additional leading proton detectors are required at about 420 m from the interaction point in addition to the already approved detectors. Using these additional detectors, a mass resolution of the order of 1 GeV can be achieved for masses beyond $\sim$120 GeV.

TOTEM forward measurements: leading proton acceptance

V. Avati and K. Österberg

Abstract
We report about the acceptance of forward leading protons in Roman Pot stations placed along the LHC beam line. The TOTEM stations plus additional detectors at 420 m from the interaction point have been considered using the low–β^* optics V6.5 for LHC physics runs.

Diffractive Higgs: CMS/TOTEM Level-1 Trigger Studies

M. Arneodo, V. Avati, R. Croft, F. Ferro, M. Grothe, C. Hogg, F. Oljemark, K. Österberg and M. Ruspa

Abstract
Retaining events containing a Higgs Boson with mass around 120 GeV poses a special challenge to triggering at the LHC due to the relatively low transverse momenta of the decay products. We discuss the potential of including into the CMS trigger the TOTEM forward detectors and possible additional detectors at a distance of 420 m from the CMS interaction point. We find that the output rate of a 2-jet Level-1 trigger condition with thresholds sufficiently low for the decay products of a 120 GeV Higgs Boson can be limited to $\mathcal{O}(1)$ kHz for luminosities of up to $2 \times 10^{33}\mathrm{cm}^{-2}\mathrm{s}^{-1}$ by including the TOTEM forward detectors in the Level-1 trigger.

Proposal to upgrade the very forward region at CMS

V. Andreev, A.Bunyatyan, H. Jung, M. Kapishin and L. Lytkin

Abstract
The possibilities of extending the acceptance of LHC experiments beyond 7 units of pseudorapidity are investigated. With additional detectors it would be possible to measure the particles with energies above 2 TeV in the pseudorapidity range between 7 and 11.

TOTEM forward measurements: exclusive central diffraction

J. Kalliopuska, J.W. Lämsä[*]*, T. Mäki, N. Marola, R. Orava, K. Österberg*[†]*, M. Ottela and S. Tapprogge*[‡]
High Energy Physics Division, Department of Physical Sciences, University of Helsinki and
Helsinki Institute of Physics, P.O. Box 64, FIN-00014 University of Helsinki, Finland

Abstract

In this contribution, we present a first systematic study of the precision of the momentum measurement of protons produced in the central exclusive diffractive processes, $p\,p \rightarrow p + X + p$, as well as the accuracy of the reconstructed mass for particle state X based on these proton measurements. The scattered protons are traced along the LHC beam line using the nominal LHC optics, accounting for uncertainties related to beam transport and proton detection.

To search for and precisely measure new particle states X with masses below 200 GeV, additional leading proton detectors are required at about 420 m from the interaction point in addition to the already approved detectors. Using these additional detectors, a mass resolution of the order of 1 GeV can be achieved for masses beyond ∼120 GeV.

1 Introduction

It has been recently suggested that the Higgs boson mass could be measured to an accuracy of $\mathcal{O}$(1 GeV) in the central exclusive diffractive process (CED) [1, 2]:

$$p\,p \rightarrow p\,+\,H\,+\,p \tag{1}$$

In contrast to this, the direct measurement of the Higgs boson mass, based on the two final state b-jets in $H \rightarrow b\bar{b}$, is estimated to yield a precision of $\mathcal{O}$(10 GeV). The precise reconstruction of the centrally produced system X, i.e. the Higgs mass in Eq. 1, is based on the four-momenta of the incoming ($p_{1,2}$) and scattered ($p'_{1,2}$) protons and since the two scattered protons are expected to have small transverse momenta, the following approximation for the mass of the centrally produced system can be made:

$$M^2 = (p_1 + p_2 - p'_1 - p'_2)^2 \approx \xi_1 \xi_2 s\,, \tag{2}$$

where $\xi_{1,2} = 1 - |\vec{p}\,'_{1,2}|/|\vec{p}_{1,2}|$ denote the momentum loss fractions of the two scattered protons.

The acceptance for forward leading protons for nominal LHC runs ($\beta^* \sim 0.5$ m) is described in detail elsewhere (see [3]). This contribution focuses on the CED process and the precision with which the proton momenta and the mass of the centrally produced system can be reconstructed.

2 Leading proton uncertainties and transport

The study is done in multiple steps, which include the event generation (ExHuME [4] or PHOJET [5]), simulation of the interaction point (IP) region, tracking of the protons through the LHC beam line, a detector simulation and a proton momentum reconstruction algorithm using the detector information [6]. The following beam related uncertainties are inputs to the study[1]:

- pp interaction region width: $\sigma_{x,y}$ = 16 μm, σ_z = 5 cm,
- beam angular divergence: $\Theta_{x,y}$ = 30 μrad

[*] also Physics Department, Iowa State University, Ames, USA
[†] corresponding author: kenneth.osterberg@helsinki.fi
[‡] currently at Institute of Physics, Johannes-Gutenberg Universität Mainz, Germany

[1] The reference system (x, y, z) used in the study corresponds to the reference orbit in the accelerator; the z-axis is tangent to the orbit and positive in the beam direction; the x-axis (horizontal) is negative toward the center of the ring.

– beam energy spread: $1.1 \cdot 10^{-4}$.

Concerning the detector response, only the horizontal plane is considered with the following inputs:

– The detector is assumed to be fully efficient at a distance $10\sigma_x(z) + 0.5$ mm from the beam center[2], where $\sigma_x(z)$ is the horizontal beam width at distance z. The second term takes into account the distance from the bottom of the vacuum window to the edge of the fully sensitive detector area.
– For the protons within the fully sensitive detector area, a position reconstruction uncertainty is introduced by smearing the hit coordinates according to a Gaussian distribution with a σ of 10 μm.
– The uncertainty due to the beam position knowledge at each detector location is accounted for by smearing the hit coordinates by a correlated Gaussian distribution with a σ of 5 μm.

The transverse displacement $(x(z), y(z))$ of a scattered proton at a distance z from the IP is determined by tracing the proton along the LHC beam line using the MAD program [7]. The optics layout version 6.2 for nominal LHC runs (β^* = 0.5 m) with a 150 μrad horizontal crossing angle is used [8]. Although the study was carried out for CMS/TOTEM (IP5), the results should be equally valid for ATLAS (IP1).

3 Proton momentum reconstruction

The x-coordinate of the proton observed at any given location along the beam line, depends on three initial parameters of the scattered proton: its fractional momentum loss, ξ, its initial horizontal scattering angle, Θ_x^*, and its horizontal position of origin, x^*, at the IP. Consequently, more than one x-measurement of a particular proton is needed to constrain its parameters. In the procedure chosen, two x-measurements from a detector doublet are used to determine ξ and Θ_x^*, neglecting the x^* dependence. The effect of the x^* on the reconstructed proton momentum will be treated as an independent source of uncertainty.

To obtain a large acceptance in ξ, the following two detector locations, each consisting of a doublet of proton detectors, are chosen based on the LHC optics layout:

– 215 and 225 meters from IP5 (”215 m location”), and
– 420 and 430 meters from IP5 (”420 m location”).

The 215 m location corresponds to a TOTEM approved Roman Pot location [9], while the 420 m location in the cryogenic section of the accelerator will require special design and further investigation.

Each detector doublet yields two observables, which are related to the horizontal offset and angle with respect to the beam axis. The ξ dependence of these observables has been derived by fitting a functional form to the simulated average values of ξ, as a function of the values of the two observables [6].

4 Acceptance and resolution on ξ and mass

The ξ and t acceptance of protons moving in the clockwise and counter-clockwise directions are slightly different due to differences in the optical functions, for details see [3]. As a summary: a proton from the CED process is seen when its ξ is between 0.025 (0.002) and 0.20 (0.015) for the 215 (420) location.

The relative resolution on ξ, $\Delta\xi/\xi = (\xi - \xi_{rec})/\xi$ as a function of ξ for protons produced in the CED process and seen in either the 215 m or the 420 m location is shown in Fig. 1 for protons circulating in the LHC both in the clockwise and counter-clockwise direction. Included are the separate effects from the uncertainty of the transverse IP position, the resolution of the proton detector, the beam energy uncertainty, the beam angular divergence at the IP, and the beam position resolution at the proton detector.

At both detector locations, major contributors to the over-all ξ resolution are the uncertainty of the transverse IP position and the resolution of the proton detector. In addition to these two uncertainties, the beam energy uncertainty contributes significantly to the resolution at the 420 m location.

[2]The LHC collimators extend to $6\sigma_x(z)$. The closest safe position can be assumed to lay anywhere between 10 and 15.

The acceptance as function of the mass of the centrally produced system is shown in Fig. 2a. Each leading proton is required to be within the acceptance of either the 215 or 420 m locations. Independently shown is the case (sub-set of above) where both protons are within the acceptance of the 420 m locations. In the mass range shown, there is no acceptance for detecting both protons at the 215 m location. The ξ_1-ξ_2 combinations result from the gluon density function in the proton and the mass of the centrally produced system (see Eq. 2). The ExHuME generator favours a harder gluon distribution than that of PHOJET. Thus, the Higgses are produced more centrally. This yields a higher acceptance for ExHuME.

The resolution effects of the two scattered protons are, in general, uncorrelated from each other. The only correlation comes from the production point, whose transverse component is determined by the rms spread of the beam at the IP and by an independent measurement using the Higgs decay products [10]. It can be determined to 10 μm or better, and therefore for the mass resolution of the centrally produced system, a 10 μm uncertainty on the transverse IP position is used. For the mass resolution, all other uncertainties are assumed to be uncorrelated between the two protons.

The mass resolutions for events with protons within the acceptance of the 420 m location on both sides, and for events with one proton within the acceptance of the 215 m location on one side and the other proton within the acceptance of the 420 m location on the other side (labelled "asym." in the figure) are shown as a function of the mass of the centrally produced system in Fig. 2b. The values quoted in the figure are based on Gaussian fits to the reconstructed mass distributions. The two-proton acceptance requirement imposes a restriction on the allowed ξ_1-ξ_2 combinations; as a result the mass resolutions obtained with ExHuME and PHOJET are very similar.

5 Conclusions

The first comprehensive study of the CED process at the LHC is reported. The study is based on detailed simulations along the LHC beam line of the diffractively scattered protons, accounting for the known sources of uncertainties related to beam transport and proton detection. The feasibility of measuring such events during nominal LHC runs for masses of the central system, X, below $\sim$200 GeV is addressed.

On the basis of this study, it is concluded that with an additional pair of leading proton detectors at $\pm$420 m from the interaction point, a Higgs boson with a mass of 120–180 GeV could be measured with a mass resolution of the order of 1 GeV. Such additional proton detectors would also enable large statistics of pure gluon jets to be collected, thereby turning the LHC into a gluon factory.

References

[1] A. De Roeck, V.A. Khoze, A.D. Martin, R. Orava and M.G. Ryskin, Eur. Phys. J. **C35**, 391 (2002).

[2] J. Kalliopuska, T. Mäki, N. Marola, R. Orava, K. Österberg, M. Ottela and S. Tapprogge, **HIP-2003-11/EXP** (2003).

[3] V. Avati and K. Österberg, "TOTEM forward measurements: leading proton acceptance", these proceedings.

[4] J. Monk and A. Pilkington, **hep-ph/0502077** (2005).

[5] R. Engel, Phys. Rev. **D51**, 3220 (1995).

[6] T. Mäki, Master thesis: "Exclusive production of Higgs boson at LHC collider: Higgs mass measurement via leading proton detection", Helsinki University of Technology (2003).

[7] The MAD program, Methodical Accelerator Design, `http://www.cern.ch/mad`.

[8] Lattice & Optics, `http://lhc-new-homepage.web.cern.ch/lhc-new-homepage/`.

[9] The TOTEM collaboration, TOTEM Technical Design Report, **CERN-LHCC-2004-002** (2004).

[10] P. Vanlaer, Hadron Collider Physics Conference, Les Diablerets, Switzerland (2005).

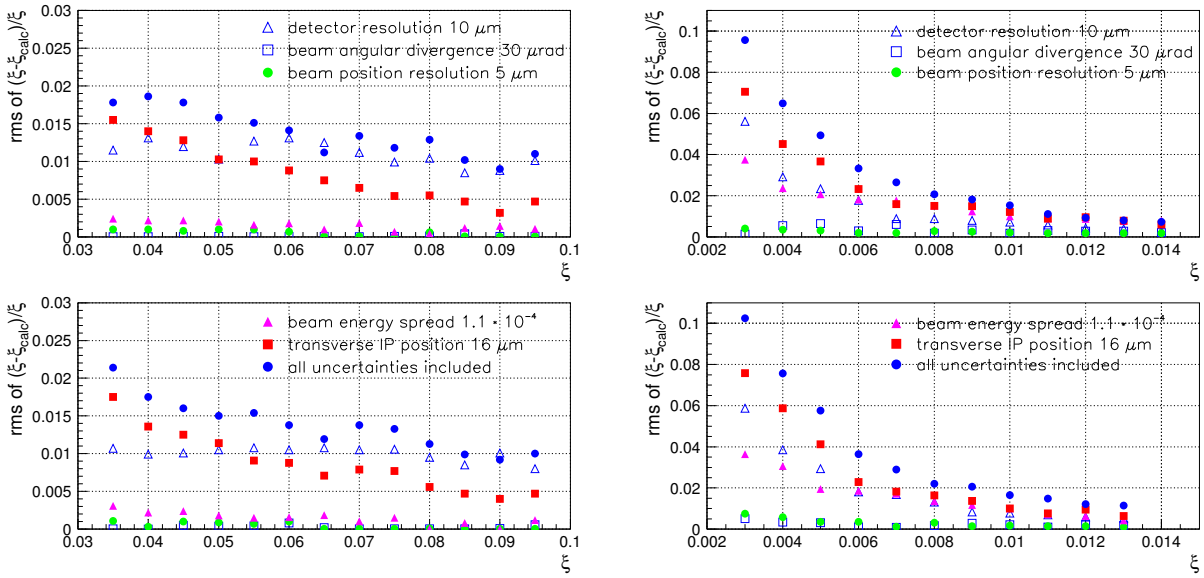

Fig. 1: Summary of all effects studied contributing to the over-all ξ resolution for the 215 m (left) and 420 m location (right). The upper and lower plots are for protons circulating clockwise and counter-clockwise along the LHC beam line, respectively. The t values of the protons used for each ξ bin is similar to the t distribution originating from central exclusive diffraction.

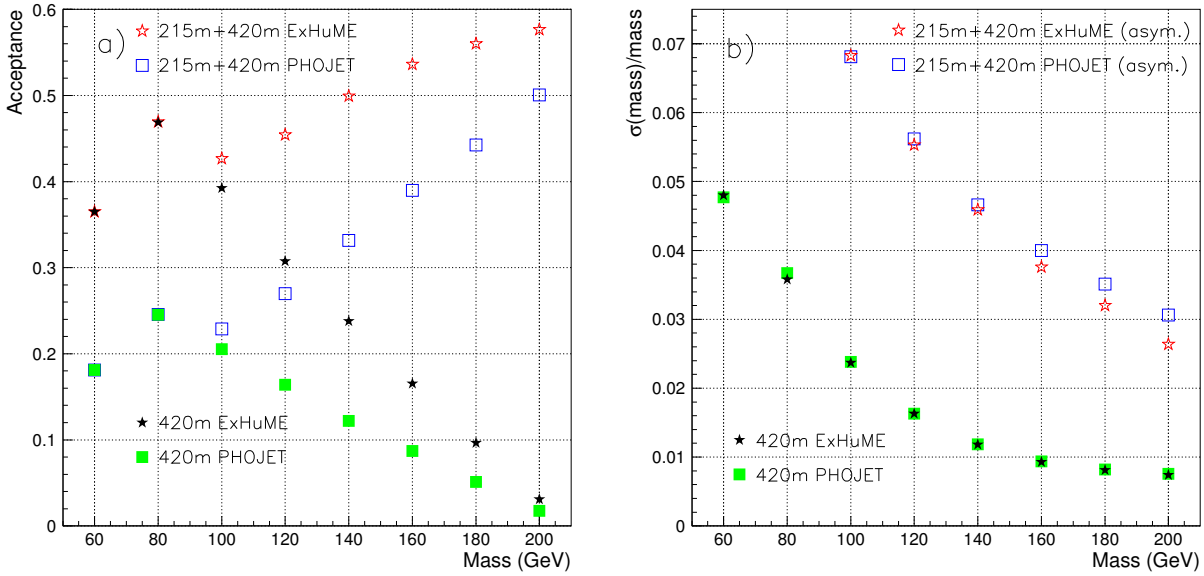

Fig. 2: a) Mass acceptance for events with protons within the acceptance of the 420 m location on each side of the interaction point ("420m"); and for events with protons within the combined acceptance of the 215 m and 420 m location on each side of the interaction point ("215m+420m"). b) Mass resolution for events with protons within the acceptance of the 420 m location on each side of the interaction point ("420m"); and for events with one proton within the acceptance of the 215 m location on one side of the interaction point and the other proton within the acceptance of the 420 m location on the other side ("215m+420m (asym.)"). ExHuME or PHOJET denotes the generator used for producing the central exclusive diffractive events.

TOTEM forward measurements: leading proton acceptance

V. Avati[a] *and K. Österberg*[b]
[a] CERN, Geneva, Switzerland and Case Western Reserve University, Cleveland, OH, USA
[b] Department of Physical Sciences, University of Helsinki and Helsinki Institute of Physics, Finland

Abstract
We report about the acceptance of forward leading protons in Roman Pot stations placed along the LHC beam line. The TOTEM stations plus additional detectors at 420 m from the interaction point have been considered using the low–β^* optics V6.5 for LHC physics runs.

1 Introduction

The TOTEM very forward detectors consist of telescopes of "Roman Pots" (RP) placed symmetrically on both sides of the interaction region IP5. The RP stations will be placed at 147 m and 220 m from IP5: each station is composed of two units separated by 2.5–4 m and each unit is equipped with two vertical and one horizontal silicon detector package. For more details on the TOTEM RPs, please refer to [1]. The possibility to add a detector in the cryogenic sections of the LHC is under investigation, therefore, we have included one more RP station at 420 m in these acceptance studies. This work is an update, due to the release of a new LHC optics, of previous studies done by the TOTEM Collaboration [2].

1.1 Low β* optics acceptance study

The transverse displacement $(x(s), y(s))$[1] of a scattered leading proton (with momentum loss $\xi = \Delta P/P < 0$) at distance s from the interaction point (IP) is determined by tracking the proton through the accelerator lattice using the MAD-X program [3].

The new optics version 6.5 for the standard LHC physics runs is used. Notable changes (at IP5) from the previous versions are :

- β^* = 0.55 m (previously 0.5 m)
- Beam offset in the horizontal plane = 0.5 mm (previously zero)
- Horizontal crossing angle = 142 μrad (previously 150 μrad)

The protons at the IP are generated with flat distributions in the azimuthal angle ϕ, in Log$(-\xi)$ and in Log$(-t)$ in the kinematically allowed region of the ξ–t plane, i.e. for physical values of the scattering angle of the proton. The Mandelstam variable t is defined as $t = (p_{\text{orig}} - p_{\text{scatt}})^2$, where $p_{\text{orig(scatt)}}$ is the four-momentum of the incoming (scattered) proton. The scattering angle of the proton is physical when $t \geq t_0(\xi)$, where $t_0(\xi)$ is given by

$$t_0\left(\xi\right) = 2\left(P_{\text{orig}}^2 + m_p^2\right)\left[\sqrt{1 + \left(P_{\text{orig}}^2\left[\xi^2 + 2\xi\right]\right) / \left(P_{\text{orig}}^2 + m_p^2\right)} - 1\right] - 2\xi P_{\text{orig}}^2 \,. \qquad (1)$$

In Eq. 1, P_{orig} is the momentum of the incoming proton and m_p is the proton mass.

The transverse vertex position and the scattering angle at the IP are smeared assuming Gaussian distributions with widths given by the transverse beam size (16 μm) and the beam divergence (30 μrad).

[1] The reference system (x,y,s) defines the reference orbit in the accelerator; the s-axis is tangent to the orbit and positive in the beam direction; the two other axes are perpendicular to the reference orbit. The x-axis (horizontal, bending plane) is negative toward the center of the ring.

To determine the acceptance of a RP station, the minimum distance of a detector to the beam and constraints imposed by the beam pipe or beam screen size are considered.

The minimum distance of detector approach to the beam is proportional to the beam size:

$$x(y)_{min} = 10\sigma_{x(y)}{}^{beam} + c\,, \tag{2}$$

where c is a constant that takes into account the distance from the edge of the sensitive detector area to the bottom of the RP window ($\sim$ 0.5 mm). For the nominal transverse beam emittance ϵ = 3.75 $\mu\mathrm{m}\cdot\mathrm{rad}$ typical values of the horizontal detector distance are $\sim$1 mm (at 220 m) and $\sim$4 mm (at 420 m). In the results shown later, the detector shape has not been included. The beam pipe apertures can be found in the LHC–LAYOUT Database [4].

1.2 Results

Figures 1–3 show the acceptance in Log($-\xi$), Log($-t$) for the RP stations at 220 and 420 m for the clockwise ("beam1") and counter–clockwise ("beam2") circulating beam.

One should note that these results refer to non-physical distributions in the variables ξ and t in order to have good statistics in each interval and describe all possible processes. To use these results in a general simulation program, the ϕ dependence has to be taken into account, since it is not negligible in many kinematical configurations. More detailed analysis such as detector alignment samples, collimator effects, etc. can be found in [5].

These results have been included in FAMOS (FAst MOntecarlo Simulation of the CMS detector) by M. Tasevsky ("Diffractive Higgs production", these proceedings) and they have been used in the CMS/TOTEM studies on triggering a diffractively produced light Higgs boson with the CMS Level-1 trigger ("Diffractive Higgs: CMS/TOTEM Level-1 Trigger Studies", these proceedings).

References

[1] The TOTEM collaboration, TOTEM Technical Design Report, **CERN-LHCC-2004-002 TOTEM-TDR-001** (2004).

[2] The TOTEM collaboration, Status Report to the LHCC (`http://www.cern.ch/totem`) (2002);
J. Kalliopuska, J.W. Lämsä, T. Mäki, N. Marola, R. Orava, K. Österberg, M. Ottela and S. Tapprogge, "TOTEM forward measurements: exclusive central diffraction", these proceedings and J. Kalliopuska, T. Mäki, N. Marola, R. Orava, K. Österberg, M. Ottela and S. Tapprogge, **HIP-2003-11/EXP** (2003).

[3] The MAD-X Program, Methodical Accelerator Design, `http://www.cern.ch/mad`.

[4] LHC Layout, `http://lhclayout.web.cern.ch/lhclayout/`.

[5] V. Avati and K. Österberg, "Acceptance calculations methods for low–β^* optics", **TOTEM Internal Note 05-2 (`http://www.cern.ch/totem`)** (2005).

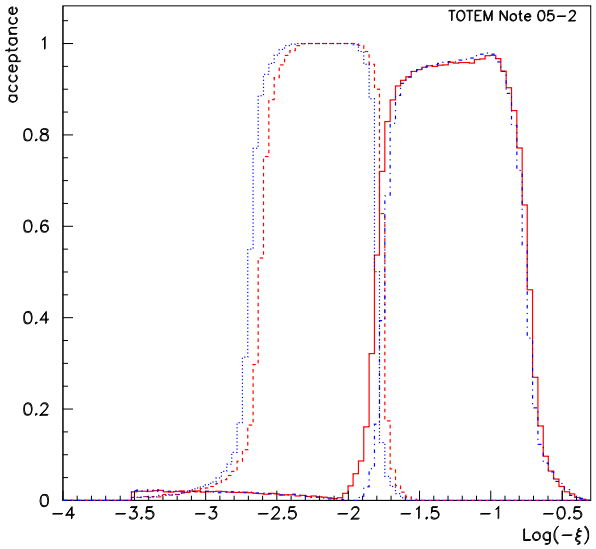

Fig. 1: Log($-\xi$) acceptance for: beam1 station at 220 m (solid-red) and 420 m (dashed-red) and beam2 station at 220 m (dashed-dotted-blue) and 420 m (dotted-blue).

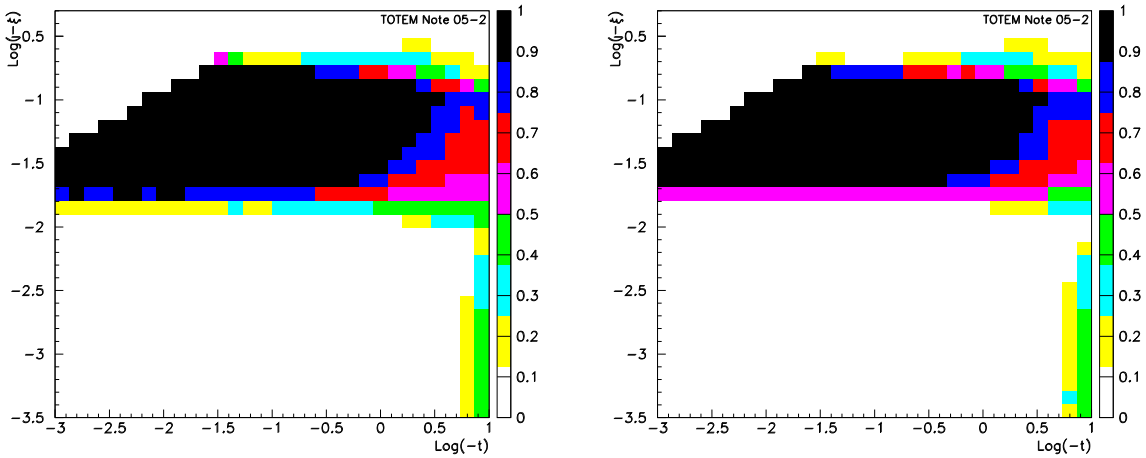

Fig. 2: Log($-\xi$) vs Log($-t$) acceptance for beam1 (left) and beam2 (right) stations at 220 m.

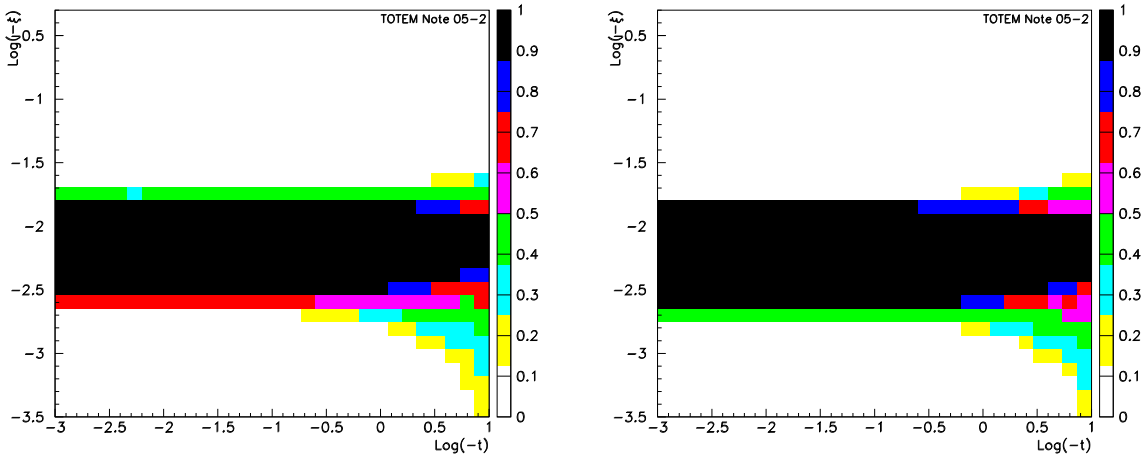

Fig. 3: Log($-\xi$) vs Log($-t$) acceptance for beam1 (left) and beam2 (right) stations at 420 m.

Diffractive Higgs: CMS/TOTEM Level-1 Trigger Studies

M. Arneodo[a], V. Avati[b], R. Croft[c], F. Ferro[d], M. Grothe[e] † , C. Hogg[f], F. Oljemark[g], K. Österberg[g], M. Ruspa[a]*

[a]Università del Piemonte Orientale, Novara, and INFN-Torino, Italy

[b] European Organisation for Nuclear Research CERN, Geneva, Switzerland, and Case Western Reserve University, Cleveland, OH, USA

[c] University of Bristol, Bristol, UK

[d] University of Genova and INFN-Genova, Italy

[e] University of Torino and INFN-Torino, Italy; also at University of Wisconsin, Madison, WI, USA

[f] University of Wisconsin, Madison, WI, USA

[g] Department of Physical Sciences, University of Helsinki, and Helsinki Institute of Physics, Finland

Abstract

Retaining events containing a Higgs Boson with mass around 120 GeV poses a special challenge to triggering at the LHC due to the relatively low transverse momenta of the decay products. We discuss the potential of including into the CMS trigger the TOTEM forward detectors and possible additional detectors at a distance of 420 m from the CMS interaction point. We find that the output rate of a 2-jet Level-1 trigger condition with thresholds sufficiently low for the decay products of a 120 GeV Higgs Boson can be limited to $\mathcal{O}(1)$ kHz for luminosities of up to $2 \times 10^{33}\mathrm{cm}^{-2}\mathrm{s}^{-1}$ by including the TOTEM forward detectors in the Level-1 trigger.

1 Introduction

A Higgs Boson with mass close to the current exclusion limit poses a special challenge to triggering at the LHC. The dominant decay of a Standard Model Higgs Boson of mass $\sim$120 GeV is into two b-quarks and generates 2 jets with at most 60 GeV transverse momentum, p_T, each. The so far considered Level-1 (L1) trigger tables of CMS [1] are optimized for events with high p_T; the necessity of keeping the overall L1 rate at acceptable levels requires thresholds in two-jet events above p_T =100 GeV per jet. Conversely, triggering is not a problem should the mass of the Higgs Boson be sufficiently high so that its final states are rich in high p_T leptons, as is the case for $H \rightarrow WW^{\star}$.

In order to retain a potential Higgs signal with mass close to the current exclusion limit, information beyond that from the central CMS detector needs to be included in the L1 trigger. A proton that scatters diffractively at the CMS interaction point (IP) may be detected by Roman Pot (RP) detectors further downstream. Roman Pot detectors up to 220 m downstream of CMS will be part of the TOTEM experiment [2]. Information from TOTEM will be available to the CMS L1 trigger. Furthermore, detectors at up to 420 m distance from the IP are currently discussed as part of the FP420 project [3]. Including information from them into the CMS L1 trigger is however not possible without an increase in the trigger latency.

This article discusses the effect of including the TOTEM forward detectors and/or those planned at 420 m distance on rate and selection efficiency of the CMS L1 trigger. All results reported in the following are preliminary; further studies are still on-going at the time of writing.

* Work supported by the Italian Ministry for Education, University and Scientific Research under the program "Incentivazione alla mobilità di studiosi stranieri e italiani residenti all'estero".

† Corresponding author: Monika.Grothe@cern.ch

2 Experimental apparatus

The CMS trigger system is designed to reduce the input rate of 10^9 interactions per second at the nominal LHC luminosity of $10^{34}\mathrm{cm}^{-2}\mathrm{s}^{-1}$ to an output rate of not more than 100 Hz. This reduction of 10^7 is achieved in two steps, by the CMS L1 trigger (output rate 100 kHz) and the CMS Higher-Level Trigger (HLT). The L1 trigger carries out its data selection algorithms with the help of three principal components: the Calorimeter Trigger, the Muon Trigger and the Global Trigger. The decision of the Calorimeter Trigger is based on the transverse energy, E_T, information of the CMS calorimeters (pseudorapidity coverage $|\eta| < 5$). A L1 jet consists of 3×3 regions, each with 4×4 trigger towers, where the E_T in the central region is above the E_T in any of the outer regions. A typical L1 jet has dimensions $\Delta\eta \times \Delta\phi = 1 \times 1$, where ϕ is the azimuthal angle. The E_T reconstructed by the L1 trigger for a given jet corresponds on the average only to 60% of its true E_T. All studies in this article use calibrated jet E_T values, obtained from the reconstructed value by means of an η and E_T dependent correction.

The TOTEM experiment [2] will have two identical arms, one at each side of the CMS IP. Each arm will comprise two forward tracker telescopes, T1 (Cathode Strip Chambers) and T2 (Gas Electron Multipliers), as well as Silicon detectors housed in RP stations along the LHC beam-line. The TOTEM detectors will provide input data to the Global Trigger of the CMS L1 trigger. Track finding in T1 and T2 (combined coverage $3.2 < |\eta| < 6.6$) for triggering purposes is optimized with respect to differentiating between beam-beam events that point back to the IP and beam-gas and beam-halo events that do not. The TOTEM RP stations will be placed at a distance of ± 147 m and ± 220 m from the CMS IP. Each station will consist of two units, 2.5 m and 4 m apart, each with one horizontally and two vertically movable pots equipped with Silicon strip detectors. The possibility of implementing a cut on ξ in the L1 trigger is currently under investigation.

The fractional momentum loss, ξ, of diffractively scattered protons peaks at $\xi = 0$ ("diffractive peak"). The combination of CMS and TOTEM will permit to measure protons that have undergone a fractional momentum loss $0.2 > \xi > 0.02$. Detectors at a distance of 420 m, in the cryogenic region of the LHC ring, are currently being considered by the FP420 project [3]. They would provide a coverage of $0.02 > \xi > 0.002$, complementary to that of the TOTEM detectors, but cannot be included in the L1 trigger without an increase in the L1 latency of 3.2 μs. A special, long latency running mode might be feasible at lower luminosities. This option is currently under investigation. Using detectors at 420 m in the L1 trigger is included as an option in the studies discussed in this article.

The studies discussed in the following assume that the RP detectors are 100% efficient in detecting all particles that emerge at a distance of at least $10\sigma_{beam} + 0.5$ mm from the beam axis. Their acceptance was calculated by way of a simulation program that tracks particles through the accelerator lattice [4]. This has been done for the nominal LHC optics, the so-called low-β^* optics, version V6.5. Further details can be found in [5]. All Monte Carlo samples used in the following assume LHC bunches with 25 ns spacing.

3 Level-1 trigger rates and signal efficiencies

We consider here perhaps the most challenging case, that of a low-mass (120 GeV) Standard Model Higgs Boson, decaying into two b-jets. There, the jets have transverse energies of at most 60 GeV. In order to retain as large a signal fraction as possible, as low an E_T threshold as possible is desirable. In practice, the threshold value cannot be chosen much lower than 40 GeV per jet. The L1 trigger applies cuts on the calibrated E_T value of the jet. Thus, a threshold of 40 GeV corresponds to 20 to 25 GeV in reconstructed E_T, i.e. to values where noise effects start becoming sizable.

In the trigger tables forseen for the first LHC running period, a L1 2-jet rate of $\mathcal{O}(1)$ kHz is planned. For luminosities of $10^{32}\mathrm{cm}^{-2}\mathrm{s}^{-1}$ and above, the rate from standard QCD processes for events with at least 2 central jets ($|\eta| < 2.5$) with $E_T > 40$ GeV is above this. Thus additional conditions need to be employed in the L1 trigger to reduce the rate from QCD processes. The efficiency of several conditions

was investigated and, in the following, the corresponding rate reduction factors are always quoted with respect to the rate of QCD events that contain at least 2 central jets with $E_T > 40$ GeV per jet. These conditions are:

1) Condition based on additional central detector quantities available to the Calorimeter Trigger.
2) Condition based on T1 and T2 as vetoes.
3) Condition based on the RP detectors at ± 220 m and ± 420 m distance from the CMS IP.
4) Condition based on the Muon Trigger.

The QCD background events were generated with the Pythia Monte Carlo generator.

At higher luminosities more than one interaction takes place per bunch crossing; the central exclusive production of a Higgs boson is overlaid with additional, typically soft events, the so-called pile-up. In order to assess the effect when the signal is overlaid with pile-up, a sample of 500,000 pile-up events was generated with Pythia. This sample includes inelastic as well as elastic and diffractive events. Pythia underestimates the number of final state protons in this sample. The correction to the Pythia leading proton spectrum described in [6] was used to obtain the results discussed in the following.

The effect from beam-halo and beam-gas events on the L1 rate is not yet included in the studies discussed here. Preliminary estimates suggest that the size of their contribution is such that the conclusions of this article are not invalidated.

Table 1 summarizes the situation for luminosities between $10^{32}\mathrm{cm}^{-2}\mathrm{s}^{-1}$ and $10^{34}\mathrm{cm}^{-2}\mathrm{s}^{-1}$. Given a target rate for events with 2 central L1 jets of $\mathcal{O}(1)$ kHz, a total rate reduction between a factor 20 at $1 \times 10^{33}\mathrm{cm}^{-2}\mathrm{s}^{-1}$ and 200 at $1 \times 10^{34}\mathrm{cm}^{-2}\mathrm{s}^{-1}$ is necessary.

Table 1: Reduction of the rate from standard QCD processes for events with at least 2 central L1 jets with $E_T > 40$ GeV, achievable with requirements on the tracks seen in the RP detectors. Additional rate reductions can be achieved with the H_T condition and with a topological condition (see text). Each of them yields, for all luminosities listed, an additional reduction by about a factor 2.

Luminosity $[\mathrm{cm}^{-2}\mathrm{s}^{-1}]$	# Pile-up events per bunch crossing	L1 2-jet rate [kHz] for $E_T > 40$GeV per jet	Total reduction needed	Reduction when requiring track in RP detectors				
				at 220 m		at 420 m	at 220 m & 420 m (asymmetric)	
					$\xi < 0.1$			$\xi < 0.1$
1×10^{32}	0	2.6	2	370				
1×10^{33}	3.5	26	20	7	15	27	160	380
2×10^{33}	7	52	40	4	10	14	80	190
5×10^{33}	17.5	130	100	3	5	6	32	75
1×10^{34}	35	260	200	2	3	4	17	39

3.1 Condition based on central CMS detector quantities

In addition to the E_T values of individual L1 jets, the CMS Calorimeter Trigger has at its disposal the scalar sum, H_T, of the E_T values of all jets. Requiring that essentially all the E_T be concentrated in the two central L1 jets with highest E_T, i.e. $[E_T^1 + E_T^2]/H_T > 0.9$ (H_T condition), corresponds to imposing a rapidity gap of at least 2.5 units with respect to the beam direction. This condition reduces the rate of QCD events by approximately a factor 2, independent of the presence of pile-up and with only a small effect on the signal efficiency.

3.2 Condition based on TOTEM detectors T1 and T2

Using T1 and T2 as vetoes in events with 2 central L1 jets imposes the presence of a rapidity gap of at least 4 units. This condition suppresses QCD background events by several orders of magnitude. At luminosities low enough so that not more than one interaction takes place per bunch crossing, the signal efficiency is very high ($> 90\%$). In the presence of pile-up, the signal efficiency falls rapidly. The non-diffractive component in pile-up events tends quickly to fill in the rapidity gap in the Higgs production process. Only about 20 (5) % of signal events survive in the presence of 1 (2) pile-up event(s).

3.3 Condition based on Roman Pot detectors

Demanding that a proton be seen in the RP detectors at 220 m results in excellent suppression of QCD background events in the absence of pile-up. This is demonstrated in Figure 1 for a luminosity of $10^{32}\mathrm{cm}^{-2}\mathrm{s}^{-1}$. There, the rate of QCD background events with at least 2 central L1 jets with E_T above a threshold is shown as function of the threshold value. The two histograms reflect the rate without and with the requirement that a proton be seen in the RP detectors at 220 m. The rate of QCD background events containing at least 2 central L1 jets with $E_T > 40$ GeV each is reduced by a factor ~ 370. At $2 \times 10^{33}\mathrm{cm}^{-2}\mathrm{s}^{-1}$, where on the average 7 pile-up events overlay the signal event, the diffractive component in the pile-up causes the reduction to decrease to a factor ~ 4, and at $10^{34}\mathrm{cm}^{-2}\mathrm{s}^{-1}$, to a factor ~ 2, as can be seen from table 1.

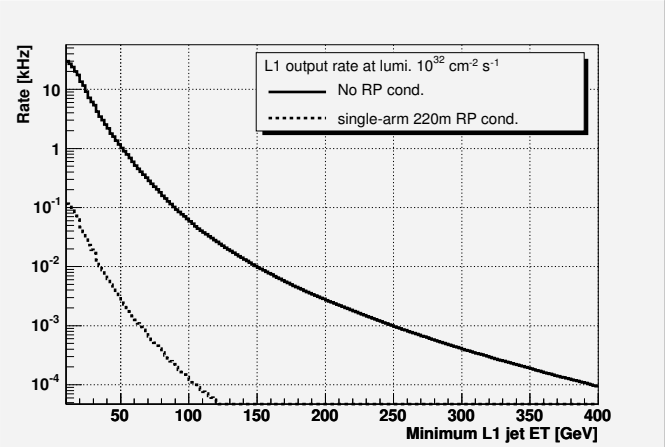

Fig. 1: L1 rate for the QCD background at a luminosity of $10^{32}\mathrm{cm}^{-2}\mathrm{s}^{-1}$ as function of the L1 threshold value when requiring at least 2 central L1 jets with E_T above threshold.

Table 1 summarizes the reduction factors achieved with different conditions for tracks in the RP detectors: a track in the RP detectors at 220 m distance on one side of the IP (single-arm 220 m), without and with a cut on ξ, a track in the RP detectors at 420 m distance on one side of the IP (single-arm 420 m), a track in the RP detectors at 220 m and 420 m distance (asymmetric). Because the detectors at 220 m and 420 m have complementary coverage in ξ, the last condition in effect selects events with two tracks of very different ξ value, in which one track is seen at 220 m distance on one side of the IP and a second track is seen on the other side at 420 m. If not by the L1 trigger, these asymmetric events can be selected by the HLT and are thus of highest interest. The effect on the acceptance of the RP detectors of a collimator located in front of the LHC magnet Q5, which will be operative at higher luminosities, has not been taken into account in table 1.

A further reduction of the QCD rate could be achieved with the help of a topological condition. The 2-jet system has to balance the total momentum component of the two protons along the beam axis. In signal events with asymmetric ξ values, the proton seen on one side in the RP detectors at 220 m distance is the one with the larger ξ and thus has lost more of its initial momentum component along the

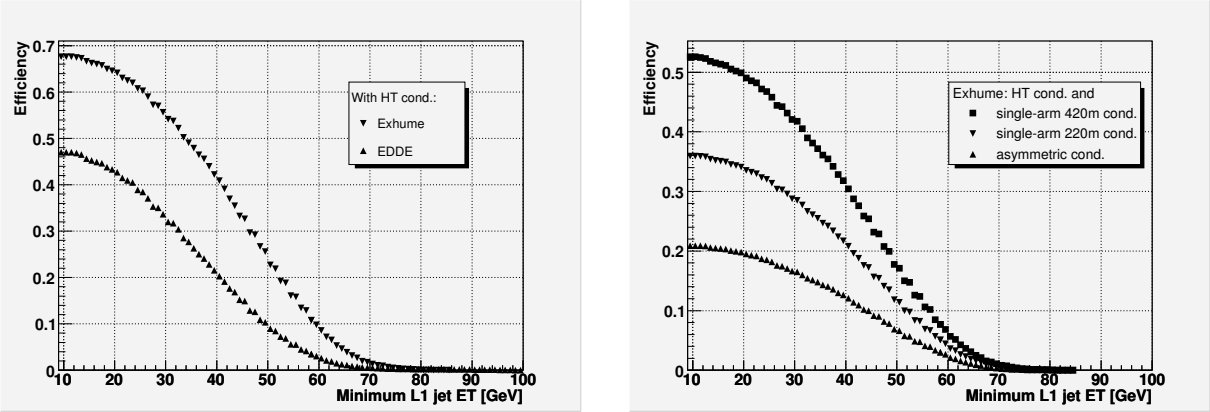

Fig. 2: L1 selection efficiency as function of the E_T threshold value when requiring at least 2 central L1 jets with E_T above threshold. All plots are for the non-pile-up case and the H_T condition (see text) has been applied. Left: Comparison between the EDDE and Exhume Monte Carlo generators, without applying any additional RP conditions. Right: Comparison of the effect of different RP conditions on the efficiency in the Exhume Monte Carlo sample.

beam axis. Hence the jets tend to be located in the same η-hemisphere as the RP detectors that detect this proton. A trigger condition requiring that $[\eta^{jet1} + \eta^{jet2}] \times \mathrm{sign}(\eta^{220m\ RP}) > 0$ would reduce the QCD background by a factor 2, independent of pile-up, and with no loss in signal efficiency.

A reduction of the QCD rate to levels compatible with the trigger bandwidth requirements by including RP detectors at a distance of 220 m from the CMS IP thus appears feasible for luminosities up to $2 \times 10^{33} \mathrm{cm}^{-2}\mathrm{s}^{-1}$, as long as a ξ cut can be administered in the L1 trigger such that the accepted events can be restricted to the diffractive peak region around $\xi = 0$. Higher luminosities would necessitate inclusion of the RP detectors at 420 m distance in the L1 trigger.

In order to study the effect of the L1 trigger selection on the Higgs signal, signal samples of 20,000 events with central exclusive production of a Higgs Boson were generated with the Monte-Carlo programs EDDE [7] (version 1.1) and Exhume [8] (version 0.9). Figure 2 shows the L1 selection efficiency as a function of the E_T threshold values when requiring at least 2 central L1 jets with E_T above threshold. The histograms show the case when no pile-up is present. The presence of pile-up has only a small effect on the efficiency curves. The plot on the left-hand side compares the efficiency curves obtained for EDDE and Exhume. For a threshold of 40 GeV per jet, Exhume yields an efficiency of about 40%. As a consequence of its less central jet η distribution (see [9]), the efficiency for EDDE is about 20% lower than the one of Exhume. The plot on the right-hand side overlays the efficiency curves obtained with Exhume when including three different RP detector conditions in the L1 2-jet trigger: single-arm 220 m, single-arm 420 m and the asymmetric 220 & 420 m condition. At an E_T threshold of 40 GeV per jet, the single-arm 220 m (420 m) condition results in an efficiency of the order 20% (30%), the asymmetric condition in one of 15%. This also means that even without the possibility of including the RP detectors at 420 m distance from the CMS IP in the L1 trigger, 15% of the signal events can be triggered with the single-arm 220 m condition, but will have a track also in the 420 m detectors which can be used in the HLT.

3.4 Condition based on the Muon Trigger

An alternative trigger strategy may be to exploit the relatively muon-rich final state from B-decays. We estimate that up to 10% of the signal events could be retained using this technique. Further investigations are underway at the time of writing.

4 Conclusions

Retaining a Higgs Boson with mass around 120 GeV poses a special challenge to triggering at the LHC. The relatively low transverse momenta of its decay products necessitate L1 jet E_T thresholds as low as 40 GeV. Thresholds that low would result in a L1 trigger rate of more than 50 kHz, essentially saturating the available output bandwidth.

The results we presented in this article are preliminary and should be taken as a snapshot of our present understanding. They can be summarized as follows: The output rate of a 2-jet L1 trigger condition with thresholds of 40 GeV per jet can be kept at an acceptable $\mathcal{O}(1)$ kHz by including the TOTEM forward detectors in the CMS L1 trigger. In the absence of pile-up, either using the TOTEM T1 and T2 detectors as vetoes or requiring that a proton be seen in the TOTEM RP detectors at 220 m on one side of the CMS IP (single-sided 220 m condition) results in a sufficient reduction of the QCD event rate that dominates the L1 trigger output rate. At higher luminosities, up to $2 \times 10^{33}\mathrm{cm}^{-2}\mathrm{s}^{-1}$, where pile-up is present, it is necessary to combine the single-sided 220 m condition with conditions based on event topology and on H_T, the scalar sum of all L1 jet E_T values. Going to even higher luminosities, up to $1 \times 10^{34}\mathrm{cm}^{-2}\mathrm{s}^{-1}$, would necessitate additional L1 trigger conditions, such as inclusion of RP detectors at 420 m distance from the CMS IP, which, however, would require an increase in the L1 trigger latency. These L1 trigger conditions result in signal efficiencies between 15% and 20%.

We expect no trigger problems for final states rich in high p_T leptons, such as the WW decay modes of the Standard Model Higgs Boson.

Acknowledgement

We are grateful to Sridhara Dasu for sharing with us his expertise on the CMS L1 trigger simulation and for providing considerable pratical help with it. We would like to thank him and Dan Bradley for their invaluable help with producing the Monte Carlo event samples used in this article.

References

[1] "CMS: The TRIDAS project – Technical Design Report Vol.1: The trigger systems", CMS collab., CERN-LHCC-2000-038.
"CMS: The TRIDAS project – Technical Design Report Vol.2: Data Acquisition and High-Level Trigger", CMS collab., CERN-LHCC-2002-026.

[2] "TOTEM Technical Design Report", TOTEM collab., CERN-LHCC-2004-002
and Addendum to the TOTEM-TDR, TOTEM collab., CERN-LHCC-2004-020.

[3] "FP420: A proposal to investigate the feasibility of installing proton tagging detectors in the 420 m region of the LHC", M.G.Albrow et al., CERN-LHCC-2005-025, LHCC-I-015.
available from: `glodwick.hep.man.ac.uk/brian/fp420loi.doc`

[4] The MAD-X Program, Methodical Accelerator Design, available from `www.cern.ch/mad`.

[5] "TOTEM forward measurements: leading proton acceptance", V. Avati, K. Österberg, these proc.
"TOTEM forward measurements: exclusive central diffraction", J. Kalliopuska et al., these proc.

[6] "Leading proton production in ep and pp experiments: how well do high-energy physics Monte Carlos reproduce the data ?", G.Bruni et al., these proc.

[7] "EDDE Monte Carlo event generator", R.A. Ryutin, hep-ph/0409180.

[8] "Exhume: A Monte Carlo event generator for exclusive diffraction", J. Monk, A. Pilkington, hep-ph/0502077.

[9] "Monte-Carlo generators for central exclusive diffraction", M. Boonekamp et al., these proc.

Proposal to upgrade the very forward region at CMS

V. Andreev[1], *A.Bunyatyan*[2,3], *H. Jung*[4], *M. Kapishin*[5], *L. Lytkin*[3,5]
[1] Lebedev Physics Institute, Moscow, [2] Yerevan Physics Institute,
[3] MPI-K Heidelberg, [4] DESY Hamburg, [5] JINR Dubna

Abstract
The possibilities of extending the acceptance of LHC experiments beyond 7 units of pseudorapidity are investigated. With additional detectors it would be possible to measure the particles with energies above 2 TeV in the pseudorapidity range between 7 and 11.

1 Introduction

At the LHC experiments, CMS and ATLAS, the acceptance for forward energy measurements is limited to about 5 units of pseudorapidity. The acceptance of CMS detector will be extended by proposed CASTOR calorimeter, which will cover the angular range $5.4 < \eta < 6.7$. Already with this device small-x parton dynamics can be studied down to very small x-values of $10^{-6} - 10^{-7}$ with Drell-Yan, prompt photon and jet events at small invariant masses of the order of $M \sim 10$ GeV.

In the present work we investigate the technical possibilities of extending the angular acceptance for forward energy measurement beyond 7 units of pseudorapidity. Extending the acceptance down to $\eta \sim 11$, x-values down to 10^{-8} can be reached, which is a completely unexplored region of phase space. In this region, effects coming from new parton dynamics are expected to show up, as well as effects coming from very high density gluonic systems, where saturation and recombination effects will occur. In this region of phase space, a breakdown of the usual factorization formalism is expected, and multiple

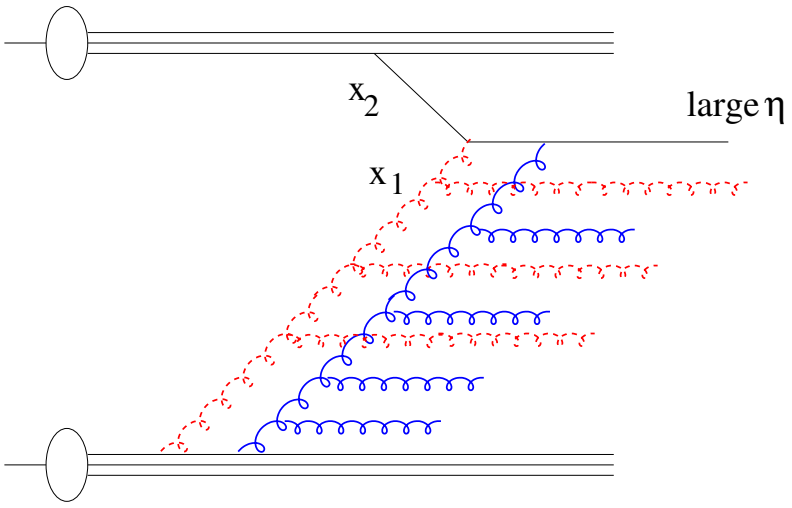

Fig. 1: Schematic picture of multiple interactions at small x

interactions will be dominant (see Fig 1) [1]. The full angular coverage from the central to the most forward region allows a systematic study of the transition from single particle exchange processes to complex systems and a systematic understanding of non-linear and collective phenomena.

The interest in the very forward region of phase space is not only motivated by the fundamental understanding of QCD in a new phase of matter, but is also important for the further understanding of high energetic cosmic rays [2].

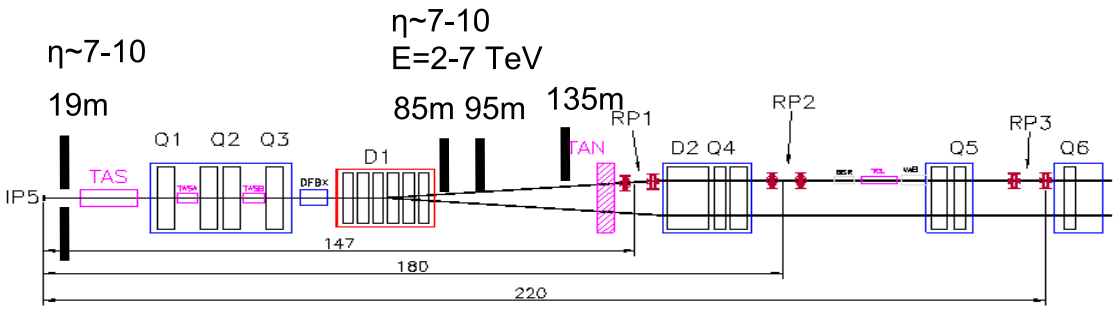

Fig. 2: Schematic view of forward beamline at CMS detector up to 220m. The positions of proposed tracking devices at 19m, 85m and 95m and calorimeter at 135m are indicated.

2 Tracking and energy measurement in the very forward region

For this study the geometry of the beam-line around the CMS detector up to 150m from interaction point has been implemented in the GEANT-3 [3] simulation program. The PYTHIA Monte-Carlo generator program [4] was used to generate charged particles produced in the interaction point, which were subsequently fed into the beam-line simulation.

The main restriction for additional installations is the very limited space available between magnetic elements. Up to about 80m there is no space for a calorimeter, and there one can only consider the installation of tracking devices, such as Roman Pots or micro-stations [5]. On the other hand, to be able to measure the particle momenta, the tracking devices should be placed after bending magnets.

Therefore the idea is to have tracking devices before and after dipoles, to be able to measure both the integrated particle flow and the particle momenta. The free space after 135 m can be used for a calorimeter.

Taking into account the limited space available for new detectors, the background conditions and magnetic field, the following strategy is proposed (Fig.2):

- the 25 cm space in front of TAS absorber at 19 m from interaction point can be used to install two micro-stations with two half-ring radiation hard silicon or diamond detectors approaching the beam horizontally up to 5-10mm. At this position the particles can not be separated by their momenta, thus the micro-stations will measure the charged particle flow integrated up to energies of $\sim$ 7 TeV in the pseudorapidity range between 7.3 and 9 or 10.5, depending on how close the counter can go to the beam (see Fig. 3). The detector will also provide accurate position measurement which is necessary for linking with roman-pots/micro-stations installed further down the beam line. Combining the position and time-of-flight measurement of these micro-stations with the event vertex measured in central detector will allow to suppress beam-wall background and pile-up events;
- a combination of two horizontal roman-pots/micro-stations can be installed behind the dipole magnets D1 at 85m and 95m. The detectors are the half-rings and approach the beam horizontally from one side up to 10mm. These detectors will cover the pseudorapidity range above 8 units (see Fig. 5). The particles with energies below 2 TeV will escape the detector acceptance, as shown in Fig. 4 and 5.
- a hadronic calorimeter at 135m (in front of TAN iron absorber) with a minimal distance to the beam of 10cm (radius of beam-pipe) will measure the energy in the range 2-5.5 TeV and pseudorapidity between 7 and 11 (see Fig.6). This can be a sandwich type calorimeter with radiation hard sensitive layers, with a transverse size up to 1×1 m^2 and depth about 7-9 hadronic interaction length. Optionally one can consider to instrument the TAN absorber with sensitive layers.

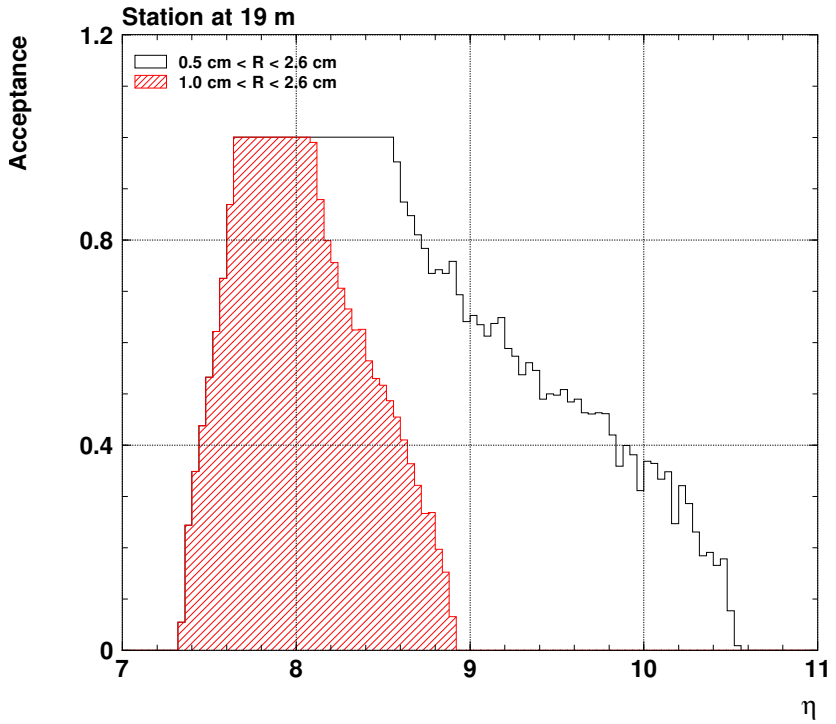

Fig. 3: Acceptance of micro-station detector at 19m as a function of pseudorapidity.

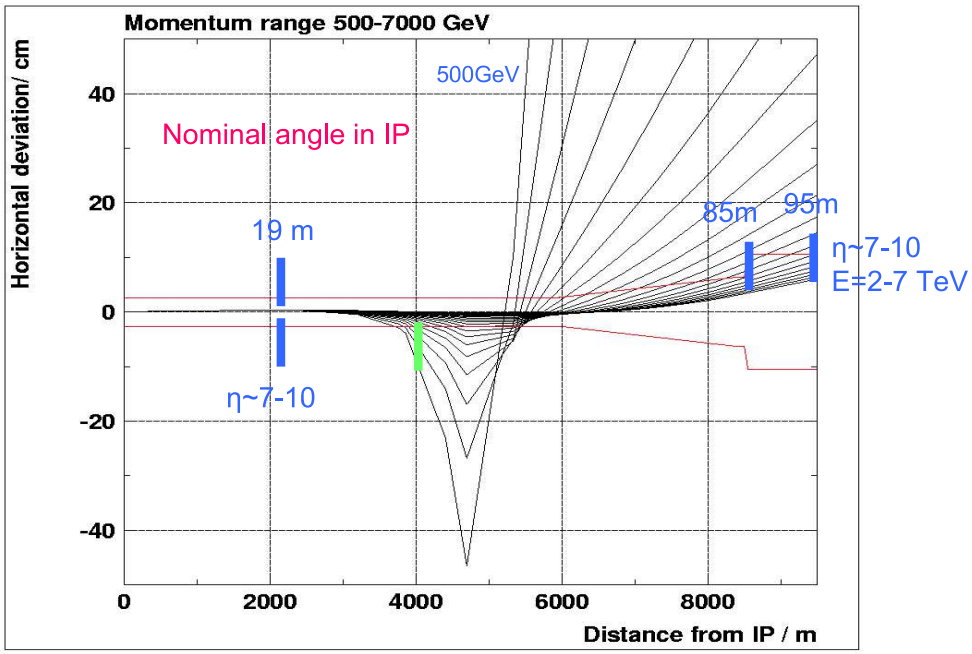

Fig. 4: The trajectory of particles in momentum range 500-7000 GeV, scattered from interaction point at 0 deg. The positions of proposed tracking devices at 19m, 85m and 95m are indicated.

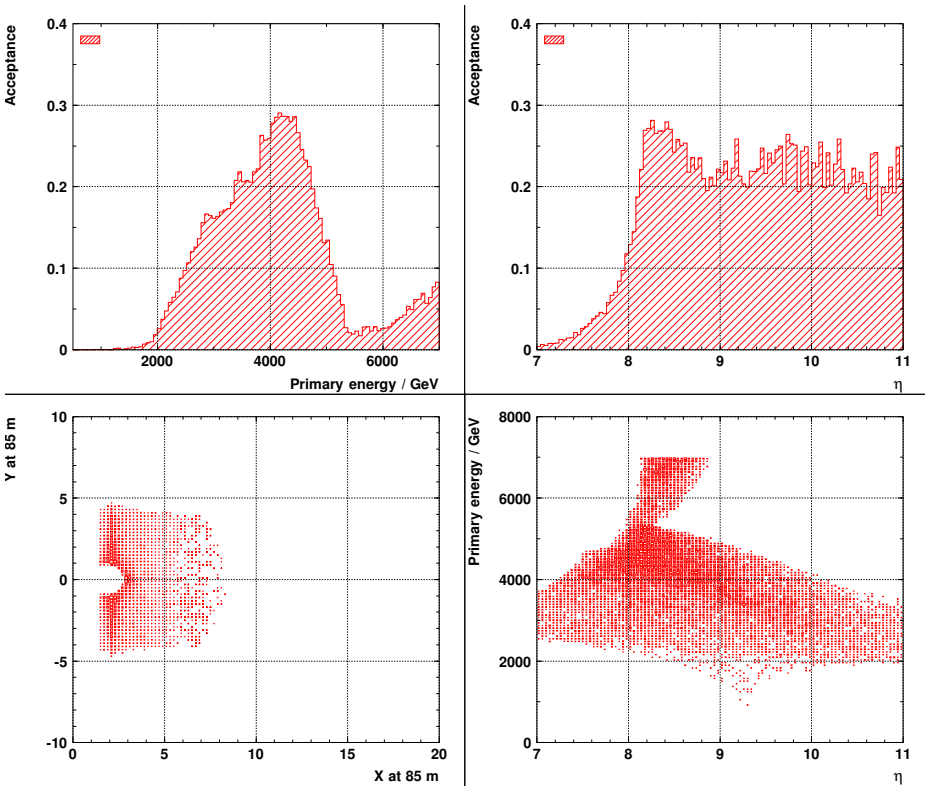

Fig. 5: Acceptance of roman pots/micro-station detector at 85 m and 95m as a function of energy and pseudorapidity.

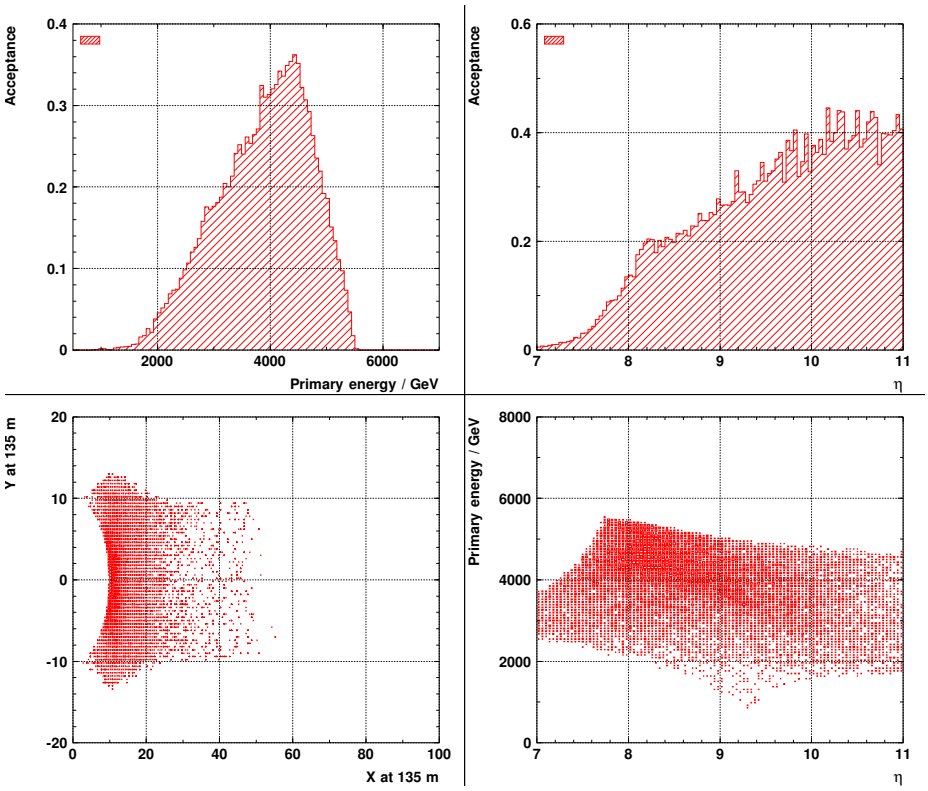

Fig. 6: Acceptance of calorimeter at 135 m as a function of energy and pseudorapidity.

The calorimeter covers basically the same kinematic range as the micro-stations at 85 and 95m, but it is needed for energy measurement. In addition it can be used for redundancy, background subtraction and cross calibration.

The acceptances of the proposed detectors as function of energy and pseudorapidity are summarized in Table 1. The result shows that with the proposed installations it will be possible to measure the energy flow in the energy range between 2 and 7 GeV and the pseudorapidity range between 7 and 11.

Table 1: Acceptance as a function of E_p and η

	0.5–7 TeV	2–5.5 TeV
two roman-pots/micro-stations at 85 and 95m		
$\eta = 7 - 10$	11%	21%
$\eta = 7 - 8$	10%	10–20%
$\eta = 8 - 9$	15-25%	30–55%
$\eta = 9 - 11$	20-25%	55–60%
Calorimeter at 135m		
$\eta = 7 - 8$	15%	25%
$\eta = 8 - 9$	20-25%	35–55%
$\eta = 9 - 11$	25-40%	45–60%

To be able to measure the particles with momenta below 2 TeV one would need to install detectors in the cold area between the quadrupoles at 40–50 m. This will require essential modifications of cryogenic lines, and can be considered for a future upgrade program.

3 Conclusions

We have studied the possibilities of extending the angular acceptance for forward energy measurement at LHC. With additional roman-pots/micro-stations and a calorimeter it will be possible to measure the forward energy in the rapidity range between 7 and 11 units. Such installation will be a valuable addition to the LHC physics program.

References

[1] J. Bartels, *AGK cutting rules for pp collisions*. Talk at HERA-LHC workshop, March 2005.

[2] J. Ellis, *LHC - physics*. Plenary talk at HERA-LHC workshop, March 2005.

[3] Brun, R. and Bruyant, F. and Maire, M. and McPherson, A. C. and Zanarini, P., *GEANT3*. CERN-DD/EE/84-1.

[4] Sjostrand, Torbjorn and others, Comput. Phys. Commun. **135**, 238 (2001). Hep-ph/0010017.

[5] Nomokonov, V. P., *The microstation concept for forward physics*. Prepared for 1st Workshop on Forward Physics and Luminosity Determination at LHC, Helsinki, Finland, 31 Oct - 4 Nov 2000.

Diffractive Higgs production: theory

Jeff Forshaw
Particle Physics Group, School of Physics & Astronomy,
University of Manchester, Manchester, M13 9PL. United Kingdom.

Abstract
We review the calculation for Higgs production via the exclusive reaction $pp \to p + H + p$. In the first part we review in some detail the calculation of the Durham group and emphasise the main areas of uncertainty. Afterwards, we comment upon other calculations.

1 Introduction

Our aim is to compute the cross-section for the process $pp \to p + H + p$. We shall only be interested in the kinematic situation where all three final state particles are very far apart in rapidity with the Higgs boson the most central. In this "diffractive" situation the scattering protons lose only a very small fraction of their energy, but nevertheless enough to produce the Higgs boson. Consequently, we are in the limit where the incoming protons have energy E much greater than the Higgs mass m_H and so we will always neglect terms suppressed by powers of m_H/E. In the diffractive limit cross-sections do not fall as the beam energy increases as a result of gluonic (spin-1) exchanges in the t-channel.

Given the possibility of instrumenting the LHC to detect protons scattered through tiny angles with a high resolution [1–4], diffractive production of any central system X via $pp \to p + X + p$ is immediately of interest if the production rate is large enough. Even if X is as routine as a pair of high p_T jets we can learn a great deal about QCD in a new regime [2, 3, 5, 6]. But no doubt the greatest interest arises if X contains "new physics" [7–19]. The possibility arises to measure the new physics in a way that is not possible using the LHC general purpose detectors alone. For example, its invariant mass may be measured most accurately, and the spin and CP properties of the system may be explored in a manner more akin to methods hitherto thought possible only at a future linear collider. Our focus here is on the production of a Standard Model Higgs boson [7, 8, 13, 18, 19]. Since the production of the central system X effectively factorizes, our calculation will be seen to be of more general utility.

Most of the time will be spent presenting what we shall call the "Durham Model" of central exclusive production [7, 8]. It is based in perturbative QCD and is ultimately to be justified a posteriori by checking that there is not a large contribution arising from physics below 1 GeV. A little time will also be spent explaining the non-perturbative model presented by the Saclay group [13] and inspired by the original paper of Bialas and Landshoff [20]. Even less time will be devoted to other approaches which can be viewed, more-or-less, as hybrids of the other two [18, 19].

Apart from the exclusive process we study here, there is also the possibility to produce the new physics in conjunction with other centrally produced particles, e.g. $pp \to p + H + X + p$. This more inclusive channel typically has a much higher rate but does not benefit from the various advantages of exclusive production. Nevertheless, it must be taken into account in any serious phenomenological investigation into the physics potential of central exclusive production [21, 22]

2 The Durham Model

The calculation starts from the easier to compute parton level process $qq \to q + H + q$ shown in Figure 1. The Higgs is produced via a top quark loop and a minimum of two gluons need to be exchanged in order that no colour be transferred between the incoming and outgoing quarks. Quark exchange in the t-channel leads to contributions which are suppressed by an inverse power of the beam energy and so the diagram in Figure 1 is the lowest order one. Our strategy will be to compute only the imaginary part

of the amplitude and we shall make use of the Cutkosky rules to do that – the relevant cut is indicated by the vertical dotted line in Figure 1. There is of course a second relevant diagram corresponding to the Higgs being emitted from the left-hand gluon. We shall assume that the real part of the amplitude is negligible, as it will be in the limit of asymptotically high centre-of-mass energy when the quarks are scattered through small angles and the Higgs is produced centrally.

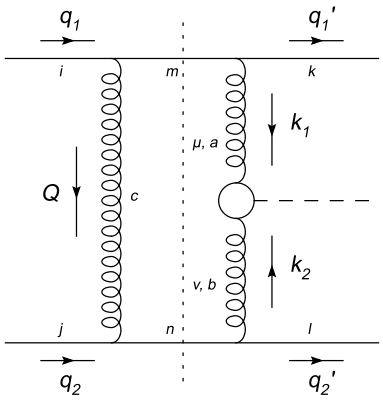

Fig. 1: The relevant Feynman graph for $qq \to q + H + q$.

The calculation can be further simplified by making use of the eikonal approximation for those vertices which couple the gluons to the external quarks. The gluons are very soft and so, modulo corrections which are suppressed by the inverse of the beam energy, we can approximate the qqg vertices by $2g\tau^a_{ij}q_{1,2}\delta_{\lambda,\lambda'}$, where τ^a is a Gell-Mann matrix, g is the QCD coupling and the Kronecker delta tells us that the quark does not change its helicity. The calculation of the amplitude is now pretty straightforward:

$$\begin{aligned} \mathrm{Im}A^{ik}_{jl} &= \frac{1}{2}\times 2\int d(PS)_2\;\delta((q_1-Q)^2)\delta((q_2+Q)^2) \\ &\quad \frac{2gq_1^\alpha}{Q^2}\,\frac{2gq_{2\alpha}}{}\,\frac{2gq_1^\mu}{k_1^2}\,\frac{2gq_2^\nu}{k_2^2}\,V^{ab}_{\mu\nu}\,\tau^c_{im}\tau^c_{jn}\tau^a_{mk}\tau^b_{nl}\,. \end{aligned} \tag{1}$$

The factor of $1/2$ is from the cutting rules and the factor of 2 takes into account that there are two diagrams. The phase-space factor is

$$d(PS)_2 = \frac{s}{2}\int\frac{d^2\mathbf{Q_T}}{(2\pi)^2}\,d\alpha d\beta \tag{2}$$

where we have introduced the Sudakov variables via $Q = \alpha q_1 + \beta q_2 + Q_T$. The delta functions fix the cut quark lines to be on-shell, which means that $\alpha \approx -\beta \approx \mathbf{Q_T}^2/s \ll 1$ and $Q^2 \approx Q_T^2 \equiv -\mathbf{Q_T}^2$. As always, we are neglecting terms which are energy suppressed such as the product $\alpha\beta$. For the Higgs production vertex we take the Standard Model result:

$$V^{ab}_{\mu\nu} = \delta^{ab}\left(g_{\mu\nu} - \frac{k_{2\mu}k_{1\nu}}{k_1\cdot k_2}\right)V \tag{3}$$

where $V = m_H^2\alpha_s/(4\pi v)F(m_H^2/m_t^2)$ and $F \approx 2/3$ provided the Higgs is not too heavy. The Durham group also include a NLO K-factor correction to this vertex. After averaging over colours we have

$$\tau^c_{im}\tau^c_{jn}\tau^a_{mk}\tau^b_{nl} \to \frac{\delta^{ab}}{4N_c^2}.$$

We can compute the contraction $q_1^\mu V_{\mu\nu}^{ab} q_2^\nu$ either directly or by utilising gauge invariance which requires that $k_1^\mu V_{\mu\nu}^{ab} = k_2^\nu V_{\mu\nu}^{ab} = 0$. Writing[1] $k_i = x_i q_i + k_{iT}$ yields

$$q_1^\mu V_{\mu\nu}^{ab} q_2^\nu \approx \frac{k_{1T}^\mu}{x_1}\frac{k_{2T}^\nu}{x_2} V_{\mu\nu}^{ab} \approx \frac{s}{m_H^2} k_{1T}^\mu k_{2T}^\nu V_{\mu\nu}^{ab} \tag{4}$$

since $2k_1 \cdot k_2 \approx x_1 x_2 s \approx m_H^2$. Note that it is as if the gluons which fuse to produce the Higgs are transversely polarized, $\epsilon_i \sim k_{iT}$. Moreover, in the limiting case that the outgoing quarks carry no transverse momentum $Q_T = -k_{1T} = k_{2T}$ and so $\epsilon_1 = -\epsilon_2$. This is an important result; it clearly generalizes to the statement that the centrally produced system should have a vanishing z-component of angular momentum in the limit that the protons scatter through zero angle (i.e. $q_{iT}'^2 \ll Q_T^2$). Since we are experimentally interested in very small angle scattering this selection rule is effective. One immediate consequence is that the Higgs decay to b-quarks may now be viable. This is because, for massless quarks, the lowest order $q\bar{q}$ background vanishes identically (it does not vanish at NLO). The leading order $b\bar{b}$ background is therefore suppressed by a factor $\sim m_b^2/m_H^2$. Beyond leading order, one also needs to worry about the $b\bar{b}g$ final state.

Returning to the task in hand, we can write the colour averaged amplitude as

$$\frac{\mathrm{Im}A}{s} \approx \frac{N_c^2 - 1}{N_c^2} \times 4\alpha_s^2 \int \frac{d^2\mathbf{Q_T}}{\mathbf{Q_T}^2 \mathbf{k_{1T}}^2 \mathbf{k_{2T}}^2} \frac{-\mathbf{k_{1T}} \cdot \mathbf{k_{2T}}}{m_H^2}\, V. \tag{5}$$

Using $d^3\mathbf{q_1}' d^3\mathbf{q_2}' d^3\mathbf{q_H} \delta^{(4)}(q_1 + q_2 - q_1' - q_2' - q_H) = d^2\mathbf{q_{1T}}' d^2\mathbf{q_{2T}}' dy\ E_H$ (y is the rapidity of the Higgs) the cross-section is therefore

$$\frac{d\sigma}{d^2\mathbf{q_{1T}}' d^2\mathbf{q_{2T}}' dy} \approx \left(\frac{N_c^2 - 1}{N_c^2}\right)^2 \frac{\alpha_s^6}{(2\pi)^5}\frac{G_F}{\sqrt{2}} \left[\int \frac{d^2\mathbf{Q_T}}{2\pi} \frac{\mathbf{k_{1T}} \cdot \mathbf{k_{2T}}}{\mathbf{Q_T}^2 \mathbf{k_{1T}}^2 \mathbf{k_{2T}}^2} \frac{2}{3}\right]^2 \tag{6}$$

and for simplicity here we have taken the large top mass limit of V (i.e. $m_t \gg m_H$). We are mainly interested in the forward scattering limit whence

$$\frac{\mathbf{k_{1T}} \cdot \mathbf{k_{2T}}}{\mathbf{Q_T}^2 \mathbf{k_{1T}}^2 \mathbf{k_{2T}}^2} \approx -\frac{1}{\mathbf{Q_T}^4}.$$

As it stands, the integral over Q_T diverges. Let us not worry about that for now and instead turn our attention to how to convert this parton level cross-section into the hadron level cross-section we need.[2]

What we really want is the hadronic matrix element which represents the coupling of two gluons into a proton, and this is really an off-diagonal parton distribution function [23]. At present we don't have much knowledge of these distributions, however we do know the diagonal gluon distribution function. Figure 2 illustrates the Durham prescription for coupling the two gluons into a proton rather than a quark. The factor K would equal unity if $x' = x$ and $k_T = 0$ which is the diagonal limit. That we should, in the amplitude, replace a factor of $\alpha_s C_F/\pi$ by $\partial G(x, Q_T)/\partial \ln Q_T^2$ can be easily derived starting from the DGLAP equation for evolution off an initial quark distribution given by $q(x) = \delta(1-x)$. The Durham approach makes use of a result derived in [24] which states that in the case $x' \ll x$ and $k_T^2 \ll Q_T^2$ the off-diagonality can be approximated by a multiplicative factor, K. Assuming a Gaussian form factor suppression for the k_T-dependence they estimate that

$$K \approx e^{-bk_T^2/2} \frac{2^{2\lambda+3}}{\sqrt{\pi}} \frac{\Gamma(\lambda + 5/2)}{\Gamma(\lambda + 4)} \tag{7}$$

[1] We can do this because $x_i \sim m_H/\sqrt{s}$ whilst the other Sudakov components are $\sim Q_T^2/s$.

[2] We note that (6) was first derived by Bialas and Landshoff, except that they made a factor of 2 error in the Higgs width to gluons.

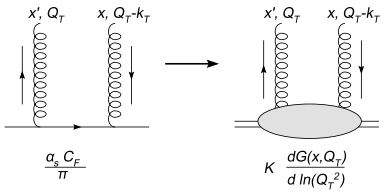

Fig. 2: The recipe for replacing the quark line (left) by a proton line (right).

and this result is obtained assuming a simple power-law behaviour of the gluon density, i.e. $G(x,Q) \sim x^{-\lambda}$. For the production of a 120 GeV Higgs boson at the LHC, $K \sim 1.2 \times e^{-bk_T^2/2}$. In the cross-section, the off-diagonality therefore provides an enhancement of $(1.2)^4 \approx 2$. Clearly the current lack of knowledge of the off-diagonal gluon is one source of uncertainty in the calculation. We also do not really know what to take for the slope parameter b. It should perhaps have some dependence upon Q_T and for $Q_T \sim 1.5$ GeV, which it will turn out is typical for a 120 GeV scalar Higgs, one might anticipate the same k_T-dependence as for diffractive J/ψ production which is well measured, i.e. $b \approx 4$ GeV^{-2}.

Thus, after integrating over the transverse momenta of the scattered protons we have

$$\frac{d\sigma}{dy} \approx \frac{1}{256\pi b^2} \frac{\alpha_s G_F \sqrt{2}}{9} \left[\int \frac{d^2\mathbf{Q_T}}{\mathbf{Q_T}^4} \, f(x_1, Q_T) f(x_2, Q_T) \right]^2 \tag{8}$$

where $f(x,Q) \equiv \partial G(x,Q)/\partial \ln Q^2$ and we have neglected the exchanged transverse momentum in the integrand. Notice that in determining the total rate we have introduced uncertainty in the normalisation arising from our lack of knowledge of b. This uncertainty, as we shall soon see, is somewhat diminished as the result of a similar b-dependence in the gap survival factor.

We should about the fact that our integral diverges in the infra-red. Fortunately we have missed some crucial physics. The lowest order diagram is not enough, virtual graphs possess logarithms in the ratio Q_T/m_H which are very important as $Q_T \to 0$; these logarithms need to be summed to all orders. This is Sudakov physics: thinking in terms of real emissions we must be sure to forbid real emissions into the final state. Let's worry about real gluon emission off the two gluons which fuse to make the Higgs. The emission probability for a single gluon is (assuming for the moment a fixed coupling α_s)

$$\frac{C_A \alpha_s}{\pi} \int_{Q_T^2}^{m_H^2/4} \frac{dp_T^2}{p_T^2} \int_{p_T}^{m_H/2} \frac{dE}{E} \sim \frac{C_A \alpha_s}{4\pi} \ln^2 \left(\frac{m_H^2}{Q_T^2} \right).$$

The integration limits are kinematic except for the lower limit on the p_T integral. The fact that emissions below Q_T are forbidden arises because the gluon not involved in producing the Higgs completely screens the colour charge of the fusing gluons if the wavelength of the emitted radiation is long enough, i.e. if $p_T < Q_T$. Now we see how this helps us solve our infra-red problem: as $Q_T \to 0$ so the screening gluon fails to screen and real emission off the fusing gluons cannot be suppressed. To see this argument through to its conclusion we realise that multiple real emissions exponentiate and so we can write the non-emission probability as

$$e^{-S} = \exp\left(-\frac{C_A \alpha_s}{\pi} \int_{Q_T^2}^{m_H^2/4} \frac{dp_T^2}{p_T^2} \int_{p_T}^{m_H/2} \frac{dE}{E} \right). \tag{9}$$

As $Q_T \to 0$ the exponent diverges and the non-emission probability vanishes faster than any power of Q_T. In this way our integral over Q_T becomes (its value is finite):

$$\int \frac{dQ_T^2}{Q_T^4} f(x_1, Q_T) f(x_2, Q_T) \, e^{-S} \, . \tag{10}$$

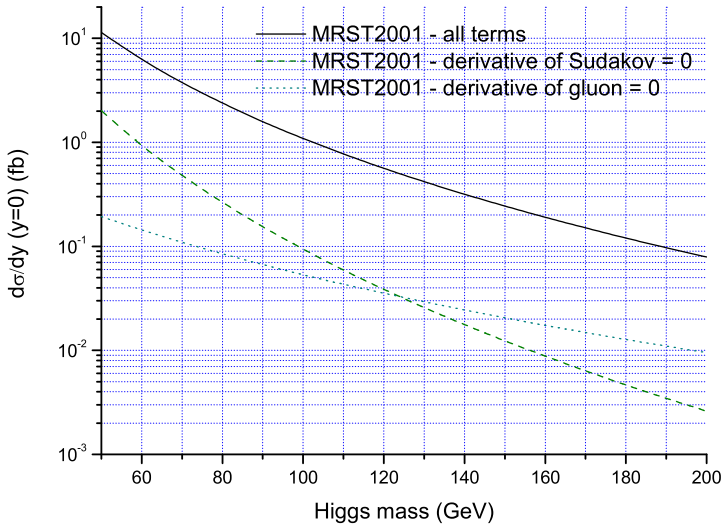

Fig. 3: The Higgs cross-section at zero rapidity, and the result obtained if one were to assume that $\partial G(x,Q)/\partial Q = 0$ or that $\partial S/\partial Q = 0$.

There are two loose ends to sort out before moving on. Firstly, note that emission off the screening gluon is less important since there are no associated logarithms in m_H/Q_T. Secondly, (9) is correct only so far as the leading double logarithms. It is of considerable practical importance to correctly include also the single logarithms. To do this we must re-instate the running of α_s and allow for the possibility that quarks can be emitted. Including this physics means we ought to use

$$e^{-S} = \exp\left(-\int_{Q_T^2}^{m_H^2/4} \frac{dp_T^2}{p_T^2}\frac{\alpha_s(p_T^2)}{2\pi}\int_0^{1-\Delta} dz\,\left[zP_{gg}(z) + \sum_q P_{qg}(z)\right]\right) \tag{11}$$

where $\Delta = 2p_T/m_H$, and $P_{gg}(z)$ and $P_{qg}(z)$ are the leading order DGLAP splitting functions. To correctly sum all single logarithms requires some care in that what we want is the distribution of gluons in Q_T with no emission up to m_H, and this is in fact [25]

$$\tilde{f}(x,Q_T) = \frac{\partial}{\partial \ln Q_T^2}\left(e^{-S/2}\,G(x,Q_T)\right).$$

The integral over Q_T is therefore

$$\int \frac{dQ_T^2}{Q_T^4}\tilde{f}(x_1,Q_T)\tilde{f}(x_2,Q_T) \tag{12}$$

which reduces to (10) in the double logarithmic approximation where the differentiation of the Sudakov factor is subleading.

The numerical effect of correctly including the single logarithms is large. For production of a 120 GeV Higgs at the LHC, there is a factor ~ 30 enhancement compared to the double logarithmic approximation, with a large part of this coming from terms involving the derivative of the Sudakov. Figure 3 shows just how important it is to keep those single logarithmic terms coming from differentiation of the Sudakov factor. For the numerical results we used the MRST2001 leading order gluon [26], as included in LHAPDF [27]. Here and elsewhere (unless otherwise stated), we use a NLO QCD K-factor of 1.5 and the one-loop running coupling with $n_f = 4$ and $\Lambda_{\rm QCD} = 160$ MeV. As discussed in the next paragraph, we also formally need an infra-red cut-off Q_0 for the Q_T-integral; we take $Q_0 = 0.3$ GeV

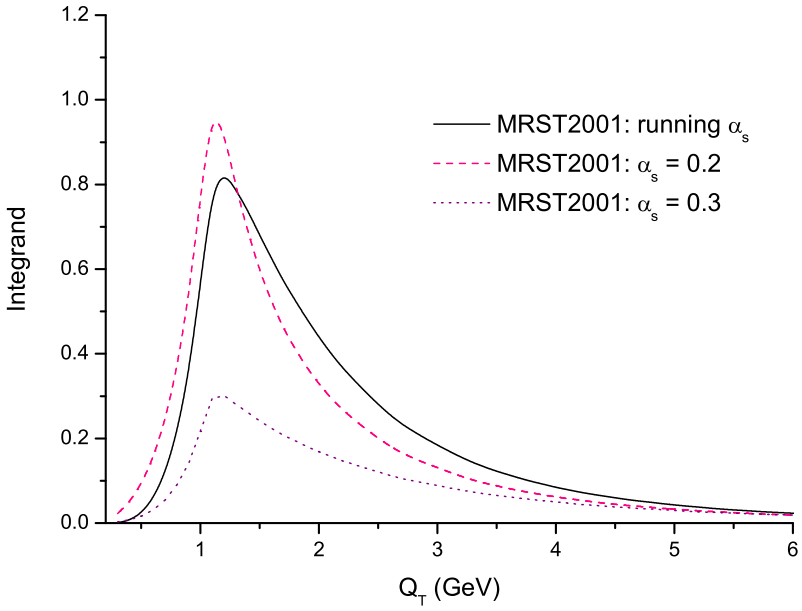

Fig. 4: The integrand of the Q_T integral for three different treatments of α_s and $m_H = 120$ GeV.

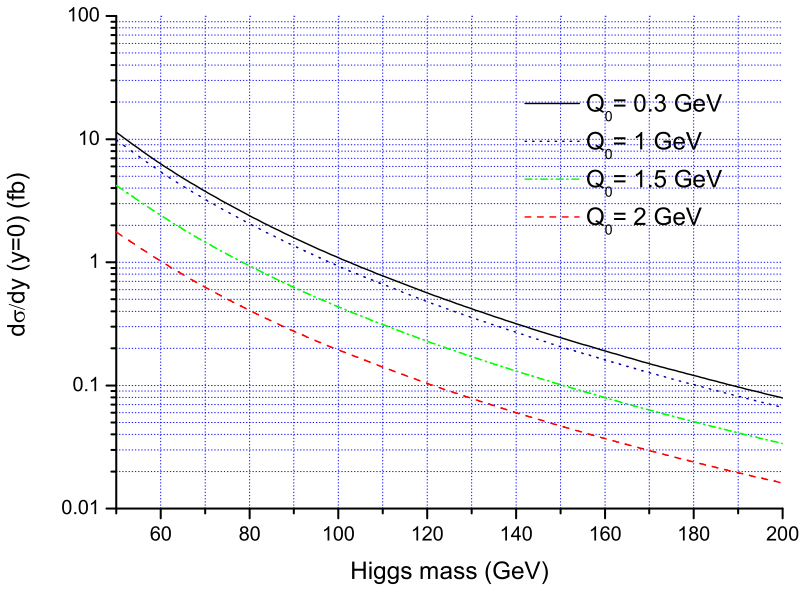

Fig. 5: The Higgs cross-section dependence upon the infra-red cutoff Q_0.

although as we shall see results are insensitive to Q_0 provided it is small enough. Finally, all our results include an overall multiplicative "gap survival factor" of 3% (gap survival is discussed shortly).

Formally there is the problem of the pole in the QCD coupling at $p_T = \Lambda_{\rm QCD}$. However, this problem can be side-stepped if the screening gluon has "done its job" sufficiently well and rendered an integrand which is peaked at $Q_T \gg \Lambda_{\rm QCD}$ since an infra-red cutoff on p_T can then safely be introduced. We must be careful to check whether or not this is the case in processes of interest. Indeed, a saddle point estimate of (10) reveals that

$$\exp(\langle \ln Q_T \rangle) \sim \frac{m_H}{2} \exp\left(-\frac{c}{\alpha_s}\right) \tag{13}$$

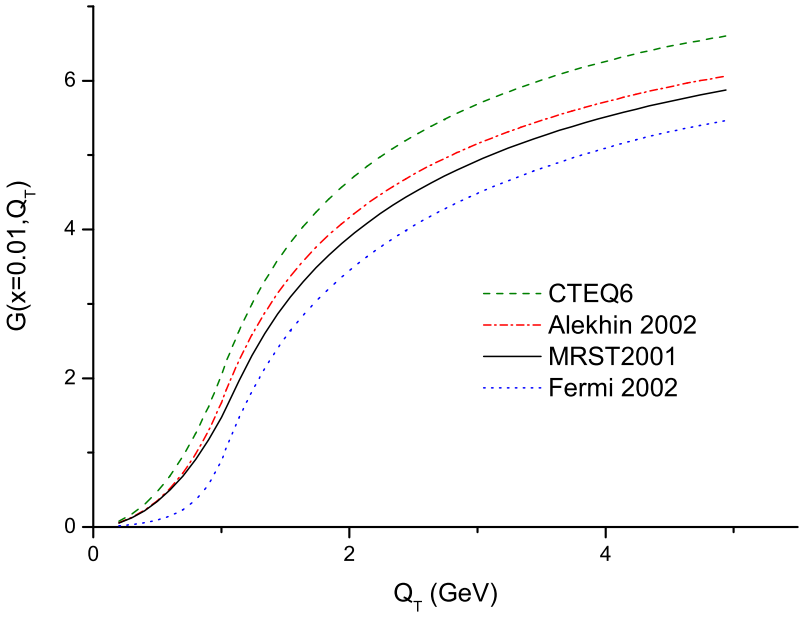

Fig. 6: The gluon density function in four different parameterisations.

where c is a constant if the gluon density goes like a power of Q_T^2. Clearly there is a tension between the Higgs mass, which encourages a large value of the loop momentum, and the singular behaviour of the $1/Q_T^4$ factor which encourages a low value. Also, as α_s reduces so real emission is less likely and the Sudakov suppression is less effective in steering Q_T away from the infra-red. Putting in the numbers one estimates that $\exp(\langle \ln Q_T^2 \rangle) \approx 4$ GeV^2 for the production of a 120 GeV scalar at the LHC which is just about large enough to permit an analysis using perturbative QCD. Figure 4 provides the quantitative support for these statements in the case of a Higgs of mass 120 GeV. The integrand of the Q_T integral in equation (12) is shown for both running and fixed α_s. We see that the integrand peaks just above 1 GeV and that the Sudakov factor becomes increasingly effective in suppressing the cross-section as α_s increases. Although it isn't too easy to see on this plot, the peak does move to higher values of Q_T as α_s increases in accord with (13). This plot also illustrates quite nicely that the cross-section is pretty much insensitive to the infra-red cutoff for $Q_0 < 1$ GeV and this is made explicit in Figure 5.

Discussion of the infra-red sensitivity would not be complete without returning to the issue of the unintegrated gluon density. In all our calculations we model the off-diagonality as discussed below equation (7) and we shan't discuss this source of uncertainty any further here.[3] Figure 6 shows the gluon density $G(x, Q)$ as determined in four recent global fits (rather arbitrarily chosen to illustrate the typical variety) [26, 28–30]. Apart from the Fermi2002 fit, they are all leading order fits. Now, none of these parameterisations go down below $Q = 1$ GeV, so what is shown in the figure are the gluons extrapolated down to $Q = 0$. We have extrapolated down assuming that the gluon and its derivative are continuous at $Q = 1$ GeV and that $G(x, Q) \sim Q^2$ at $Q \to 0$.[4] The gluons plotted in Figure 6 are all determined at $x = 0.01$ which would be the value probed in the production of a 120 GeV Higgs at $y = 0$ at the LHC. The key point is to note that it is hard to think of any reasonable parameterisation of the gluon below 1 GeV which could give a substantial contribution to the cross-section. The Sudakov factor suppresses the low Q^2 region and also the size of the gluon and its derivative are crucial, and one cannot keep both of these large for $Q < 1$ GeV. Figure 7 shows the integrand of the Q_T integral for different fits to the gluon. In all cases the contribution below 1 GeV is small, although there are clearly important uncertainties

[3] We actually assume a constant enhancement factor of 1.2 per gluon density.

[4] To be precise we extrapolate assuming $G(x, Q) \sim Q^{2+(\gamma-2)Q}$.

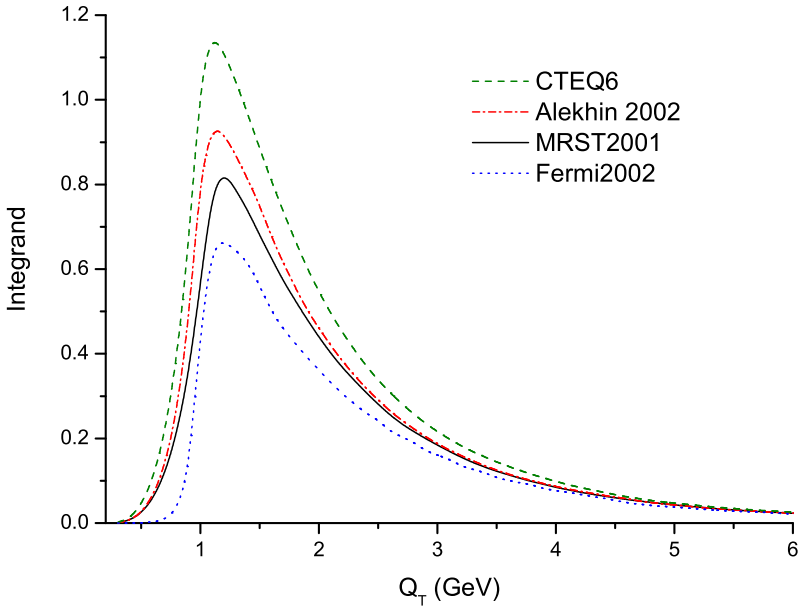

Fig. 7: The integrand of the Q_T integral for four recent global fits to the gluon.

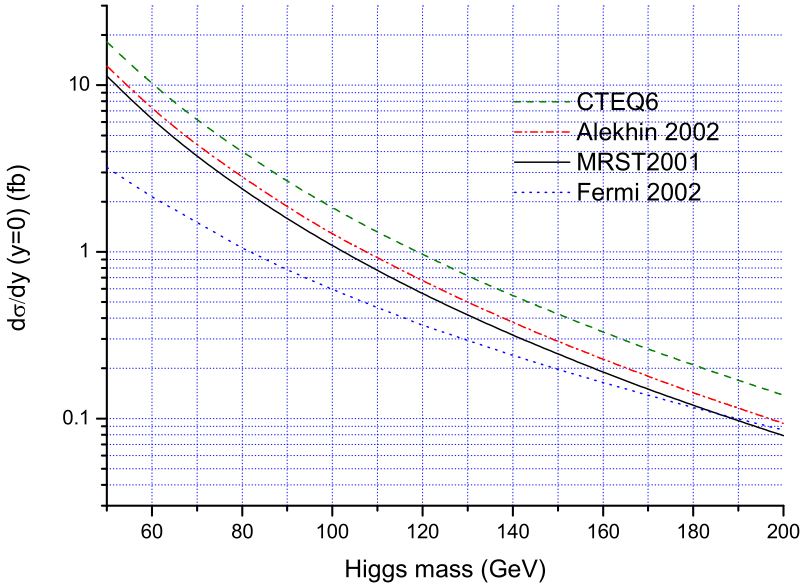

Fig. 8: The Higgs cross-section for four recent global fits to the gluon.

in the cross-section. These uncertainties are better seen in Figure 8 which illustrates that one might anticipate a factor of a few uncertainty from this source.

We note that although a variety of parameterizations are presented in Figure 8 the way that the actual Q_T dependence of the integrand is obtained is the same in each case. In [31, 32] the uncertainties arising from the way the unintegrated parton densities are obtained from the integrated ones are examined. Here we have followed the prescription presented in [33] which amounts to performing one backward step in a DGLAP parton shower. However, it is known that such showers tend to underestimate the hardness of, for example, the W/Z $p_\perp$ spectra in hadron colliders unless a large intrinsic transverse momentum is added to the perturbative $k_\perp$ distribution of the colliding partons [34, 35]. In [32] it was

shown that adding such an intrinsic transverse momentum would harden the Q_T distribution of the integrand in (12) for small Q_T which in turn lowers the cross-section for central exclusive Higgs production by a factor 2 (for a Gaussian intrinsic transverse momentum with $\langle k_\perp^2 \rangle = 2$ GeV^2). Investigations into how one could use unintegrated gluon densities obtained by CCFM [36] and LDC [37] evolution for central exclusive Higgs production have also been performed [32]. However, as discussed in more detail elsewhere in these proceedings [23], the available parameterizations, which are all fitted to HERA data only, are not constrained enough to allow for reliable predictions for Higgs production at the LHC.

This is perhaps a good place to mention pseudo-scalar production, as might occur in an extension to the Standard Model. The scalar product, $\mathbf{k_{1T}} \cdot \mathbf{k_{2T}}$, in (6) now becomes $(\mathbf{k_{1T}} \times \mathbf{k_{2T}}) \cdot \mathbf{n}$, where $\mathbf{n}$ is a unit vector along the beam axis. After performing the angular integral the only surviving terms are proportional to the vector product of the outgoing proton transverse momenta, i.e. $\mathbf{q_1}' \times \mathbf{q_2}'$. Notice that this term vanishes, in accord with the spin-0 selection rule, as $\mathbf{q_i}' \to 0$. Notice also that the integrand now goes like $\sim 1/Q_T^6$ (in contrast to the $1/Q_T^4$ in the scalar case). As a result c in (13) is larger (in fact it is linearly proportional to the power of Q_T) and the mean value of Q_T smaller. This typically means that pseudo-scalar production is not really accessible to a perturbative analysis.

The Sudakov factor has allowed us to ensure that the exclusive nature of the final state is not spoilt by perturbative emission off the hard process. What about non-perturbative particle production? The protons can in principle interact quite apart from the perturbative process discussed hitherto and this interaction could well lead to the production of additional particles. We need to account for the probability that such emission does not occur. Provided the hard process leading to the production of the Higgs occurs on a short enough timescale, we might suppose that the physics which generates extra particle production factorizes and that its effect can be accounted for via an overall factor multiplying the cross-section we have just calculated. This is the "gap survival factor". Gap survival is discussed in detail elsewhere in these proceedings and so we'll not dwell on it here [38].

The gap survival, S^2, is given by

$$d\sigma(p + H + p|\text{no soft emission}) = d\sigma(p + H + p) \times S^2$$

where $d\sigma(p+H+p)$ is the differential cross-section computed above. The task is to estimate S^2. Clearly this is not straightforward since we cannot utilize QCD perturbation theory. Let us at this stage remark that data on a variety of processes observed at HERA, the Tevatron and the LHC can help us improve our understanding of "gap survival".

The model presented here provides a good starting point for understanding the more sophisticated treatments [39–41]. Dynamically, one expects that the likelihood of extra particle production will be greater if the incoming protons collide at small transverse separation compared to collisions at larger separations. The simplest model which is capable of capturing this feature is one which additionally assumes that there is a single soft particle production mechanism, let us call it a "re-scattering event", and that re-scattering events are independent of each other for a collision between two protons at transverse separation r. In such a model we can use Poisson statistics to model the distribution in the number of re-scattering events per proton-proton interaction:

$$P_n(r) = \frac{\chi(r)^n}{n!} \exp(-\chi(r)) \, . \tag{14}$$

This is the probability of having n re-scattering events where $\chi(r)$ is the mean number of such events for proton-proton collisions at transverse separation r. Clearly the important dynamics resides in $\chi(r)$; we expect it to fall monatonically as r increases and that it should be much smaller than unity for r much greater than the QCD radius of the proton. Let us for the moment assume we know $\chi(r)$, then we can determine S^2 via

$$S^2 = \frac{\int dr \;\; d\sigma(r) \;\; \exp(-\chi(r))}{\int dr \;\; d\sigma(r)} \tag{15}$$

where $d\sigma(r)$ is the cross-section for the hard process that produces the Higgs expressed in terms of the transverse separation of the protons. Everything except the r dependence of $d\sigma$ cancels when computing S^2 and so we need focus only on the dependence of the hard process on the transverse momenta of the scattered protons ($\mathbf{q_i}'$), these being Fourier conjugate to the transverse position of the protons, i.e.

$$\begin{aligned} d\sigma(r) &\propto [(\int d^2\mathbf{q_1}'\, e^{i\mathbf{q_1}'\cdot\mathbf{r}/2}\, \exp(-b\mathbf{q_1}'^2/2)) \times (\int d^2\mathbf{q_2}'\, e^{-i\mathbf{q_2}'\cdot\mathbf{r}/2}\, \exp(-b\mathbf{q_2}'^2/2))]^2 \\ &\propto \exp\left(-\frac{r^2}{2b}\right) . \end{aligned} \tag{16}$$

Notice that since the b here is the same as that which enters into the denominator of the expression for the total rate there is the aforementioned reduced sensitivity to b since as b decreases so does S^2 (since the collisions are necessarily more central) and what matters is the ratio S^2/b^2.

It remains for us to determine the mean multiplicity $\chi(r)$. If there really is only one type of re-scattering event[5] independent of the hard scattering, then the inelastic scattering cross-section can be written

$$\sigma_{\rm inelastic} = \int d^2\mathbf{r}(1-\exp(-\chi(r))), \tag{17}$$

from which it follows that the elastic and total cross-sections are

$$\sigma_{\rm elastic} = \int d^2\mathbf{r}(1-\exp(-\chi(r)/2))^2, \tag{18}$$

$$\sigma_{\rm total} = 2\int d^2\mathbf{r}(1-\exp(-\chi(r)/2)). \tag{19}$$

There is an abundance of data which we can use to test this model and we can proceed to perform a parametric fit to $\chi(r)$. This is essentially what is done in the literature, sometimes going beyond a single-channel approach. Suffice to say that this simple approach works rather well. Moreover, it also underpins the models of the underlying event currently implemented in the PYTHIA [42] and HERWIG [43, 44] Monte Carlo event generators which have so far been quite successful in describing many of the features of the underlying event [45–47]. Typically, models of gap survival predict S^2 of a few percent at the LHC. Although data support the existing models of gap survival there is considerable room for improvement in testing them further and in so doing gaining greater control of what is perhaps the major theoretical uncertainty in the computation of exclusive Higgs production. In all our plots we took $S^2 = 3\%$ which is typical of the estimates in the literature for Higgs production ath the LHC.

3 Other Models

We'll focus in this section mainly on the model presented by what we shall call the Saclay group [13]. The model is a direct implementation of the original Bialas-Landshoff (BL) calculation [20] supplemented with a gap survival factor. It must be emphasised that BL did not claim to have computed for an exclusive process, indeed they were careful to state that "additional...interactions...will generate extra particles...Thus our calculation really is an inclusive one".

Equation (6) is the last equation that is common to both models. BL account for the coupling to the proton in a very simple manner: they multiply the quark level amplitude by a factor of 9 (which corresponds to assuming that there are three quarks in each proton that are able to scatter off each other). Exactly like the Durham group they also include a form factor suppression factor $\exp(-bq_{iT}'^2)$ for each proton at the cross-section level with $b = 4$ GeV^{-2}. Since BL are not interested in suppressing radiation, they do have a problem with the infra-red since there is no Sudakov factor. They dealt with this

[5] Clearly this is not actually the case, but such a "single channel eikonal" model has the benefit of being simple.

by following the earlier efforts of Landshoff and Nachtmann (LN) in replacing the perturbative gluon propagators with non-perturbative ones [48, 49]:

$$\frac{g^2}{k^2} \to A \exp(-k^2/\mu^2).$$

Rather arbitrarily, $g^2 = 4\pi$ was assumed, except for the coupling of the gluons to the top quark loop, where $\alpha_s = 0.1$ was used.

Following LN, μ and A are determined by assuming that the $p\bar{p}$ elastic scattering cross-section at high energy can be approximated by the exchange of two of these non-perturbative gluons between the 3×3 constituent quarks: the imaginary part of this amplitude determines the total cross-section for which there are data which can be fitted to. In order to carry out this procedure successfully, one needs to recognize that a two-gluon exchange model is never going to yield the gentle rise with increasing centre-of-mass energy characteristic of the total cross-section. BL therefore also include an additional "reggeization" factor of $s^{\alpha(t)-1}$ in the elastic scattering amplitude where

$$\alpha(t) = 1 + \epsilon + \alpha' \, t$$

is the pomeron trajectory which ensures that a good fit to total cross-section data is possible for $\epsilon = 0.08$ and $\alpha' = 0.25$ GeV^{-2}. In this way the two-gluon system is modelling pomeron exchange. They found that $\mu \approx 1$ GeV and $A \approx 30$ GeV^{-2} gave a good fit to the data. Similarly, the amplitude for central Higgs production picks up two reggeization factors.

The inclusive production of a Higgs boson in association with two final state protons is clearly much more infra-red sensitive than the exclusive case where the Sudakov factor saves the day. Having said that, the Saclay model does not include the Sudakov suppression factor. Instead it relies upon the behaviour of the non-perturative gluon propagators to render the Q_T integral finite. As a result, the typical Q_T is much smaller than in the Durham case. Indeed it may be sufficiently small to make the approximation $Q_T^2 \gg q_{iT}'^2$ invalid which means that the spin-0 selection rule is no longer applicable.

Pulling everything together, the Saclay model of the cross-section for $pp \to p + H + p$ gives

$$\begin{aligned}\frac{d\sigma}{d^2\mathbf{q_{1T}}' d^2\mathbf{q_{2T}}' dy} \approx\ & S^2 \left(\frac{N_c^2-1}{N_c^2}\right)^2 \frac{\alpha_s^2}{(2\pi)^5} \left(\frac{g^2}{4\pi}\right)^4 \frac{G_F}{\sqrt{2}} e^{-bq_{1T}'^2} e^{-bq_{2T}'^2} \\ & x_1^{2-2\alpha(q_{1T}'^2)} x_2^{2-2\alpha(q_{2T}'^2)} \left[9 \int \frac{d^2\mathbf{Q_T}}{2\pi} \mathbf{Q_T}^2 \left(\frac{A}{g^2}\right)^3 \exp(-3\mathbf{Q_T}^2/\mu^2) \frac{2}{3}\right]^2 \quad (20)\end{aligned}$$

The reggeization factors depend upon the momentum fractions x_1 and x_2 which satisfy $x_1 x_2 s = m_H^2$ and $y = \frac{1}{2}\ln(x_1/x_2)$. The only difference[6] between this and the original BL result is the factor of S^2. Integrating over the final state transverse momenta and simplifying a little gives

$$\frac{d\sigma}{dy} \approx S^2 \frac{\pi}{b + 2\alpha' \ln(1/x_1)} \frac{\pi}{b + 2\alpha' \ln(1/x_2)} \left(\frac{N_c^2-1}{N_c^2}\right)^2 \frac{G_F}{\sqrt{2}} \frac{\alpha_s^2}{(2\pi)^5} \frac{1}{(4\pi)^4} \left(\frac{s}{m_H^2}\right)^{2\epsilon} \frac{1}{g^4} \left[\frac{A^3\mu^4}{3}\right]^2 . \quad (21)$$

Figure 9 shows how the Saclay model typically predicts a rather larger cross-section with a weaker dependence upon m_H than the Durham model. The weaker dependence upon m_H arises because the Saclay model does not contain the Sudakov suppression, which is more pronounced at larger m_H, and also because of the choice $\epsilon = 0.08$. A larger value would induce a correspondingly more rapid fall. The Durham use of the gluon density function does indeed translate into an effective value of ϵ subtantially larger than 0.08. This effect is also to be seen in the dependence of the model predictions upon the centre-of-mass energy as shown in Figure 10. We have once again assumed a constant $S^2 = 3\%$ in this figure despite the fact that one does expect a dependence of the gap survival factor upon the energy.

[6] Apart from the factor 2 error previously mentioned.

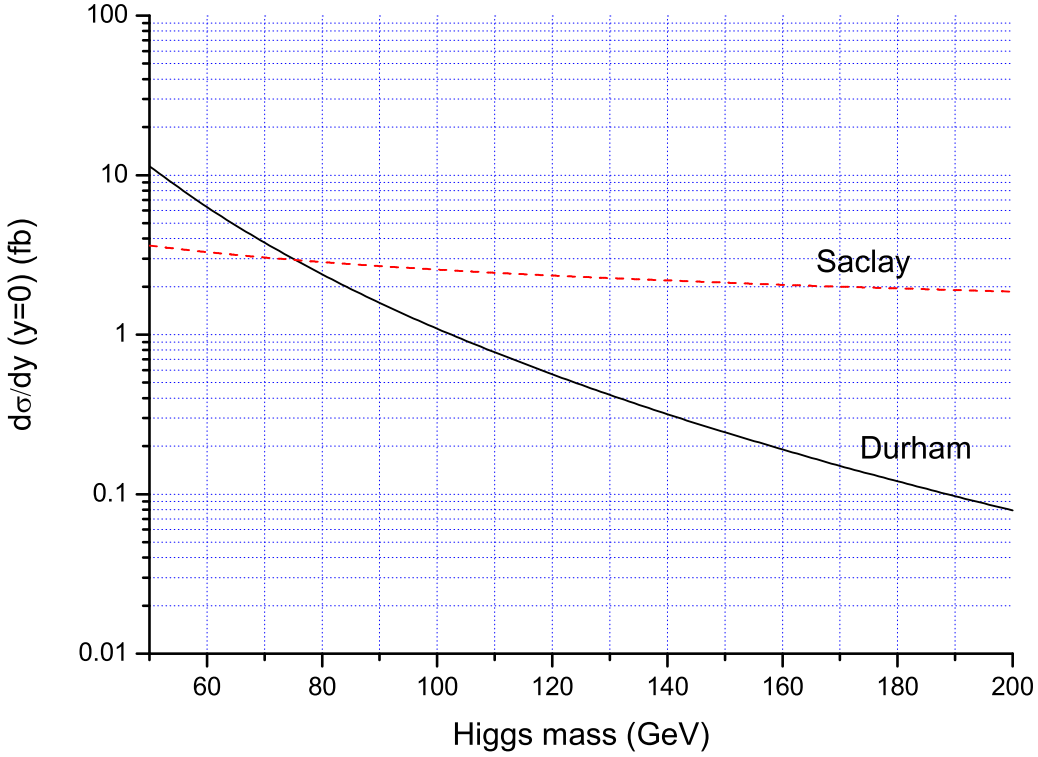

Fig. 9: Comparing dependence upon m_H of the Saclay and Durham predictions. $S^2 = 3\%$ in both cases.

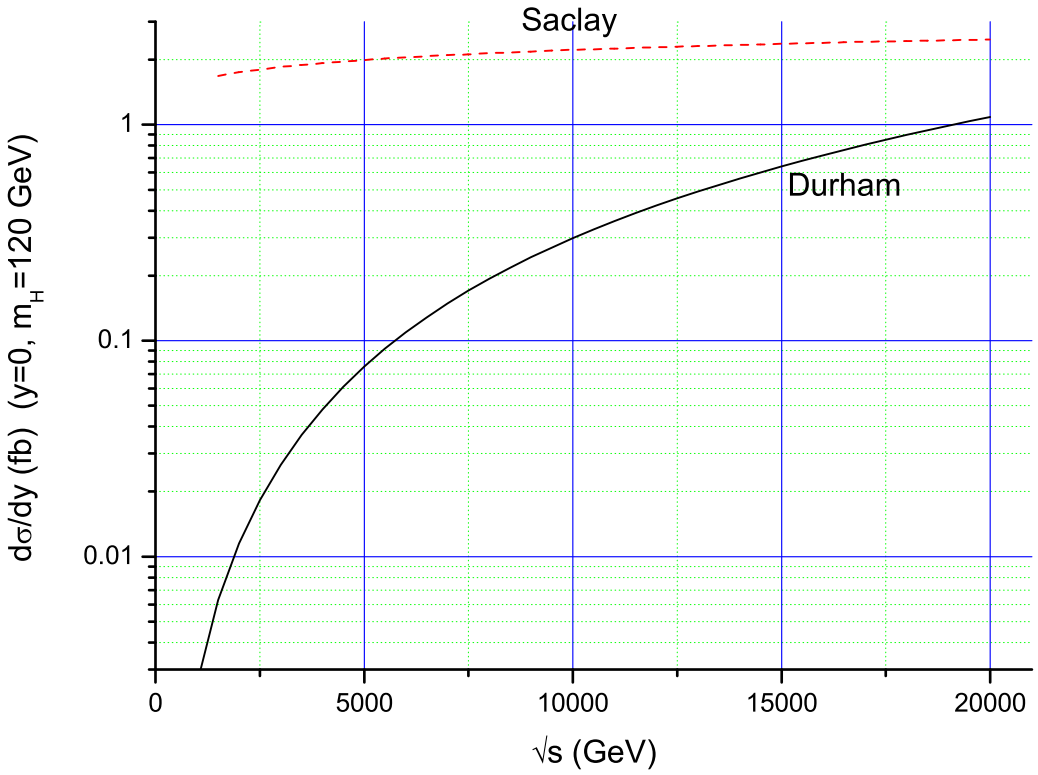

Fig. 10: Comparing dependence upon $\sqrt{s}$ of the Saclay and Durham predictions for $m_H = 120$ GeV.

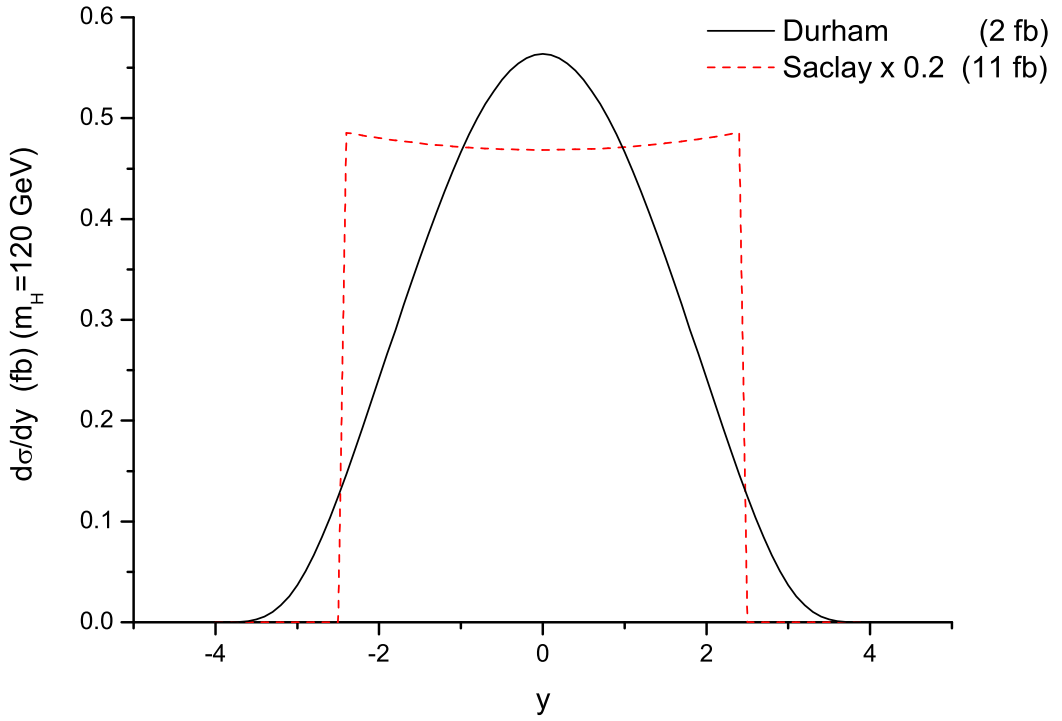

Fig. 11: Comparing the y dependence of the Saclay and Durham predictions for $m_H = 120$ GeV. Note that the Saclay prediction has been reduced by a factor 5 to make the plot easier to read. The numbers in parenthesis are the total cross-sections, i.e. integrated over rapidity.

Figure 11 compares the rapidity dependence of the Higgs production cross-section in the two models. The Saclay prediction is almost y-independent. Indeed the only y-dependence is a consequence of $\alpha' \neq 0$. In both models the calculations are really only meant to be used for centrally produced Higgs bosons, i.e. $|y|$ not too large since otherwise one ought to revisit the approximations implicit in taking the high-energy limit. Nevertheless, the Durham prediction does anticipate a fall as $|y|$ increases, and this is coming because one is probing larger values of x in the gluon density. In contrast, the Saclay prediction does not anticipate this fall and so a cutoff in rapidity needs to be introduced in quoting any cross-section integrated over rapidity. In Figure 11 a cut on $x_{1,2} < 0.1$ is made (which is equivalent to a cut on $|y| < 2.5$) for the Saclay model. After integrating over rapidity, the Durham model predicts a total cross-section of 2 fb for the production of a 120 GeV Higgs boson at the LHC whilst the Saclay model anticipates a cross-section a factor ~ 5 larger.

The essentially non-perturbative Saclay prediction clearly has some very substantial uncertainties associated with it. The choice of an exponentially falling gluon propagator means that there is no place for a perturbative component. However, as the Durham calculation shows, there does not seem to be any good reason for neglecting contributions from perturbatively large values of Q_T. It also seems entirely reasonable to object on the grounds that one should not neglect the Sudakov suppression factor and that including it would substantially reduce the cross-section.

In [18], the Sudakov factor of equation (11) is included, with the rest of the amplitude computed following Bialas-Landshoff. The perturbative Sudakov factor is also included in the approach of [19], albeit only at the level of the double logarithms. This latter approach uses perturbative gluons throughout the calculation but Regge factors are included to determine the coupling of the gluons into the protons, i.e. rather than the unintegrated partons of the Durham model. In both cases the perturbative Sudakov factor, not suprisingly, is important.

4 Concluding remarks

We hope to have provided a detailed introduction to the Durham model for central exclusive Higgs production. The underlying theory has been explained and the various sources of uncertainty highlighted with particular emphasis on the sensitivity of the predictions to gluon dynamics in the infra-red region. We also made some attempt to mention other approaches which can be found in the literature.

The focus has been on the production of a Standard Model Higgs boson but it should be clear that the formalism can readily be applied to the central production of any system X which has a coupling to gluons and invariant mass much smaller than the beam energy. There are many very interesting possibilities for system X which have been explored in the literature and we have not made any attempt to explore them here [2, 3, 8, 11, 15–17]. Nor have we paid any attention to the crucial challenge of separating signal events from background [5, 9]. The inclusion of theoretical models into Monte Carlo event generators and a discussion of the experimental issues relating to central exclusive particle production have not been considered here but can be found in other contributions to these proceedings [50, 51].

It seems that perturbative QCD can be used to compute cross-sections for processes of the type $pp \to p + X + p$. The calculations are uncertain but indicate that rates ought to be high enough to be interesting at the LHC. In the case that the system X is a pair of jets there ought to be the possibility to explore this physics at the Tevatron [52]. Information gained from such an analysis would help pin down theoretical uncertainties, as would information on the rarer but cleaner channel where X is a pair of photons [53]. Of greatest interest is when X contains "new physics" whence this central exclusive production mechanism offers new possibilities for its exploration.

5 Acknowledgments

Special thanks to Hannes Jung for all his efforts in making the workshop go so well. Thanks also to Brian Cox, Markus Diehl, Valery Khoze, Peter Landshoff, Leif Lönnblad, James Monk, Leszek Motyka, Andy Pilkington and Misha Ryskin for very helpful discussions.

References

[1] M.G. Albrow and A. Rostovtsev, *Searching for the Higgs at hadron colliders using the missing mass method*. E-Print Archive: hep-ph/0009336.

[2] M.G. Albrow et al, *FP420: An R&D proposal to investigate the feasibility of installing proton tagging detectors in the 420-m region at LHC*. CERN-LHCC-2005-025.

[3] B.E. Cox, AIP Conference Proceedings **753**, 103 (2005). E-Print Archive: hep-ph/0409144.

[4] J. Kalliopuska, T. Mäki, N. Marola, R. Orava, K. Österberg and M. Ottela, *Resolution studies of the leading proton measurement in exclusive central diffraction at LHC*.

[5] V.A. Khoze, A.D. Martin and M.G. Ryskin, Eur. Phys. J. **C19**, 477 (2001). Erratum-ibid. **C20**, 599 (2001). E-Print Archive: hep-ph/0011393.

[6] V.A. Khoze, A.D. Martin and M.G. Ryskin, Eur. Phys. J. **C24**, 581 (2002). E-Print Archive: hep-ph/0203122.

[7] V.A. Khoze, A.D. Martin and M.G. Ryskin, Phys. Lett. **B401**, 330 (1997). E-Print Archive: hep-ph/9701419;
V.A. Khoze, A.D. Martin and M.G. Ryskin, Eur. Phys. J. **C14**, 525 (2000). E-Print Archive: hep-ph/0002072.

[8] V.A. Khoze, A.D. Martin and M.G. Ryskin, Eur. Phys. J. **C23**, 311 (2002). E-Print Archive: hep-ph/0111078.

[9] A. De Roeck, V.A. Khoze, A.D. Martin, R. Orava and M.G. Ryskin, Eur. Phys. J. **C25**, 391 (2002). E-Print Archive: hep-ph/0207042.

[10] V.A. Khoze, A.D. Martin and M.G. Ryskin, Eur. Phys. J. **C26**, 229 (2002). E-Print Archive: hep-ph/0207313;
A.B. Kaidalov, V.A. Khoze, A.D. Martin and M.G. Ryskin, Eur. Phys. J. **C31**, 387 (2003). E-Print Archive: hep-ph/0307064.

[11] A.B. Kaidalov, V.A. Khoze, A.D. Martin and M.G. Ryskin, Eur. Phys. J. **C33**, 261 (2004). E-Print Archive: hep-ph/0311023;
V.A. Khoze, A.D. Martin and M.G.Ryskin, Eur. Phys. J. **C34**, 327 (2004). E-Print Archive: hep-ph/0401078;
K. Belotsky, V.A. Khoze, A.D. Martin and M.G. Ryskin, Eur. Phys. J. **C36**, 503 (2004). E-Print Archive: hep-ph/0406037.

[12] B.E. Cox et al, *Detecting the standard model Higgs boson in the WW decay channel using forward proton tagging at the LHC*. E-Print Archive: hep-ph/0505240.

[13] M. Boonekamp, R. Peschanski and C. Royon, Nucl. Phys. **B669**, 277 (2003). Erratum-ibid. **B676**, 493 (2004). E-Print Archive: hep-ph/0301244.

[14] M. Boonekamp, R. Peschanski and C. Royon, Phys. Lett. **B598**, 243 (2004). E-Print Archive: hep-ph/0406061;
M. Boonekamp, J. Cammin, R. Peschanski and C. Royon. E-Print Archive: hep-ph/0504199.

[15] M. Boonekamp, J. Cammin, S. Lavignac, R. Peschanski and C. Royon. E-Print Archive: hep-ph/0506275.

[16] J.R. Ellis, J.S. Lee and A. Pilaftsis, Phys. Rev. **D71**, 075007 (2005). E-Print Archive: hep-ph/0502251.

[17] B.E. Cox, J.R. Forshaw, J.S. Lee, J. Monk and A. Pilaftsis, Phys. Rev. **D68**, 075004 (2003). E-Print Archive: hep-ph/0303206.

[18] A. Bzdak, *Exclusive Higgs and dijet production by double pomeron exchange: The CDF upper limits*. E-print Archive: hep-ph/0504086.

[19] V.A. Petrov and R.A. Ryutin, Eur. Phys. J. **C36**, 509 (2004). E-Print Archive: hep-ph/0311024.

[20] A. Bialas and P.V. Landshoff, Phys. Lett. **B256**, 540 (1991).

[21] B.E. Cox and J.R. Forshaw, Comput. Phys. Commun. **144**, 104 (2002). E-Print Archive: hep-ph/0010303.

[22] M. Boonekamp and T. Kucs, Comput. Phys. Commun. **167**, 217 (2005). E-Print Archive: hep-ph/0312273.

[23] J.C. Collins et al, *Unintegrated parton density functions*. These proceedings.

[24] A.G. Shuvaev, K.J. Golec-Biernat, A.D. Martin and M.G. Ryskin, Phys. Rev. **D60**, 014015 (1999). E-Print Archive: hep-ph/9902410.

[25] M.A. Kimber, A.D. Martin, M.G. Ryskin, Phys. Rev. **D63**, 114027 (1999). E-Print Archive: hep-ph/0101348;
M.A. Kimber, A.D. Martin and M.G. Ryskin, Eur. Phys. J. **C12**, 655 (2000). E-Print Archive: hep-ph/9911379;
A.D. Martin and M.G. Ryskin, Phys. Rev. **D64**, 094017 (2001). E-Print Archive: hep-ph/0107149.

[26] A.D. Martin, R.G. Roberts, W.J. Stirling and R.S. Thorne, Eur. Phys. J. **C23**, 73 (2002). E-print Archive: hep-ph/0110215.

[27] `http://durpdg.dur.ac.uk/lhapdf4/`.

[28] J. Pumplin, D.R. Stump, J. Huston, H.L. Lai, P. Nadolsky and W.K. Tung, JHEP **0207**, 012 (2002). E-print Archive: hep-ph/0201195.

[29] S. Alekhin, Phys. Rev. **D68**, 014002 (2003). E-print Archive: hep-ph/0104052.

[30] W.T. Giele, S.A. Keller and D.A. Kosower. E-print Archive: hep-ph/0104052.

[31] L. Lönnblad and M. Sjödahl, JHEP **02**, 042 (2004). E-Print Archive: hep-ph/0311252.

[32] L. Lönnblad and M. Sjödahl, JHEP **05**, 038 (2005). E-Print Archive: hep-ph/0412111.

[33] A.D. Martin, R.G. Roberts, W.J. Stirling and R.S. Thorne, Eur. Phys. J. **C4**, 463 (1998). E-Print Archive: hep-ph/9803445.

[34] E. Thome, *Perturbative and nonperturbative effects in transverse momentum generation*. E-Print Archive: hep-ph/0401121.

[35] E.L. Nurse, *A measurement of the inclusive $z/\gamma^* \to \mu^+\mu^-$ cross section and study of W and Z events in $p\bar{p}$ collisions at D0*. FERMILAB-THESIS-2005-05.

[36] M. Ciafaloni, Nucl. Phys. **B296**, 49 (1988);
S. Catani, F. Fiorani and G. Marchesini, Phys. Lett. **B234**, 339 (1990);
S. Catani, F. Fiorani and G. Marchesini, Nucl. Phys. **B336**, 18 (1990);
G. Marchesini, Nucl. Phys. **B445**, 49 (1995). E-Print Archive: hep-ph/9412327.

[37] B. Andersson, G. Gustafson and J. Samuelsson, Nucl. Phys. **B467**, 443 (1996);
B. Andersson, G. Gustafson and H. Kharraziha, Phys. Rev. **D57**, 5543 (1998). E-Print Archive: hep-ph/9711403.

[38] E. Gotsman et al, *Survival probabilities of large rapidity gaps*. These proceedings.

[39] E. Gotsman, E. Levin and U. Maor, Phys. Lett. **B438**, 229 (1998). E-Print Archive: hep-ph/9804404;
E. Gotsman, E. Levin and U. Maor, Phys. Lett. **B452**, 387 (1999). E-Print Archive: hep-ph/9901416;
E. Gotsman, E. Levin and U. Maor, Phys. Rev. **D60**, 094011 (1999). E-Print Archive: hep-ph/9902294;
U. Maor, *LRG production of di-jets as a probe of s-channel unitarity*. E-Print Archive: hep-ph/0406303.

[40] V.A. Khoze, A.D. Martin and M.G. Ryskin, Eur. Phys. J. **C18**, 167 (2000). E-Print Archive: hep-ph/0007359;
A.B. Kaidalov, V.A. Khoze, A.D. Martin and M.G. Ryskin, Eur. Phys. J. **C21**, 521 (2001). E-Print Archive: hep-ph/0105145.

[41] M.M. Block and F. Halzen, Phys. Rev. **D63**, 114004 (2001). E-Print Archive: hep-ph/0101022.

[42] T. Sjöstrand and M. van Zijl, Phys. Rev. **D36**, 2019 (1987).

[43] J.M. Butterworth and J.R. Forshaw, J. Phys. **G19**, 1657 (1993).

[44] J.M. Butterworth, J.R. Forshaw and M.H. Seymour, Z. Phys. **C72**, 637 (1996). E-Print Archive: hep-ph/9601371.

[45] I. Borozan and M.H. Seymour, JHEP **0209**, 015 (2002). E-Print Archive: hep-ph/0207283.

[46] T. Sjöstrand and P.Z. Skands, JHEP **0403**, 053 (2004). E-Print Archive: hep-ph/0402078.

[47] K. Odagiri, JHEP **0408**, 019 (2004). E-Print Archive: hep-ph/0407008.

[48] P.V. Landshoff and O. Nachtmann, Z. Phys. **C35**, 405 (1987).

[49] A. Donnachie and P.V. Landshoff, Nucl. Phys. **B311**, 509 (1989).

[50] M. Boonekamp et al, *Monte Carlo generators for central exclusive diffraction*. These proceedings.

[51] B.E. Cox et al, *Experimental aspects of central exclusive diffraction*. These proceedings.

[52] B.E. Cox and A. Pilkington, *Central exclusive dijet production at the Tevatron*. E-Print Archive: hep-ph/0508249.

[53] V.A. Khoze, A.D. Martin, M.G. Ryskin and W.J. Stirling, Eur. Phys. J. **C38**, 475 (2005). E-Print Archive: hep-ph/0409037.

Monte Carlo generators for central exclusive diffraction

Maarten Boonekamp, Creighton Hogg, James Monk, Andrew Pilkington & Marek Tasevsky

Abstract
We review the three Monte Carlo generators that are available for simulating the central exclusive reaction, $pp \to p + X + p$.

1 Introduction

The central exclusive mechanism is defined as $pp \to p + X + p$ with no radiation emitted between the intact outgoing beam hadrons and the central system X. The study of central exclusive Higgs boson production has been aided with the recent development of Monte Carlo simulations to enable parton, hadron and detector level simulation. The three generators that we shall examine here are DPEMC [1], EDDE [2] and ExHuME [3]. From an experimental perspective, it is important to examine both the similarities and differences between the models in order to assess the physics potential in terms of forward proton tagging at the LHC [4].

Each of the Monte Carlos implements a different model of central exclusive production that is either perturbative or non-perturbative. ExHuME is an implementation of the perturbative calculation of Khoze, Martin and Ryskin [5], the so-called "Durham Model". In this calculation (depicted in fig 1(a)), the two gluons couple perturbatively to the off-diagonal unintegrated gluon distribution in the proton. The Durham approach includes a Sudakov factor to suppress radiation into the rapidity gap between the central system and the outgoing protons and which renders the loop diagram infra-red safe. The bare cross section is suppressed by a soft-survival probability, $\mathcal{S}^2$, that accounts for additional momentum transfer between the proton lines that lead to particle production that could fill in the gap. The current ExHuME default takes $\mathcal{S}^2$ to be 0.03 at the LHC.

In contrast, DPEMC and EDDE treat the proton vertices non-perturbatively. This is acheived in the context of Regge theory, by pomeron exchange from each of the proton lines. DPEMC follows the Bialas-Landshoff approach [6] of parameterising the pomeron flux within the proton. DPEMC also sets the default value of $\mathcal{S}^2$ to 0.03 at the LHC. EDDE uses an improved Regge-eikonal approach [7] to calculate the soft proton vertices and includes a Sudakov suppression factor to prohibit real gluon emission. There is no explicit soft-survival factor present in EDDE: it is assumed that the Regge parameterisation includes the effect of additional interactions between the proton lines. For further details of the calculations underlying both DPEMC and ExHuME please refer to [8].

The connection between the parton level process and the hadronic final state is not the same in the three Monte Carlos. Both ExHuME and EDDE are linked to Pythia [9, 10] for final state parton showering and hadronisation. DPEMC however, overrides the HERWIG [11] internal $\gamma\gamma$ interactions in e^+e^- collisions to simulate double pomeron exchange.

The processes available are similar in each Monte Carlo. Perhaps the most interesting is Higgs boson production with all subsequent decays. In addition, di-jet production is included in all three generators. None of the Monte Carlos yet includes the next-to-leading order 3 jet process, which could be an important, or even the dominant, background to the central exclusive $H \to b\bar{b}$ search channel.

Finally, inclusive double pomeron exchange (shown in figure 1(b)) will also act as a backgound to the exclusive process as there are 2 protons in the final state. These processes are always accompanied by pomeron remnants in the central system and it may be a challenge experimentally to separate these from the system of interest. Two models for these processes are the Cox-Forshaw model (CF), implemented in POMWIG [12], and the Boonekamp-Peschanski-Royon model (BPR) [13] that is included in DPEMC.

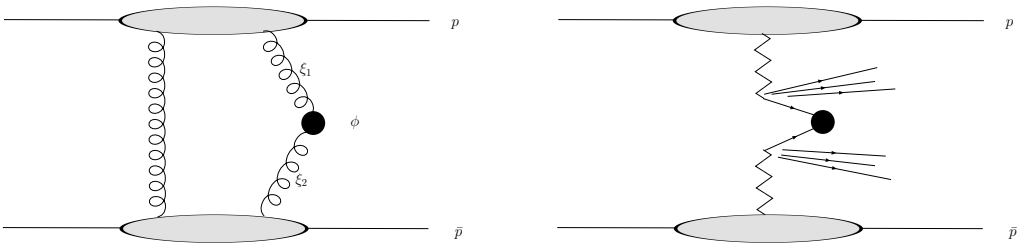

Fig. 1: The exclusive production process (a) and the inclusive (double pomeron) production process (b).

2 Results

Unless otherwise stated, all plots shown here were produced by using each of the Monte Carlos as they are distributed. constant soft survival factor, $\mathcal{S}^2$, of 0.03 was used in all three generators. In the case of ExHuME, where a parton distribution set must be chosen, the default is the 2002 MRST set, usually supplied via the LHAPDF library.

Using the default settings at the LHC energy of 14 TeV the total cross sections for production of a 120 GeV Higgs boson are 3.0 fb, 1.94 fb and 2.8 fb for DPEMC, EDDE and ExHuME respectively. However, despite these similar cross section predictions, the physics reach of the central exclusive process is predicted to differ significantly between the Monte Carlos. Figure 2(a) shows that ExHuME and EDDE predict that the cross section for exclusive Higgs boson production will fall much faster than DPEMC with an increase in Higgs boson mass. This is a direct effect of the Sudakov suppression factors growing as the available phase space for gluon emission increases with the mass of the central system. The different gluon momentum fraction, ξ, dependences lead to the differences in figure 2(b). With a fixed central mass an increase in collision energy is identical to a decrease in ξ, and the flatter ξ distributions of DPEMC and EDDE are reflected in the flatter $\sqrt{s}$ dependence compared to ExHuME.

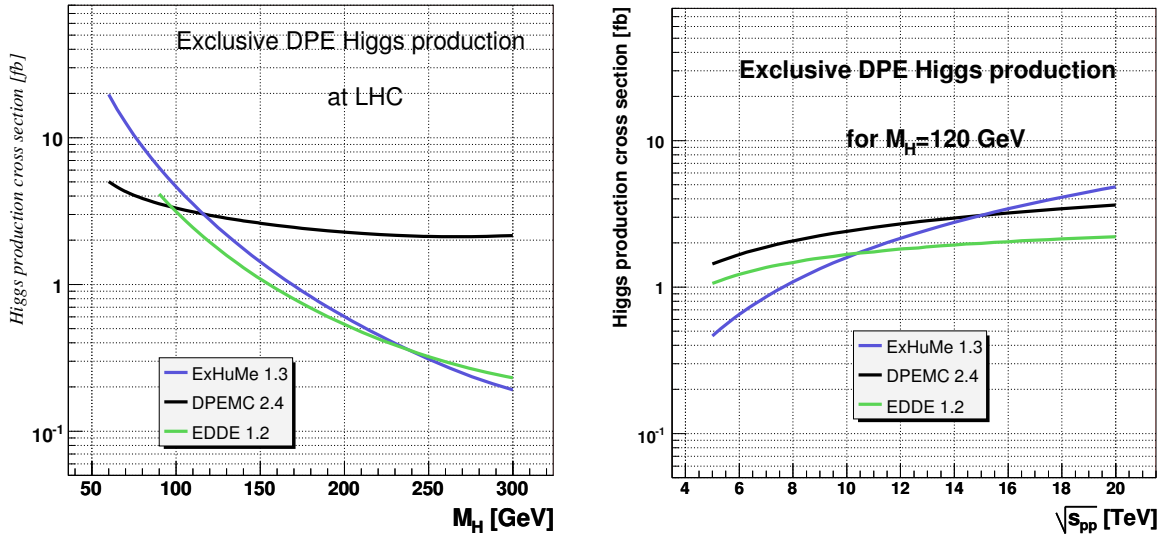

Fig. 2: (a) The left hand plot shows the higgs cross section as a function of higgs mass. (b) The right hand plot shows the increase in cross section with the collision energy (fixed gap survival factor).

The physics potential is dependent not only on the total cross section, but also on the rapidity distribution of the central system, which is shown in figure 3(b) together with the ξ distribution for the gluons. The more central rapidity distribution of ExHuME is due to the gluon distributions falling more sharply than the pomeron parameterisation present in DPEMC.

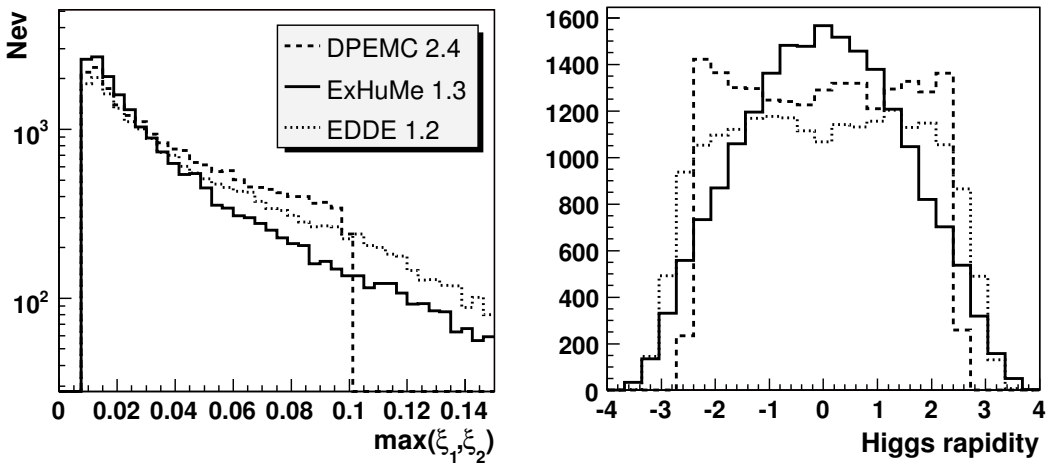

Fig. 3: The $max(\xi_1, \xi_2)$(a) and rapidity(b) of the 120 GeV Higgs. ExHuME predicts a steeper fall off in the number of events at high ξ and hence favours a less broad rapidity distribution compared to the soft non-perturbative models. Note that a cut is applied in DPEMC at $\xi = 0.1$, as required by the Bialas-Landshoff approach.

The acceptances of any forward proton taggers that might be installed at the LHC are sensitive to the rapidity distributions of the central system. The differences seen in figure 3(b) are reflected in different acceptance curves shown in figure 4. The predicted acceptances using taggers at 420 and 220 metres as a function of the mass of the central system were obtained using a fast simulation of the CMS detector. The fast simulation includes a parameterisation of the responses of the forward taggers based on a detailed simulation of the detectors [14]. As seen in figure 4, as the mass of the central system increases the combined acceptance using detectors at *both* 220 and 420 metres increases, with the relative difference between the predictions from the three generators decreasing (from about 40% down to 15% for the most extreme relative differences). For a Higgs boson of mass 120 GeV the acceptances are predicted to be 46, 50 and 57% for EDDE, DPEMC and ExHuME respectively.

Changes from the default generator settings can have an effect on all of these distributions. As an example Fig. 5(a) shows the rapidity distribution from ExHuME using the CTEQ6M set compared to the MRST 2002 set of parton distribution functions. The CTEQ pdf has a flatter ξ dependence in the sensitive region of $Q_\perp \simeq 3$ GeV, which leads to a broader peak and sharper fall in the rapidity distribution and a larger cross section of 3.75 fb. This in turn should improve the efficiency of the forward proton taggers because not only are there more events, but there are more events at low rapidity. It is also possible to change the DPEMC code to add a harder ξ dependence of the form $(1-\xi)^\alpha$ to the pomeron flux parameterisation. This would favour a more central rapidity distribution, thus increasing the acceptance in the forward pots.

In di-jet production the di-jet mass fraction, R_{jj} is defined as $R_{jj} = M_{jj}/\sqrt{\hat{s}}$, where M_{jj} is the mass of the di-jet system and $\sqrt{\hat{s}}$ is the total invariant mass of the central system. R_{jj} should be large in a central exclusive event. In current searches for central exclusive di-jet production at the Tevatron [15], the CDF collaboration have experimentally defined exclusive events to be those where $R_{jj} > 0.8$. It should be noted that M_{jj} depends on the particular jet reconstruction algorithm used and the $\sqrt{\hat{s}}$ measurement is dependent either on tagging the outgoing protons or on reconstructing the missing mass using the calorimeter. In figure 6(a) we show the prediction for the R_{jj} fraction in exclusive events at the LHC, whilst in figure 6(b) we show two examples of the inclusive background with pomeron remnants from Pomwig and DPEMC. It is clear that the $R_{jj} > 0.8$ definition for central exclusive production leads to an overlap between the exclusive and inclusive regions for all of the Monte Carlo predictions.

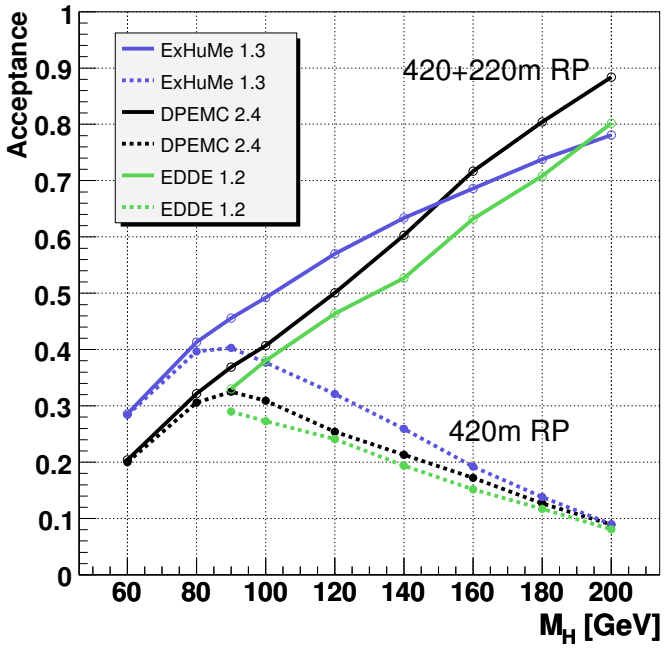

Fig. 4: The predicted acceptances for the proposed forward taggers at 420 metres and for a combination of taggers at 220 and 420 metres from the central detector.

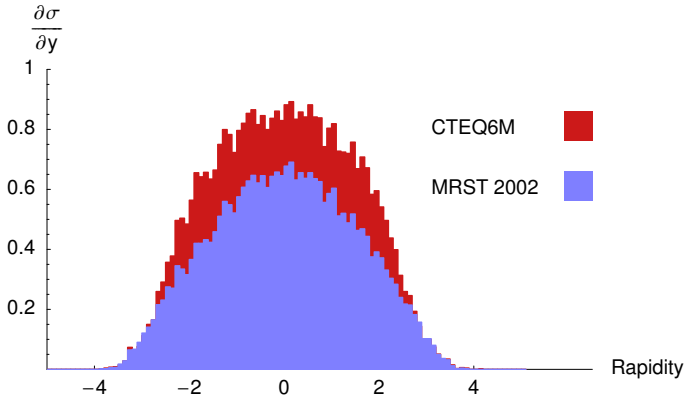

Fig. 5: The ExHuME rapidity distributions for production of a 120 GeV Higgs using MRST 2002 pdfs and the CTEQ6M pdfs.

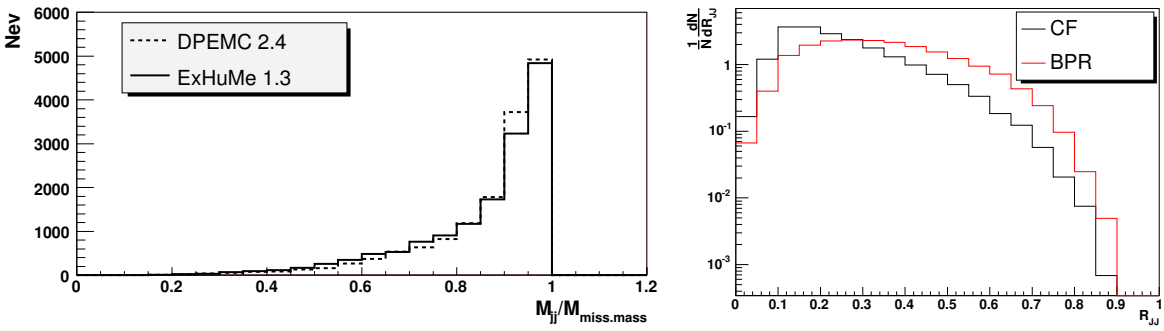

Fig. 6: R_{jj} distributions for (a) exclusive di-jet production using DPEMC and ExHuME and (b) the background inclusive di-jet production as predicted by the Cox-Forshaw (CF) and Boonekamp-Peschanski-Royon (BPR) models.

3 Summary

At a Higgs boson mass of 120GeV, all three Monte Carlo simulations give similar predictions for the cross section. However, the physics potential decreases for models that include Sudakov suppression, which will limit Higgs boson searches. The differing rapidity distributions of the central system result in different efficiencies for a forward proton tagging programme. In order to fully study the background to the $H \rightarrow b\bar{b}$ channel, future additions to the Monte Carlo programs should include the next to leading order three jet process.

Acknowledgements

We would like to thank Brian Cox, Jeff Forshaw, Valery Khoze, Misha Ryskin and Roman Ryutin for discussion throughout the proceedings.

References

[1] M. Boonekamp and T. Kucs, Comput. Phys. Commun. **167** (2005). E-Print Archive: hep-ph/0312273.

[2] R. Ryutin, *Edde monte carlo event generator*. E-Print Archive: hep-ph/0409180.

[3] J. Monk and A. Pilkington, *Exhume: A monte carlo event generator for exclusive diffraction*. E-Print Archive: hep-ph/0502077.

[4] M. G. Albrow et al., CERN-LHCC **25** (2005).

[5] V. A. Khoze, A. D. Martin and M. G. Ryskin, Eur. Phys. J **C23**, 311 (2002). E-print Archive: hep-ph/0111078.

[6] A. Bialas and P. V. Landshoff, Phys. Lett. B **B256**, 540 (1991).

[7] V. A. Petrov and R. Ryutin, Eur. Phys. Journ **C36**, 509 (2004).

[8] J. Forshaw, *Diffractive higgs production: theory*. These proceedings.

[9] T. Sjostrand, P. Eden, C. Friberg, L. Lonnblad, G. Miu, S. Mrenna and E. Norrbin, Comput. Phys. Commun **135**, 238 (2001). E-Print Archive: hep-ph/0010017.

[10] T. Sjostrand, L. Lonnblad, S. Mrenna and P. Skands, *Pythia 6.3: Physics and manual*. E-Print Archive: hep-ph/0308153.

[11] G. Corcella, I. G. Knowles, G. Marchesini, S. Moretti, K. Odagiri, P. Richardson, M. H. Seymour and B. R. Webber, JHEP **0101**, 010 (2001).

[12] B. E. Cox and J. R. Forshaw, Comput. Phys. Commun **144**, 104 (2002). E-Print Archive: hep-ph/0010303.

[13] M. Boonekamp, R. Peschanski and C. Royon, Phys. Rev. Lett **87**, 251806 (2001).

[14] V. Avati and K. Osterberg, *Roman pot acceptances*. These proceedings.

[15] T. Affolder et al., Phys. Rev. Lett. **85**, 4215 (2000).

Diffractive Structure Functions and Diffractive PDFs

Editors: M. Arneodo[a] and P. van Mechelen[b]
[a]Università del Piemonte Orientale, Novara, Italy
[b]University of Antwerpen, Antwerpen, Belgium

Abstract

This section of the Proceedings contains papers summarising the current status of the F_2^D measurements at HERA, the extraction of the diffractive parton distribution functions and the relevance of a direct measurement of F_L^D.

The selection of a pure sample of inclusive diffractive events, $ep \to eXp$, is a challenging task. Three alternative approaches have been used so far by the H1 and ZEUS collaborations at HERA:

1. a fast proton in the final state is required;
2. a rapidity gap in the forward direction is required;
3. the different shape of the M_X distribution for diffractive and non-diffractive events is exploited.

The results obtained with these approaches exhibit a level of agreement which varies from tolerable to poor. This is not surprising since different final states are selected, in which the reaction $ep \to eXp$ appears with different degrees of purity. The paper by Newman and Schilling presents a systematic comparison of the results available, quantifies the differences and discusses their origins, when understood.

NLO QCD fits to the diffractive structure function F_2^D are used to extract the diffractive parton distribution functions (dPDFs) in the proton. They can be interpreted as conditional probabilities to find a parton in the proton when the final state of the process contains a fast proton of given four-momentum. They are essential to determine the cross sections of less inclusive processes in ep diffractive scattering, such as dijet or charm production. They are also a non-negotiable ingredient for the prediction of the cross sections for inclusive diffractive processes at the LHC.

Several groups have so far performed such fits to the available data. The results of these fits are presented in the papers by Newman and Schilling, Groys et al. and Watt et al. All fits give diffractive PDFs largely dominated by gluons. However, significant differences are apparent, reflecting the differences in the data, but also in the fitting procedure. Newman and Schilling and Groys et al. assume the so-called Regge factorisation hypothesis, i.e. take $F_2^D = f_{I\!P}(x_{I\!P}, t) \cdot F_2^{I\!P}(\beta, Q^2)$. This assumption has no basis in QCD and is critically discussed by Groys et al. and by Watt et al. The latter also argue that the leading-twist formula used by Newman and Schilling and by Groys et al. is inadequate in large parts of the measured kinematics, and use a modified expression which includes an estimate of power-suppressed effects.

The parametrisations of the dPDFs discussed in these three papers are available in a code library discussed in the paper by Schilling.

Finally, the paper by Newman addreses the importance of measuring the longitudinal diffractive structure function F_L^D. A measurement of F_L^D to even modest precision would provide a very powerful independent tool to verify our understanding of diffraction and to test the gluon density extracted indirectly in QCD fits from the scaling violations of F_2^D.

HERA Diffractive Structure Function Data and Parton Distributions

Paul Newman[a]*, Frank-Peter Schilling*[b]
[a] School of Physics and Astronomy, University of Birmingham, B15 2TT, United Kingdom
[b] CERN/PH, CH-1211 Geneva 23, Switzerland

Abstract
Recent diffractive structure function measurements by the H1 and ZEUS experiments at HERA are reviewed. Various data sets, obtained using systematically different selection and reconstruction methods, are compared. NLO DGLAP QCD fits are performed to the most precise H1 and ZEUS data and diffractive parton densities are obtained in each case. Differences between the Q^2 dependences of the H1 and ZEUS data are reflected as differences between the diffractive gluon densities.

1 Introduction

In recent years, several new measurements of the semi-inclusive 'diffractive' deep inelastic scattering (DIS) cross section for the process $ep \to eXY$ at HERA have been released by the H1 and ZEUS experiments [1–6]. The data are often presented in the form of a t-integrated reduced diffractive neutral current cross section $\sigma_r^{D(3)}$, defined through[1]

$$\frac{d^3\sigma^{ep\to eXY}}{\mathrm{d}x_{I\!P}\,\mathrm{d}x\,\mathrm{d}Q^2} = \frac{4\pi\alpha^2}{xQ^4}\left(1-y+\frac{y^2}{2}\right)\sigma_r^{D(3)}(x_{I\!P},x,Q^2)\,, \tag{1}$$

or in terms of a diffractive structure function $F_2^{D(3)}(x_{I\!P},\beta,Q^2)$. Neglecting any contributions from Z^0 exchange,

$$\sigma_r^{D(3)} = F_2^{D(3)} - \frac{y^2}{1+(1-y)^2}F_L^{D(3)}\,, \tag{2}$$

such that $\sigma_r^{D(3)} = F_2^{D(3)}$ is a good approximation except at very large y. The new data span a wide kinematic range, covering several orders of magnitude in Q^2, β and $x_{I\!P}$.

Within the framework of QCD hard scattering collinear factorisation in diffractive DIS [7], these data provide important constraints on the diffractive parton distribution functions (dpdf's) of the proton. These dpdf's are a crucial input for calculations of the cross sections for less inclusive diffractive processes in DIS, such as dijet or charm production [8, 9]. In contrast to the case of inclusive scattering, the dpdf's extracted in DIS are not expected to be directly applicable to hadron-hadron scattering [7, 10–12]. Indeed, diffractive factorisation breaks down spectacularly when HERA dpdf's are applied to diffractive proton-proton interactions at the TEVATRON [13]. It may, however, be possible to recover good agreement by applying an additional 'rapidity gap survival probability' factor to account for secondary scattering between the beam remnants [14–17]. The HERA dpdf's thus remain an essential ingredient in the prediction of diffractive cross sections at the LHC, notably the diffractive Higgs cross section [18]. Although the poorly known rapidity gap survival probability leads to the largest uncertainty in such calculations, the uncertainty due to the input dpdf's also plays a significant role. In [3], the H1 collaboration made a first attempt to assess the uncertainty from this source, propagating the experimental errors from the data points to the 'H1 2002 NLO fit' parton densities and assessing the theoretical uncertainties from various sources.

In this contribution, we investigate the compatibility between various different measurements of F_2^D by H1 and ZEUS. We also apply the techniques developed in [3] to ZEUS data in order to explore the consequences of differences between the H1 and ZEUS measurements in terms of dpdf's.

[1] For a full definition of all terms and variables used, see for example [3].

2 Diffractive Selection Methods and Data Sets Considered

One of the biggest challenges in measuring diffractive cross sections, and often the source of large systematic uncertainties, is the separation of diffractive events in which the proton remains intact from non-diffractive events and from proton-dissociation processes in which the proton is excited to form a system with a large mass, $M_{\rm Y}$. Three distinct methods have been employed by the HERA experiments, which select diffractive events of the type $ep \to eXY$, where Y is a proton or at worst a low mass proton excitation. These methods are complimentary in that their systematics due to the rejection of proton dissociative and non diffractive contributions are almost independent of one another. They are explained in detail below.

- **Roman Pot Spectrometer Method.** Protons scattered through very small angles are detected directly in detectors housed in 'Roman Pot' insertions to the beampipe well downstream the interaction point. The proton 4-momentum at the interaction point is reconstructed from the position and slope of the tracks in these detectors, given a knowledge of the beam optics in the intervening region. The Roman Pot devices are known as the Leading Proton Spectrometer (LPS) in the case of ZEUS and the Forward Proton Spectrometer (FPS) in H1. The Roman pot method provides the cleanest separation between elastic, proton dissociative and non-diffractive events. However, acceptances are rather poor, such that statistical uncertainties are large in the data sets obtained so far.
- **Rapidity Gap Method.** This method is used by H1 for diffractive structure function measurements and by both H1 and ZEUS for the investigation of final state observables. The outgoing proton is not observed, but the diffractive nature of the event is inferred from the presence of a large gap in the rapidity distribution of the final state hadrons, separating the X system from the unobserved Y system. The diffractive kinematics are reconstructed from the mass of the X system, which is well measured in the main detector components. The rapidity gap must span the acceptance regions of various forward[2] detector components. For the H1 data presented here, these detectors efficiently identify activity in the pseudorapidity range $3.3 < \eta \lesssim 7.5$. The presence of a gap extending to such large pseudorapidities is sufficient to ensure that $M_{\rm Y} \lesssim 1.6$ GeV. In light of the poor knowledge of the $M_{\rm Y}$ spectrum at low masses, no attempt is made to correct the data for the small remaining proton dissociation contribution, but rather the cross sections are quoted integrated over $M_{\rm Y} < 1.6$ GeV.
- **$M_{\rm X}$ Method.** Again the outgoing proton is not observed, but rather than requiring a large rapidity gap, diffractive events are selected on the basis of the inclusive $\ln M_{\rm X}^2$ distribution. Diffractive events are responsible for a plateau in this distribution at low $\ln M_{\rm X}^2$, such that they can be selected cleanly for the lowest $M_{\rm X}$ values. At intermediate $M_{\rm X}$, non-diffractive contributions are subtracted on the basis of a two component fit in which the non-diffractive component rises exponentially. This method is used for diffractive structure function measurements by ZEUS. It does not discriminate between elastic and low $M_{\rm Y}$ proton-dissociative contributions. Results are quoted for $M_{\rm Y} < 2.3$ GeV.

Four recent data sets are considered, for which full details of luminosities and kinematic ranges can be found in Table 1.

- Published data from ZEUS taken in 1998 and 1999, using the $M_{\rm X}$ method and taking advantage of the increased forward acceptance offered by a new plug calorimeter ('ZEUS-$M_{\rm X}$') [1].
- Published ZEUS data obtained with the LPS using data taken in 1997 ('ZEUS-LPS') [2].
- Preliminary H1 data obtained using the rapidity gap method, combining three measurements using different data sets from the period 1997-2000 for different regions in Q^2 ('H1-LRG') [3–5].
- Preliminary H1 data obtained using the FPS, based on data taken in 1999 and 2000 ('H1-FPS') [6].

[2]The forward hemisphere is that of the outgoing proton beam, where the pseudorapidity $\eta = -\ln\tan\theta/2$ is positive.

Table 1: Overview of the data sets discussed here. The quoted kinematic ranges in Q^2, β and $x_{I\!P}$ correspond to the bin centres.

Label	Ref.	Reconstruction Method	Lumi $\mathcal{L}[\mathrm{pb}^{-1}]$	Kinematic range $M_Y[\mathrm{GeV}]$	$Q^2[\mathrm{GeV}^2]$	β	$x_{I\!P}$
ZEUS-M_X	[1]	M_X method	4.2	< 2.3	2.7..55	0.003..0.975	0.0001..0.03
ZEUS-LPS	[2]	Roman Pot	12.8	M_p	2.4..39	0.007..0.48	0.0005..0.06
H1-LRG	[3–5]	Rapidity Gap	3.4..63	< 1.6	1.5..1600	0.01..0.9	0.0001..0.05
H1-FPS	[6]	Roman Pot	25	M_p	2.6..20	0.01..0.7	0.002..0.05

3 Comparisons between Data Sets

In this section, the $x_{I\!P}$ dependences of the data from the different measurements are compared at fixed values of Q^2 and β. Since the various measurements are generally presented at different Q^2 and β values, it is necessary to transport the data to the same values. The β and Q^2 values of the H1-LRG data are chosen as the reference points. The factors applied to data points from the other measurements are evaluated using two different parameterisations, corresponding to the results of QCD fits to 1994 H1 data [19] and to a subset of the present H1-LRG data at intermediate Q^2 [3] (see also section 4). In order to avoid any significant bias arising from this procedure, data points are only considered further here if the correction applied is smaller than 50% in total and if the correction factors obtained from the two parameterisations are in agreement to better than 25%. In practice, these criteria only lead to the rejection of data points in the ZEUS-M_X data set at $Q^2 = 55\ \mathrm{GeV}^2$ and $\beta = 0.975$, where the poorly known high β dependence of the diffractive cross section implies a large uncertainty on the factors required to transport them to $\beta = 0.9$. Elsewhere, there is reasonable agreement between the factors obtained from the two parameterisations and no additional uncertainties are assigned as a consequence of this procedure.

Since the various data sets correspond to different ranges in the outgoing proton system mass, M_Y, additional factors are required before comparisons can be made. For all data and fit comparisons, all data are transported to the H1 measurement range of $M_Y < 1.6\ \mathrm{GeV}$ and $|t| < 1\ \mathrm{GeV}^2$. The leading proton data are scaled by a factor 1.1 [20] to correspond to the range $M_Y < 1.6\ \mathrm{GeV}$ and the ZEUS-M_X data are scaled to the same range by a further factor of 0.7 [1], such that the overall factor is 0.77. The uncertainties on these factors are large, giving rise to normalisation uncertainties of perhaps 15% between the different data sets.

The ZEUS-LPS and H1-FPS data are compared in figure 1. Within the experimental uncertainties, the two data sets are in good agreement. Both data sets are also consistent with a parameterisation of the H1-LRG data [3] based on the H1 2002 NLO QCD fit, which is also shown. This good agreement between the H1-LRG and the Roman Pot data is also shown explicitly in figure 3.

In figure 2, a comparison is made between the H1-LRG and the ZEUS-M_X data after all factors have been applied. For much of the kinematic range, there is tolerable agreement between the two data sets. However, there are clear regions of disagreement. One is at the largest β (smallest M_X), where the H1 data lie significantly above the ZEUS data for $Q^2 \lesssim 20\ \mathrm{GeV}^2$. Another is at intermediate and low β, where the two data sets show significantly different dependences on Q^2. With the factor of 0.77 applied to the ZEUS data, there is good agreement at low Q^2, but the ZEUS data lie below the H1 data at large Q^2. If the factor of 0.77 is replaced with a value closer to unity, the agreement improves at large Q^2, but the H1 data lie above the ZEUS data at low Q^2. These inconsistencies between the different data sets are discussed further in section 4.

For completeness, figure 3 shows a comparison between all four data sets considered.

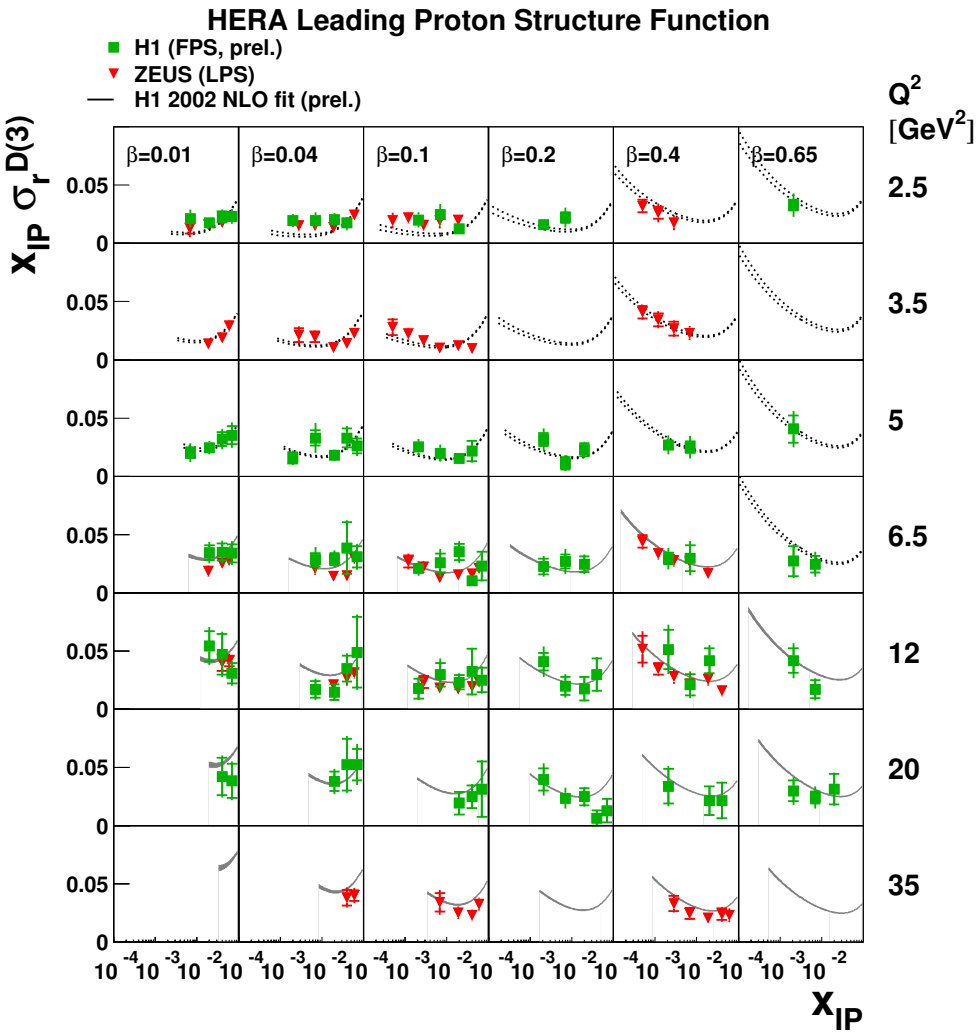

Fig. 1: Comparison of the Roman Pot data from H1 and ZEUS, scaled by a factor 1.1 such that they correspond to $M_Y < 1.6$ GeV. The Q^2 and β values have been shifted to the H1-LRG bin centres using small translation factors. The upper and lower curves form an error band on the predictions from the H1 2002 NLO QCD fit to the H1-LRG data (experimental errors only). Dotted lines are used for kinematic regions which were not included in the fit. Normalisation uncertainties of $^{+12\%}_{-10\%}$ on the ZEUS LPS data and 15% on the factor applied to shift the datasets to $M_Y < 1.6$ GeV are not shown.

4 Diffractive Parton Distributions

4.1 Theoretical Framework and Fit to H1-LRG Data

In this contribution, we adopt the fitting procedure used by H1 in [3], where next-to-leading order (NLO) QCD fits are performed to diffractive reduced cross section, $\sigma_r^{D(3)}$, data [3, 21] with $6.5 \leq Q^2 \leq 800$ GeV^2 and the β and $x_{I\!P}$ ranges given in table 1.

The proof that QCD hard scattering collinear factorisation can be applied to diffractive DIS [7] implies that in the leading $\log(Q^2)$ approximation, the cross section for the diffractive process $ep \to eXY$ can be written in terms of convolutions of universal partonic cross sections $\hat{\sigma}^{ei}$ with diffractive parton distribution functions (dpdf's) f_i^D [11, 22, 23], representing probability distributions for a parton i in the proton under the constraint that the proton is scattered with a particular 4 momentum. Thus, at

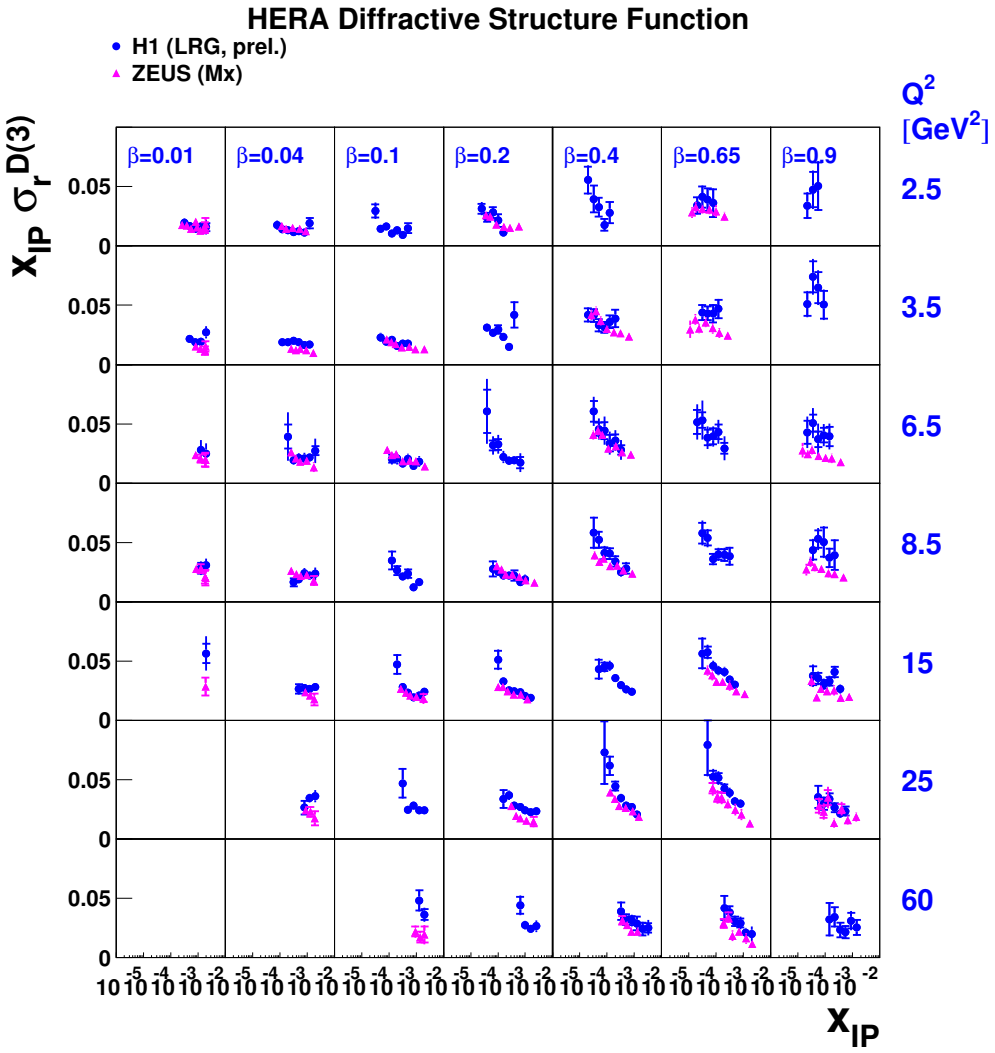

Fig. 2: Comparison of the ZEUS-M_X data with a subset of the H1-LRG data. The Q^2 and β values of the ZEUS data have been shifted to the H1 bin centres using small translation factors. The ZEUS data have also been multiplied by a universal factor of 0.77, such that both data sets correspond to $M_Y < 1.6$ GeV. Normalisation uncertainties of 15% on this factor and of $\pm 6.7\%$ on the H1 data are not shown.

leading twist,[3]

$$\frac{\mathrm{d}^2\sigma(x,Q^2,x_{I\!P},t)^{ep\to eXp'}}{\mathrm{d}x_{I\!P}\,\mathrm{d}t} = \sum_i \int_x^{x_{I\!P}} \mathrm{d}\xi\, \hat{\sigma}^{ei}(x,Q^2,\xi)\, f_i^D(\xi,Q^2,x_{I\!P},t)\,. \tag{3}$$

This factorisation formula is valid for sufficiently large Q^2 and fixed $x_{I\!P}$ and t. It also applies to the case of proton dissociation into a system of fixed mass M_Y and thus to any cross section which is integrated over a fixed range in M_Y. The partonic cross sections $\hat{\sigma}^{ei}$ are the same as those for inclusive DIS and the dpdf's f_i^D, which are not known from first principles, should obey the DGLAP evolution equations [25].

In addition to the rigorous theoretical prescription represented by equation (3), an additional assumption is necessary for the H1 fits in [3], that the shape of the dpdf's is independent of $x_{I\!P}$ and t and that their normalisation is controlled by Regge asymptotics [26]. Although this assumption has no

[3] A framework also exists to include higher order operators [24].

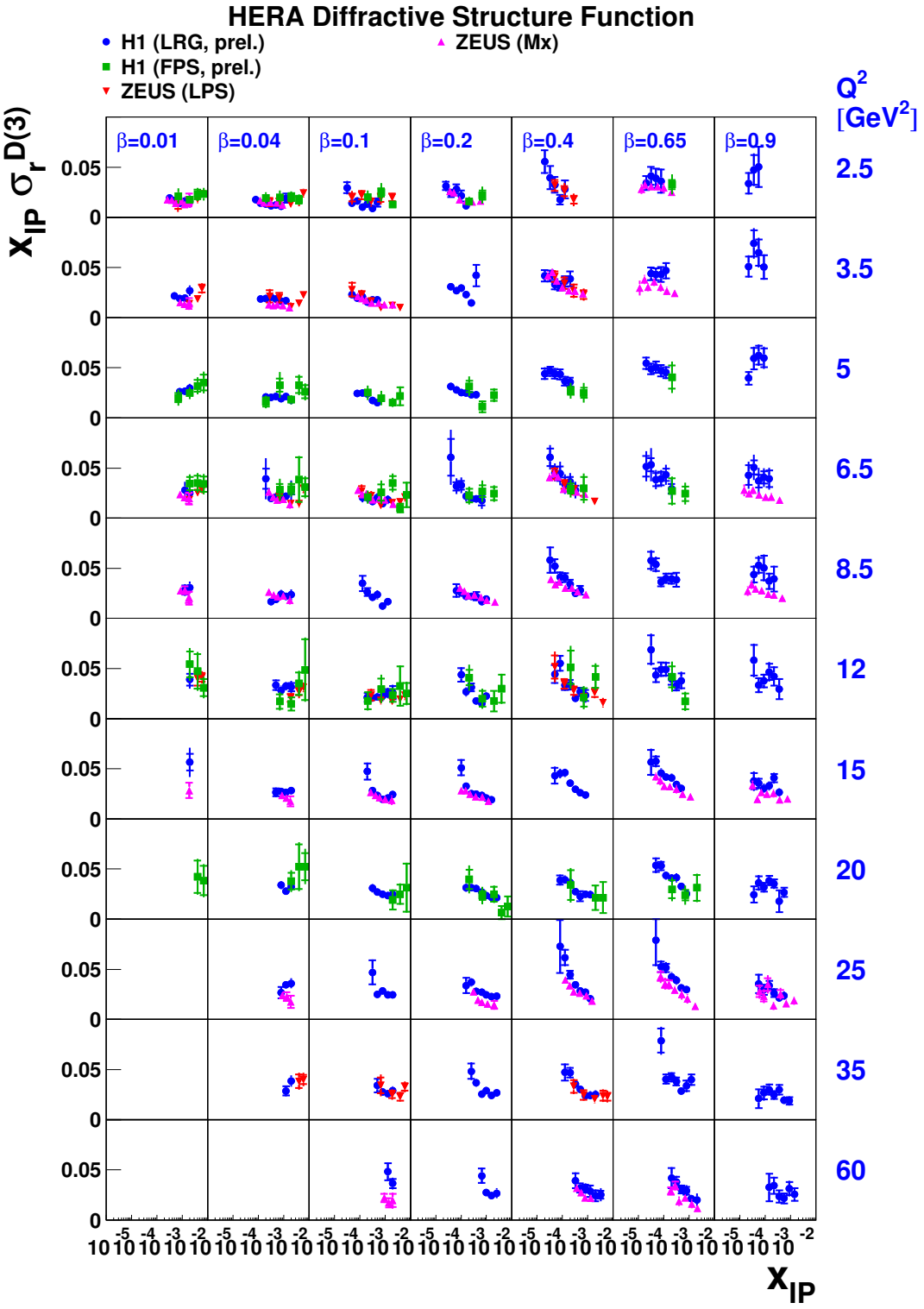

Fig. 3: Summary plot of all diffractive DIS data sets considered here. Additional H1-LRG data with $Q^2 < 2.5$ GeV^2, $Q^2 = 45$ GeV^2 and $Q^2 > 60$ GeV^2 are not shown. The Q^2 and β values for all data sets have been shifted to the H1 bin centres using small translation factors. The ZEUS data have been multiplied by a universal factor of 0.77 and the LPS and FPS data by factors of 1.1, such that all data sets correspond to $M_Y < 1.6$ GeV. Relative normalisation uncertainties of 15% due to these factors and further normalisation uncertainties of $\pm 6.7\%$ (H1-LRG) and $^{+12\%}_{-10\%}$ (ZEUS-LPS) data are not shown.

solid basis in QCD, it is compatible with the data fitted. The diffractive parton distributions can then be factorised into a term depending only on $x_{I\!P}$ and t and a term depending only on x (or β) and Q^2:

$$f_i^D(x_{I\!P}, t, x, Q^2) = f_{I\!P/p}(x_{I\!P}, t) \cdot f_i^{I\!P}(\beta = x/x_{I\!P}, Q^2) \; . \tag{4}$$

Under this 'Regge' factorisation assumption, the diffractive exchange can be treated as an object (a 'pomeron', $I\!P$) with a partonic structure given by parton distributions $f_i^{I\!P}(\beta, Q^2)$. The variable β then corresponds to the fraction of the pomeron longitudinal momentum carried by the struck parton. The 'pomeron flux factor' $f_{I\!P/p}(x_{I\!P}, t)$ represents the probability that a pomeron with particular values of $x_{I\!P}$ and t couples to the proton.

In the fit, the $x_{I\!P}$ dependence is parameterised using a Regge flux factor

$$f_{I\!P/p}(x_{I\!P}, t) = A \cdot \int_{t_{cut}}^{t_{min}} \frac{e^{B_{I\!P} t}}{x_{I\!P}^{2\alpha_{I\!P}(t)-1}} \, \mathrm{d}t \; , \tag{5}$$

where $t_{cut} = -1.0$ GeV^2, $|t_{min}|$ is the minimum kinematically allowed value of $|t|$ and the pomeron trajectory is assumed to be linear, $\alpha_{I\!P}(t) = \alpha_{I\!P}(0) + \alpha'_{I\!P} t$. The parameters $B_{I\!P}$ and α' and their uncertainties are fixed as described in [3]. The value of A is chosen such that the flux factor is normalised to unity at $x_{I\!P} = 0.003$. The pomeron intercept is then obtained from the $x_{I\!P}$ dependence of the data and takes the value $\alpha_{I\!P}(0) = 1.173 \; \pm 0.018 \; (\mathrm{stat.}) \; \pm 0.017 \; (\mathrm{syst.}) \; ^{+0.063}_{-0.035} \; (\mathrm{model})$.

The description of the data is improved with the inclusion of an additional separately factorisable sub-leading exchange with a trajectory intercept of $\alpha_{I\!R}(0) = 0.50$ and parton densities taken from a parameterisation of the pion [27]. This exchange contributes significantly only at low β and large $x_{I\!P}$.

The dpdf's are modelled in terms of a light flavour singlet

$$\Sigma(z) = u(z) + d(z) + s(z) + \bar{u}(z) + \bar{d}(z) + \bar{s}(z) \; , \tag{6}$$

with $u = d = s = \bar{u} = \bar{d} = \bar{s}$ and a gluon distribution $g(z)$ at a starting scale $Q_0^2 = 3$ GeV^2. Here, z is the momentum fraction of the parton entering the hard sub-process with respect to the diffractive exchange, such that $z = \beta$ for the lowest-order quark parton model process, whereas $0 < \beta < z$ for higher order processes. The singlet quark and gluon distributions are parameterised using the form

$$z p_i(z, Q_0^2) = \left[\sum_{j=1}^{n} C_j^i P_j(2z-1) \right]^2 e^{\frac{0.01}{z-1}} \; , \tag{7}$$

where $P_j(\xi)$ is the j^{th} member of a set of Chebychev polynomials[4]. The series is squared to ensure positivity. The exponential term is added to guarantee that the dpdf's tend to zero in the limit of $z \to 1$. It has negligible influence on the extracted partons at low to moderate z. The numbers of terms in the polynomial parameterisations are optimised to the precision of the data, with the first three terms in the series used for both the quark singlet and the gluon distributions, yielding 3 free parameters (C_j^{Σ} and C_j^g) for each. The normalisation of the sub-leading exchange contribution at high $x_{I\!P}$ is also determined by the fit such that the total number of free parameters is 7. The data used in the fit are restricted to $M_{\mathrm{X}} > 2$ GeV to suppress non-leading twist contributions. The effects of F_L^D are considered through its relation to the NLO gluon density, such that no explicit cut on y is required.

The NLO DGLAP equations are used to evolve the dpdfs to $Q^2 > Q_0^2$ using the method of [28], extended for diffraction. No momentum sum rule is imposed. Charm quarks are treated in the massive scheme (appearing via boson gluon fusion processes) with $m_c = 1.5 \pm 0.1$ GeV. The strong coupling is set via[5] $\Lambda^{\overline{\mathrm{MS}}}_{\mathrm{QCD}} = 200 \pm 30$ MeV. The statistical and experimental systematic errors on the data points

[4] $P_1 = 1$, $P_2 = \xi$ and $P_{j+1}(\xi) = 2\xi P_j(\xi) - P_{j-1}(\xi)$.

[5] Although this value is rather different from the world average, we retain it here for consistency with previous H1 preliminary results, where it has been used consistently for QCD fits [3] and final state comparisons [8, 9].

and their correlations are propagated to obtain error bands for the resulting dpdfs, which correspond to increases in the χ^2 by one unit [29]. A theoretical error on the dpdfs is estimated by variations of $\Lambda_{\rm QCD}$, m_c and the parameterisation of the $x_{I\!P}$ dependences as described in [3]. No theoretical uncertainty is assigned for the choice of parton parameterisation, though the results are consistent within the quoted uncertainties if alternative approaches [30] are used. No inhomogeneous term of the type included in [31] is considered here. The presence of such a term would lead to a reduction in the gluon density extracted.

The central fit gives a good description of the data, with a χ^2 of 308.7 for 306 degrees of freedom. The resulting diffractive quark singlet and gluon distributions are shown in figure 4. Both extend to large fractional momenta z. Whereas the singlet distribution is well constrained by the fit, there is a substantial uncertainty in the gluon distribution, particularly for $z \gtrsim 0.5$. The fraction of the exchanged momentum carried by gluons integrated over the range $0.01 < z < 1$ is $75 \pm 15\%$ (total error), confirming the conclusion from earlier work [19] that diffraction is a gluon-induced phenomenon. These dpdf's have been astonishingly successful in describing diffractive final state data in DIS such as charm [9] and jet [8] production, which, being induced by boson-gluon fusion-type processes, are roughly proportional to the diffractive gluon density.

4.2 Fit to ZEUS Data

A very similar fit to that described in section 4.1 is performed to the ZEUS-$M_{\rm X}$ data and the implications of the differences between the data sets to the dpdf's are investigated. The data are fitted in their original binning scheme, but are scaled to $M_{\rm Y} < 1.6$ GeV using the factor of 0.77. As for the fit to the H1 data, the first 3 terms are included in the polynomial expansions for the quark and gluon densities at the starting scale for QCD evolution. The same fit program, prescription and parameters are used as was the case for the H1 2002 NLO fit, with the following exceptions.

- ZEUS-$M_{\rm X}$ data with $Q^2 > 4$ GeV^2 are included in the fit, whereas only H1 data with $Q^2 > 6.5$ GeV^2 are included. It has been checked that the result for ZEUS is not altered significantly if the minimum Q^2 value is increased to 6 GeV^2.
- The quadratic sum of the statistical and systematic error is considered, i.e. there is no treatment of correlations between the data points through the systematics.
- No sub-leading Reggeon exchange component is included in the parameterisation. Including one does not improve or alter the fit significantly.
- The Pomeron intercept is fitted together with the dpdf's, in contrast to the two stage process of [3]. This does not influence the results significantly, though it does decrease the uncertainty on $\alpha_{I\!P}(0)$.

The fit describes the ZEUS-$M_{\rm X}$ data well ($\chi^2 = 90$ for 131 degrees of freedom) and yields a value for the Pomeron intercept of $\alpha_{I\!P}(0) = 1.132 \pm 0.006$ (experimental error only). This value is in agreement with the H1 result if the full experimental and theoretical errors are taken into account. A good fit is thus obtained without any variation of $\alpha_{I\!P}(0)$ with Q^2 or other deviation from Regge factorisation.

The diffractive parton densities from the fit to the ZEUS-$M_{\rm X}$ data are compared with the results from H1 in figure 4. The differences observed between the H1 and the ZEUS data are directly reflected in the parton densities. The quark singlet densities are closely related to the measurements of F_2^D themselves. They are similar at low Q^2 where the H1 and ZEUS data are in good agreement, but become different at larger Q^2, where discrepancies between the two data sets are observed. This difference between the Q^2 dependences of the H1 and ZEUS data is further reflected in a difference of around a factor of 2 between the gluon densities, which are roughly proportional to the logarithmic Q^2 derivative $\partial F_2^D / \partial \ln Q^2$ [32].

The H1-LRG and ZEUS-$M_{\rm X}$ data are shown together with the results from both QCD fits in figure 5. Both fits give good descriptions of the data from which they are obtained. The differences between the two data sets are clearly reflected in the fit predictions, most notably in the Q^2 dependence.

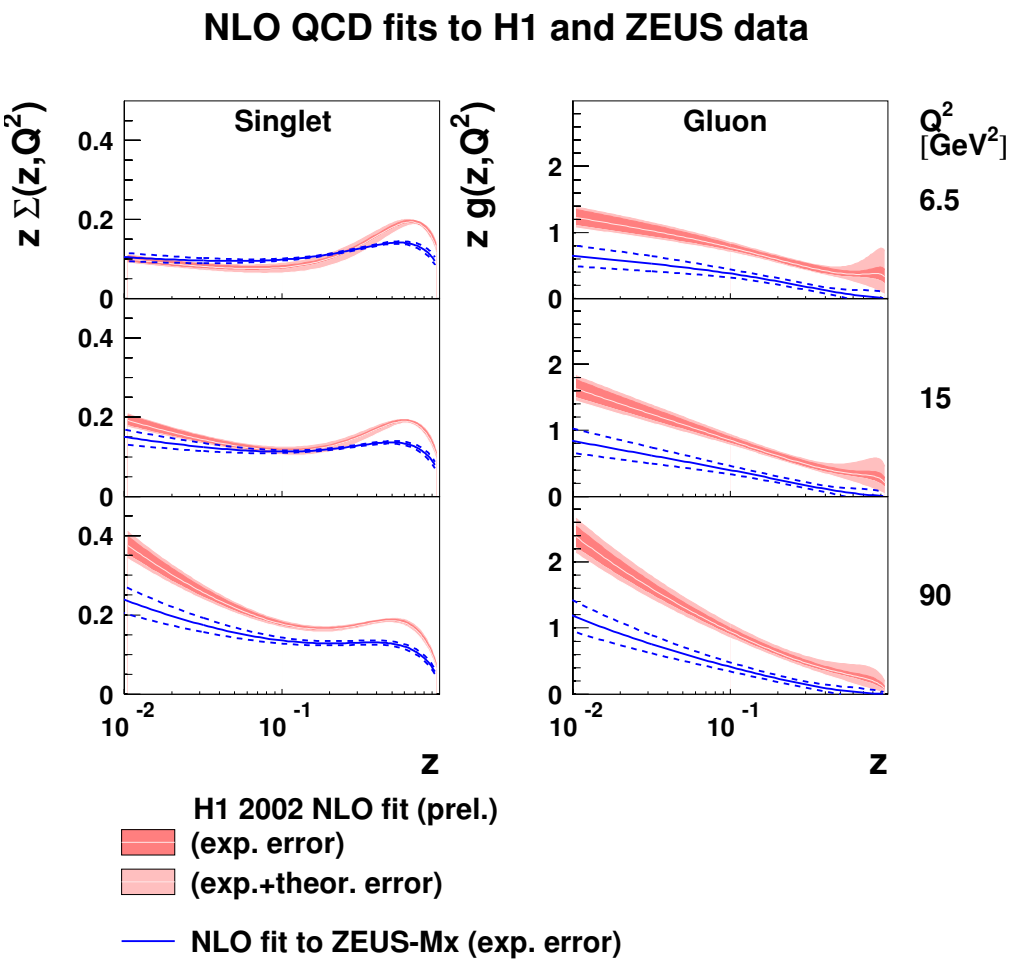

Fig. 4: Diffractive quark singlet and gluon pdf's for various Q^2 values, as obtained from the NLO DGLAP fits to the H1-LRG and ZEUS-$M_{\rm X}$ data. The bands around the H1 result indicate the experimental and theoretical uncertainties. The dotted lines around the result for ZEUS indicate the experimental uncertainty. The ZEUS data used in the fit are scaled by a normalisation factor of 0.77 to match the H1-LRG range of $M_{\rm Y} < 1.6$ GeV. This factor is reflected in the normalisations of the quark and gluon densities. An uncertainty of 15% on this factor is not included in the error bands shown.

5 Summary

Recent diffractive structure function data from H1 and ZEUS have been compared directly. The leading proton data from both experiments (H1-FPS and ZEUS-LPS) are in good agreement with one other and with the H1 large rapidity gap data (H1-LRG). There is reasonable agreement between the H1-LRG and the ZEUS-$M_{\rm X}$ data over much of the kinematic range. However, differences are observed at the highest β (smallest $M_{\rm X}$) and the Q^2 dependence at intermediate to low β is weaker for the ZEUS-$M_{\rm X}$ data than is the case for the H1-LRG data.

An NLO DGLAP QCD fit has been performed to the ZEUS-$M_{\rm X}$ data, using the same theoretical framework, assumptions and parameterisations as have been employed previously for the H1-2002-prelim NLO QCD fit to a subset of the H1-LRG data. As a consequence of the differences between the Q^2 dependences of the H1-LRG and ZEUS-$M_{\rm X}$ data, the gluon density obtained from the ZEUS data is significantly smaller than that for H1.

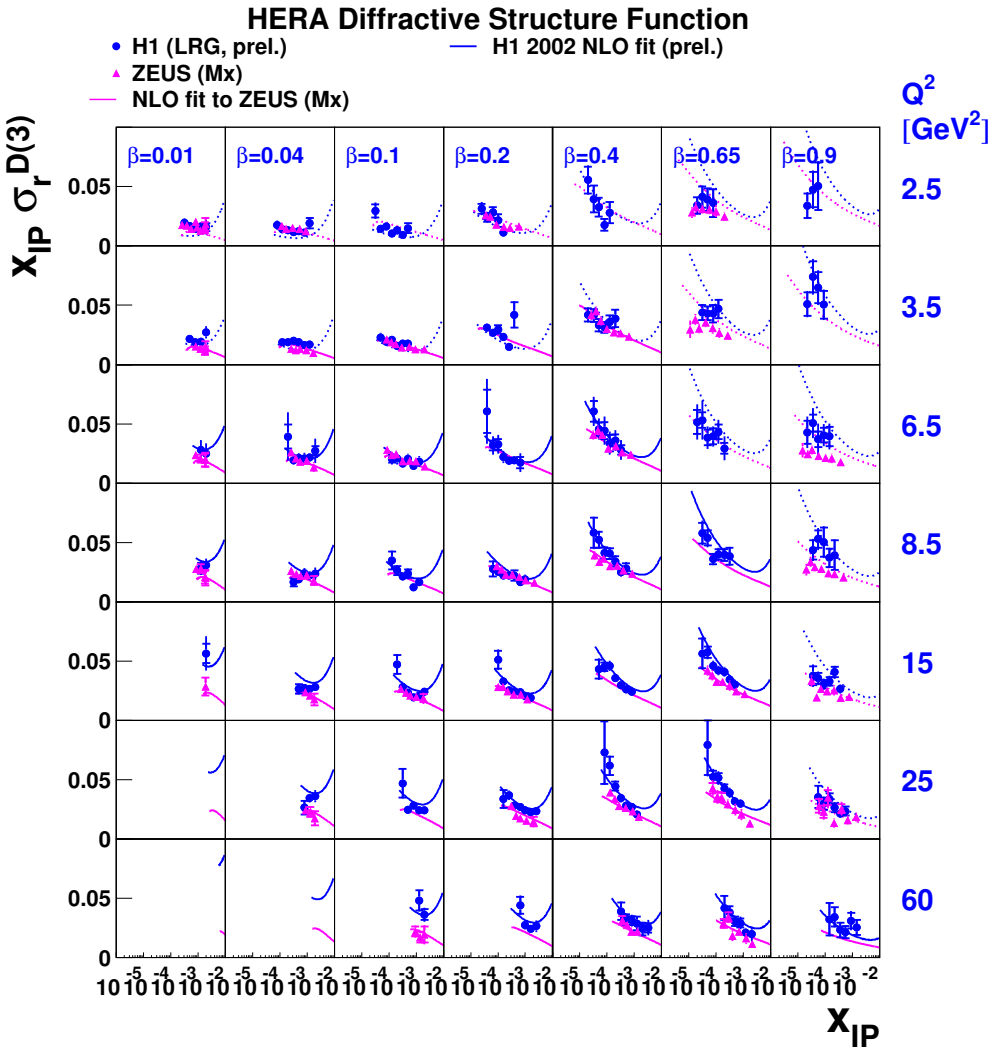

Fig. 5: As figure 2, but also showing the predictions using the NLO QCD fits to the H1-LRG and ZEUS-M_X data (uncertainties not shown).

References

[1] S. Chekanov et al. [ZEUS Collaboration], Nucl. Phys. **B713**, 3 (2005).

[2] S. Chekanov et al. [ZEUS Collaboration], Eur. Phys. J. **C38**, 43 (2004).

[3] H1 Collaboration, paper 980 contributed to ICHEP 2002, Amsterdam. H1prelim-02-012.

[4] H1 Collaboration, paper 981 contributed to ICHEP 2002, Amsterdam. H1prelim-02-112.

[5] H1 Collaboration, paper 5-090 contributed to EPS 2003, Aachen. H1prelim-03-011.

[6] H1 Collaboration, paper 984 contributed to ICHEP 2002, Amsterdam. H1prelim-01-112.

[7] J. Collins, Phys. Rev. **D57**, 3051 (1998). Erratum ibid **D61** (2000) 019902.

[8] H1 Collaboration, paper 6-0177 contributed to ICHEP 2004, Beijing. H1prelim-04-113.

[9] H1 Collaboration, paper 6-0178 contributed to ICHEP 2004, Beijing. H1prelim-04-111.

[10] J. Collins, L. Frankfurt, M. Strikman, Phys. Lett. **B307**, 161 (1993).

[11] A. Berera, D. Soper, Phys. Rev. **D50**, 4328 (1994).

[12] A. Berera, D. Soper, Phys. Rev. **D53**, 6162 (1996).

[13] T. Affolder et al. [CDF Collaboration], Phys. Rev. Lett. **84**, 5043 (2000).
[14] J. Bjorken, Phys. Rev. **D47**, 101 (1993).
[15] E. Gotsman, E. Levin, U. Maor, Phys. Lett. **B438**, 229 (1998).
[16] B. Cox, J. Forshaw, L. Lonnblad, JHEP **10**, 023 (1999).
[17] A. Kaidalov, V. Khoze, A. Martin, M. Ryskin, Phys. Lett. **B567**, 61 (2003).
[18] J. Forshaw, these proceedings.
[19] C. Adloff et al. [H1 Collaboration], Z. Phys. **C76**, 613 (1997).
[20] C. Adloff et al. [H1 Collaboration], Z. Phys. **C74**, 221 (1997).
[21] H1 Collaboration, paper 571 contributed to ICHEP 1998, Vancouver.
[22] L. Trentadue, G. Veneziano, Phys. Lett. **B323**, 201 (1994).
[23] M. Grazzini, L. Trentadue, G. Veneziano, Nucl. Phys. **B519**, 394 (1998).
[24] J. Blumlein, D. Robaschik, Phys. Rev. **D65**, 096002 (2002).
[25] A. Hebecker, Nucl. Phys. **B505**, 349 (1997).
[26] G. Ingelman, P. Schlein, Phys. Lett. **B152**, 256 (1985).
[27] J. Owens, Phys. Rev. **D30**, 943 (1984).
[28] C. Adloff et al. [H1 Collaboration], Eur. Phys. J. **C21**, 33 (2001).
[29] C. Pascaud, F. Zomer, Preprint LAL-95-05.
[30] A. Martin, R. Roberts, J. Stirling, R. Thorne, Phys. Lett. **B531**, 216 (2002).
[31] G. Watt, A. Martin, M. Ryskin, these proceedings.
[32] K. Prytz, Phys. Lett. **B311**, 286 (1993).

Diffractive parton distributions from the HERA data

Michael Groys[a]*, Aharon Levy*[a] *and Alexander Proskuryakov*[b]
[a]Raymond and Beverly Sackler Faculty of Exact Sciences, School of Physics and Astronomy, Tel Aviv University, Tel Aviv, Israel
[b]Institute of Nuclear Physics, Moscow State University, Moscow, Russia

Abstract

Measurements of the diffractive structure function, F_2^D, of the proton at HERA are used to extract the partonic structure of the Pomeron. Regge Factorization is tested and is found to describe well the existing data within the selected kinematic range. The analysis is based on the next to leading order QCD evolution equations. The results obtained from various data sets are compared.

1 Introduction

In the last 10 years a large amount of diffractive data was accumulated at the HERA collider [1–3]. There are three methods used at HERA to select diffractive events. One uses the Leading Proton Spectrometer (LPS) [3] to detect the scattered proton and by choosing the kinematic region where the scattered proton looses very little of its initial longitudinal energy, it ensures that the event was diffractive. A second method [2] simply requests a large rapidity gap (LRG) in the event and fits the data to contributions coming from Pomeron and Reggeon exchange. The third method [1] relies on the distribution of the mass of the hadronic system seen in the detector, M_X, to isolate diffractive events and makes use of the Forward Plug Calorimeter (FPC) to maximize the phase space coverage. We will refer to these three as ZEUS LPS, H1 and ZEUS FPC methods.

The experiments [4–6] provide sets of results for inclusive diffractive structure function, $x_{I\!P} F_2^{D(3)}$, in different regions of phase space. In extracting the initial Pomeron parton distribution functions (pdfs), the data are fitted assuming the validity of Regge factorization.

In the present study, Regge factorization is tested. New fits, based on a NLO QCD analysis, are provided and include the contribution of the longitudinal structure function. The obtained PDFs are systematically analyzed. A comparison of the different experimental data sets is provided. Additional quantities derived from the fit results are also presented.

In order to make sure that diffractive processes are selected, a cut of $x_{I\!P} < 0.01$ was performed, where $x_{I\!P}$ is the fraction of the proton momentum carried by the Pomeron. It was shown [7] that this cuts ensures the dominance of Pomeron exchange. In addition, a cut of $Q^2 > 3$ GeV^2 was performed on the exchanged photon virtuality for applying the NLO analysis. Finally, a cut on $M_X > 2$ GeV was used so as to exclude the light vector meson production.

2 Regge factorization

The Regge Factorization assumption can be reduced to the following,

$$F_2^{D(4)}(x_{I\!P}, t, \beta, Q^2) = f(x_{I\!P}, t) \cdot F(\beta, Q^2), \quad (1)$$

where $f(x_{I\!P}, t)$ represents the Pomeron flux which is assumed to be independent of β and Q^2 and $F(\beta, Q^2)$ represents the Pomeron structure and is β and Q^2 dependent. In order to test this assumption, we check whether the flux $f(x_{I\!P}, t)$ is indeed independent of β and Q^2 on the basis of the available experimental data.

The flux is assumed to have a form $\sim x_{I\!P}^{-A}$ (after integrating over t which is not measured in the data) . A fit of this form to the data was performed in different Q^2 intervals, for the whole β range, and for different β intervals for the whole Q^2 range.

Figure 1 shows the Q^2 dependence of the exponent A for all three data sets, with the $x_{I\!P}$ and M_X cuts as described in the introduction. The H1 and the LPS data show no Q^2 dependence. The ZEUS FPC data show a small increase in A at the higher Q^2 region. It should be noted that while for the H1 and LPS data, releasing the $x_{I\!P}$ cut to 0.03 seems to have no effect, the deviation of the ZEUS FPC data from a flat dependence increases from a 2.4 standard deviation (s.d.) to a 4.2 s.d. effect (not shown).

The β dependence of A is shown in figure 2. All three data sets seem to show no β dependence, within the errors of the data. Note however, that by releasing the $x_{I\!P}$ cut to higher values, a strong dependence of the flux on β is observed (not shown).

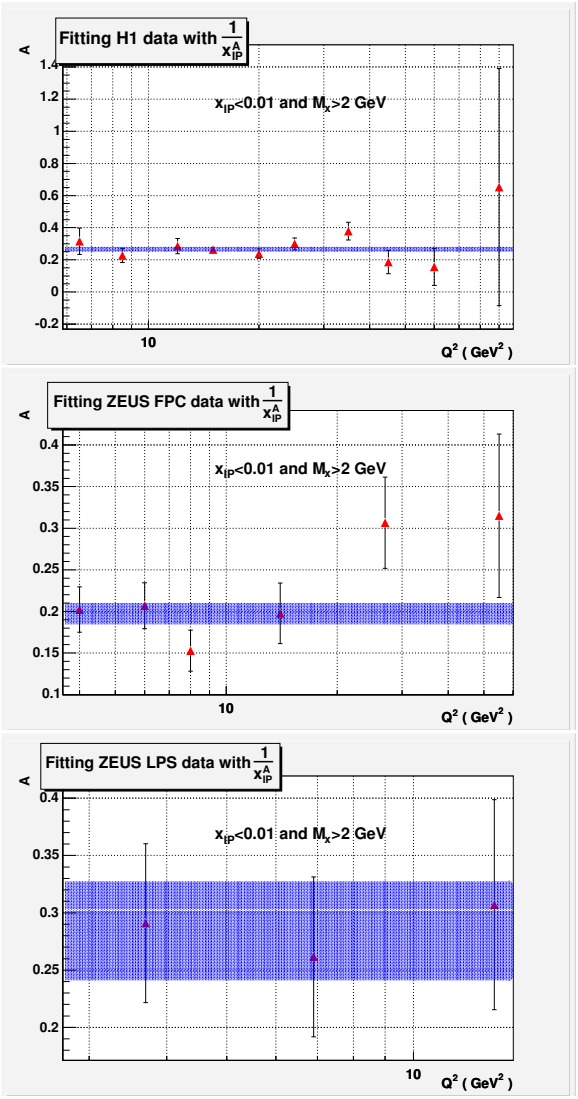

Fig. 1: A as a function of Q^2 for $x_{I\!P} < 0.01$ and $M_X > 2$ GeV, for the three data sets, as indicated in the figure. The line corresponds to a fit over the whole Q^2 region

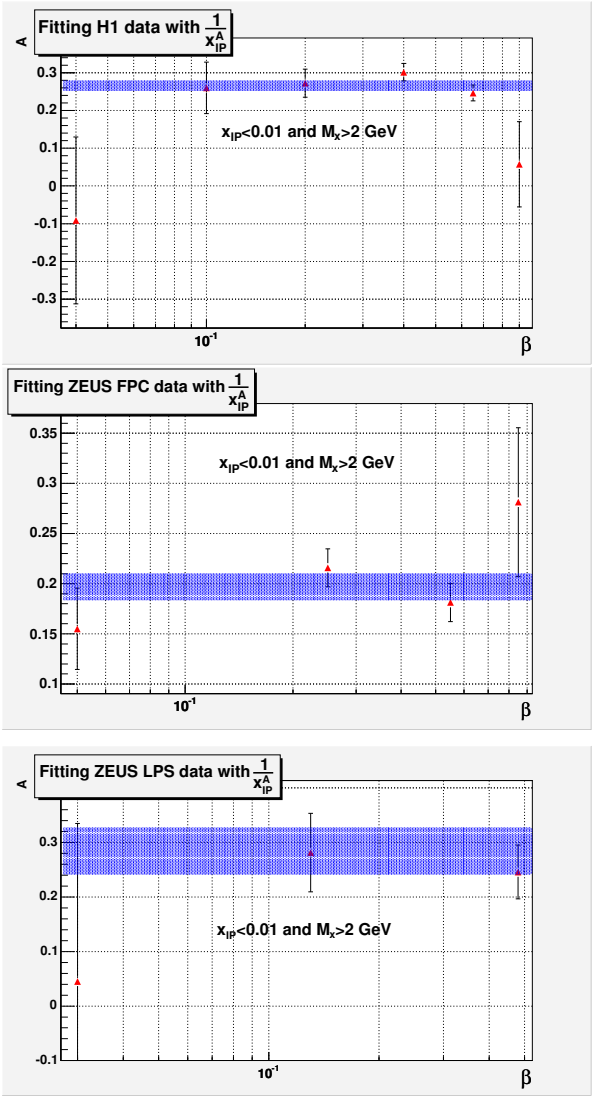

Fig. 2: A as a function of β for $x_{I\!P} < 0.01$ and $M_X > 2$ GeV, for the three data sets, as indicated in the figure. The line corresponds to a fit over the whole β region

We thus conclude that for $x_{I\!P} < 0.01$, the Pomeron flux seems to be independent of Q^2 and of β and thus the Regge factorization hypothesis holds.

3 NLO QCD fits

We parameterized the parton distribution functions of the Pomeron at $Q_0^2 = 3$ GeV^2 in a simple form of $Ax^b(1-x)^c$ for u and d quarks (and anti-quarks) and set all other quarks to zero at the initial scale. The gluon distribution was also assumed to have the same mathematical form. We thus had 3 parameters for quarks, 3 for gluons and an additional parameter for the flux, expressed in terms of the Pomeron intercept $\alpha_{I\!P}(0)$. Each data set was fitted to 7 parameters and a good fit was achieved for each. The H1 and ZEUS FPC had χ^2/df ≈ 1, while for the LPS data, the obtained value was 0.5. The data together with the results of the fits are shown in figure 3. The following values were obtained

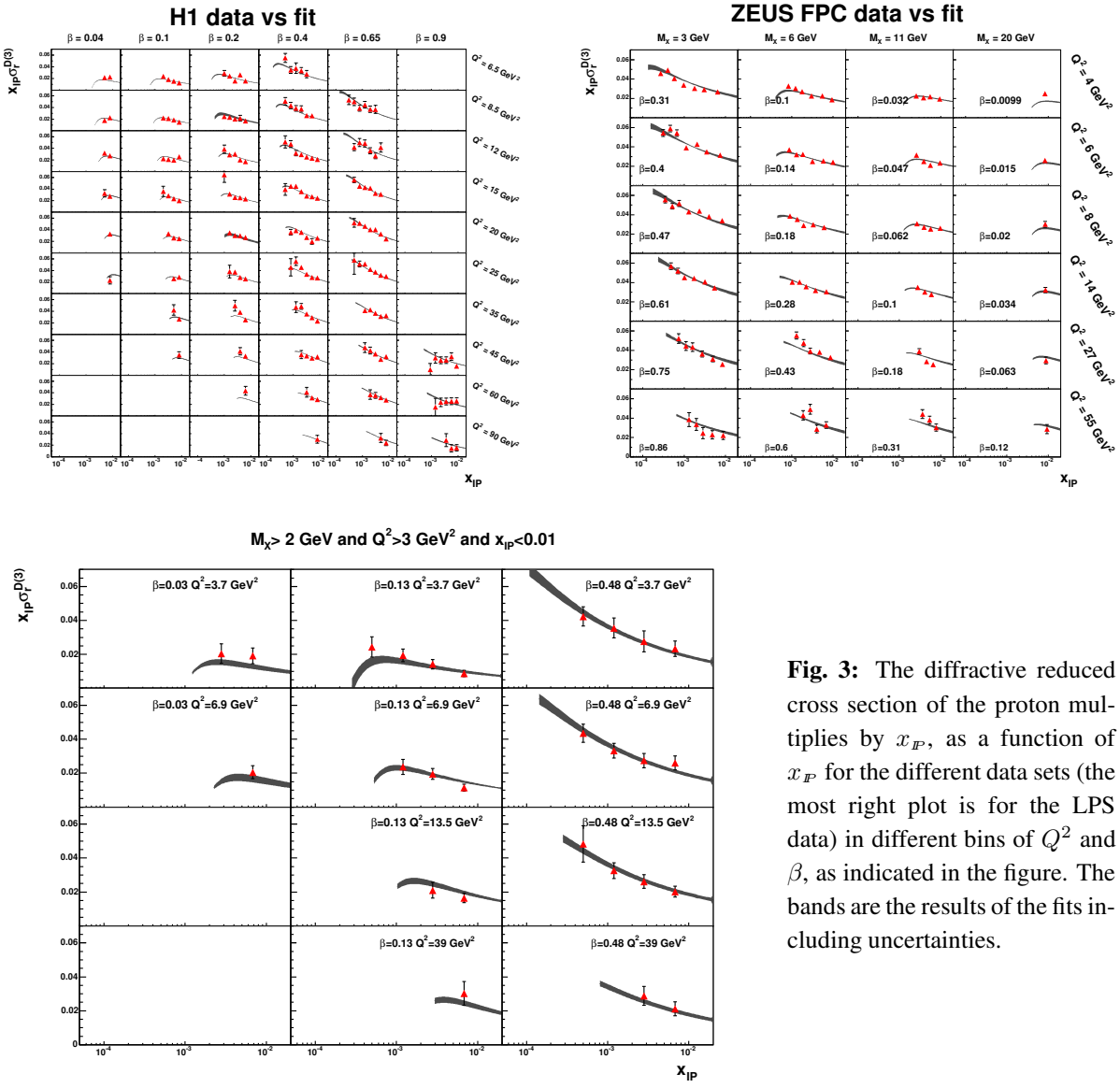

Fig. 3: The diffractive reduced cross section of the proton multiplies by $x_{I\!P}$, as a function of $x_{I\!P}$ for the different data sets (the most right plot is for the LPS data) in different bins of Q^2 and β, as indicated in the figure. The bands are the results of the fits including uncertainties.

for $\alpha_{I\!P}(0)$, for each of the three data sets: $\alpha_{I\!P}(0) = 1.138 \pm 0.011$, for the ZEUS FPC data, $\alpha_{I\!P}(0) = 1.189 \pm 0.020$, for the ZEUS LPS data, $\alpha_{I\!P}(0) = 1.178 \pm 0.007$, for the H1 data.

The parton distribution functions are shown in figure 4 for the H1 and the ZEUS FPC data points. Because of the limited β range covered by the LPS data, the resulting pdfs uncertainties are large and are not shown here. In fact one gets two solutions; one where the gluon contribution is dominant and another one where the gluons and the quarks contribute about equally. Note however that once the diffractive

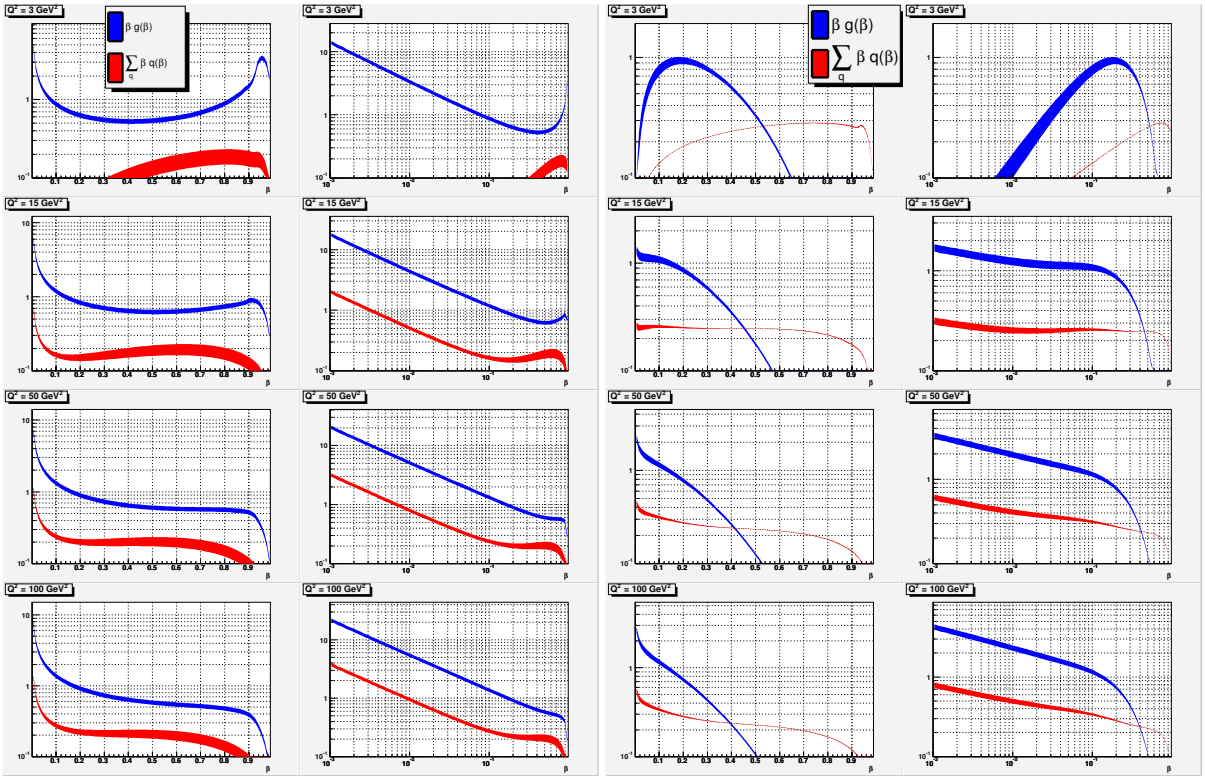

Fig. 4: Quark and gluon pdfs of the Pomeron as obtained from the H1 data fit (left two figures) and from the ZEUS FPC data fit (two rightmost figures) as a function of β, at different values of Q^2.

charm structure function data [8] are included in the fit, the gluon dominant solution is chosen (see below). For the H1 fit one sees the dominance of the gluons in all the β range. For the ZEUS FPC data, the quark constituent of the Pomeron dominates at high β while gluons dominate at low β. We can quantify this by calculating the Pomeron momentum carried by the gluons. Using the fit results one gets for the H1 data 80-90%. while for the ZEUS FPC data, 55-65%.

4 Comparison of the data sets

One way of checking the compatibility of all three data sets is to make an overall fit for the whole data sample. Since the coverage of the β range in the LPS data is limited, we compare only the H1 and the ZEUS FPC data. A fit with a relative overall scaling factor of the two data sets failed. Using the fit results of one data sets superimposed on the other shows that the fit can describe some kinematic regions, while failing in other bins. This leads to the conclusion that there seems to be some incompatibility between the two data sets.

5 Comparison to $F_2^{D(3)}$(charm)

The ZEUS collaboration measured the diffractive charm structure function, $F_2^{D(3),c\bar{c}}$ [8] and these data were used together with the LPS data for a combined fit [6]. The charm data are shown in figure 5 as function of β. The full line shown the resulting best fit, where the contribution from charm was calculated as photon-gluon fusion. In the same figure one sees the prediction from the NLO QCD fit to the ZEUS FPC data (dashed line). Clearly, the gluons from the ZEUS FPC fit can not describe the diffractive charm data.

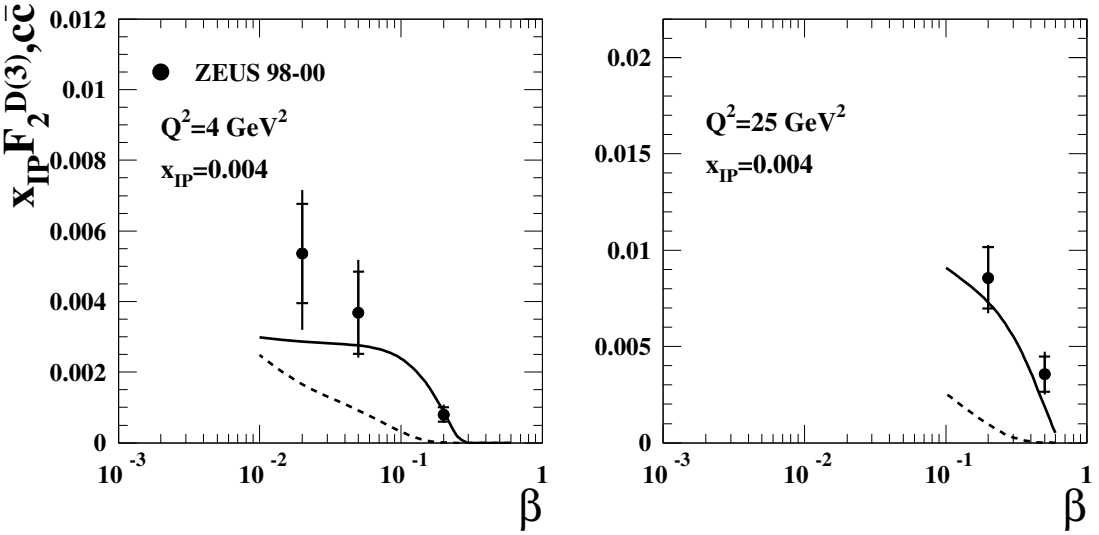

Fig. 5: Diffractive charm structure function, $F_2^{D(3),c\bar{c}}$, as a function of β for values of Q^2 and $x_{I\!P}$ as indicated in the figure. The full line is the result of a combined fit to the LPS and the diffractive charm data. The dashed line is the prediction using the gluons from the ZEUS FPC fit.

Acknowledgements

We would like to thank Prof. Halina Abramowicz for her useful and clarifying comments during this analysis. We would also like to thank Prof. John Collins for providing the program to calculate the NLO QCD equations for the diffractive data. This work was supported in part by the Israel Science Foundation (ISF).

References

[1] ZEUS Collab., M. Derrick et al., *Phys. Lett.* **315** (1993) 481; J. Breitweg et al., *Eur. Phys. J.* **C6** (1999) 43.

[2] H1 Collab., C. Adloff et al., *Zeit. Phys.* **C76** (1997) 613.

[3] ZEUS Collab., S. Chekanov et al., *Eur. Phys. J.* **C25** (2002) 169.

[4] ZEUS Collaboration, S. Chekanov et al., *Nucl. Phys.* **B713** (2005) 3.

[5] H1 Collaboration, "Measurement and NLO DGLAP QCD Interpretation of Diffractive Deep-Inelastic Scattering at HERA," paper 089 submitted to EPS 2003, Aachen.

[6] ZEUS Collaboration, S. Chekanov et al., *Eur. Phys. J.* **C38** (2004) 43.

[7] K. Golec-Biernat, J. Kwiecinski and A. Szczurek, *Phys. Rev.* **D56** (1997) 3955.

[8] ZEUS Collaboration, S. Chekanov et al., *Nucl. Phys.* **B672** (2003) 3.

Diffractive parton distributions

G. Watt[a], A.D. Martin[b], M.G. Ryskin[b,c]
[a] Deutsches Elektronen-Synchrotron DESY, 22607 Hamburg, Germany
[b] Institute for Particle Physics Phenomenology, University of Durham, DH1 3LE, UK
[c] Petersburg Nuclear Physics Institute, Gatchina, St. Petersburg, 188300, Russia

Abstract
We discuss the perturbative QCD description of diffractive deep-inelastic scattering, and extract diffractive parton distributions from recent HERA data. The asymptotic collinear factorisation theorem has important modifications in the sub-asymptotic HERA regime. In addition to the usual *resolved* Pomeron contribution, the *direct* interaction of the Pomeron must also be accounted for. The diffractive parton distributions are shown to satisfy an *inhomogeneous* evolution equation, analogous to the parton distributions of the photon.

1 Diffractive parton distributions from Regge factorisation

It is conventional to extract diffractive parton distribution functions (DPDFs) from diffractive deep-inelastic scattering (DDIS) data using two levels of factorisation. Firstly, collinear factorisation means that the diffractive structure function can be written as [1]

$$F_2^{\mathrm{D}(3)}(x_{I\!P}, \beta, Q^2) = \sum_{a=q,g} C_{2,a} \otimes a^{\mathrm{D}}, \tag{1}$$

where the DPDFs $a^{\mathrm{D}} = zq^{\mathrm{D}}$ or zg^{D} satisfy DGLAP evolution:

$$\frac{\partial a^{\mathrm{D}}}{\partial \ln Q^2} = \sum_{a'=q,g} P_{aa'} \otimes a'^{\mathrm{D}}, \tag{2}$$

and where $C_{2,a}$ and $P_{aa'}$ are the *same* hard-scattering coefficients and splitting functions as in inclusive DIS. The factorisation theorem (1) applies when Q is made large, therefore it is correct up to power-suppressed corrections. It says nothing about the mechanism for diffraction. What *is* the exchanged object with vacuum quantum numbers ('Pomeron') which *causes* the large rapidity gap (LRG) characterising diffractive interactions?

In a second stage [2] Regge factorisation is usually assumed, such that

$$a^{\mathrm{D}}(x_{I\!P}, z, Q^2) = f_{I\!P}(x_{I\!P})\, a^{I\!P}(z, Q^2), \tag{3}$$

where the Pomeron PDFs $a^{I\!P} = zq^{I\!P}$ or $zg^{I\!P}$. The Pomeron flux factor $f_{I\!P}$ is taken from Regge phenomenology,

$$f_{I\!P}(x_{I\!P}) = \int_{t_{\mathrm{cut}}}^{t_{\mathrm{min}}} \mathrm{d}t \quad \mathrm{e}^{B_{I\!P}\, t}\; x_{I\!P}^{1-2\alpha_{I\!P}(t)}. \tag{4}$$

Here, $\alpha_{I\!P}(t) = \alpha_{I\!P}(0) + \alpha'_{I\!P}\, t$, and the parameters $B_{I\!P}$, $\alpha_{I\!P}(0)$, and $\alpha'_{I\!P}$ should be taken from fits to soft hadron data. Although the first fits to use this approach assumed a 'soft' Pomeron, $\alpha_{I\!P}(0) \simeq 1.08$ [3], all recent fits require a substantially higher value to describe the data. In addition, a secondary Reggeon contribution is needed to describe the data for $x_{I\!P} \gtrsim 0.01$. This approach is illustrated in Fig. 1(a), where the virtualities of the t-channel partons are strongly ordered as required by DGLAP evolution. The Pomeron PDFs $a^{I\!P}$ are parameterised at some arbitrary low scale Q_0^2, then evolved up to the factorisation scale, usually taken to be the photon virtuality Q^2.

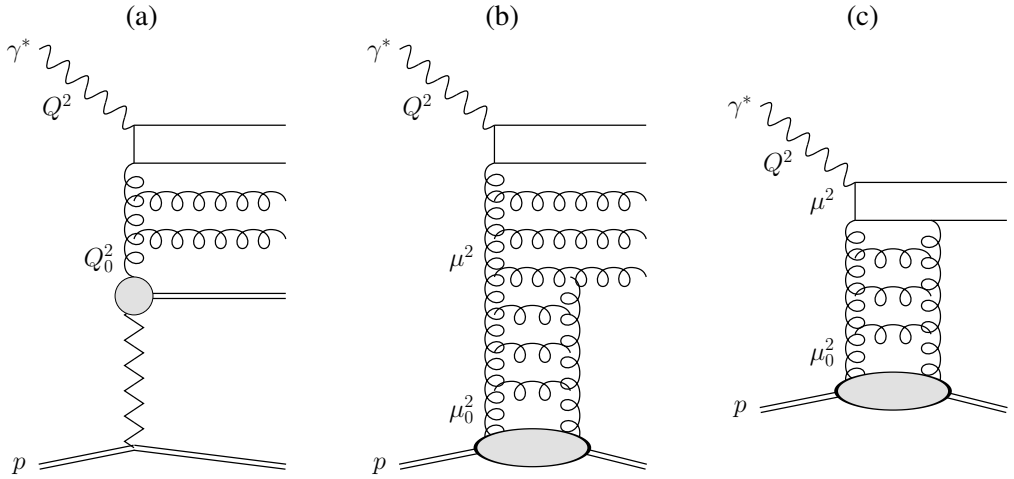

Fig. 1: (a) Resolved Pomeron contribution in the 'Regge factorisation' approach. (b) Resolved Pomeron contribution in the 'perturbative QCD' approach. (c) Direct Pomeron contribution in the 'perturbative QCD' approach.

Although this approach has been found to give a good description[1] of the DDIS data [4–7], it has little theoretical justification. The 'Regge factorisation' of (3) is merely a simple way of parameterising the $x_{I\!P}$ dependence of the DPDFs. Note, however, that the effective Pomeron intercept $\alpha_{I\!P}(0)$ has been observed to depend on Q^2 [8]. The fact that the required $\alpha_{I\!P}(0)$ is greater than the 'soft' value indicates that there is a significant perturbative QCD (pQCD) contribution to DDIS.

2 Diffractive parton distributions from perturbative QCD

In pQCD, Pomeron exchange can be described by two-gluon exchange, two gluons being the minimum number needed to reproduce the quantum numbers of the vacuum. Two-gluon exchange calculations are the basis for the colour dipole model description of DDIS, in which the photon dissociates into $q\bar{q}$ or $q\bar{q}g$ final states. Such calculations have successfully been used to describe HERA data. The crucial question, therefore, is how to reconcile two-gluon exchange with collinear factorisation as given by (1) and (2). Are these two approaches compatible?

Generalising the $q\bar{q}$ or $q\bar{q}g$ final states to an arbitrary number of parton emissions from the photon dissociation, and replacing two-gluon exchange by exchange of a parton ladder, we have diagrams like that shown in Fig. 1(b) [9–12]. Again, the virtualities of the t-channel partons are strongly ordered: $\mu_0^2 \ll \ldots \ll \mu^2 \ll \ldots \ll Q^2$. The scale μ^2 at which the Pomeron-to-parton splitting occurs can vary between $\mu_0^2 \sim 1$ GeV^2 and the factorisation scale Q^2. Therefore, to calculate the inclusive diffractive structure function, $F_2^{\mathrm{D}(3)}$, we need to integrate over μ^2:

$$F_2^{\mathrm{D}(3)}(x_{I\!P}, \beta, Q^2) = \int_{\mu_0^2}^{Q^2} \frac{\mathrm{d}\mu^2}{\mu^2}\, f_{I\!P}(x_{I\!P}; \mu^2)\, F_2^{I\!P}(\beta, Q^2; \mu^2). \tag{5}$$

Here, the perturbative Pomeron flux factor can be shown to be [12]

$$f_{I\!P}(x_{I\!P}; \mu^2) = \frac{1}{x_{I\!P} B_D} \left[R_g \frac{\alpha_S(\mu^2)}{\mu}\, x_{I\!P} g(x_{I\!P}, \mu^2) \right]^2. \tag{6}$$

The diffractive slope parameter B_D comes from the t-integration, while the factor R_g accounts for the skewedness of the proton gluon distribution [13]. There are similar contributions from sea quarks, where $g(x_{I\!P}, \mu^2)$ in (6) is replaced by $S(x_{I\!P}, \mu^2)$, together with an interference term. In the fits presented here,

[1] Note that the H1 2002 NLO fit [4] uses the 2-loop α_S with $\Lambda_{\mathrm{QCD}} = 200$ MeV for 4 flavours. This gives α_S values much smaller than the world average, meaning that the H1 2002 diffractive gluon density is artificially enhanced.

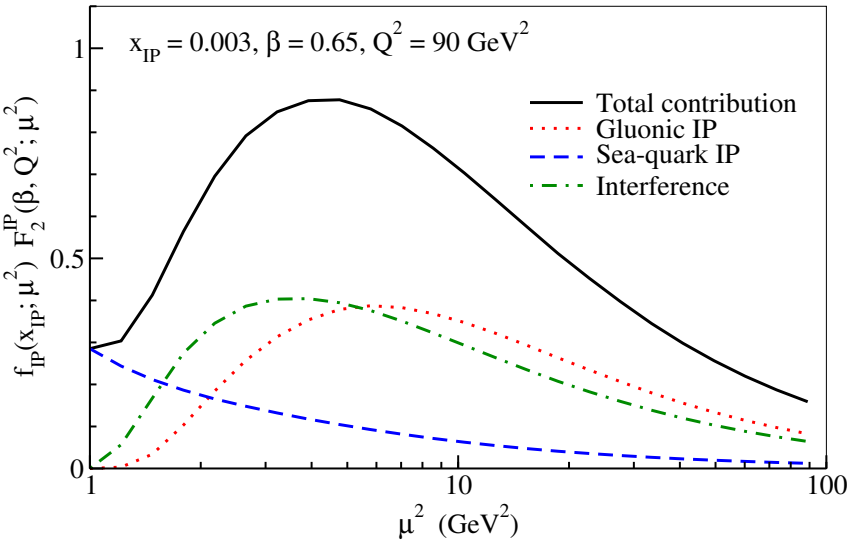

Fig. 2: Contributions to $F_2^{\mathrm{D}(3)}$ as a function of μ^2.

we use the MRST2001 NLO gluon and sea-quark distributions of the proton [14]. The Pomeron structure function in (5), $F_2^{I\!P}(\beta, Q^2; \mu^2)$, is calculated from Pomeron PDFs, $a^{I\!P}(z, Q^2; \mu^2)$, evolved using NLO DGLAP from a starting scale μ^2 up to Q^2, taking the input distributions to be LO Pomeron-to-parton splitting functions, $a^{I\!P}(z, \mu^2; \mu^2) = P_{a I\!P}(z)$ [11,12]. At first glance, it would appear that the perturbative Pomeron flux factor (6) behaves as $f_{I\!P}(x_{I\!P}; \mu^2) \sim 1/\mu^2$, so that contributions from large μ^2 are strongly suppressed. However, at large μ^2, the gluon distribution of the proton behaves as $x_{I\!P} g(x_{I\!P}, \mu^2) \sim (\mu^2)^\gamma$, where γ is the anomalous dimension. In the BFKL limit of $x_{I\!P} \to 0$, $\gamma \simeq 0.5$, so $f_{I\!P}(x_{I\!P}; \mu^2)$ would be approximately independent of μ^2. The HERA domain is in an intermediate region: γ is not small, but is less than 0.5. It is interesting to plot the integrand of (5) as a function of μ^2, as shown in Fig. 2. Notice that there is a large contribution from $\mu^2 > 3$ GeV^2, which is the value of the input scale Q_0^2 typically used in the 'Regge factorisation' fits of Sect. 1. Recall that fits using 'Regge factorisation' include contributions from $\mu^2 \leq Q_0^2$ in the input distributions, but neglect all contributions from $\mu^2 > Q_0^2$; from Fig. 2 this is clearly an unreasonable assumption.

As well as the *resolved* Pomeron contribution of Fig. 1(b), we must also account for the *direct* interaction of the Pomeron in the hard subprocess, Fig. 1(c), where there is no DGLAP evolution in the upper part of the diagram. Therefore, the diffractive structure function can be written as

$$F_2^{\mathrm{D}(3)} = \underbrace{\sum_{a=q,g} C_{2,a} \otimes a^{\mathrm{D}}}_{\text{Resolved Pomeron}} + \underbrace{C_{2,I\!P}}_{\text{Direct Pomeron}} \quad ; \tag{7}$$

cf. (1) where there is no direct Pomeron contribution. The direct Pomeron coefficient function, $C_{2,I\!P}$, calculated from Fig. 1(c), will again depend on $f_{I\!P}(x_{I\!P}; \mu^2)$ given by (6). Therefore, it is formally suppressed by a factor $1/\mu^2$, but in practice does not behave as such; see Fig. 2.

The contribution to the DPDFs from scales $\mu > \mu_0$ is

$$a^{\mathrm{D}}(x_{I\!P}, z, Q^2) = \int_{\mu_0^2}^{Q^2} \frac{\mathrm{d}\mu^2}{\mu^2} \, f_{I\!P}(x_{I\!P}; \mu^2) \, a^{I\!P}(z, Q^2; \mu^2). \tag{8}$$

Differentiating (8), we see that the evolution equations for the DPDFs are [12]

$$\frac{\partial a^{\mathrm{D}}}{\partial \ln Q^2} = \sum_{a'=q,g} P_{aa'} \otimes a'^{\mathrm{D}} + P_{a I\!P}(z) \, f_{I\!P}(x_{I\!P}; Q^2); \tag{9}$$

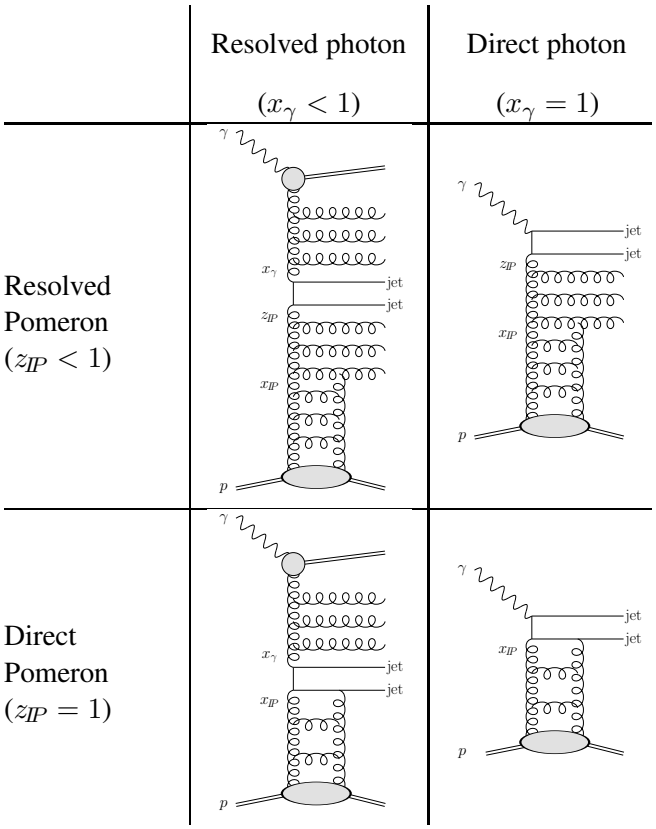

Fig. 3: The four classes of contributions to diffractive dijet photoproduction at LO. Both the photon and the Pomeron can be either 'resolved' or 'direct'.

cf. (2) where the second term of (9) is absent. That is, the DPDFs satisfy an *inhomogeneous* evolution equation [10, 12], with the extra inhomogeneous term in (9) leading to more rapid evolution than in the 'Regge factorisation' fits described in Sect. 1. Note that the inhomogeneous term will change the $x_{I\!P}$ dependence evolving upwards in Q^2, in accordance with the data, and unlike the 'Regge factorisation' assumption (3). Again, the inhomogeneous term in (9) is formally suppressed by a factor $1/Q^2$, but in practice does not behave as such; see Fig. 2.

Therefore, the diffractive structure function is analogous to the photon structure function, where there are both resolved and direct components and the photon PDFs satisfy an inhomogeneous evolution equation, where at LO the inhomogeneous term accounts for the splitting of the point-like photon into a $q\bar{q}$ pair. If we consider, for example, diffractive dijet photoproduction, there are four classes of contributions; see Fig. 3. The relative importance of each contribution will depend on the values of x_γ, the fraction of the photon's momentum carried by the parton entering the hard subprocess, and $z_{I\!P}$, the fraction of the Pomeron's momentum carried by the parton entering the hard subprocess.

3 Description of DDIS data

A NLO analysis of DDIS data is not yet possible. The direct Pomeron coefficient functions, $C_{2,I\!P}$, and Pomeron-to-parton splitting functions, $P_{aI\!P}$, need to be calculated at NLO within a given factorisation scheme (for example, $\overline{\text{MS}}$). Here, we perform a simplified analysis where the usual coefficient functions $C_{2,a}$ and splitting functions $P_{aa'}$ $(a, a' = q, g)$ are taken at NLO, but $C_{2,I\!P}$ and $P_{aI\!P}$ are taken at LO [12]. We work in the fixed flavour number scheme, where there is no charm DPDF. Charm quarks are produced via $\gamma^* g^{I\!P} \to c\bar{c}$ at NLO [15] and $\gamma^* I\!P \to c\bar{c}$ at LO [16]. For light quarks, we include the direct Pomeron process $\gamma_L^* I\!P \to q\bar{q}$ at LO [12], which is higher-twist and known to be important at large β.

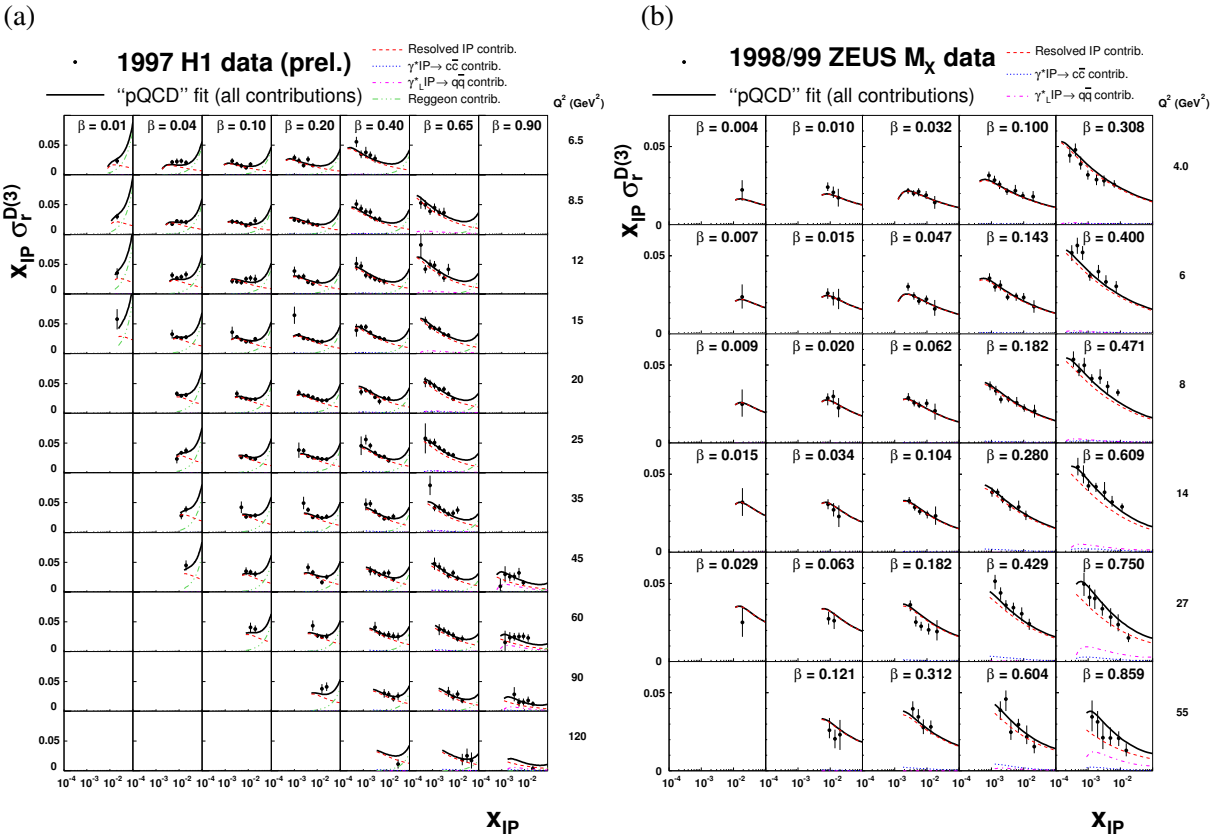

Fig. 4: "pQCD" fits to (a) H1 LRG and (b) ZEUS M_X data.

To see the effect of the direct Pomeron contribution and the inhomogeneous evolution, we make two types of fits:

"Regge" : The 'Regge factorisation' approach discussed in Sect. 1, where there is no direct Pomeron contribution and no inhomogeneous term in the evolution equation.

"pQCD" : The 'perturbative QCD' approach discussed in Sect. 2, where these effects are included.

We make separate fits to the recent H1 LRG (prel.) [4] and ZEUS M_X [8] $\sigma_r^{\mathrm{D}(3)}$ data, applying cuts $Q^2 \geq 3$ GeV^2 and $M_X \geq 2$ GeV, and allowing for overall normalisation factors of 1.10 and 1.43 to account for proton dissociation up to masses of 1.6 GeV and 2.3 GeV respectively. Statistical and systematic experimental errors are added in quadrature. The strong coupling is set via $\alpha_S(M_Z) = 0.1190$. We take the input forms of the DPDFs at a scale $Q_0^2 = 3$ GeV^2 to be

$$z\Sigma^{\mathrm{D}}(x_{I\!P}, z, Q_0^2) = f_{I\!P}(x_{I\!P})\, C_q\, z^{A_q}(1-z)^{B_q}, \tag{10}$$

$$zg^{\mathrm{D}}(x_{I\!P}, z, Q_0^2) = f_{I\!P}(x_{I\!P})\, C_g\, z^{A_g}(1-z)^{B_g}, \tag{11}$$

where $f_{I\!P}(x_{I\!P})$ is given by (4), and where $\alpha_{I\!P}(0)$, C_a, A_a, and B_a ($a = q, g$) are free parameters. The secondary Reggeon contribution to the H1 data is treated in a similar way as in the H1 2002 fit [4], using the GRV pionic parton distributions [17]. Good fits are obtained in all cases, with $\chi^2/\mathrm{d.o.f.} = 0.75$, 0.71, 0.76, and 0.84 for the "Regge" fit to H1 data, "pQCD" fit to H1 data, "Regge" fit to ZEUS M_X data, and "pQCD" fit to ZEUS M_X data respectively. The "pQCD" fits are shown in Fig. 4, including a breakdown of the different contributions. The DPDFs are shown in Fig. 5. Note that the "pQCD" DPDFs are smaller than the corresponding "Regge" DPDFs at large z due to the inclusion of the higher-twist $\gamma_L^* I\!P \to q\bar{q}$ contribution. Also note that the "pQCD" DPDFs have slightly more rapid evolution than the "Regge" DPDFs due to the extra inhomogeneous term in the evolution equation (9). There is a

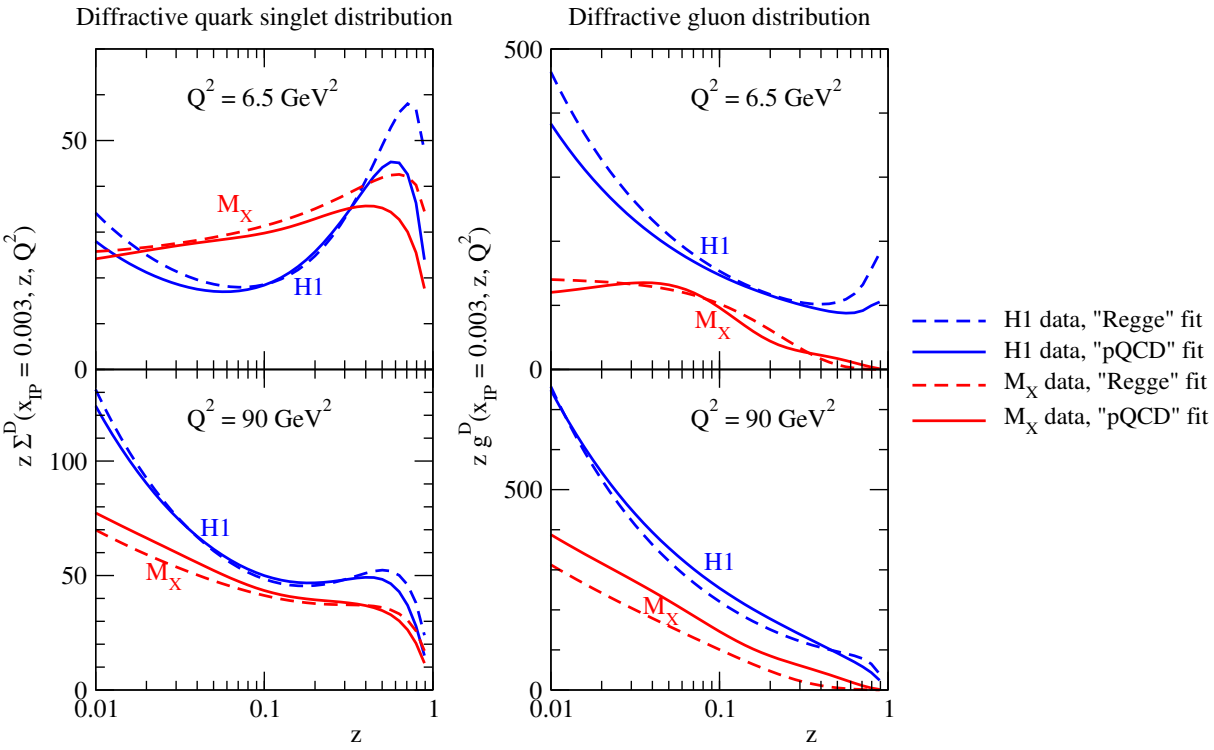

Fig. 5: DPDFs obtained from separate fits to H1 LRG and ZEUS M_X data using the "Regge" and "pQCD" approaches.

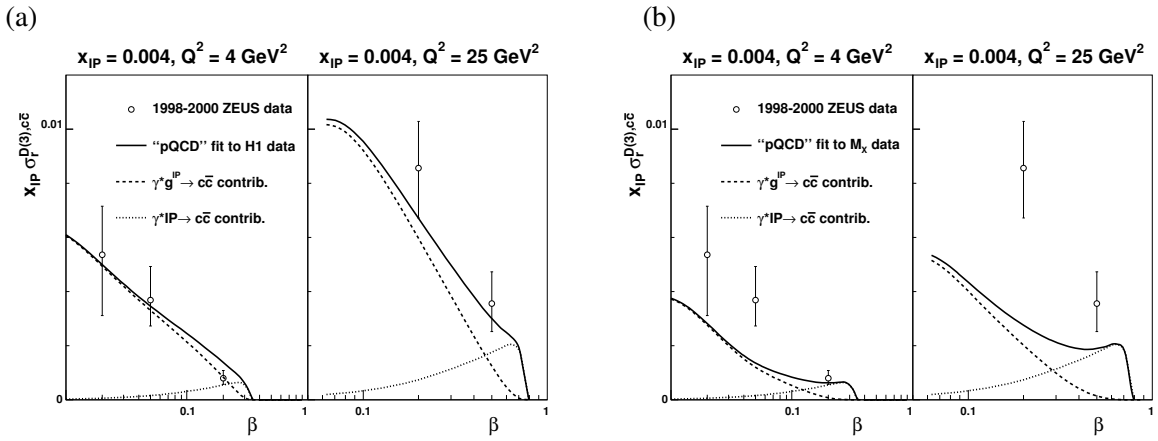

Fig. 6: Predictions for ZEUS LRG diffractive charm production data using DPDFs from the "pQCD" fits to (a) H1 LRG and (b) ZEUS M_X data. Note the large direct Pomeron ($\gamma^* IP \to c\bar{c}$) contribution at moderate β.

large difference between the DPDFs obtained from the H1 LRG and ZEUS M_X data due to the different Q^2 dependence of these data sets; see also [6, 7].

The predictions from the two "pQCD" fits for the charm contribution to the diffractive structure function as measured by ZEUS using the LRG method [18] are shown in Fig. 6. Our H1 LRG fit gives a good description, while our ZEUS M_X fit is too small at low β. Note that the direct Pomeron contribution is significant at moderate β. These charm data points were included in the determination of DPDFs from ZEUS LPS data [5], but only the resolved Pomeron ($\gamma^* g^{IP} \to c\bar{c}$) contribution was included and not the direct Pomeron ($\gamma^* IP \to c\bar{c}$) contribution. Therefore, the diffractive gluon distribution from the ZEUS LPS fit [5] needed to be artificially large to fit the charm data at moderate β.

4 Conclusions and outlook

To summarise, diffractive DIS is more complicated than inclusive DIS. Collinear factorisation holds, but we need to account for the direct Pomeron coupling, leading to an inhomogeneous evolution equation (9). Therefore, the treatment of DPDFs has more in common with photon PDFs than with proton PDFs. The H1 LRG and ZEUS M_X data seem to have a different Q^2 dependence, leading to different DPDFs. This issue needs further attention.[2] For a NLO analysis of DDIS data, the direct Pomeron coefficient functions, $C_{2,I\!P}$, and Pomeron-to-parton splitting functions, $P_{a I\!P}$, need to be calculated at NLO. There are indications [16] that there are large π^2-enhanced virtual loop corrections ('K-factors') similar to those found in the Drell–Yan process. As with all PDF determinations, the sensitivity to the form of the input parameterisation, (10) and (11), and input scale Q_0^2 needs to be studied.[3] The inclusion of jet and heavy quark DDIS data, and possibly $F_L^{\mathrm{D}(3)}$ if it is measured [19], would help to constrain the DPDFs further. The extraction of DPDFs from HERA data will provide an important input for calculations of diffraction at the LHC.

References

[1] J. C. Collins, Phys. Rev. **D57**, 3051 (1998).
[2] G. Ingelman and P. E. Schlein, Phys. Lett. **B152**, 256 (1985).
[3] A. Donnachie and P. V. Landshoff, Phys. Lett. **B296**, 227 (1992).
[4] H1 Collaboration, paper 089 submitted to EPS 2003, Aachen.
[5] S. Chekanov *et al.* [ZEUS Collaboration], Eur. Phys. J. **C38**, 43 (2004).
[6] P. Newman and F.-P. Schilling, these proceedings.
[7] M. Groys, A. Levy and A. Proskuryakov, these proceedings.
[8] S. Chekanov *et al.* [ZEUS Collaboration], Nucl. Phys. **B713**, 3 (2005).
[9] M. G. Ryskin, Sov. J. Nucl. Phys. **52**, 529 (1990).
[10] E. Levin and M. Wusthoff, Phys. Rev. **D50**, 4306 (1994).
[11] A. D. Martin, M. G. Ryskin and G. Watt, Eur. Phys. J. **C37**, 285 (2004).
[12] A. D. Martin, M. G. Ryskin and G. Watt, Eur. Phys. J. **C44**, 69 (2005).
[13] A. G. Shuvaev, K. J. Golec-Biernat, A. D. Martin and M. G. Ryskin, Phys. Rev. **D60**, 014015 (1999).
[14] A. D. Martin, R. G. Roberts, W. J. Stirling and R. S. Thorne, Eur. Phys. J. **C23**, 73 (2002).
[15] S. Riemersma, J. Smith and W. L. van Neerven, Phys. Lett. **B347**, 143 (1995).
[16] E. M. Levin, A. D. Martin, M. G. Ryskin and T. Teubner, Z. Phys. **C74**, 671 (1997).
[17] M. Gluck, E. Reya and A. Vogt, Z. Phys. **C53**, 651 (1992).
[18] S. Chekanov *et al.* [ZEUS Collaboration], Nucl. Phys. **B672**, 3 (2003).
[19] P. Newman, these proceedings.

[2] In particular, the main assumption of the M_X method, that the diffractive contribution to the $\ln M_X^2$ distribution is constant, while the non-diffractive contribution rises exponentially, is motivated by Regge theory in the limit that $t = 0$, $\alpha_{I\!P}(0) \equiv 1$, and $Q^2 \ll M_X^2$, and it is not clear that this should be true in general.

[3] The ZEUS LPS fit [5], where the data have large statistical uncertainties, found that the shape of the DPDFs had a significant dependence on the functional form of the initial parameterisation. Even for the other data sets, where the statistical uncertainties are smaller, there seems to be a fairly strong dependence on the value of the input scale Q_0^2.

DPDF: A Library for Diffractive Parton Distributions

Frank-Peter Schilling
CERN/PH, CH-1211 Geneva 23, Switzerland

Abstract
A code library is presented which provides a common interface to available parameterizations of diffractive parton distribution functions determined from QCD fits to HERA diffractive structure function data.

1 Introduction

In recent years, various precise measurements of the diffractive reduced cross section[1] $\sigma_r^{D(3)}(x_{I\!P}, \beta, Q^2)$ have been made by the HERA experiments H1 and ZEUS. Within the framework of QCD factorization in diffractive DIS [1], several sets of *diffractive parton distributions* (dpdf's) have been obtained from leading or next-to-leading order DGLAP QCD fits to these data[2]. The extracted dpdf's are a crucial input for the calculations of the cross sections of less inclusive diffractive processes such as diffractive jet, heavy quark or even Higgs production.

Since these diffractive pdf's are used in many different Monte-Carlo generators as well as in fixed order QCD calculations, it is desirable to provide them through a common software interface, similar in spirit to the common PDFLIB [2] and LHAPDF [3] packages for non-diffractive pdf's. To achieve this, the DPDF library has been developed. When a new dpdf set becomes available, it then needs to be implemented only in one place. Furthermore, additional features such as custom QCD evolution, structure function calculation and error information are available. Thus, the DPDF library provides a useful way to make the knowledge from HERA available to the TEVATRON, LHC and theory communities.

2 Theoretical Framework

The concept of QCD factorization in diffractive DIS implies that the diffractive $\gamma^* p$ cross section can be expressed as a convolution of universal diffractive parton distributions f_i^D with process-dependent coefficient functions:

$$\frac{\mathrm{d}^2\sigma(x, Q^2, x_{I\!P}, t)^{\gamma^* p \to p' X}}{\mathrm{d}x_{I\!P}\,\mathrm{d}t} = \sum_i \int_x^{x_{I\!P}} \mathrm{d}\xi\, \hat{\sigma}^{\gamma^* i}(x, Q^2, \xi)\, f_i^D(x_{I\!P}, t, \xi, Q^2)\,. \tag{1}$$

The diffractive pdf's $f_i^D(x_{I\!P}, t, \beta, Q^2)$ can be extracted from a DGLAP QCD analysis of the diffractive reduced cross section σ_r^D.

For many (but not all) of the included parameterizations the $(x_{I\!P}, t)$ dependence factorizes ("Regge factorization") so that a *flux factor* $f_{I\!P/p}(x_{I\!P}, t)$ and dpdf's $f_i^{I\!P}(\beta, Q^2)$ are defined separately:

$$f_i^D(x_{I\!P}, t, \beta, Q^2) = f_{I\!P/p}(x_{I\!P}, t) \cdot f_i^{I\!P}(\beta, Q^2)\,. \tag{2}$$

For those parameterizations which include a secondary Reggeon exchange contribution (often using a pion structure function) in order to describe the data at high $x_{I\!P}$, such a possibility is also included. The dpdf's are typically parameterized in terms of a light quark flavor singlet and a gluon distribution, which are evolved using the (N)LO DGLAP equations[3].

[1] The reduced cross section σ_r^D corresponds to the structure function F_2^D if contributions from F_L^D and xF_3^D are neglected.
[2] In some cases, final state data were used in addition in order to better constrain the diffractive gluon density.
[3] For details of the parameterizations, see the original publications.

Table 1: Overview of the diffractive pdf sets implemented in the DPDF package. The Q^2, β and $x_{I\!P}$ ranges correspond to the approximate kinematic range of the data used in the fit.

Set	Fit	Var	Name	Ref.	Order	Q^2 (GeV^2)	β	$x_{I\!P}$
1	4	–	H1-1997-LO-Fit-1	H1 Coll. [5]	LO	4.5..75	0.04..0.9	< 0.05
1	5	–	H1-1997-LO-Fit-2		LO			
1	6	–	H1-1997-LO-Fit-3		LO			
2	1	–	H1-2002-NLO	H1 Coll. (prel.) [6]	NLO	6.5..800	0.01..0.9	< 0.05
2	2	–	H1-2002-LO		LO			
3	1	1..3	ACTW-NLO-A	Alvero et al. [7]	NLO	6.0..75	0.20..0.7	< 0.01
3	2	1..3	ACTW-NLO-B		NLO			
3	3	1..3	ACTW-NLO-C		NLO			
3	4	1..3	ACTW-NLO-D		NLO			
3	5	1..3	ACTW-NLO-SG		NLO			
4	–	–	BGH-LO	Buchmueller et al. [8]	LO	4.5..75	0.04..0.9	< 0.01
5	–	–	HS-NLO	Hautmann and Soper [9]	NLO			
6	–	–	ZEUS-LPS	ZEUS Coll. [11, 12]	NLO	2.4..39	0.01..0.5	< 0.01
7	1	–	MRW-NLO-Lambda	Martin et al. [10]	NLO	2.4..90	0.01..0.9	< 0.05
7	2	–	MRW-NLO-MRST		NLO			
8	–	–	ZEUS-MX	Groys et al. [13]	NLO	4.0..55	0.01..0.9	< 0.01

3 Implementation

DPDF is a FORTRAN 77 package. A C++ wrapper will be provided. There is an external dependency on the QCDNUM [4] package, which can be disabled.

3.1 Available Parameterizations

Currently the following dpdf sets are implemented: the fits performed by the H1 collaboration in [5], the preliminary H1 fits presented in [6], the fits by Alvero et al. [7], a parameterization of the semi-classical model by Buchmueller et al. [8], the fits by Hautmann and Soper [9] and by Martin et al. [10], the ZEUS fit from [11, 12] and a fit to recent ZEUS data presented at this workshop [12, 13].

Details of the available dpdf sets are presented in table 1, including the kinematic ranges of the data which were included in the fits. This information can be used as a guideline for the range of validity of the fits. Note in particular that typically only data for $x_{I\!P} < 0.05$ or < 0.01 are included in the fits, which introduces an additional uncertainty when these fits are used for comparisons with experimental data at higher $x_{I\!P}$.

3.2 Interface to QCDNUM

DPDF provides an interface to the NLO DGLAP QCD evolution package QCDNUM [4]. It is possible to perform a QCD evolution of the given pdf set from its starting scale Q_0^2 using either the original evolution scheme and parameters, or by providing modified parameters. The benefits are:

- QCDNUM calculates the full (N)LO structure functions F_2 and F_L for light and heavy quarks, which can be used for consistent comparisons with experimental data;
- The QCD evolution parameters such as α_s can be varied for systematic studies;

– The dpdf's can be evolved to Q^2 or β values beyond the grid on which the original parameterization is provided, which is particularly interesting for LHC applications.

3.3 Usage

The DPDF package can be obtained from [14]. In the following the principal user subroutines of the library are listed.

– The package is initialized for a given dpdf by calling `dpdf_init(iset,ifit,ivar)` where `iset`, `ifit` and `ivar` are the parameters as given in table 1.
– The diffractive proton pdf's for either Pomeron or sub-leading Reggeon exchange or their sum (if provided) are returned at given values of $(x_{I\!P}, t, \beta, Q^2)$ in an array `xpq(-6:6)` using `dpdf_ppdf`. The result may also be integrated over t.
– If provided, the flux factors $f_{I\!P}(x_{I\!P}, t)$ and the parton densities $f_i(\beta, Q^2)$ can be obtained separately from `dpdf_flux` and `dpdf_pdf`.
– The diffractive structure function can be obtained from `dpdf_f2d`.
– QCD evolution using QCDNUM can be performed using default parameters for the given set with `dpdf_evolve_std` and using modified evolution parameters with `dpdf_evolve`.

Note that the details of the user interface may change in the future. For details refer to the user manual available from [14].

4 Outlook

It is planned to update DPDF if new dpdf sets become available. Additional features such as the possibility of error dpdf's (as for LHAPDF) are foreseen. The code and manual are available from [14].

References

[1] J.C. Collins, Phys. Rev. **D57**, 3051 (1998).
[2] H. Plothow-Besch, Comput. Phys. Commun. **75**, 396 (1993).
[3] S. Alekhin, W. Giele and J. Pumplin, *The lhapdf interface*, in *The QCD/SM working group: Summary report, Physics at TeV Colliders II Workshop, Les Houches, France*. 2002. `http://durpdg.dur.ac.uk/lhapdf`.
[4] M. Botje, *QCDNUM version 16.12*. ZEUS-97-066. `http://www.nikhef.nl/~h24/qcdnum`.
[5] C. Adloff et al. [H1 Collaboration], Z. Phys. **C76**, 613 (1997).
[6] H1 Collaboration, *Measurement and NLO DGLAP QCD Interpretation of Diffractive Deep-Inelastic Scattering at HERA*. Paper 980 contributed to ICHEP 2002, Amsterdam.
[7] L. Alvero, J.C. Collins, J. Terron and J.J. Whitmore, Phys. Rev. **D59**, 074022 (1999).
[8] W. Buchmuller, T. Gehrmann and A. Hebecker, Nucl. Phys. **B537**, 477 (1999).
[9] F. Hautmann and D.E. Soper, Phys. Rev. **D63**, 011501 (2000).
[10] A.D. Martin, M.G. Ryskin and G. Watt, Eur. Phys. J. **C37**, 285 (2004).
[11] S. Chekanov et al. [ZEUS Collaboration], Eur. Phys. J. **C38**, 43 (2004).
[12] A. Proskuryakov. Private communucation.
[13] M. Groys, A. Levy and A. Proskuryakov, *Diffractive Parton Distributions from the HERA Data*. These proceedings.
[14] F.-P. Schilling, *DPDF web page*. `http://fpschill.home.cern.ch/fpschill/dpdf`.

Prospects for F_L^D Measurements at HERA-II

Paul Newman
School of Physics and Astronomy, University of Birmingham, B15 2TT, United Kingdom

Abstract
The theoretical interest in the longitudinal diffractive structure function F_L^D is briefly motivated and possible measurement methods are surveyed. A simulation based on realistic scenarios with a reduced proton beam energy at HERA-II using the H1 apparatus shows that measurements are possible with up to 4σ significance, limited by systematic errors.

1 Introduction

In order to understand inclusive diffraction fully, it is necessary to separate out the contributions from transversely and longitudinally polarised exchange photons. Here, the formalism of [1] is adopted, where by analogy with inclusive scattering and neglecting weak interactions, a reduced cross section σ_r^D is defined,[1] related to the experimentally measured cross section by

$$\frac{d^3\sigma^{ep\to eXY}}{\mathrm{d}x_{I\!P}\,\mathrm{d}\beta\,\mathrm{d}Q^2} = \frac{2\pi\alpha^2}{\beta\,Q^4}\cdot Y_+\cdot\sigma_r^D(x_{I\!P},\beta,Q^2)\,, \quad \text{where} \quad \sigma_r^D = F_2^D - \frac{y^2}{Y_+}F_L^D \tag{1}$$

and $Y_+ = 1+(1-y)^2$. The structure function F_L^D, is closely related to the longitudinal photon contribution, whereas the more familiar F_2^D contains information on the sum of transverse and longitudinal photon contributions.

It is generally understood [2] that at high β and low-to-moderate Q^2, σ_r^D receives a significant, perhaps dominant, higher twist contribution due to longitudinally polarised photons. Definite predictions [3] exist for this contribution, obtained by assuming 2-gluon exchange, with a similar phenomenology to that successfully applied to vector meson cross sections at HERA. The dominant role played by gluons in the diffractive parton densities [1] implies that the leading twist F_L^D must also be relatively large. Assuming the validity of QCD hard scattering collinear factorisation [4], this gluon dominance results in a leading twist F_L^D which is approximately proportional to the diffractive gluon density. A measurement of F_L^D to even modest precision would provide a very powerful independent tool to verify our understanding of the underlying dynamics and to test the gluon density extracted indirectly in QCD fits from the scaling violations of F_2^D. This is particularly important at the lowest x values, where direct information on the gluon density cannot be obtained from jet or D^* data due to kinematic limitations and where novel effects such as parton saturation or non-DGLAP dynamics are most likely to become important.

Several different methods have been proposed to extract information on F_L^D. It is possible in principle to follow the procedure adopted by H1 in the inclusive case [5, 6], exploiting the decrease in σ_r^D at large y relative to expectations for F_2^D alone (see equation 1). This method may yield significant results if sufficient precision and y range can be achieved [7], though assumptions are required on the $x_{I\!P}$ dependence of F_2^D, which is currently not well constrained by theory. An alternative method, exploiting the azimuthal decorrelation between the proton and electron scattering planes caused by interference between the transverse and longitudinal photon contributions [8], has already been used with the scattered proton measured in the ZEUS LPS [9]. However, due to the relatively poor statistical precision achievable with Roman pots at HERA-I, the current results are consistent with zero. If the potential of the H1 VFPS is fully realised, this method may yet yield significant results in the HERA-II data [10]. However, if

[1] It is assumed here that all results are integrated over t. The superscript (3) usually included for $F_2^{D(3)}$ and other quantities is dropped for convenience.

the necessary data are taken, the most promising possibility is to extract F_L^D by comparing data at the same Q^2, β and $x_{I\!P}$, but from different centre of mass energies $\sqrt{s}$ and hence from different y values. The longitudinal structure function can then be extracted directly and model-independently from the measured data using equation 1. In this contribution, one possible scenario is investigated, based on modified beam energies and luminosities which are currently under discussion as a possible part of the HERA-II programme.

2 Simulated F_L^D Measurement

Given the need to obtain a large integrated luminosity at the highest possible beam energy for the remainder of the HERA programme and the fixed end-point in mid 2007, it is likely that only a relatively small amount of data can be taken with reduced beam energies. A possible scenario is investigated here in which 10 pb^{-1} are taken at just one reduced proton beam energy of $E_p = 400$ GeV, the electron beam energy being unchanged at 27.5 GeV. Since the maximum achievable instantaneous luminosity at HERA scales like the proton beam energy squared [11], this data sample could be obtained in around 2-3 months at the current level of HERA performance. It is assumed that a larger data volume of 100 pb^{-1} is available at $E_p = 920$ GeV, which allows for downscaling of high rate low Q^2 inclusive triggers.[2] The results presented here can be used to infer those from other scenarios given that the statistical uncertainty scales like $\sigma_r^{D\,400}/\sqrt{\mathcal{L}_{400}} + \sigma_r^{D\,920}/\sqrt{\mathcal{L}_{920}}$, where $\sigma_r^{D\,E_p}$ and $\mathcal{L}_{E_p}$ are the reduced cross section and the luminosity at a proton beam energy of E_p, respectively.

The longitudinal structure function can be extracted from the data at the two beam energies using

$$F_L^D = \frac{Y_+^{400}\, Y_+^{920}}{y_{400}^2 Y_+^{920} - y_{920}^2 Y_+^{400}} \left(\sigma_r^{D\,920} - \sigma_r^{D\,400}\right) , \tag{2}$$

where y_{E_p} and $Y_+^{E_p}$ denote y and Y_+ at a beam energy E_p. It is clear from equation 2 that the best sensitivity to F_L^D requires the maximum difference between the reduced cross sections at the two beam energies, which (equation 1) implies the maximum possible y at $E_p = 400$ GeV. By measuring scattered electrons with energies E_e' as low as 3 GeV [5], the H1 collaboration has obtained data at $y = 0.9$. This is possible with the use of the SPACAL calorimeter in combination with a measurement of the electron track in either the backward silicon tracker (BST) or the central jet chamber (CJC). For HERA-II running, the corresponding available range of scattered electron polar angle is $155^\circ < \theta_e' < 173^\circ$, which is used in the current study.[3] Three intervals in y are considered, corresponding at $E_p = 400$ GeV to $0.5 < y_{400} < 0.7$, $0.7 < y_{400} < 0.8$ and $0.8 < y_{400} < 0.9$. It is ensured that identical ranges in β, $x_{I\!P}$ and Q^2 are studied at $E_p = 920$ GeV by choosing the bin edges such that $y_{920} = y_{400} \cdot 400/920$. Since the highest possible precision is required in this measurement, the restriction $x_{I\!P} < 0.02$ is imposed, which leads to negligible acceptance losses with a typical cut on the forwardmost extent of the diffractive system $\eta_{\max} < 3.3$. The kinematic restrictions on E_e', θ_e' and $x_{I\!P}$ lead to almost no change in the mean Q^2, M_{X}^2 or $\beta \simeq Q^2/(Q^2 + M_{\mathrm{X}}^2)$ as either y or E_p are varied. In contrast, $x_{I\!P} = Q^2/(s\,y\,\beta)$ varies approximately as $1/y$. As is shown in Fig. 1, at the average $\beta = 0.23$, there is at least partial acceptance for all y bins in the range $7 < Q^2 < 30$ GeV^2, which is chosen for this study, leading to an average value of Q^2 close to 12 GeV^2.

The simulation is performed using the RAPGAP [13] Monte Carlo generator to extract the number of events per unit luminosity in each bin at each centre of mass energy. The values of F_2^D and F_L^D, and hence $\sigma_r^{D\,920}$ and $\sigma_r^{D\,400}$ are obtained using an updated version of the preliminary H1 2002 NLO QCD fit [1].

[2] Alternative scenarios in which a smaller data volume at large E_p is taken in a short, dedicated run, could potentially lead to better controlled systematics at the expense of increased statistical errors.

[3] One interesting alternative running scenario [12] is to obtain data at $E_p = 920$ GeV with the vertex shifted by 20 cm in the outgoing proton direction, which would allow measurements up to $\theta_e' = 175^\circ$, giving a low Q^2 acceptance range which closely matches that for the $E_p = 400$ GeV data at the normal vertex position.

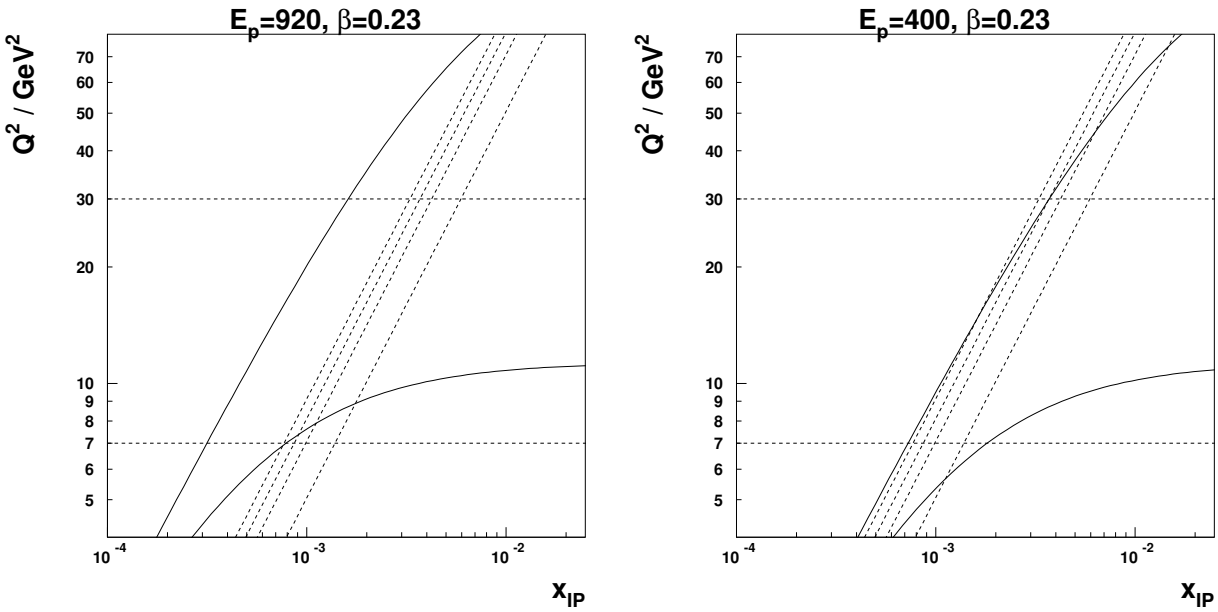

Fig. 1: Illustration of the kinematic plane in Q^2 and $x_{I\!P}$ at proton energies of 920 GeV and 400 GeV, with fixed $\beta = x/x_{I\!P} = 0.23$. The solid lines illustrate the experimental limits of $155^\circ < \theta'_e < 173^\circ$. The horizontal dashed lines illustrate the Q^2 range used for the simulation. The diagonal dashed lines illustrate the binning in y, corresponding at $E_p = 400$ GeV to $y = 0.9$ (leftmost line), $y = 0.8$, $y = 0.7$ and $y = 0.5$ (rightmost line).

The expected precision on F_L^D is obtained by error propagation through equation 2. The systematic uncertainties are estimated on the basis of previous experience with the H1 detector [1, 5]. At the large y values involved, the kinematic variables are most accurately reconstructed using the electron energy and angle alone. The systematic uncertainties on the measurements of these quantities are assumed to be correlated between the two beam energies. With the use of the BST and CJC, the possible bias in the measurement of θ'_e is at the level of 0.2 mrad. The energy scale of the SPACAL calorimeter is known with a precision varying linearly from 2% at $E'_e = 3$ GeV to 0.2% at $E'_e = 27.5$ GeV. Other uncertainties which are correlated between the two beam energies arise from the photoproduction background subtraction (important at large y and assumed to be known with a precision of 25%) and the energy scale for the hadronic final state used in the reconstruction of $M_{\rm X}$ and hence $x_{I\!P}$ (taken to be known to 4%, as currently). Sources of uncertainty which are assumed to be uncorrelated between the low and high E_p measurements are the luminosity measurement (taken to be $\pm 1\%$), the trigger and electron track efficiencies ($\pm 1\%$ combined) and the acceptance corrections, obtained using RAPGAP ($\pm 2\%$). The combined uncorrelated error is thus 2.4%. Finally, a normalisation uncertainty of $\pm 6\%$ due to corrections for proton dissociation contributions is taken to act simultaneously in the two measurements. Other sources of uncertainty currently considered in H1 measurements of diffraction are negligible in the kinematic region studied here.

Full details of the simulated uncertainties on the F_L^D measurements are given in Table 1. An illustration of the corresponding expected measurement, based on the F_L^D from the H1 2002 fit is shown in Fig. 2. The most precise measurement is obtained at the highest y, where F_L^D would be determined to be unambiguously different from its maximum value of F_2^D and to be non-zero at the 4σ level. Two further measurements are obtained at lower y values. The dominant errors arise from statistical uncertainties and from uncertainties which are uncorrelated between the two beam energies. Minimising the latter is a major experimental challenge to be addressed in the coming years.

Table 1: Summary of the simulation at $Q^2 = 12$ GeV and $\beta = 0.23$. The first three columns contain the y ranges used at $E_p = 400$ GeV and $E_p = 920$ GeV and the $x_{I\!P}$ values. The next two columns contain the values of the diffractive structure functions. These are followed by the uncorrelated ($\delta_{\rm unc}$) and proton dissociation ($\delta_{\rm norm}$) uncertainties and the correlated systematics due to the electron energy ($\delta E'_e$) and angle ($\delta\theta'_e$) measurements, the hadronic energy scale ($\delta M_{\rm X}$) and the photoproduction background ($\delta\gamma p$), all in percent. The last three columns summarise the systematic, statistical and total uncertainties.

y_{400}	y_{920}	$x_{I\!P}$	F_2^D	F_L^D	$\delta_{\rm unc}$	$\delta_{\rm norm}$	$\delta E'_e$	$\delta\theta'_e$	$\delta M_{\rm X}$	$\delta\gamma p$	$\delta_{\rm syst}$	$\delta_{\rm stat}$	$\delta_{\rm tot}$
0.5 – 0.7	0.217 – 0.304	0.0020	15.72	3.94	34	6	8	2	7	0	36	20	41
0.7 – 0.8	0.304 – 0.348	0.0016	20.87	5.25	19	6	3	2	5	6	22	17	28
0.8 – 0.9	0.348 – 0.391	0.0014	24.47	6.16	14	6	6	1	2	13	21	13	25

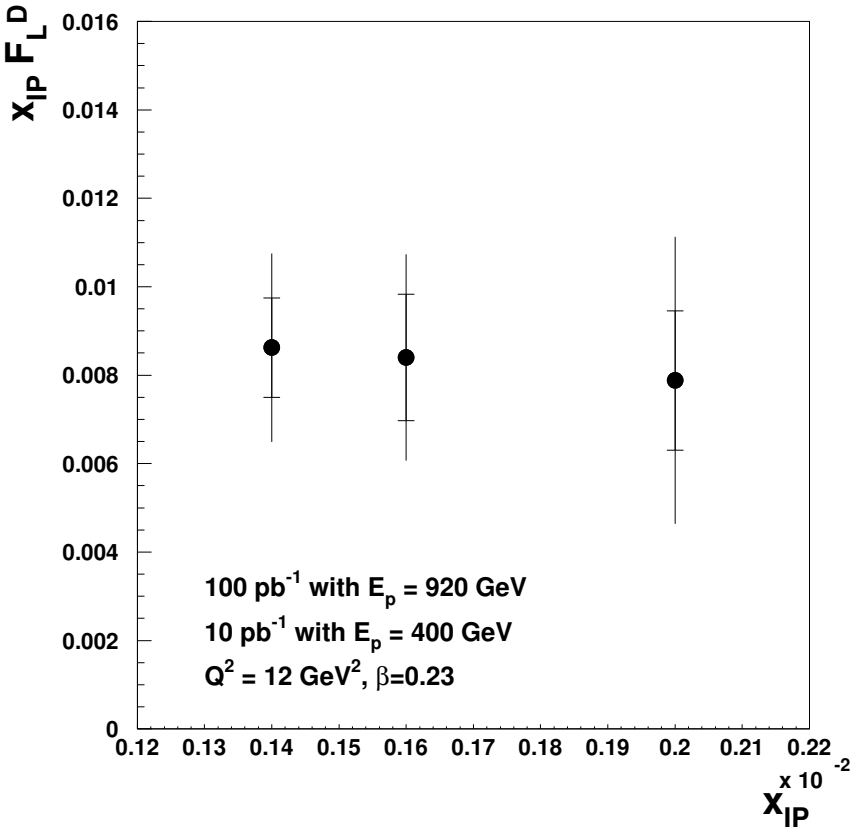

Fig. 2: Illustration of the simulated result for F_L^D, showing the three data points with statistical (inner bars) and total (outer bars) errors.

Only one possible scenario has been investigated here, leading to a highly encouraging result at relatively low β, which would provide a very good test of the leading twist F_L^D and thus of the gluon density extracted in QCD fits to F_2^D. It may also be possible to obtain results at high β, giving information on the higher twist contributions in that region, for example by restricting the analysis to lower $x_{I\!P}$.

Acknowledgements

For comments, corrections, cross-checks and code, thanks to Markus Diehl, Joel Feltesse, Max Klein and Frank-Peter Schilling!

References

[1] H1 Collaboration, paper 980 contributed to ICHEP 2002, Amsterdam (H1prelim-02-012).

[2] J. Bartels, J. Ellis, H. Kowalski, M. Wusthoff, Eur. Phys. J. **C7**, 443 (1999).

[3] A. Hebecker, T. Teubner, Phys. Lett. **B498**, 16 (2001).

[4] J. Collins, Phys. Rev. **D57**, 3051 (1998). Erratum ibid **D61** (2000) 019902.

[5] C. Adloff et al. [H1 Collaboration], Eur. Phys. J. **C21**, 33 (2001).

[6] H1 Collaboration, paper 4-083 contributed to EPS 2003, Aachen (H1prelim-03-043).

[7] A. Mehta, J. Phillips, B. Waugh, proceedings of the workshop 'Future Physics at HERA', DESY, 1996, ed. Ingelman, de Roeck, Klanner, pg 704.

[8] M. Diehl, proceedings of the XIth International Conference on Elastic and Diffractive Scattering, Blois, France, 2005 [hep-ph/0509107].

[9] S. Chekanov et al. [ZEUS Collaboration], Eur. Phys. J. **C38**, 43 (2004).

[10] L. Favart et al., 'Proposal for Installation of a Very Forward Proton Spectrometer in H1 after 2000', DESY-PRC 01/00.

[11] F. Willeke, 'Issues for HERA Future Operation', talk at the Workshop on the Future of Lepton-Nucleon Scattering, Durham, UK, 2001.

[12] M. Klein. Proceedings of the 12th International Workshop on Deep Inelastic Scattering (DIS 2004), Strbske Pleso, Slovakia, 2004.

[13] H. Jung, Comp. Phys. Commun. **86**, 147 (1995). See also http://www.desy.de/ jung/rapgap.html.

Diffractive Dijet Production at HERA

A. Bruni[1]*, M. Klasen*[2,3]*, G. Kramer*[3] *and S. Schätzel*[4]
[1] INFN Bologna, Via Irnerio 46, 40156 Bologna, Italy
[2] Laboratoire de Physique Subatomique et de Cosmologie, Université Joseph Fourier/CNRS-IN2P3, 53 Avenue des Martyrs, 38026 Grenoble, France
[3] II. Inst. für Theoret. Physik, Universität Hamburg, Luruper Chaussee 149, 22761 Hamburg, Germany
[4] DESY FLC, Notkestr. 85, 22607 Hamburg, Germany

Abstract
We present recent experimental data from the H1 and ZEUS Collaborations at HERA for diffractive dijet production in deep-inelastic scattering (DIS) and photoproduction and compare them with next-to-leading order (NLO) QCD predictions using diffractive parton densities. While good agreement is found for DIS, the dijet photoproduction data are overestimated by the NLO theory, showing that factorization breaking occurs at this order. While this is expected theoretically for resolved photoproduction, the fact that the data are better described by a global suppression of direct *and* resolved contribution by about a factor of two comes as a surprise. We therefore discuss in some detail the factorization scheme and scale dependence between direct and resolved contributions and propose a new factorization scheme for diffractive dijet photoproduction.

1 Introduction

It is well known that in high-energy deep-inelastic ep-collisions a large fraction of the observed events are diffractive. These events are defined experimentally by the presence of a forward-going system Y with four-momentum p_Y, low mass M_Y (in most cases a single proton and/or low-lying nucleon resonances), small momentum transfer squared $t = (p - p_Y)^2$, and small longitudinal momentum transfer fraction $x_{I\!P} = q(p - p_Y)/qp$ from the incoming proton with four-momentum p to the system X (see Fig. 1).

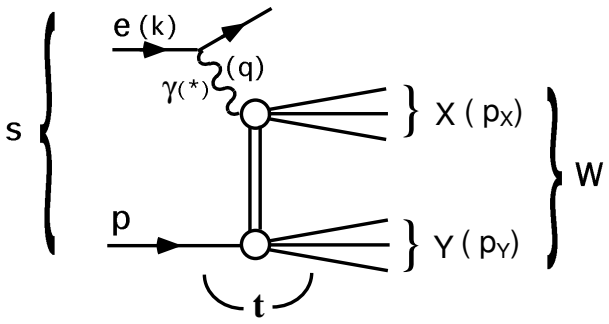

Fig. 1: Diffractive scattering process $ep \to eXY$, where the hadronic systems X and Y are separated by the largest rapidity gap in the final state.

The presence of a hard scale, as for example the photon virtuality $Q^2 = -q^2$ in deep-inelastic scattering (DIS) or the large transverse jet momentum p_T^* in the photon-proton centre-of-momentum frame, should then allow for calculations of the production cross section for the central system X with the known methods of perturbative QCD. Under this assumption, the cross section for the inclusive production of two jets, $e + p \to e + 2\,\mathrm{jets} + X' + Y$, can be predicted from the well-known formulæ for jet production

in non-diffractive ep collisions, where in the convolution of the partonic cross section with the parton distribution functions (PDFs) of the proton the latter ones are replaced by the diffractive PDFs. In the simplest approximation, they are described by the exchange of a single, factorizable pomeron/Reggepole.

The diffractive PDFs have been determined by the H1 Collaboration at HERA from high-precision inclusive measurements of the DIS process $ep \to eXY$ using the usual DGLAP evolution equations in leading order (LO) and next-to-leading order (NLO) and the well-known formula for the inclusive cross section as a convolution of the inclusive parton-level cross section with the diffractive PDFs [1]. For a similar analysis of the inclusive measurements of the ZEUS Collaboration see [2,3]. A longer discussion of the extraction of diffractive PDFs can also be found in these proceedings [4] and in [5]. For inclusive diffractive DIS it has been proven by Collins that the formula referred to above is applicable without additional corrections and that the inclusive jet production cross section for large Q^2 can be calculated in terms of the same diffractive PDFs [6]. The proof of this factorization formula, usually referred to as the validity of QCD factorization in hard diffraction, may be expected to hold for the direct part of photoproduction ($Q^2 \simeq 0$) or low-Q^2 electroproduction of jets [6]. However, factorization does not hold for hard processes in diffractive hadron-hadron scattering. The problem is that soft interactions between the ingoing two hadrons and their remnants occur in both the initial and final state. This agrees with experimental measurements at the Tevatron [7]. Predictions of diffractive dijet cross sections for $p\bar{p}$ collisions as measured by CDF using the same PDFs as determined by H1 [1] overestimate the measured cross section by up to an order of magnitude [7]. This suppression of the CDF cross section can be explained by considering the rescattering of the two incoming hadron beams which, by creating additional hadrons, destroy the rapidity gap [8].

Processes with real photons ($Q^2 \simeq 0$) or virtual photons with fixed, but low Q^2 involve direct interactions of the photon with quarks from the proton as well as resolved photon contributions, leading to parton-parton interactions and an additional remnant jet coming from the photon (for a review see [9]). As already said, factorization should be valid for direct interactions as in the case of DIS, whereas it is expected to fail for the resolved process similar as in the hadron-hadron scattering process. In a two-channel eikonal model similar to the one used to calculate the suppression factor in hadron-hadron processes [8], introducing vector-meson dominated photon fluctuations, a suppression by about a factor of three for resolved photoproduction at HERA is predicted [10]. Such a suppression factor has recently been applied to diffractive dijet photoproduction [11,12] and compared to preliminary data from H1 [13] and ZEUS [14]. While at LO no suppression of the resolved contribution seemed to be necessary, the NLO corrections increase the cross section significantly, showing that factorization breaking occurs at this order at least for resolved photoproduction and that a suppression factor R must be applied to give a reasonable description of the experimental data.

As already mentioned elsewhere [11, 12], describing the factorization breaking in hard photoproduction as well as in electroproduction at very low Q^2 [15] by suppressing the resolved contribution only may be problematic. An indication for this is the fact that the separation between the direct and the resolved process is uniquely defined only in LO. In NLO these two processes are related. The separation depends on the factorization scheme and the factorization scale M_γ. The sum of both cross sections is the only physically relevant cross section, which is approximately independent of the factorization scheme and scale [16]. As demonstrated in Refs. [11, 12] multiplying the resolved cross section with the suppression factor $R = 0.34$ destroys the correlation of the M_γ-dependence between the direct and resolved part, and the sum of both parts has a stronger M_γ-dependence than for the unsuppressed case ($R = 1$), where the M_γ-dependence of the NLO direct cross section is compensated to a high degree against the M_γ-dependence of the LO resolved part.

In the second Section of this contribution, we present the current experimental data from the H1 and ZEUS Collaborations on diffractive dijet production in DIS and photoproduction and compare these data to theoretical predictions at NLO for two different scenarios: suppression of only the resolved

part by a factor $R = 0.34$ as expected from LO theory and proposed in [8], and equal suppression of all direct and resolved contributions by a factor $R = 0.5$, which appears to describe the data better phenomenologically. This motivates us to investigate in the third Section the question whether certain parts of the direct contribution might break factorization as well and therefore need a suppression factor.

The introduction of the resolved cross section is dictated by perturbation theory. At NLO, collinear singularities arise from the photon initial state, which are absorbed at the factorization scale into the photon PDFs. This way the photon PDFs become M_γ-dependent. The equivalent M_γ-dependence, just with the opposite sign, is left in the NLO corrections to the direct contribution. With this knowledge, it is obvious that we can obtain a physical cross section at NLO, *i.e.* the superposition of the NLO direct and LO resolved cross section, with a suppression factor $R < 1$ and no M_γ-dependence left, if we also multiply the $\ln M_\gamma$-dependent term of the NLO correction to the direct contribution with the same suppression factor as the resolved cross section. We are thus led to the theoretical conclusion that, contrary to what one may expect, not *all* parts of the direct contribution factorize. Instead, the *initial state* singular part appearing beyond LO breaks factorization even in direct photoproduction, presumably through soft gluon attachments between the proton and the collinear quark-antiquark pair emerging from the photon splitting. This would be in agreement with the general remarks about initial state singularities in Ref. [6].

In the third Section of this contribution, we present the special form of the $\ln M_\gamma$-term in the NLO direct contribution and demonstrate that the M_γ-dependence of the physical cross section cancels to a large extent in the same way as in the unsuppressed case ($R = 1$). These studies can be done for photoproduction ($Q^2 \simeq 0$) as well as for electroproduction with fixed, small Q^2. Since in electroproduction the initial-state singularity in the limit $Q^2 \to 0$ is more directly apparent than for the photoproduction case, we shall consider in this contribution the low-Q^2 electroproduction case just for demonstration. This diffractive dijet cross section has been calculated recently [15]. A consistent factorization scheme for low-Q^2 virtual photoproduction has been defined and the full (direct and resolved) NLO corrections for inclusive dijet production have been calculated in [17]. In this work we adapt this inclusive NLO calculational framework to diffractive dijet production at low-Q^2 in the same way as in [15], except that we multiply the $\ln M_\gamma$-dependent terms as well as the resolved contributions with the same suppression factor $R = 0.34$, as an example, as in our earlier work [11, 12, 15]. The exact value of this suppression factor may change in the future, when better data for photoproduction and low-Q^2 electroproduction have been analyzed. We present the $\ln M_\gamma$-dependence of the partly suppressed NLO direct and the fully suppressed NLO resolved cross section $\mathrm{d}\sigma/\mathrm{d}Q^2$ and their sum for the lowest Q^2 bin, before we give a short summary in section 4.

2 Comparison of H1 and ZEUS Data with NLO Theory Predictions

In this Section, diffractive PDFs [1–3] extracted from diffractive structure function data are used in NLO calculations to test factorisation in diffractive dijet production. Dijet production is directly sensitive to the diffractive gluon (Fig. 2) whereas in inclusive measurements the gluon is determined from scaling violations.

2.1 Diffractive Dijet Production in DIS

H1 has measured the cross sections for dijet production [13] in the kinematic range $Q^2 > 4$ GeV^2, $165 < W < 242$ GeV (photon-proton centre-of-mass energy) and $x_{I\!P} < 0.03$. Jets are identified using the inclusive k_T cluster algorithm and selected by requiring $E_T^{*,\mathrm{jet}}(1,2) > 5,4$ GeV and $-3 < \eta^*_{\mathrm{jet}} < 0$.[1] NLO predictions have been obtained by interfacing the H1 diffractive PDFs with the DISENT program [18]. The renormalisation and factorisation scales were set to the transverse energy of the leading parton jet. The NLO parton jet cross sections have been corrected for hadronisation effects using the

[1] The '$*$' denotes variables in the photon-proton centre-of-mass system.

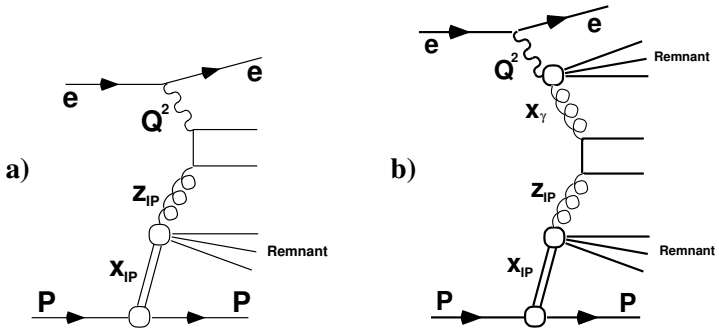

Fig. 2: Example processes for a) direct photon and b) resolved photon interactions.

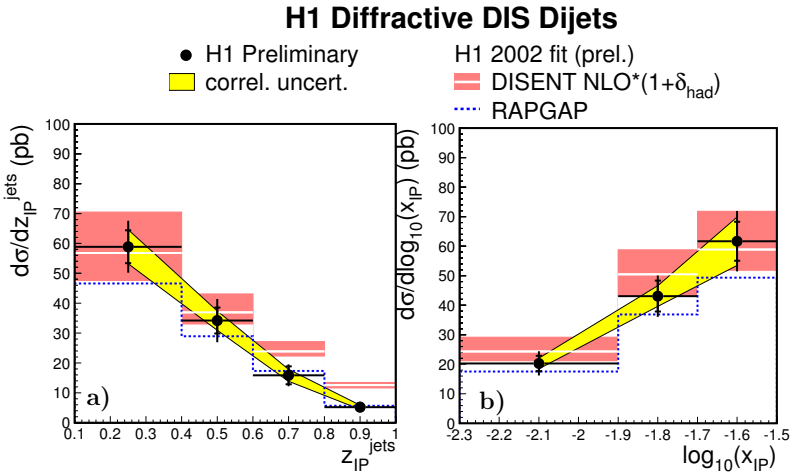

Fig. 3: Diffractive DIS dijet cross sections compared with a NLO prediction based on diffractive PDFs and with RAPGAP.

leading order (LO) generator RAPGAP [19] with parton showers and the Lund string fragmentation model. Comparisons of the DISENT and RAPGAP predictions with the measured cross section differential in $z_{I\!P}^{\rm jets}$, an estimator for the fraction of the momentum of the diffractive exchange entering the hard scatter, are shown in Fig. 3a. The inner band around the NLO calculation indicates the $\approx 20\%$ uncertainty resulting from a variation of the renormalisation scale by factors 0.5 and 2. The uncertainty in the diffractive PDFs is not shown. Within this additional uncertainty, which is large at high $z_{I\!P}^{\rm jets}$, the cross section is well described. The cross section differential in $\log_{10}(x_{I\!P})$, $p_T^{\rm jet1}$, and Q^2 is shown in Figs. 3b and 4. All distributions are well described and QCD factorisation is therefore in good agreement with dijet production in diffractive DIS.

Similar results are presented by ZEUS [20]; the dijet cross sections have been measured in the kinematic range $5 < Q^2 < 100$ GeV^2, $100 < W < 200$ GeV, $x_{I\!P} < 0.03$. The jets were identified using the inclusive k_T algorithm in the γp frame and required to satisfy $E_T^{*,\rm jet}(1,2) > 5,4$ GeV and $-3.5 < \eta^*_{\rm jet} < 0.0$. NLO predictions have been obtained with the DISENT program interfaced to three different sets of diffractive PDFs: from fit to H1 data [1], from fit to the ZEUS M_X data (GLP) [3] and from fit to ZEUS LPS and $F_2^{D,charm}$ data [2]. Comparisons of the DISENT predictions with the measured cross section differential in $E_T^{*,\rm jet}$, $\eta^*_{\rm jet}$, $z_{I\!P}^{\rm jets}$ and x_γ^{obs} are shown in Fig. 5. The $20-30\%$ uncertainty in the NLO calculations resulting from a variation of the renormalisation and factorisation scales is not shown. Within the experimental and QCD scale uncertainties, the predictions based on the H1 and ZEUS-LPS PDFs give a good description of the dijet cross section. The normalisation of the prediction using the GLP fit is substantially lower than those from the other two sets of PDFs. For

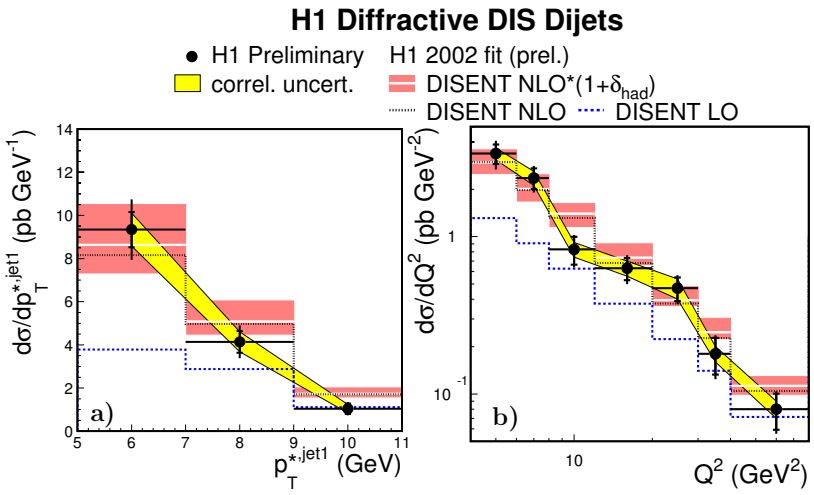

Fig. 4: Diffractive DIS dijet cross sections compared with a NLO prediction based on diffractive PDFs.

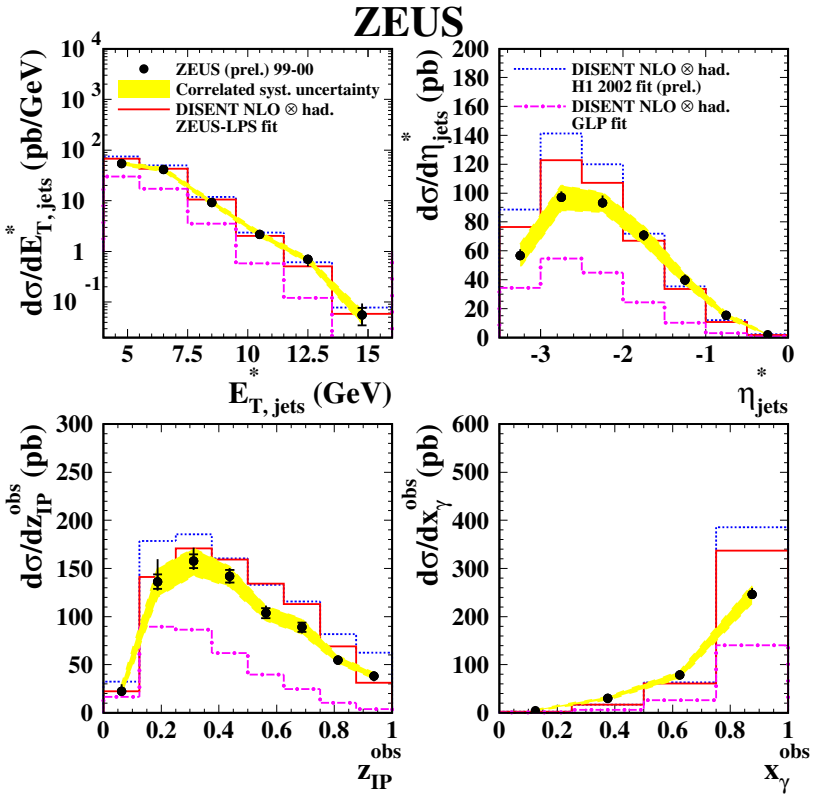

Fig. 5: Diffractive DIS dijet cross sections compared with NLO predictions based on three sets of diffractive PDFs.

ZEUS, the difference observed between the three sets may be interpreted as an estimate of the uncertainty associated with the diffractive PDFs and with the definition of the diffractive region. The dijet data could be included in future fits in order to better constrain the diffractive gluon distribution.

Within the experimental and theoretical uncertainties and assuming the H1 diffractive PDFs, factorisation is in good agreement with diffractive D^* production [21, 22] in the DIS kinematic region.

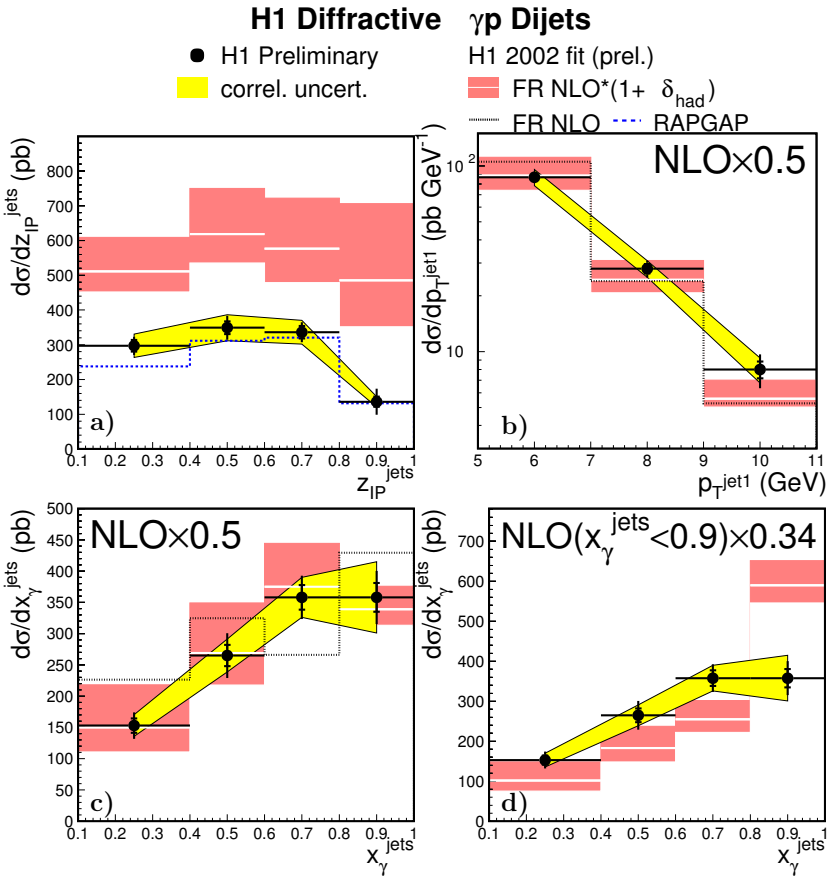

Fig. 6: a) Diffractive dijet photoproduction cross section differential in $z_{I\!P}^{\rm jets}$ compared with a NLO prediction based on diffractive PDFs and RAPGAP. b)-d): Cross section differential in $p_T^{\rm jet1}$and $x_\gamma^{\rm jets}$, compared with the NLO prediction modified as follows: in b) and c) the calculation is scaled by a global factor 0.5 whereas in d) only the "resolved" part is scaled by 0.34.

2.2 Diffractive Photoproduction of Dijets

In photoproduction, a sizeable contribution to the cross section is given by resolved photon processes (Fig. 2b) in which only a fraction $x_\gamma < 1$ of the photon momentum enters the hard scatter. The photoproduction dijet cross section measured by H1 ($Q^2 < 0.01$ GeV^2, $165 < W < 242$ GeV, $x_{I\!P} < 0.03$, $E_T^{\rm jet}(1,2) > 5,4$ GeV, $-1 < \eta_{\rm jet} < 2$, inclusive k_T algorithm) is shown in Fig. 6 [13]. NLO predictions have been obtained with the Frixione *et al.* program [23] interfaced to the H1 diffractive PDFs. The parton jet calculation is corrected for hadronisation effects using RAPGAP. The cross section differential in $z_{I\!P}^{\rm jets}$ is shown in Fig. 6a. The calculation lies a factor ≈ 2 above the data. Fig. 6b and 6c show the cross section as a function of $p_T^{\rm jet1}$ and $x_\gamma^{\rm jets}$ and the NLO predictions have been scaled down by a factor 0.5. Good agreement is obtained for this global suppression. In Fig. 6d, only the "resolved" part for which $x_\gamma^{\rm jets} < 0.9$ at the parton level is scaled by a factor 0.34. This factor was proposed by Kaidalov *et al.* [10] for the suppression of the resolved part in LO calculations. The calculation for $x_\gamma^{\rm jets} > 0.9$ is left unscaled. This approach is clearly disfavoured.

The ZEUS measurement [24] ($Q^2 < 0.01$ GeV^2, $x_{I\!P} < 0.025$, $0.2 < y < 0.85$, $E_T^{\rm jet}(1,2) > 7.5, 6.5$ GeV, $-1.5 < \eta < 1.5$, inclusive k_T algorithm) is shown in Figs. 7 and 8 separately for samples enriched in "direct" ($x_\gamma^{\rm jets} > 0.75$) and "resolved" ($x_\gamma^{\rm jets} < 0.75$) processes, respectively. The NLO [12] prediction using the H1 diffractive PDFs is also presented corrected for hadronization effects and with the "resolved" part scaled by the factor 0.34. No evidence is observed for a suppression of resolved photon processes relative to direct photon processes in any particular kinematic region.

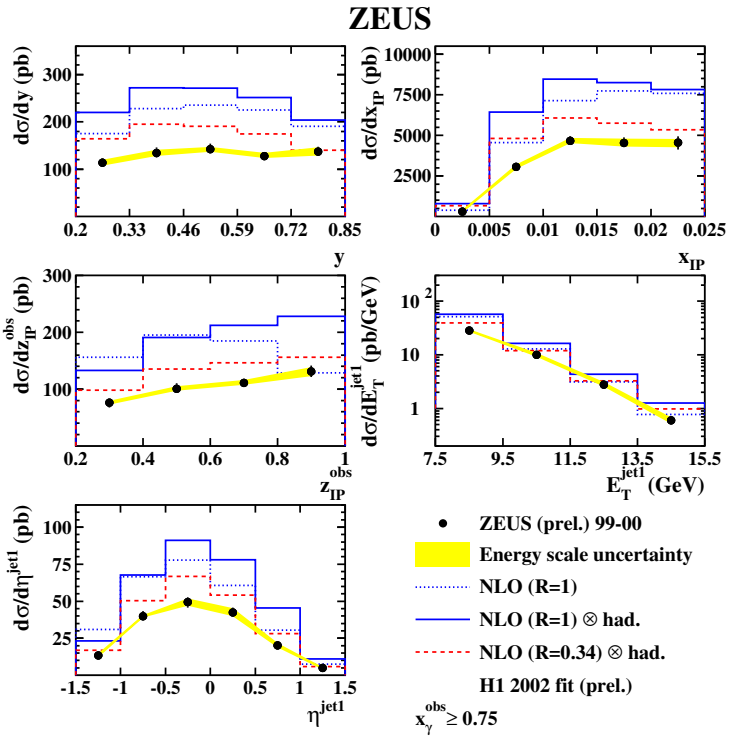

Fig. 7: Direct enriched photoproduction. Diffractive dijet photoproduction cross section differential in y, $x_{I\!P}$, $z_{I\!P}^{\rm jets}$, $E_T^{\rm jet\,1}$ and $\eta_{\rm jet\,1}$ compared with a NLO prediction based on diffractive PDFs. The NLO prediction is also presented corrected for hadronization effects and with the "resolved" part scaled by 0.34.

Diffractive dijet photoproduction is overestimated by calculations based on PDFs which give a good description of the diffractive DIS data. Factorisation is broken in photoproduction relative to DIS by a factor ≈ 0.5 with no observed dependence on x_γ or other kinematic variables.

3 Factorization and its Breaking in Diffractive Dijet Production

The fact that equal suppression of direct *and* resolved photoproduction by a factor $R = 0.5$ appears to describe the H1 and ZEUS data better phenomenologically motivates us to investigate in some detail the question whether certain parts of the direct contribution might break factorization as well and therefore need a suppression factor. These studies can be done for photoproduction ($Q^2 \simeq 0$) as well as for electroproduction with fixed, small Q^2. Since in electroproduction the initial-state singularity in the limit $Q^2 \to 0$ is more directly apparent than for the photoproduction case, we shall consider in this contribution the low-Q^2 electroproduction case just for demonstration.

A factorization scheme for virtual photoproduction has been defined and the full NLO corrections for inclusive dijet production have been calculated in [17]. They have been implemented in the NLO Monte Carlo program JETVIP [25] and adapted to diffractive dijet production in [15]. The subtraction term, which is absorbed into the PDFs of the virtual photon $f_{a/\gamma}(x_\gamma, M_\gamma)$, can be found in [26]. The main term is proportional to $\ln(M_\gamma^2/Q^2)$ times the splitting function

$$P_{q_i \leftarrow \gamma}(z) = 2N_c Q_i^2 \frac{z^2 + (1-z)^2}{2}, \tag{1}$$

where $z = p_1 p_2 / p_0 q \in [x; 1]$ and Q_i is the fractional charge of the quark q_i. p_1 and p_2 are the momenta of the two outgoing jets, and p_0 and q are the momenta of the ingoing parton and virtual photon, respec-

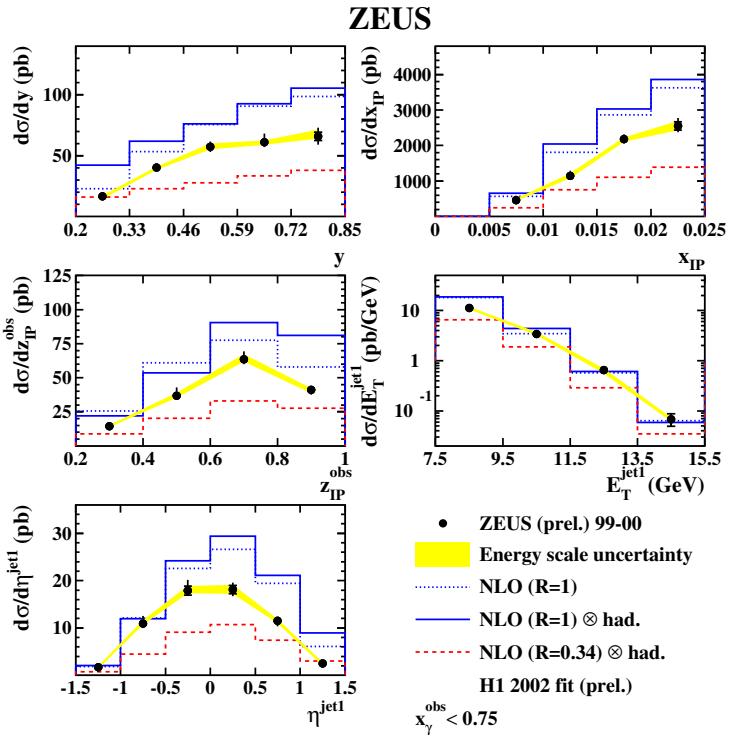

Fig. 8: Resolved enriched photoproduction. Diffractive dijet photoproduction cross section differential in y, $x_{I\!P}$, $z_{I\!P}^{\rm jets}$, $E_T^{\rm jet\,1}$ and $\eta_{\rm jet\,1}$ compared with a NLO prediction based on diffractive PDFs. The NLO prediction is also presented corrected for hadronization effects and with the "resolved" part scaled by 0.34.

tively. Since $Q^2 = -q^2 \ll M_\gamma^2$, the subtraction term is large and is therefore resummed by the DGLAP evolution equations for the virtual photon PDFs. After this subtraction, the finite term $M(Q^2)_{\overline{\rm MS}}$, which remains in the matrix element for the NLO correction to the direct process [17], has the same M_γ-dependence as the subtraction term, *i.e.* $\ln M_\gamma$ is multiplied with the same factor. As already mentioned, this yields the M_γ-dependence before the evolution is turned on. In the usual non-diffractive dijet photoproduction these two M_γ-dependences cancel, when the NLO correction to the direct part is added to the LO resolved cross section [16]. Then it is obvious that the approximate M_γ-independence is destroyed, if the resolved cross section is multiplied by a suppression factor R to account for the factorization breaking in the experimental data. To remedy this deficiency, we propose to multiply the $\ln M_\gamma$-dependent term in $M(Q^2)_{\overline{\rm MS}}$ with the same suppression factor as the resolved cross section. This is done in the following way: we split $M(Q^2)_{\overline{\rm MS}}$ into two terms using the scale p_T^* in such a way that the term containing the slicing parameter y_s, which was used to separate the initial-state singular contribution, remains unsuppressed. In particular, we replace the finite term after the subtraction by

$$\begin{aligned} M(Q^2,R)_{\overline{\rm MS}} \;=\; & \left[-\frac{1}{2N_c}P_{q_i\leftarrow\gamma}(z)\ln\left(\frac{M_\gamma^2 z}{p_T^{*2}(1-z)}\right)+\frac{Q_i^2}{2}\right]R \\ & -\frac{1}{2N_c}P_{q_i\leftarrow\gamma}(z)\ln\left(\frac{p_T^{*2}}{zQ^2+y_s s}\right), \end{aligned} \tag{2}$$

where R is the suppression factor. This expression coincides with the finite term after subtraction (see Ref. [26]) for $R=1$, as it should, and leaves the second term in Eq. (2) unsuppressed. In Eq. (2) we have suppressed in addition to $\ln(M_\gamma^2/p_T^{*2})$ also the z-dependent term $\ln(z/(1-z))$, which is specific to the $\overline{\rm MS}$ subtraction scheme as defined in [17]. The second term in Eq. (2) must be left in its original form,

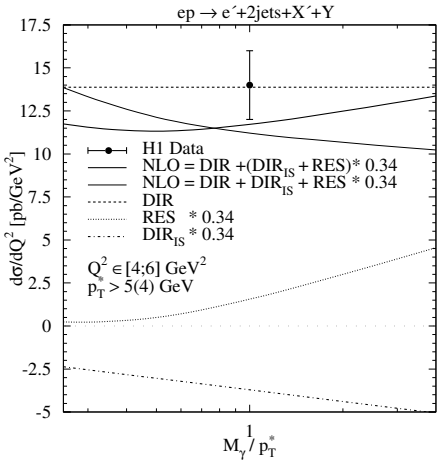

Fig. 9: Photon factorization scale dependence of resolved and direct contributions to $\mathrm{d}\sigma/\mathrm{d}Q^2$ together with their weighted sums for (i) suppression of the resolved cross section and for (ii) additional suppression of $\mathrm{DIR}_{\mathrm{IS}}$, using SaS1D virtual photon PDFs [30].

i.e. being unsuppressed, in order to achieve the cancellation of the slicing parameter (y_s) dependence of the complete NLO correction in the limit of very small Q^2 or equivalently very large s. It is clear that the suppression of this part of the NLO correction to the direct cross section will change the full cross section only very little as long as we choose $M_\gamma \simeq p_T^*$. The first term in Eq. (2), which has the suppression factor R, will be denoted by $\mathrm{DIR}_{\mathrm{IS}}$ in the following.

To study the left-over M_γ-dependence of the physical cross section, we have calculated the diffractive dijet cross section with the same kinematic constraints as in the H1 experiment [27]. Jets are defined by the CDF cone algorithm with jet radius equal to one and asymmetric cuts for the transverse momenta of the two jets required for infrared stable comparisons with the NLO calculations [28]. The original H1 analysis actually used a symmetric cut of 4 GeV on the transverse momenta of both jets [29]. The data have, however, been reanalyzed for asymmetric cuts [27].

For the NLO resolved virtual photon predictions, we have used the PDFs SaS1D [30] and transformed them from the DIS_γ to the $\overline{\mathrm{MS}}$ scheme as in Ref. [17]. If not stated otherwise, the renormalization and factorization scales at the pomeron and the photon vertex are equal and fixed to $p_T^* = p_{T,jet1}^*$. We include four flavors, *i.e.* $n_f = 4$ in the formula for α_s and in the PDFs of the pomeron and the photon. With these assumptions we have calculated the same cross section as in our previous work [15]. First we investigated how the cross section $\mathrm{d}\sigma/\mathrm{d}Q^2$ depends on the factorization scheme of the PDFs for the virtual photon, *i.e.* $\mathrm{d}\sigma/\mathrm{d}Q^2$ is calculated for the choice SaS1D and SaS1M. Here $\mathrm{d}\sigma/\mathrm{d}Q^2$ is the full cross section (sum of direct and resolved) integrated over the momentum and rapidity ranges as in the H1 analysis. The results, shown in Fig. 2 of Ref. [26], demonstrate that the choice of the factorization scheme of the virtual photon PDFs has negligible influence on $\mathrm{d}\sigma/\mathrm{d}Q^2$ for all considered Q^2. The predictions agree reasonably well with the preliminary H1 data [27].

We now turn to the M_γ-dependence of the cross section with a suppression factor for $\mathrm{DIR}_{\mathrm{IS}}$. To show this dependence for the two suppression mechanisms, (i) suppression of the resolved cross section only and (ii) additional suppression of the $\mathrm{DIR}_{\mathrm{IS}}$ term as defined in Eq. (2) in the NLO correction of the direct cross section, we consider $\mathrm{d}\sigma/\mathrm{d}Q^2$ for the lowest Q^2-bin, $Q^2 \in [4,6]$ GeV^2. In Fig. 9, this cross section is plotted as a function of $\xi = M_\gamma/p_T^*$ in the range $\xi \in [0.25;4]$ for the cases (i) (light full curve) and (ii) (full curve). We see that the cross section for case (i) has an appreciable ξ-dependence in the considered ξ range of the order of 40%, which is caused by the suppression of the resolved contribution only. With the additional suppression of the $\mathrm{DIR}_{\mathrm{IS}}$ term in the direct NLO

correction, the ξ-dependence of $\mathrm{d}\sigma/\mathrm{d}Q^2$ is reduced to approximately less than 20%, if we compare the maximal and the minimal value of $\mathrm{d}\sigma/\mathrm{d}Q^2$ in the considered ξ range. The remaining ξ-dependence is caused by the NLO corrections to the suppressed resolved cross section and the evolution of the virtual photon PDFs. How the compensation of the M_γ-dependence between the suppressed resolved contribution and the suppressed direct NLO term works in detail is exhibited by the dotted and dashed-dotted curves in Fig. 9. The suppressed resolved term increases and the suppressed direct NLO term decreases by approximately the same amount with increasing ξ. In addition we show also $\mathrm{d}\sigma/\mathrm{d}Q^2$ in the DIS theory, *i.e.* without subtraction of any $\ln Q^2$ terms (dashed line). Of course, this cross section must be independent of ξ. This prediction agrees very well with the experimental point, whereas the result for the subtracted and suppressed theory (full curve) lies slightly below. We notice, that for $M_\gamma = p_T^*$ the additional suppression of $\mathrm{DIR}_{\mathrm{IS}}$ has only a small effect. It increases $\mathrm{d}\sigma/\mathrm{d}Q^2$ by 5% only.

4 Summary

Experimental data from the H1 and ZEUS Collaborations at HERA for diffractive dijet production in DIS and photoproduction have been compared with NLO QCD predictions using diffractive parton densities from H1 and ZEUS. While good agreement was found for DIS assuming the H1 diffractive PDFs, the dijet photoproduction data are overestimated by the NLO theory, showing that factorization breaking occurs at this order. While this is expected theoretically for resolved photoproduction, the fact that the data are better described by a global suppression of direct *and* resolved contribution by about a factor of two has come as a surprise. We have therefore discussed in some detail the factorization scheme and scale dependence between direct and resolved contributions and proposed a new factorization scheme for diffractive dijet photoproduction.

Acknowledgements

M.K. thanks the II. Institute for Theoretical Physics at the University of Hamburg for hospitality while this work was being finalized.

References

[1] H1 Collaboration, Abstract 980, contributed to the 31^{st} International Conference on High Energy Physics (ICHEP 2002), Amsterdam, July 2002.

[2] S. Chekanov et al. [ZEUS Collaboration], *Eur. Phys. J.* **C 38** (2004) 43, and A. Proskuryakov, private communication.

[3] M. Groys, A. Levy and A. Proskuryakov, these proceedings.

[4] F.-P. Schilling and P. Newman, these proceedings.

[5] A. D. Martin, M. G. Ryskin and G. Watt, Eur. Phys. J. C **37**, 285 (2004) and DESY 05-055, IPPP/05/07, DCPT/05/14, hep-ph/0504132.

[6] J. C. Collins, Phys. Rev. D **57**, 3051 (1998) [Erratum-ibid. D **61**, 019902 (2000)].

[7] T. Affolder *et al.* [CDF Collaboration], Phys. Rev. Lett. **84**, 5043 (2000).

[8] A. B. Kaidalov, V. A. Khoze, A. D. Martin and M. G. Ryskin, Eur. Phys. J. C **21**, 521 (2001).

[9] M. Klasen, Rev. Mod. Phys. **74**, 1221 (2002).

[10] A. B. Kaidalov, V. A. Khoze, A. D. Martin and M. G. Ryskin, Phys. Lett. B **567**, 61 (2003).

[11] M. Klasen and G. Kramer, hep-ph/0401202, Proceedings of the 12^{th} International Workshop on Deep Inelastic Scattering (DIS 2004), eds. D. Bruncko, J. Ferencei and P. Strizenec, Kosice, Inst. Exp. Phys. SAS, 2004, p. 492.

[12] M. Klasen and G. Kramer, Eur. Phys. J. C **38**, 93 (2004).

[13] H1 Collaboration, Abstract 6-0177, contributed to the 32^{nd} International Conference on High Energy Physics (ICHEP 2004), Beijing, August 2004.

[14] ZEUS Collaboration, Abstract 6-0249, contributed to the $32^{\rm nd}$ International Conference on High Energy Physics (ICHEP 2004), Beijing, August 2004.

[15] M. Klasen and G. Kramer, Phys. Rev. Lett. **93**, 232002 (2004).

[16] D. Bödeker, G. Kramer and S. G. Salesch, Z. Phys. C **63**, 471 (1994).

[17] M. Klasen, G. Kramer and B. Pötter, Eur. Phys. J. C **1**, 261 (1998).

[18] S. Catani, M.H. Seymour, *Nucl. Phys.* **B 485** (1997) 291; erratum ibid. **B510** (1997) 503.

[19] H. Jung, *Comp. Phys. Commun.* **86** (1995) 147.

[20] ZEUS Collaboration, Abstract 295 and addendum, contributed to the $22^{\rm nd}$ International Symposium on Lepton-Photon Interactions oh High Energy, Uppsala, Sweden, June 2005.

[21] H1 Collaboration, Abstract 6-0178, contributed to the $32^{\rm nd}$ International Conference on High Energy Physics (ICHEP 2004), Beijing, August 2004.

[22] S. Chekanov et al. [ZEUS Collaboration], *Nucl. Phys.* **B 672** (2003) 3,

[23] S. Frixione, Z. Kunszt and A. Signer, *Nucl. Phys.* **B 467** (1996) 399;
S. Frixione, *Nucl. Phys.* **B 507** (1997) 295.

[24] ZEUS Collaboration, Abstract 293, contributed to the $22^{\rm nd}$ International Symposium on Lepton-Photon Interactions oh High Energy, Uppsala, Sweden, June 2005.

[25] B. Pötter, Comput. Phys. Commun. **133**, 105 (2000).

[26] M. Klasen and G. Kramer, hep-ph/0506121, accepted for publication in J. Phys. G.

[27] S. Schätzel, hep-ex/0408049, Proceedings of the $12^{\rm th}$ International Workshop on Deep Inelastic Scattering (DIS 2004), eds. D. Bruncko, J. Ferencei and P. Strizenec, Kosice, Inst. Exp. Phys. SAS, 2004, p. 529; H1 Collaboration, Abstract 6-0176, contributed to the $32^{\rm nd}$ International Conference on High Energy Physics (ICHEP 2004), Beijing, August 2004.

[28] M. Klasen and G. Kramer, Phys. Lett. B **366**, 385 (1996).

[29] C. Adloff *et al.* [H1 Collaboration], Eur. Phys. J. C **20**, 29 (2001).

[30] G. A. Schuler and T. Sjöstrand, Phys. Lett. B **376**, 193 (1996).

Effect of absorptive corrections on inclusive parton distributions

G. Watt[a], A.D. Martin[b], M.G. Ryskin[b,c]
[a] Deutsches Elektronen-Synchrotron DESY, 22607 Hamburg, Germany
[b] Institute for Particle Physics Phenomenology, University of Durham, DH1 3LE, UK
[c] Petersburg Nuclear Physics Institute, Gatchina, St. Petersburg, 188300, Russia

Abstract
We study the effect of absorptive corrections due to parton recombination on the parton distributions of the proton. A more precise version of the GLRMQ equations, which account for non-linear corrections to DGLAP evolution, is derived. An analysis of HERA F_2 data shows that the small-x gluon distribution is enhanced at low scales when the absorptive effects are included, such that there is much less need for a negative gluon distribution at 1 GeV.

1 Parton recombination at small x

At very small values of x it is expected that the number density of partons within the proton becomes so large that they begin to recombine with each other. This phenomenon of parton recombination is also referred to as absorptive corrections, non-linear effects, screening, shadowing, or unitarity corrections, all leading to saturation. The first perturbative QCD (pQCD) calculations describing the fusion of two Pomeron ladders into one were made by Gribov-Levin-Ryskin (GLR) [1] and by Mueller-Qiu (MQ) [2]. The GLRMQ equations add an extra non-linear term, quadratic in the gluon density, to the usual DGLAP equations for the gluon and sea-quark evolution. The evolution of the gluon distribution is then given by

$$\frac{\partial x g(x,Q^2)}{\partial \ln Q^2} = \frac{\alpha_S}{2\pi} \sum_{a'=q,g} P_{ga'} \otimes a' \; - \; \frac{9}{2} \frac{\alpha_S^2(Q^2)}{R^2\, Q^2} \int_x^1 \frac{\mathrm{d}x'}{x'} \left[x' g(x',Q^2)\right]^2, \tag{1}$$

where $R \sim 1$ fm is of the order of the proton radius. The GLRMQ equations account for all 'fan' diagrams, that is, all possible $2 \to 1$ ladder recombinations, in the double leading logarithmic approximation (DLLA) which resums all powers of the parameter $\alpha_S \ln(1/x) \ln(Q^2/Q_0^2)$.

There has been much recent theoretical activity in deriving (and studying) more precise non-linear evolution equations, such as the Balitsky-Kovchegov (BK) and Jalilian-Marian–Iancu–McLerran–Weigert–Leonidov–Kovner (JIMWLK) equations (see [3] for a review). Note that the BK and JIMWLK equations are both based on BFKL evolution. However, for the most relevant studies in the HERA and LHC domain ($x \gtrsim 10^{-4}$), the predominant theoretical framework is collinear factorisation with DGLAP-evolved parton distribution functions (PDFs). At very small values of x it might be expected that the DGLAP approximation would break down, since large $\alpha_S \ln(1/x)$ (BFKL) terms would appear in the perturbation series in addition to the $\alpha_S \ln(Q^2/Q_0^2)$ terms resummed by DGLAP evolution. However, it turns out that the resummed NLL BFKL calculations of the gluon splitting function P_{gg} [4] and the gluon transverse momentum distribution [5] are rather close to the DGLAP calculations. Moreover, the convolution $P_{gg} \otimes g(x,Q^2)$ coincides with the NNLO DGLAP result and is close to the NLO DGLAP result for $x \gtrsim 10^{-4}$ [6]. Hence, in the analysis of current data, it is reasonable to ignore BFKL effects.

If recombination effects are significant, it is therefore important that they be incorporated into the global DGLAP parton analyses which determine the PDFs from deep-inelastic scattering (DIS) and related hard-scattering data. Such a programme, based on GLRMQ evolution (which accounts for gluon-induced screening only), was implemented some years ago [7], before the advent of HERA. The input gluon and sea-quark distributions were *assumed* to have a small-x behaviour of the form $xg, xS \sim x^{-0.5}$ at an input scale of $Q_0^2 = 4$ GeV^2. The inclusion of shadowing effects, both in the form of the input PDFs and in the GLRMQ evolution, was found to significantly *decrease* the size of the small-x gluon

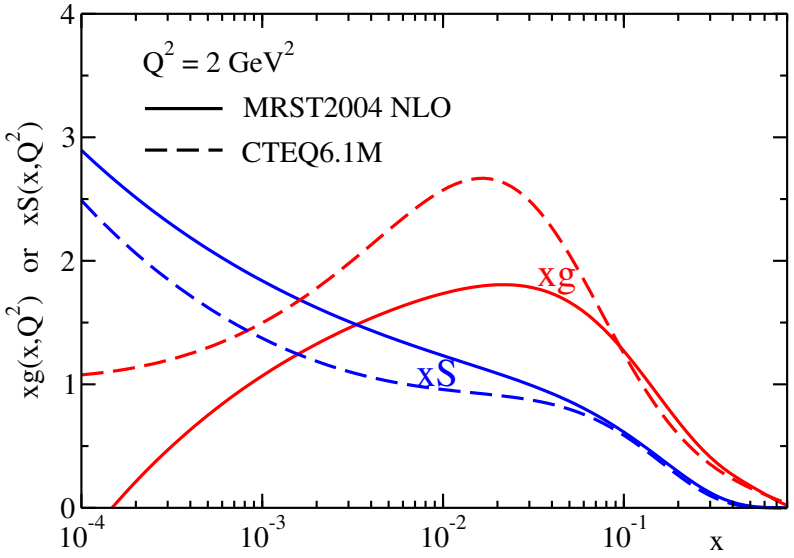

Fig. 1: The behaviour of the gluon and sea-quark distributions at $Q^2 = 2$ GeV^2 found in the MRST2004 NLO and CTEQ6.1M global analyses. The valence-like behaviour of the gluon is evident.

distribution in comparison with the result with no absorptive corrections. A crucial observation is that, at that time (1990), F_2 data were only available for $x_B \geq 0.07$, and so these results were largely dependent on the theoretical assumptions made for the starting distributions. However, with HERA, we now have F_2 data down to $x_B \sim 10^{-4}$ or less, and so the PDFs at small x can be determined directly from the HERA data.

In fact, the advent of HERA data has led to a puzzling behaviour of the small-x gluon and sea-quark PDFs at low scales Q^2. If we write $xg \sim x^{-\lambda_g}$ and $xS \sim x^{-\lambda_S}$, then the expectation of Regge theory is that $\lambda_g = \lambda_S = \lambda_{\rm soft}$ for low scales $Q \lesssim Q_0 \sim 1$ GeV, where $\lambda_{\rm soft} \simeq 0.08$ [8] is the power of s obtained from fitting soft hadron data. At higher $Q \gtrsim 1$ GeV, QCD evolution should take over, increasing the powers λ_g and λ_S. However, the current MRST2004 NLO [9] and CTEQ6.1M [10] PDF sets exhibit a very different behaviour at low scales from that theoretically expected; see Fig. 1. In fact, the MRST group has found that a negative input gluon distribution at $Q_0 = 1$ GeV is required in all their NLO DGLAP fits since MRST2001 [11]. The CTEQ group, who take a slightly higher input scale of $Q_0 = 1.3$ GeV, also find a negative gluon distribution when evolving backwards to 1 GeV.

Since data at small x_B now exist, the introduction of the absorptive corrections is expected to *increase* the size of the input gluon distribution at small x to maintain a satisfactory fit to the data. To understand this, note that the negative non-linear term in the GLRMQ equation (1) slows down the evolution. Therefore, it is necessary to start with a *larger* small-x gluon distribution at low scales $Q \sim Q_0$ to achieve the *same* PDFs at larger scales required to describe the data. If the non-linear term is neglected, the input small-x gluon distribution is forced to be artificially small in order to *mimic* the neglected screening corrections.

We have anticipated that the introduction of absorptive corrections will *enhance*[1] the small-x gluon at low scales, and hence could possibly avoid what appears to be anomalous behaviour at small x. Thus, here, we perform such a study using an abridged version of the MRST2001 NLO analysis [11], improving on our previous analysis [13]. First, we derive a more precise form of the GLRMQ equations.

[1]Eskola *et al.* [12] have found that taking input gluon and sea-quark distributions at $Q^2 = 1.4$ GeV^2, then evolving upwards with the GLRMQ equations based on LO DGLAP evolution, improves the agreement with F_2 data at small x_B and low Q^2 compared to the standard CTEQ sets, and leads to an enhanced small-x gluon distribution for $Q^2 \lesssim 10$ GeV^2. Note, however, that there is a large NLO correction to the splitting function P_{qg} which changes completely the relationship between the quark and gluon distributions, and so weakens the conclusion of Ref. [12].

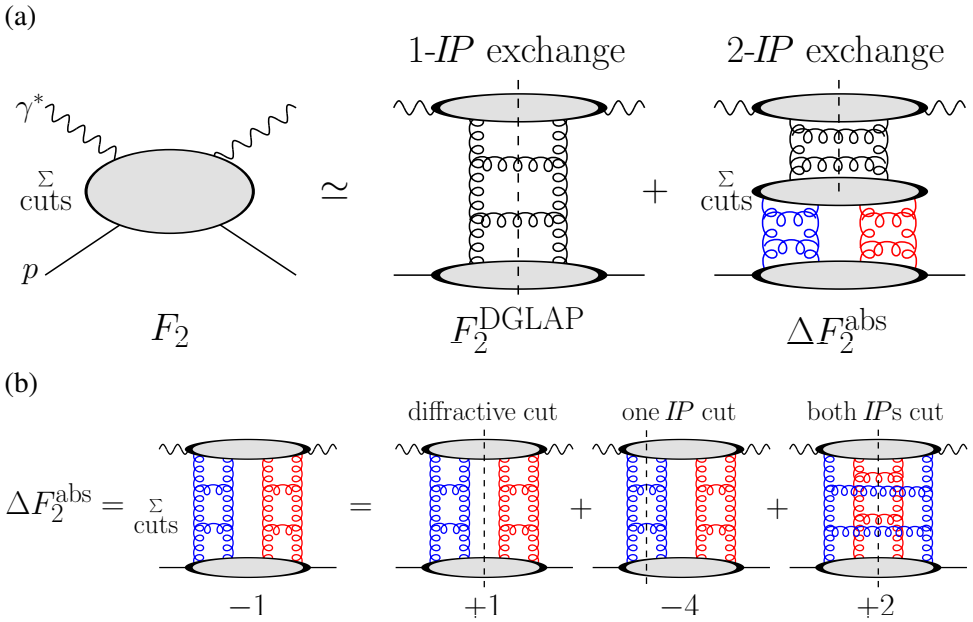

Fig. 2: (a) Absorptive corrections to F_2 due to the $2 \to 1$ Pomeron contribution. (b) Application of the AGK cutting rules. For simplicity, the upper parton ladder, shown in the right-hand diagram of (a), is hidden inside the upper blob in each diagram of (b).

2 Non-linear evolution from diffractive DIS

The inclusive proton structure function, $F_2(x_B, Q^2)$, as measured by experiment, can be approximately written as a sum of the single Pomeron exchange (DGLAP) contribution and absorptive corrections due to a $2 \to 1$ Pomeron merging; see Fig. 2(a). That is,

$$F_2(x_B, Q^2) = F_2^{\rm DGLAP}(x_B, Q^2) + \Delta F_2^{\rm abs}(x_B, Q^2). \tag{2}$$

In computing $\Delta F_2^{\rm abs}$ we need to sum over all possible cuts. The Abramovsky-Gribov-Kancheli (AGK) cutting rules [14] were originally formulated in Reggeon field theory but have been shown to also hold in pQCD [15]. Application of the AGK rules gives the result that relative contributions of $+1$, -4, and $+2$ are obtained according to whether neither Pomeron, one Pomeron, or both Pomerons are cut; see Fig. 2(b). Therefore, the sum over cuts is equal to *minus* the diffractive cut and so the absorptive corrections can be computed from a calculation of the t-integrated diffractive structure function $F_2^{\rm D(3)}(x_{I\!P}, \beta, Q^2)$, where $\beta \equiv x_B/x_{I\!P}$ and $x_{I\!P}$ is the fraction of the proton's momentum transferred through the rapidity gap.

The pQCD description of $F_2^{\rm D(3)}$ is described in [16, 17], and in a separate contribution to these proceedings. Working in the fixed flavour number scheme (FFNS), it can be written as

$$F_2^{\rm D(3)} = \underbrace{F_{2,\rm non-pert.}^{\rm D(3)}}_{\text{soft Pomeron}} + \underbrace{F_{2,\rm pert.}^{\rm D(3)} + F_{2,\rm direct}^{\rm D(3),c\bar{c}} + F_{L,\rm tw.4}^{\rm D(3)}}_{\text{QCD Pomeron}}, \tag{3}$$

apart from the secondary Reggeon contribution. The separation between the soft Pomeron and QCD Pomeron is provided by a scale $\mu_0 \sim 1$ GeV. For simplicity, we take μ_0 to be the same as the scale Q_0 at which the input PDFs are taken in the analysis of F_2 data, so $\mu_0 = Q_0 = 1$ GeV, the value used in the MRST2001 NLO analysis [11]. The contribution to the absorptive corrections arising from the soft Pomeron contribution of (3) is already included in the input PDFs, therefore

$$\Delta F_2^{\rm abs} = -\frac{1}{1 - f_{\rm p.diss.}} \int_{x_B}^{1} {\rm d}x_{I\!P} \left[F_{2,\rm pert.}^{\rm D(3)} + F_{2,\rm direct}^{\rm D(3),c\bar{c}} + F_{L,\rm tw.4}^{\rm D(3)} \right], \tag{4}$$

where $f_{\text{p.diss.}}$ is the fraction of diffractive events in which the proton dissociates. In practice, we take $f_{\text{p.diss.}} = 0.5$ and take an upper limit of 0.1 instead of 1 for $x_{I\!P}$ in (4).[2]

First consider the contribution to (4) from the $F_{2,\text{pert.}}^{\text{D}(3)}$ term.[3] It corresponds to a $2 \to 1$ Pomeron merging with a cut between the two Pomeron ladders and can be written as

$$F_{2,\text{pert.}}^{\text{D}(3)}(x_{I\!P}, \beta, Q^2) = \sum_{a=q,g} C_{2,a} \otimes a_{\text{pert.}}^{\text{D}}, \tag{5}$$

where $C_{2,a}$ are the *same* coefficient functions as in inclusive DIS. The diffractive PDFs, $a^{\text{D}} = zq^{\text{D}}$ or zg^{D}, where $z \equiv x/x_{I\!P}$, satisfy an *inhomogeneous* evolution equation [17]:

$$a_{\text{pert.}}^{\text{D}}(x_{I\!P}, z, Q^2) = \int_{\mu_0^2}^{Q^2} \frac{\text{d}\mu^2}{\mu^2}\, f_{I\!P}(x_{I\!P}; \mu^2)\, a^{I\!P}(z, Q^2; \mu^2) \tag{6}$$

$$\Longrightarrow \frac{\partial a_{\text{pert.}}^{\text{D}}}{\partial \ln Q^2} = \frac{\alpha_S}{2\pi} \sum_{a'=q,g} P_{aa'} \otimes a'^{\text{D}}_{\text{pert.}} \;+\; P_{aI\!P}(z)\, f_{I\!P}(x_{I\!P}; Q^2). \tag{7}$$

Here, $f_{I\!P}(x_{I\!P}; Q^2)$ is the perturbative Pomeron flux factor,

$$f_{I\!P}(x_{I\!P}; \mu^2) = \frac{1}{x_{I\!P} B_D} \left[R_g \frac{\alpha_S(\mu^2)}{\mu}\, x_{I\!P} g(x_{I\!P}, \mu^2) \right]^2. \tag{8}$$

The diffractive slope parameter B_D comes from the t-integration, while the factor R_g accounts for the skewedness of the proton gluon distribution [19]. There are similar contributions from (light) sea quarks, where g in (8) is replaced by $S \equiv 2(\bar{u} + \bar{d} + \bar{s})$, together with an interference term. A sum over all three contributions is implied in (6) and in the second term of (7). The Pomeron PDFs in (6), $a^{I\!P}(z, Q^2; \mu^2)$, are evolved using NLO DGLAP from a starting scale μ^2 up to Q^2, taking the input distributions to be LO Pomeron-to-parton splitting functions, $a^{I\!P}(z, \mu^2; \mu^2) = P_{aI\!P}(z)$ [17].

From (2),

$$a(x, Q^2) = a^{\text{DGLAP}}(x, Q^2) + \Delta a^{\text{abs}}(x, Q^2), \tag{9}$$

where $a(x, Q^2) = xg(x, Q^2)$ or $xS(x, Q^2)$, and

$$\Delta a^{\text{abs}}(x, Q^2) = -\frac{1}{1 - f_{\text{p.diss.}}} \int_x^1 \text{d}x_{I\!P}\; a_{\text{pert.}}^{\text{D}}(x_{I\!P}, x/x_{I\!P}, Q^2). \tag{10}$$

Differentiating (9) with respect to Q^2 gives the evolution equations for the (inclusive) gluon and sea-quark PDFs:

$$\boxed{\frac{\partial a(x, Q^2)}{\partial \ln Q^2} = \frac{\alpha_S}{2\pi} \sum_{a'=q,g} P_{aa'} \otimes a' \;-\; \frac{1}{1 - f_{\text{p.diss.}}} \int_x^1 \text{d}x_{I\!P}\; P_{aI\!P}(x/x_{I\!P})\, f_{I\!P}(x_{I\!P}; Q^2).} \tag{11}$$

Thus (11) is a more precise version of the GLRMQ equations (1), which goes beyond the DLLA and accounts for sea-quark recombination as well as gluon recombination. Consider the recombination of gluons into gluons, for example, in the DLLA where $x \ll x_{I\!P}$, then $P_{gI\!P} = 9/16$ [17]. Taking $R_g = 1$ and $f_{\text{p.diss.}} = 0$, then (11) becomes

$$\frac{\partial xg(x, Q^2)}{\partial \ln Q^2} = \frac{\alpha_S}{2\pi} \sum_{a'=q,g} P_{ga'} \otimes a' \;-\; \frac{9}{16}\, \frac{\alpha_S^2(Q^2)}{B_D\, Q^2} \int_x^1 \frac{\text{d}x_{I\!P}}{x_{I\!P}} \left[x_{I\!P} g(x_{I\!P}, Q^2) \right]^2. \tag{12}$$

[2]The value of $f_{\text{p.diss.}} = 0.5$ is justified by a ZEUS comparison [18] of proton-tagged diffractive DIS data with data which allowed proton dissociation up to masses of 6 GeV, where $f_{\text{p.diss.}} = 0.46 \pm 0.11$ was obtained.

[3]The other two contributions to (4) are described after (13).

Comparing to (1) this is simply the GLRMQ equation with $R^2 = 8B_D$. For numerical results we take $B_D = 6$ (4) GeV^{-2} for light (charm) quarks, which would correspond to $R = \sqrt{8B_D} = 1.4$ (1.1) fm.

The procedure for incorporating absorptive corrections into a (NLO) global parton analysis (in the FFNS) is as follows:

1. Parameterise the x dependence of the input PDFs at a scale $Q_0 \sim 1$ GeV.
2. Evolve the PDFs $xg(x,Q^2)$ and $xS(x,Q^2)$ using the non-linear evolution equation (11). (The non-singlet distributions are evolved using the usual linear DGLAP equations.)
3. Compute

$$F_2(x_{I\!P},Q^2) = \sum_{a=q,g} C_{2,a} \otimes a \; - \; \frac{1}{1-f_{\text{p.diss.}}} \int_{x_{I\!P}}^1 \mathrm{d}x_{I\!P} \; \left[F_{2,\text{direct}}^{\text{D(3)},c\bar{c}} + F_{L,\text{tw.4}}^{\text{D(3)}} \right], \qquad (13)$$

   and compare to data. Here, the two terms inside the square brackets are beyond collinear factorisation, that is, they cannot be written as a convolution of coefficient functions with the PDFs. The first term inside the square brackets corresponds to the process $\gamma^* I\!P \to c\bar{c}$. The second term corresponds to the process $\gamma^* I\!P \to q\bar{q}$, for light quarks with a longitudinally polarised photon. These contributions are calculated as described in Ref. [17].

As usual, these three steps should be repeated with the parameters of the input PDFs adjusted until an optimal fit is obtained. This procedure is our recommended way of accounting for absorptive corrections in a global parton analysis. However, in practice, available NLO DGLAP evolution codes, such as the QCDNUM [20] program, are often regarded as a 'black box', and it is not trivial to modify the usual linear DGLAP evolution to the non-linear evolution of (11). Therefore, we adopt an alternative iterative procedure which avoids the explicit implementation of non-linear evolution, but which is equivalent to the above procedure.

3 Effect of absorptive corrections on inclusive PDFs

We model our analysis of HERA F_2 data [21] on the MRST2001 NLO analysis [11], which was the first in which a negative gluon distribution was required at the input scale of $Q_0 = 1$ GeV. (The more recent MRST sets have not changed substantially at small x.) We apply cuts $x_{I\!P} \leq 0.01$, $Q^2 \geq 2$ GeV^2, and $W^2 \geq 12.5$ GeV^2, leaving 280 data points. The input gluon and sea-quark distributions are taken to be

$$xg(x,Q_0^2) \; = \; A_g \, x^{-\lambda_g} (1-x)^{3.70} (1 + \epsilon_g \sqrt{x} + \gamma_g x) \; - \; A_- \, x^{-\delta_-} (1-x)^{10}, \qquad (14)$$

$$xS(x,Q_0^2) \; = \; A_S \, x^{-\lambda_S} (1-x)^{7.10} (1 + \epsilon_S \sqrt{x} + \gamma_S x), \qquad (15)$$

where the powers of the $(1-x)$ factors are taken from [11], together with the valence-quark distributions, u_V and d_V, and $\Delta \equiv \bar{d} - \bar{u}$. The A_g parameter is fixed by the momentum sum rule, while the other nine parameters are allowed to go free. Since we do not fit to DIS data with $x_{I\!P} > 0.01$, we constrain the input gluon and sea-quark distributions, and their derivatives with respect to x, to agree with the MRST2001 NLO parton set [11] at $x = 0.2$. This is done by including the value of these MRST PDFs at $x = 0.2$, and their derivatives, as data points in the fit, with an error of 10% on both the value of the MRST PDFs and their derivatives. Therefore, the PDFs we obtain are not precisely constrained at large x, but this paper is primarily concerned with the small-x behaviour of the PDFs.

The procedure we adopt is as follows:

(i) Start by performing a standard NLO DGLAP fit to F_2 data with no absorptive corrections.

(ii) Tabulate ΔF_2^{abs}, given by (4), and Δa^{abs}, given by (10), using PDFs $g(x_{I\!P},\mu^2)$ and $S(x_{I\!P},\mu^2)$ obtained from the previous fit.

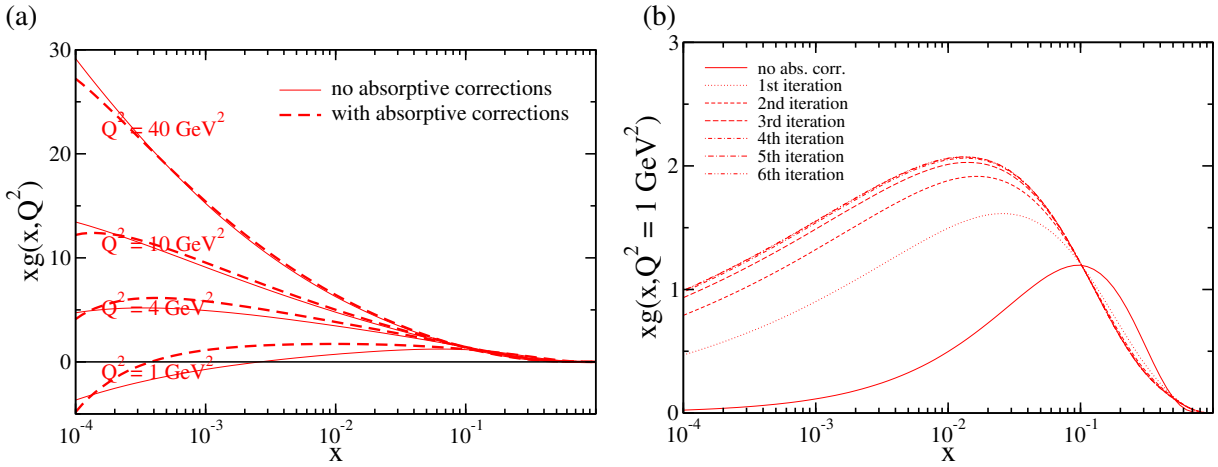

Fig. 3: (a) The gluon distribution obtained from fits to F_2 data, before and after absorptive corrections have been included. (b) The effect of successive iterations on the gluon distribution obtained from fits to F_2, taking a positive definite input gluon at 1 GeV. Each iteration introduces another level of $2 \to 1$ Pomeron mergings.

(iii) Perform a standard NLO DGLAP fit to 'corrected' data, $F_2^{\rm DGLAP} = F_2 - \Delta F_2^{\rm abs}$, to obtain PDFs $a^{\rm DGLAP}$. Then correct these PDFs to obtain $a = a^{\rm DGLAP} + \Delta a^{\rm abs}$. These latter PDFs a then satisfy the non-linear evolution equations (11).

(iv) Go to (ii).

Each successive iteration of steps (ii) and (iii) introduces another level of $2 \to 1$ Pomeron mergings, so that eventually all the 'fan' diagrams are included, achieving the same effect as the procedure described at the end of Section 2.

Note that the correction to the PDFs, $a = a^{\rm DGLAP} + \Delta a^{\rm abs}$, in each step (iii), was omitted in our previous analysis [13]. Consequently, the effect of the absorptive corrections on the PDFs at large scales was overestimated. Also in [13], the known LO $P_{a I\!P}(z)$ were multiplied by free parameters ('K-factors'), determined from separate fits to diffractive DIS data, in an attempt to account for higher-order pQCD corrections to the LO Pomeron-to-parton splitting functions. However, since these K-factors took unreasonable values, with some going to zero, here we have chosen to fix them to 1. Therefore, the updated analysis, presented here, does not require a simultaneous fit to the diffractive DIS data.

In Fig. 3(a) we show the gluon distribution at scales $Q^2 = 1$, 4, 10, and 40 GeV^2 obtained from fits before and after absorptive corrections have been included. Both fits are almost equally good with $\chi^2/{\rm d.o.f.}$ values of 0.86 and 0.87 for the fits without and with absorptive corrections respectively. At low Q^2 the absorptive corrections give an increased gluon distribution at small x, apart from at $x \lesssim 10^{-4}$ where there are only a few data points and where additional absorptive effects (Pomeron loops) may become important. The non-linear term of (11) slows down the evolution, so that by 40 GeV^2 the two gluon distributions are roughly equal; see Fig. 3(a).

We repeated the fits without the negative term in the input gluon distribution, that is, without the second term in (14). When absorptive corrections were included, almost the same quality of fit was obtained ($\chi^2/{\rm d.o.f.} = 0.90$), while without absorptive corrections the fit was slightly worse ($\chi^2/{\rm d.o.f.} = 0.95$). We conclude that absorptive corrections lessen the need for a negative gluon distribution at $Q^2 = 1$ GeV^2. The gluon distributions obtained from six successive iterations of steps (ii) and (iii) above are shown in Fig. 3(b). The convergence is fairly rapid, with only the first three iterations having a significant effect, that is, the 'fan' diagrams which include $8 \to 4 \to 2 \to 1$ Pomeron mergings.

Although we have seen that the inclusion of absorptive corrections has reduced the need for a *negative* gluon, it has not solved the problem of the *valence-like* gluon. That is, the gluon distribution at low scales still decreases with decreasing x, whereas from Regge theory it is expected to behave as

$xg \sim x^{-\lambda_{\rm soft}}$ with $\lambda_{\rm soft} \simeq 0.08$. We have studied several possibilities of obtaining a satisfactory fit with this behaviour [13]. The only modification which appears consistent with the data (and with the desired $\lambda_g = \lambda_S$ equality) is the inclusion of power-like corrections, specifically, a global shift in all scales by about 1 GeV^2. (Note that a similar shift in the scale is required in the dipole saturation model [22].) However, we do not have a solid theoretical justification for this shift. Therefore, a more detailed, and more theoretically-motivated, investigation of the effect of power corrections in DIS is called for.

References

[1] Gribov, L. V. and Levin, E. M. and Ryskin, M. G., Phys. Rept. **100**, 1 (1983).

[2] Mueller, Alfred H. and Qiu, Jian-wei, Nucl. Phys. **B268**, 427 (1986).

[3] Jalilian-Marian, Jamal and Kovchegov, Yuri V., Prog. Part. Nucl. Phys. (in press) (hep-ph/0505052).

[4] Thorne, Robert S., Phys. Lett. **B474**, 372 (2000);
Altarelli, Guido and Ball, Richard D. and Forte, Stefano, Nucl. Phys. **B674**, 459 (2003);
Ciafaloni, Marcello and Colferai, Dimitri and Salam, Gavin P. and Stasto, Anna M., Phys. Lett. **B587**, 87 (2004).

[5] Khoze, V. A. and Martin, A. D. and Ryskin, M. G. and Stirling, W. J., Phys. Rev. **D70**, 074013 (2004).

[6] Salam, G. P., hep-ph/0501097.

[7] Kwiecinski, J. and Martin, Alan D. and Stirling, W. James and Roberts, R. G., Phys. Rev. **D42**, 3645 (1990).

[8] Donnachie, A. and Landshoff, P. V., Phys. Lett. **B296**, 227 (1992).

[9] Martin, A. D. and Roberts, R. G. and Stirling, W. J. and Thorne, R. S., Phys. Lett. **B604**, 61 (2004).

[10] Pumplin, J. and others, JHEP **07**, 012 (2002).

[11] Martin, Alan D. and Roberts, R. G. and Stirling, W. J. and Thorne, R. S., Eur. Phys. J. **C23**, 73 (2002).

[12] Eskola, K. J. and Honkanen, H. and Kolhinen, V. J. and Qiu, Jian-wei and Salgado, C. A., Nucl. Phys. **B660**, 211 (2003).

[13] Martin, A. D. and Ryskin, M. G. and Watt, G., Phys. Rev. **D70**, 091502 (2004).

[14] Abramovsky, V. A. and Gribov, V. N. and Kancheli, O. V., Yad. Fiz. **18**, 595 (1973).

[15] Bartels, Jochen and Ryskin, M. G., Z. Phys. **C76**, 241 (1997).

[16] Martin, A. D. and Ryskin, M. G. and Watt, G., Eur. Phys. J. **C37**, 285 (2004).

[17] Martin, A. D. and Ryskin, M. G. and Watt, G., Eur. Phys. J. **C**, (in press) (hep-ph/0504132).

[18] Chekanov, S. and others, Eur. Phys. J. **C25**, 169 (2002).

[19] Shuvaev, A. G. and Golec-Biernat, K. J. and Martin, Alan D. and Ryskin, M. G., Phys. Rev. **D60**, 014015 (1999).

[20] Botje, M., QCDNUM version 16.12, ZEUS Note 97-066 (unpublished), available from `http://www.nikhef.nl/~h24/qcdcode/`.

[21] Breitweg, J. and others, Eur. Phys. J. **C7**, 609 (1999);
Chekanov, S. and others, Eur. Phys. J. **C21**, 443 (2001);
Adloff, C. and others, Eur. Phys. J. **C21**, 33 (2001);
Adloff, C. and others, Eur. Phys. J. **C19**, 269 (2001);
Adloff, C. and others, Eur. Phys. J. **C13**, 609 (2000).

[22] Bartels, J. and Golec-Biernat, K. and Kowalski, H., Phys. Rev. **D66**, 014001 (2002);
Kowalski, Henri and Teaney, Derek, Phys. Rev. **D68**, 114005 (2003).

Multiple Scattering at HERA and at LHC - Remarks on the AGK Rules

J. Bartels
II. Institut für Theoretische Physik, Universität Hamburg
Luruper Chaussee 149, D-22761 Hamburg, Germany

Abstract
We summarize the present status of the AGK cutting rules in perturbative QCD. Particular attention is given to the application of the AGK analysis to multiple scattering in DIS at HERA and in pp collisions at the LHC

1 Introduction

Multiple parton interactions play an important role both in electron proton scattering at HERA and in high energy proton proton collisions at the LHC. At HERA, the linear QCD evolution equations provides, for not too small Q^2, a good description of the F_2 data (and of the total $\gamma^* p$ cross section, $\sigma_{tot}^{\gamma^* p}$). This description corresponds to the emission of partons from a single chain (Fig.1a). However, at low Q^2 where the transition to nonperturbative strong interaction physics starts, this simple picture has to supplemented with corrections. First, there exists a class of models [1] which successfully describe this transition region; these models are based upon the idea of parton saturation: they assume the existence of multiple parton chains (Fig.1b) which interact with each other, and they naturally explain the observed scaling behavior, $F_2(Q^2, x) \approx F_2(Q^2/Q_s^2(x))$ with $Q_s^2(x) = Q_0^2(1/x)^\lambda$. Next, in the photoproduction region, $Q^2 \approx 0$, direct evidence for the presence of multiple interactions also comes from the analysis of final states [2]. A further strong hint at the presence of multi-chain configurations comes from the observation of a large fraction of diffractive final states in deep inelastic scattering at HERA. In the final states analysis of the linear QCD evolution equations, it is expected that the produced partons are not likely to come with large rapidity intervals between them. In the momentum-ordered single chain picture (Fig.1a), therefore, diffractive final states should be part of the initial conditions (inside the lower blob in Fig.1a), i.e. they should lie below the scale Q_0^2 which seperates the parton description from the nonperturbative strong interactions. This assignment of diffractive final states, however, cannot be complete. First, data have shown that the Pomeron which generates the rapidity gap in DIS diffraction is harder than in hadron - hadron scattering; furthermore, there are specific diffractive final states with momentum scales larger than Q_0^2, e.g. vector mesons built from heavy quarks and diffractive dijets (illustrated in Fig.2): the presence of such final states naturally requires corrections to the single chain picture (Fig.2b). From a t-channel point of view, both Fig.1b and Fig.2b belong to the same class of corrections, characterized by four gluon states in the t-channel.

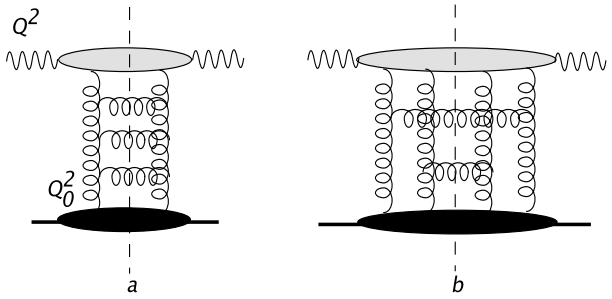

Fig. 1: Contributions to the total cross section $\sigma_{tot}^{\gamma^* p}$: (a) the single chain representing the linear QCD evolution equations; (b) gluon production from two different gluon chains.

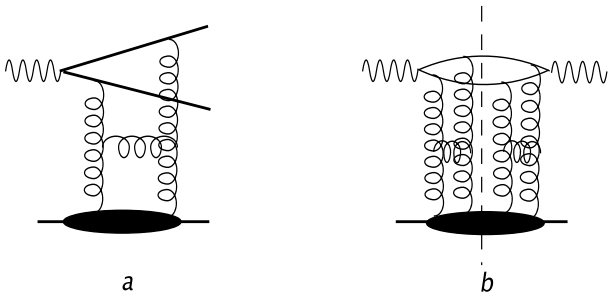

Fig. 2: Hard diffractive final states.(a) dijet production; (b) the diffractive cross section as s-channel discontinuity of a two-ladder diagram.

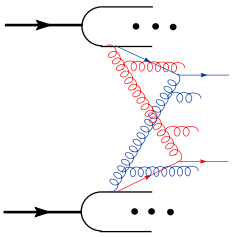

Fig. 3: Jet production in pp collisions from two different parton chains

In proton-proton collisions corrections due to multiple interactions should be important in those kinematic regions where parton densities for small momentum fractions values and for not too large momentum scales are being probed, e.g. jet production near the forward direction. Another place could be the production of multijet final states (Fig.3): multiple jets may come from different parton chains, and these contributions may very well affect the background to new physics beyond the standard model. Moreover, the modelling of multijet configurations will be necessary for understanding the underlying event structure in pp collidions [3].

From the point of view of collinear factorization, multiple interactions with momentum ordered parton chains are higher-twist effects, i.e they are suppressed by powers of the hard momentum scale. At small x, however, this suppression is compensated by powers of the large logarithms, $\ln 1/x$: multiple interactions, therefore, are mainly part of small-x physics. In this kinematic region the Abramovsky-Gribov-Kanchelli (AGK) [4] rules can be applied to the analysis of multi-gluon chains, and it is the aim of this article to present a brief overview about the current status of the AGK rules in pQCD.

As we will discuss below, in the analysis of multiple parton chains the couplings of n gluons to the proton play an essential role. Regge factorization suggests that these coupling should be universal, i.e. the couplings in $\gamma^* p$ collisions at HERA are the same as those in pp scattering at the LHC. Therefore, a thorough analysis of the role of multiple interactions in deep inelastic electron-proton scattering at HERA should be useful for a solid understanding of the structure of events at the LHC.

2 Basics of the AGK cutting rules

The original AGK paper [4], which was written before the advent QCD, addresses the question how, in the optical theorem,

$$\sigma_{tot}^{pp} = \frac{1}{s} Im\, T_{2\to 2} \;=\; \sum_f \int d\Omega_f |T_{i\to f}|^2 \qquad (1)$$

the presence of multi-Pomeron exchanges (Fig.4) in the total hadron-hadron cross section leads to observable effects in the final states (rhs of eq.(1)). Based upon a few model-independent assumptions

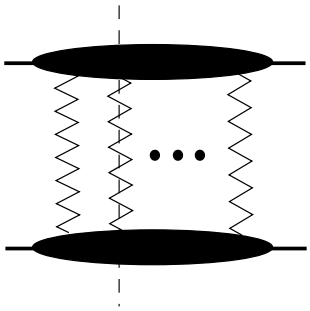

Fig. 4: s-cut through a multi-Pomeron exchange: the zig-zag lines stand for nonperturbative Pomerons.

on the couplings of multi-Pomeron exchanges to the proton, the authors derived simple 'cutting rules': different contributions to the imaginary part belong to different cuts across the multi-Pomeron diagrams, and each cut has its own, quite distinct, final state characteristics. As a result, the authors found counting rules for final states with different particle multiplicities, and they proved cancellations among rescattering corrections to single-particle and double-particle inclusive cross sections.

In the QCD description of hard (or semihard) final states a close analogy appears between (color singlet) gluon ladders and the nonperturbative Pomeron: multiple parton chains (for example, the two chains in Fig.1b) can be viewed as cuts through two perturbative BFKL Pomerons. In the same way as in the original AGK paper, the question arises how different cuts through a QCD multi-ladder diagram can be related to each other. In the following we briefly describe how AGK cutting rules can be derived in pQCD [5,6]. In the subsequent section we will present a few new results which come out from pQCD calculations, going beyond the original AGK rules.

One of the few assumptions made in the original AGK paper states that the coupling of the Pomerons to the external particle are (i) symmetric under the exchange of the Pomerons (Bose symmetry), and (ii) that they remain unchanged if some of the Pomerons are beeing cut. These properties also hold in pQCD, but they have to be reformulated: (i') the coupling of (reggeized) gluons to external particles is symmetric under the exchange of reggeized gluons, and (ii') it remains unchanged if we introduce cutting lines between the gluons. In QCD, however, the color degree of freedom also allows for another possibility: inside the n-gluon state (with total color zero), a subsystem of two gluons can form an antisymmetric color octet state: in this case the two gluons form a bound state of a reggeized gluon (bootstrap property). For the case of $\gamma^*\gamma^*$ scattering, explicit calculations [7] have shown that the coupling of n gluons to virtual photons can be written as a sum of several pieces: the fully symmetric ('irreducible') one which satisfies (i') and (ii'), and other pieces which, by using the bootstrap property, can be reduced to symmetric couplings of a smaller number of gluons ('cut reggeons'). This decomposition is illustrated in Fig.5.

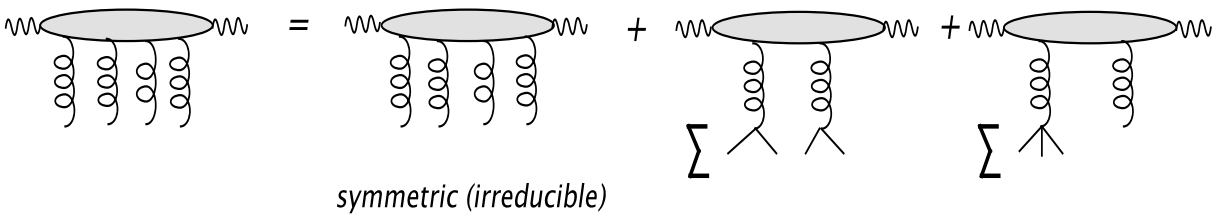

Fig.5 Decomposition of the coupling of four gluons to a virtual photon. In the last two terms on the rhs it is understood that we have to sum over different pairings of gluons at the lower end.

Since the bootstrap property is related to the regeization of the gluon and, therefore, is expected to be valid to all orders perturbation theory, also these properties of the couplings of multi-gluon states to

external particles should be of general validity. In this short review we will mainly concentrate on the symmetric couplings.

As an illustrative example, we consider the coupling of four gluons to a proton. The simplest model of a symmetric coupling is a sum of three pieces, each of which contains only the simplest color structure:

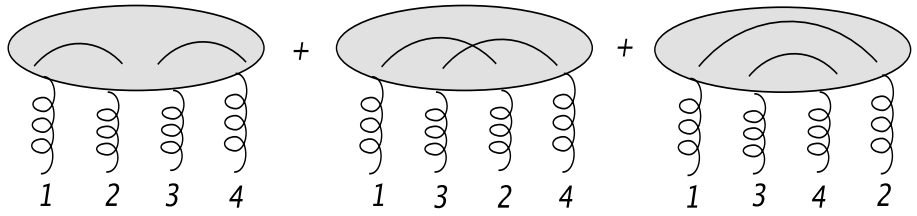

Fig.6 The symmetric coupling of four gluons to an external particle. The lines inside the blob denote the color connection, e.g. the first term has the color structure $\delta_{a_1a_2}\delta_{a_3a_4}$.

The best-known cutting rule for the four gluon exchange which follows [5,6] from this symmetry requirement is the ratio between the three different pairings of lines:

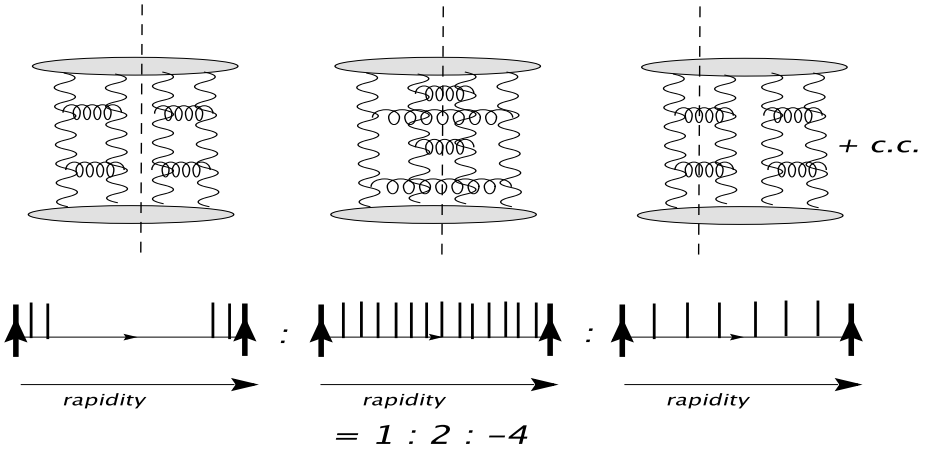

Fig 7: different cutting lines in the four-gluon exchange.

Each term, on the partonic level, corresponds to a certain multiplicity structure of the final state: a rapidity gap ('zero multiplicity'), double multiplicity, and single multiplicity. Simple combinatorics then leads to the ratio

$$1 : 2 : -4. \tag{2}$$

In order to be able to generalize and to sum over an arbitrary number of gluon chains, it is convenient to use an eikonal ansatz:

$$N_{2n}^A(\boldsymbol{k}_1, a_1; \ldots; \boldsymbol{k}_{2n}, a_{2n}; \omega) =$$

$$\frac{1}{\sqrt{(N_c^2-1)^n}} \left(\sum_{Pairings} \phi^A(\boldsymbol{k}_1, \boldsymbol{k}_2; \omega_{12}) \delta_{a_1 a_2} \cdot \ldots \cdot \phi^A(\boldsymbol{k}_{2n-1}, \boldsymbol{k}_{2n}; \omega_{2n-1,2n}) \delta_{a_{2n-1} a_{2n}} \right) . \tag{3}$$

Inserting this ansatz into the hadron - hadron scattering amplitude, using the large-N_c approximation, and switching to the impact parameter representation, one obtains, for the contribution of k cut gluon ladders, the well-known formula:

$$ImA_k = 4s \int d^2\boldsymbol{b} e^{i\boldsymbol{q}\boldsymbol{b}} P(s, \boldsymbol{b}) \tag{4}$$

where

$$P(s,\boldsymbol{b}) \;=\; \frac{[\Omega(s,\boldsymbol{b})]^k}{k!}e^{-\Omega(s,\boldsymbol{b})}, \tag{5}$$

and Ω stands for the (cut) two-gluon ladder.

Another result [6] which follows from the symmetry properties of the n gluon-particle coupling is the cancellation of rescattering effects in single and double inclusive cross sections. In analogy with the AGK results on the rescattering of soft Pomerons, it can be shown that the sum over multi-chain contributions and rescattering corrections cancels (Fig.8),

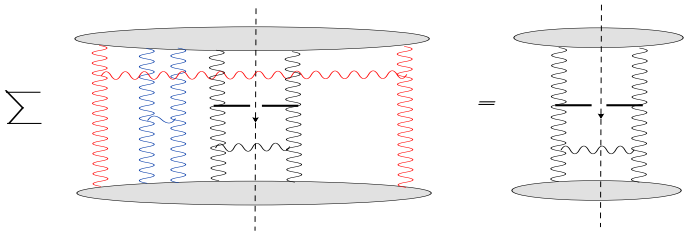

Fig 8: AGK cancellations in the one-jet inclusive cross section.

leaving only the single-chain contribution (in agreement with the factorization obtained in the collinear analysis). This statement, however, holds only for rescattering between the two projectile: it does not affect the multiple exchanges between the tagged jet and the projectile (Fig.9) which require a seperate discussion (see below).

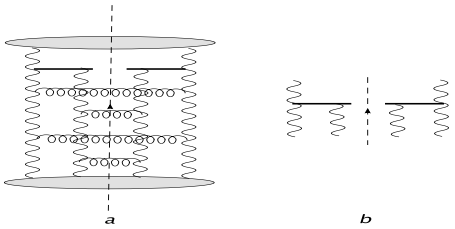

Fig 9: (a) Nonvanishing rescattering corrections in the one-jet inclusive cross section; (b) a new vertex: $g + 2g \rightarrow jet$.

All these results can be generalized to include also the soft Pomeron: all one needs to assume is that the couplings of soft Pomerons and reggeized gluons are symmetric under interchanges, and they are not altered if cutting lines are introduced.

3 New results

Explicit calculations in QCD lead to futher results on multiple interactions. First, in the four gluon exchange there are other configurations than those shown in Fig.7; one example is depicted in Fig.10. Here the pairing of gluon chains switches from $(14)(23)$ in the upper part (= left rapidity interval) to $(12)(34)$ in the lower part (= right rapidity interval).

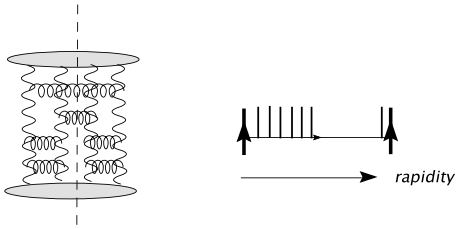

Fig 10: Decomposition into two rapidity intervals: the upper (left) interval has double multiplicity, the lower (right) one corresponds to a rapidity gap.

One can show that the ratio $1 : 2 : -4$ holds for each rapidity interval. In [6] this has been generalized to an arbitrary number of exchanged gluon lines.

Another remark applies to the applicability of the cutting rules to rescattering corrections in the single jet inclusive cross section (Fig.9). Below the jet vertex we, again, have an exchange of four gluon lines, similar to the diagram in the middle of Fig.7. As to the cutting rules, however, there is an important difference between the two situations. In Fig.7, the blob above the four gluons is totally inclusive, i.e. it contains an unrestricted sum over s-channel intermediate states, whereas in Fig.9 the part above the four gluon state is semi-inclusive , i.e. it contains the tagged jet. This 'semi-inclusive' nature destroys the symmetry above the four gluon states, and the cutting rules have to be modified [8,9]. In particular, eqs.(3) - (4) are not applicable to the rescattering corrections between the jet and projectile. A further investigation of these questions is in progress [10].

Finally a few comments on reggeization and cut reggeons. Clearly there are more complicated configurations than those which we have discussed so far; an example appears in $\gamma^* p$ scattering (deep inelastic electron proton scattering). In contrast to pp scattering, the coupling of multi-gluon chains to the virtual photon can be computed in pQCD, and the LO results, for the case of $n = 4$ gluons, are illustrated in Fig.11.

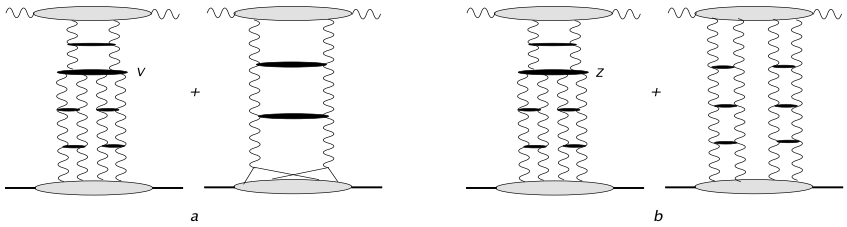

Fig.11: Four-gluon contributions to $\gamma^* p$ proton scattering: two equivalent ways of summing over all contributions. (a) the decomposition of Fig.5 with the pQCD triple Pomeron vertex. (b) an alternative way of summation which explicitly shows the coupling of two Pomerons to the photon vertex and which leads to a new vertex Z.

It turns out that we have two alternative possibilities: in the completely inclusive case (total cross section), it is convenient to chose Fig.11a, i.e. the sum of all contributions can be decomposed into two sets of diagrams. In the first set, at the top of the diagram two gluons couple to the quark-antiquark pair, and the subsequent transition to the four-gluon state goes via the pQCD triple Pomeron vertex. This vertex, as a function of the 4 gluons below, has the symmetry properties described above. As a result, we can apply the cutting rules to the four gluon state, as discussed before. However, there is also the second term in Fig.11a, which consists of a two gluon state only: this is the reggeizing contribution we have mentioned before. As indicated in the figure, the splitting of the reggized gluons at the bottom amounts to a change in the (nonperturbative) coupling. We want to stress that, because of the inclusive nature of this set of diagrams, the triple Pomeron vertex V in Fig.11a, similar to the BFKL kernel, contains both real and virtual contributions. For this reason, the decomposition in Fig.11a is applicable to inclusive cross sections, and it is not convenient for investigating specific final states such as, for example, diffractive final states with a fixed number of quarks and gluons in the final state.

There exists an alternative way of summing all contributions (Fig.11b) which is completely equivalent to Fig.11a but allows to keep track of diffractive $q\bar{q}$, $q\bar{q}g$,... final states: this form is illustrated in Fig.11b. One recognizes the 'elastic intermediate state' which was not visible in Fig.11a, and the new triple Pomeron vertex Z which contains only real gluon production. This vertex Z, as discussed in [11] is no longer symmetric under permutations of the gluons at the lower end; consequently, we cannot apply the AGK cutting rules to the four gluon states below.. These findings for multiple scattering effects in DIS imply, strictly speaking, that cross sections for diffractive $q\bar{q}$ or $q\bar{q}g$ states cannot directly be inserted into the counting rules (2).

Also pp scattering will contain corrections due to multiple interactions which are more complex. There are, for example, graphs which contain the $2 \to 4$ gluon vertex V, leading to a change of the

number of gluon lines (Fig.12).

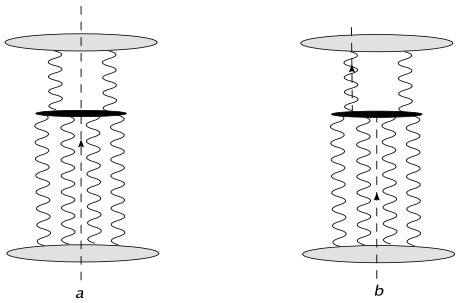

Fig 12: A correction in which the number of lines changes.
The black vertex denotes the $2 \to 4$ gluon vertex.

Since this $2 \to 4$ gluon vertex, as a function of the four gluons below the vertex, satisfies the symmetry requirements listed above, we can apply our previous analysis to the cutting lines below the vertex. In addition, however, one can ask how the lines continue above the $2 \to 4$ gluon vertex: we show two examples, one of them containing a cut (reggeized) gluon. Concentrating on this two-gluon state (i.e. we imagine that we have already summed over all possible cutting lines below the vertex V), the counting rules are quite different: in contrast to the even-signature Pomeron, the gluon is a odd-signature reggeon. Consequently, the cut gluon is suppressed w.r.t. the uncut gluon by one power in α_s, and this suppression leads to the following hierarchy of cutting lines: the cut between the gluons belongs to leading order, the cut through one of the two reggeized gluons is supressed by one power in α_s, the cut through both reggeized gluons is double suppressed (order α_s^2). A closer analysis of this question is under investigation [10].

4 Conclusions

Corrections due to multiple interactions seem to be important in DIS at small x and low Q^2; they are expected to play a significant role also in multijet production in pp scattering. The study of the AGK rules to pQCD provides help in understanding the systematics of multiple gluon chains. Results described in this review represent the beginning of a systematic analysis. We have listed a few questions which require further work.

As an immediate application, we believe that a quantitative analysis of multiple scattering at HERA will provide a useful input to the modelling of final states at the LHC.

A question of practical importance which we have not addressed at all is the hadronization of partonic final states. All statements on ratios of 'particle densities in the final states' made in this paper refer to the parton (gluon) level. However, the hadronization of events which, for example, belong to a double-cut ladder configuration may be quite different from the one obtained by applying just the normal single-chain hadronization to each chain seperately. The answer to this question [1] goes beyond the AGK analysis discussed in this paper.

References

[1] K.Golec-Biernat and M.Wusthoff, *Phys.Rev.* **D59**: 014017,1999; e-Print Archive: hep-ph/9807513; *Phys.Rev.***D60**: 114023,1999; e-Print Archive: hep-ph/9903358.
J.Bartels, K.Golec-Biernat, H.Kowalski, *Phys.Rev.***D66**: 014001,2002; e-Print Archive: hep-ph/0203258.

[2] C.Gwenlan, *Acta Phys.Polon.***B35**: 377-386,2004.

[1] I thank G.Gustafson for a very useful discussion on this point.

[3] T.Sjostrand and P.Z.Skands, *Eur.Phys.J.***C39**: 129-154, 2005; e-Print Archive: hep-ph/0408302 and references therein.

[4] V.A.Abramovsky, V.N.Gribov, O.V.Kanchelli, *Yad.Fiz.* **18**, 595 (1973) [Sov.J.Nucl.Phys.**18** 308 (1974)].

[5] J.Bartels, M.G.Ryskin, *Z.Phys.***C76**: 241-255,1997; e-Print Archive: hep-ph/9612226

[6] J.Bartels, M.Salvadore, G.P.Vacca, *Eur.Phys.J.* **C42**: 53-71,2005; e-Print Archive: hep-ph/0503049.

[7] J.Bartels, M.Wüsthoff, *Z.Phys.***C66**: 157-180,1995.

[8] Yu.V.Kovchegov, K.Tuchin, *Phys.Rev.***D65**: 074026,2002; e-Print Archive: hep-ph/0111362.

[9] M.Braun, *Eur.Phys.J.***C42**: 169-181,2005; e-Print Archive: hep-ph/0502184.

[10] J.Bartels, M.Salvadore, G.P.Vacca, in preparation.

[11] J.Bartels, M.Braun, G.P.Vacca, *Eur.Phys.J.* **C40**: 419-433,2005; e-Print Archive: hep-ph/0412218.

Multiple Interactions in DIS

Henri Kowalski
Deutsches Elektronen Synchrotron DESY, 22603 Hamburg

Abstract
The abundance of diffractive reactions observed at HERA indicates the presence of multiple interactions in DIS. These interactions are analysed, first in a qualitative way, in terms of QCD Feynman diagrams. Then a quantitative evaluation of diffractive and multiple interaction is performed with the help of the AGK cutting rules applied within an Impact Parameter Dipole Saturation Model. The cross-sections for multiple and diffractive interactions are found to be of the same order of magnitude and to exhibit a similar Q^2 dependence.

1 Introduction

One of the most important observations of HERA experiments is the rapid rise of the structure function F_2 with decreasing x indicating the presence of abundant gluon radiation processes [1]. The observation of a substantial diffractive component in DIS processes, which is also quickly rising with decreasing x, is equally important. The diffractive contribution at HERA is of a leading-twist type, i.e. the fraction of diffractive events remains constant or decreases only logarithmically with increasing Q^2. The presence of a substantial diffractive component suggests that, in addition to the usual partonic single ladder contribution, also multi-ladder processes should be present.

In this talk I will first discuss the general role of multi-ladder contributions in DIS scattering, called for historical reasons multi-Pomeron processes. The concept of a Pomeron is very useful in the discussion of high energy scattering processes since it relates, by the AGK cutting rules [2], seemingly different reactions like inclusive, diffractive and multiple scattering. I will present a numerical estimate of the magnitude of diffractive and of multi-Pomeron contributions, using AGK cutting rules within a dipole model which has been shown to provide a good description of HERA DIS data [3].

2 General Analysis

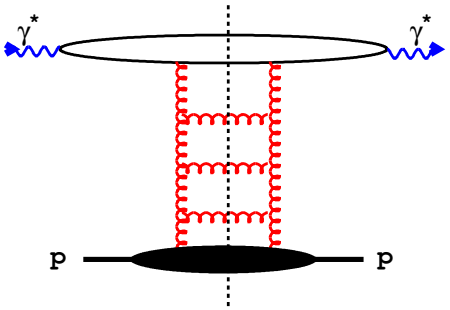

Fig. 1: The single gluon-ladder contribution to the total $\gamma^* p$ cross section. The blob at the lower end of the diagrams contains the physics below the scale Q_0^2 which seperates hard from soft physics, whereas the blob at the upper end contains hard physics that can be described by pQCD. The dashed line denotes the cut.

Let us first recall that the main properties of HERA interactions can be related to the properties of the elastic amplitude, $A_{\gamma^* p \to \gamma^* p}$, which, by the optical theorem, is directly related to the total $\gamma^* p$ cross-section:

$$\sigma_{\gamma^* p} = \frac{1}{W^2} Im\, A_{\gamma^* p \to \gamma^* p}(W^2, t = 0). \tag{1}$$

Here W denotes the $\gamma^* p$ CMS energy and t the 4-momentum transfer of the elastically scattered proton. At not too small Q^2, the total cross section is dominated by the single ladder exchange shown in Fig. 1; the ladder structure also illustrates the linear DGLAP evolution equations that are used to describe the F_2 data. In the region of small x, gluonic ladders are expected to dominate over quark ladders. The cut lines in Fig. 1 mark the final states produced in a DIS event: a cut parton (gluon) hadronizes and leads to jets or particles seen in the detector. It is generally expected that partons produced from a single chain are unlikely to generate large rapidity gaps between them, since large gaps are exponentially suppressed as a function of the gap size. Therefore, in the single ladder contribution of Fig. 1, diffractive final states only reside inside the blob at the lower end, i.e. lie below the initial scale Q_0^2.

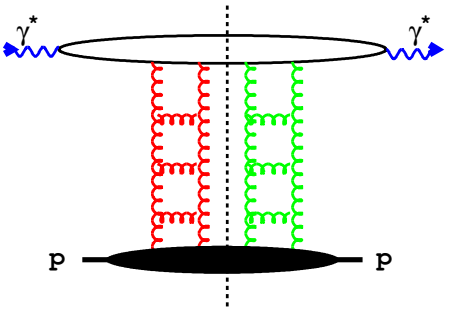

Fig. 2: The double-gluon ladder contribution to the inclusive diffractive $\gamma^* p$ cross section

The properties of diffractive reactions at HERA, however, give clear indications that significant contributions from multi-ladder exchanges should be present: not all diffractive final states are soft, in particular the diffractive production of jets and charm was observed [4, 5]. In addition, the inclusive diffractive cross-section is rising as quickly as the total cross-section with increasing W [6] and the exclusive diffractive production of J/Ψ and Υ vector meson exhibits a rise with energy which is about twice as fast [7]. In short, the Pomeron exchanged in inclusive diffractive DIS is harder than the hadronic soft Pomeron and therefore, one should expect that the majority of the observed diffractive final states cannot be absorbed into the blob of soft physics of Fig. 1. Instead, double ladder exchange, Fig. 2, provides a potential source for these harder diffractive states: the cut blob at the upper end may contain $q\bar{q}$ and $q\bar{q}g$ states which hadronize into harder jets or particles. Further evidence for the presence of multi-ladder contribution comes from saturation models which have been shown to successfully describe HERA F_2 data in the transition region at low Q^2 and small x: these models are explicitly built on the idea of summing over multiple exchanges of single ladders (or gluon densities).

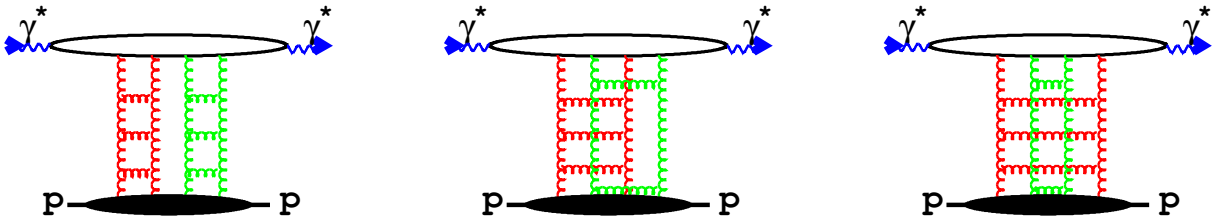

Fig. 3: The double-gluon ladder contribution to the elastic $\gamma^* p$ amplitude

Let us analyse the content of a double ladder exchange contribution (for a more detailed analysis see Ref. [8]). It is easiest to begin with the elastic $\gamma^* p$ scattering amplitude, Fig. 3: from a t-channel point of view, the two gluon ladders form a four gluon intermediate state which has to be symmetric under permutations of the gluon lines (Bose symmetry). Therefore, on the amplitude level one cannot distinguish between different diagrams of Fig. 3. Invoking now the optical theorem, (1), different contributions to the total cross section correspond to different cuts through the two-ladder diagrams: they

are shown in Fig. 4, ordered w.r.t. the density of cut gluons. In Fig. 4a, the cut runs between the two ladders: on the both sides of the cut there is a color singlet ladder, and we expect a rapidity gap between the upper blob (containing, for example, a diffractive $q\bar{q}$ final state) and the proton remnants inside the lower blob. Similarly, the diagram of Fig. 4b describes a single cut ladder with a final state similar to the one ladder contribution in Fig. 1; this contribution simply represents a correction to the one ladder contribution. Finally, the diagram of Fig. 4c belongs to final states with double density of cut partons. As outlined in [9], the correct counting of statistic factors and combinatorics leads to the result that the contributions shown in Fig. 4 a - c are identical, up to the overall counting factors $1 : -4 : 2$.

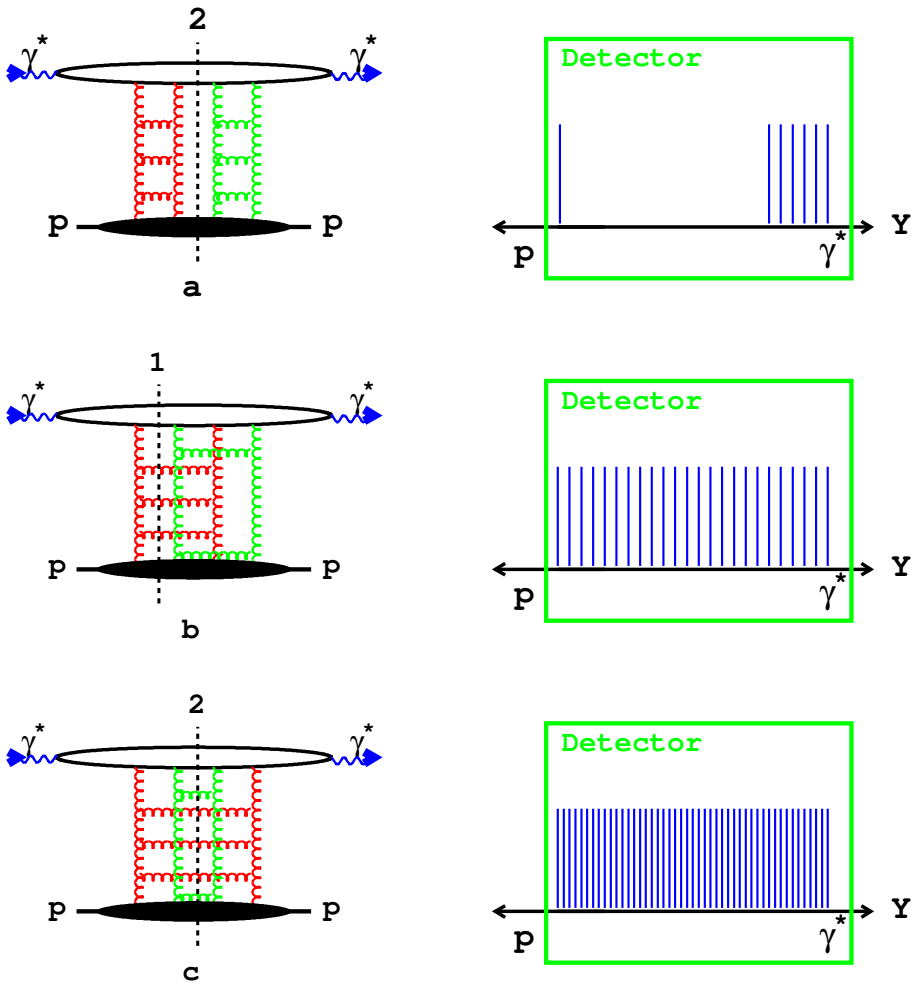

Fig. 4: Three examples of 2-ladder contributions (lhs), with the corresponding, schematical, detector signatures (rhs). *Top row*: the diagram (a) with the cut positions (2) describes diffractive scattering. *Middle row*: the diagram (b) with the cut position (1) describes inclusive final states with single densityof cut partons. *Bottom row*: the diagram (c) with the cut position (2) describes inclusive final states with increased multiplicity.

Experimentally it is easy to differentiate between diffractive and *single* or *multiple* inclusive final states since diffractive states exhibit large rapidity gaps. The *multiple* inclusive final states should also be distinct from the *single* inclusive ones since, at least naively, we would expect that in the *multiple* case the particle multiplicity should be considerably higher. At low x, however, the relation between the number of virtual states excited in the interaction (as measured by F_2) and the final particle multiplicity cannot be straight-forward since the growth of F_2 with decreasing x is faster than the multiplicity increase. This may indicate that the hadronization mechanism may be different from the string picture commonly used in the hadronization procedure of single chain parton showers. The influence of multiple scattering on

the particle multiplicity of the final states should also be damped by the energy conservation. The cut through several Pomerons leads clearly to more gluons produced in the final state, but the available energy to produce particles in the hadronization phase remains the same. A detailed Monte Carlo program is therefore necessary to evaluate this effect.

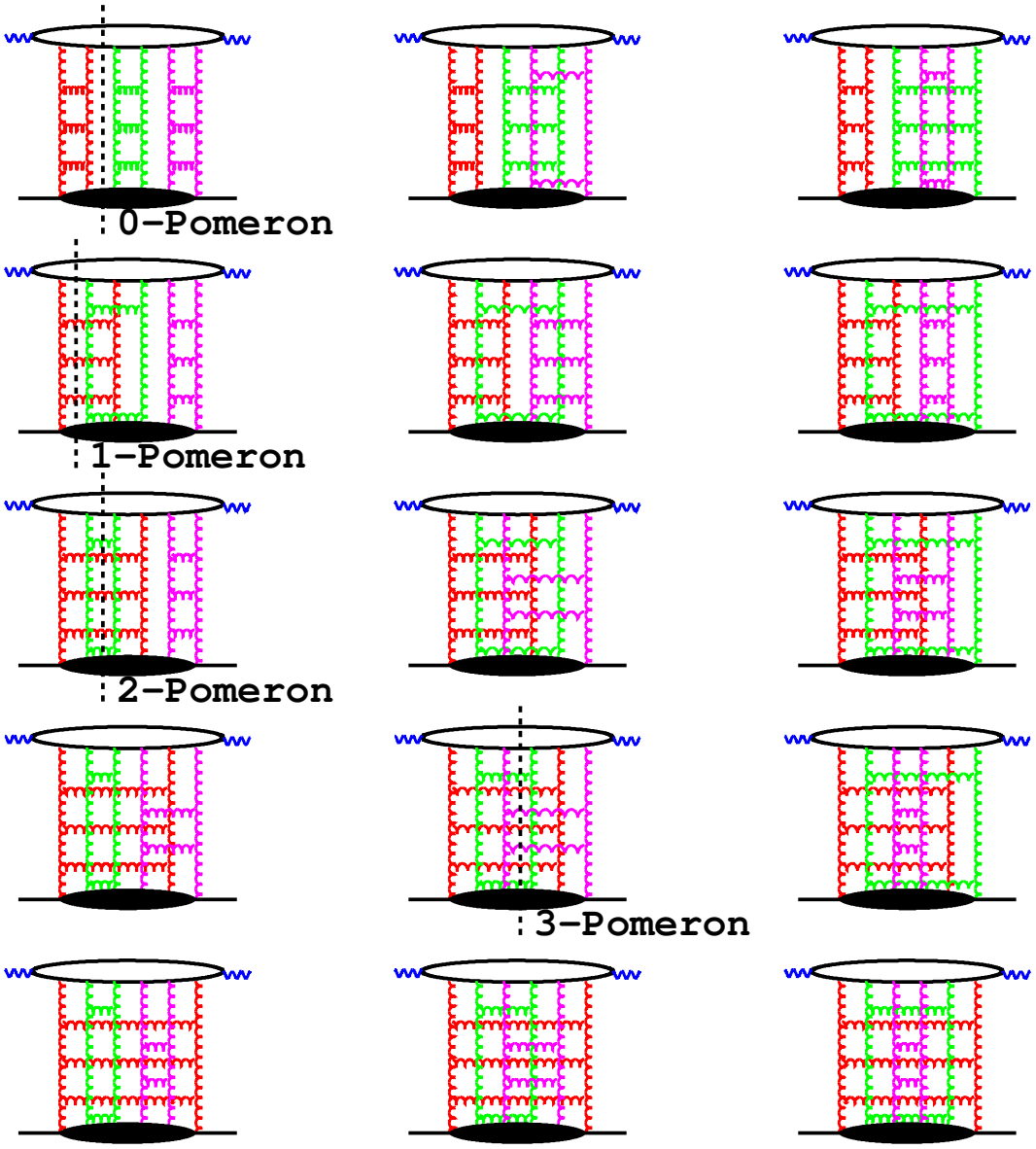

Fig. 5: 3-Pomeron contributions to the elastic $\gamma^* p$ amplitude. All 15 possible diagrams are shown with some examples of Pomeron cuts.

The number of diagrams contributing to the reaction amplitude increases very quickly with the number of Pomerons. For the 3-Pomeron amplitude the gluons can be paired in 15 possible ways, shown in Fig. 5 with the examples of 0-Pomeron, 1-Pomeron, 2-Pomeron and 3-Pomeron cuts. For m-Pomerons the number of possible gluon pairs and also diagrams is:

$$(2m-1)(2m-3)(2m-5)....=(2m-1)!/(2^{m-1}(m-1)!).$$

Assuming that all the diagrams for a given multi-Pomeron exchange amplitude contribute in the same way, the above analysis suggests that the probability for different cuts to contribute should be given

by the combinatorial factors. This is the content of the AGK rules which were obtained from the analysis of field theoretical diagrams well before QCD was established [2] and which relate the cross-section, σ_k, for observing a final state with k-cut Pomerons with the amplitudes for exchange of m Pomerons, $F^{(m)}$:

$$\sigma_k = \sum_{m=k}^{\infty} (-1)^{m-k}\, 2^m\, \frac{m!}{k!(m-k)!} F^{(m)}. \tag{2}$$

The same result is also obtained from a detailed analysis of the Feynman diagram contributions in QCD with the oversimplified assumption that only the symmetric part of the two-gluon couplings contributes [9].

3 Multiple Interactions in the Dipole Model

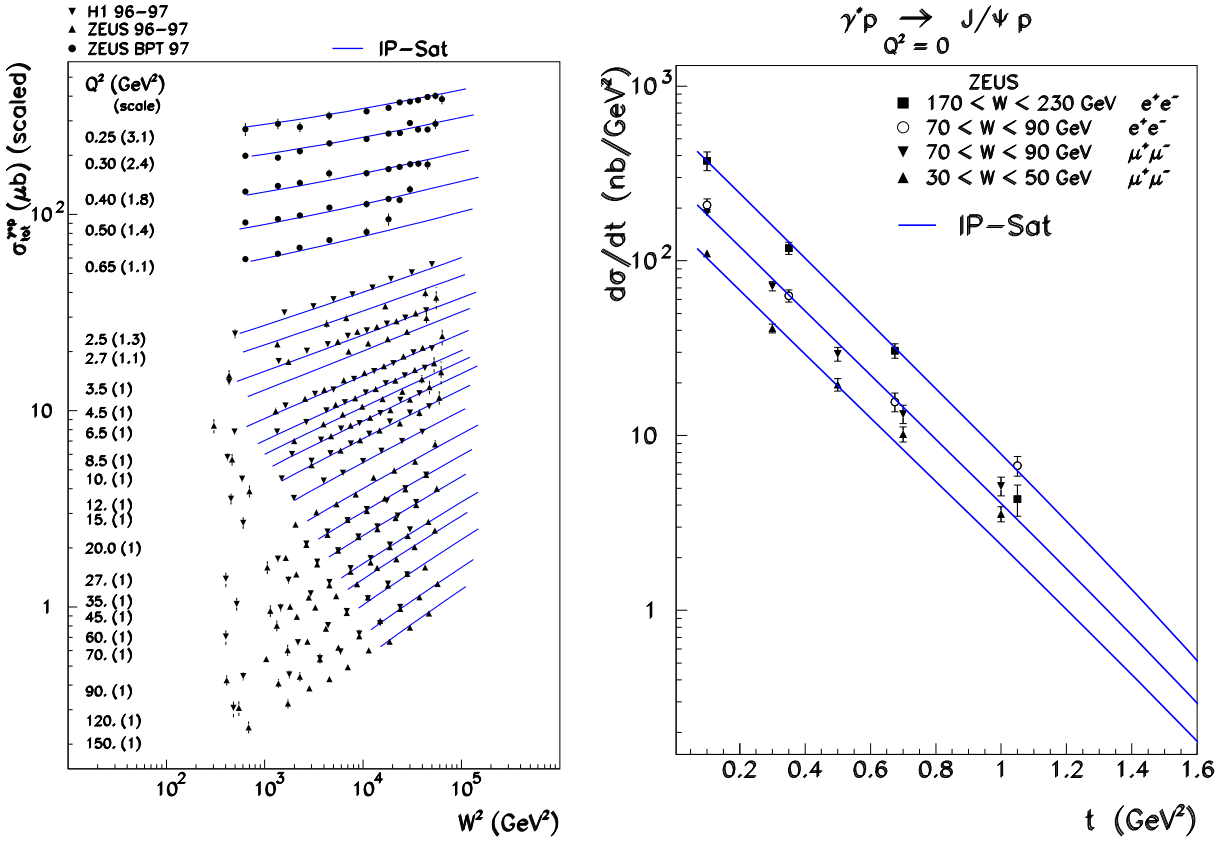

Fig. 6: LHS: The $\gamma^* p$ cross-section as a function of W^2. RHS: The differential cross section for exclusive diffractive J/Ψ production as a function of the four-momentum transfer t. The solid line shows a fit by the IP saturation model.

The properties of the multi-Pomeron amplitude and of the cut Pomeron cross-sections can be quantitatively studied in a dipole model. Let us first recall the main properties of the dipole picture, see Ref. [10, 11] and [3]. In the model the $\gamma^* p$ interaction proceeds in three stages: first the incoming vitual photon fluctuates into a quark-antiquark pair, then the $q\bar{q}$ pair elastically scatters on the proton, and finally the $q\bar{q}$ pair recombines to form a virtual photon. The total cross-section for $\gamma^* p$ scattering, or equivalently F_2, is obtained by averaging the dipole cross-sections with the photon wave functions, $\psi(r, z)$, and integrating over the impact parameter, b:

$$F_2 = \frac{Q^2}{4\pi^2 \alpha_{em}} \int d^2r \int \frac{dz}{4\pi} \psi^* \psi \int d^2b \frac{d\sigma_{qq}}{d^2b}\,. \tag{3}$$

Here $\psi^*\psi$ denotes the probability for a virtual photon to fluctuate into a $q\bar{q}$ pair, summed over all flavors and helicity states. The dipole cross-section is assumed to be a function of the opacity Ω:

$$\frac{d\sigma_{qq}}{d^2b} = 2\left(1-\exp(-\frac{\Omega}{2})\right) . \tag{4}$$

At small-x the opacity Ω can be directly related to the gluon density, $xg(x,\mu^2)$, and the transverse profile of the proton, $T(b)$:

$$\Omega = \frac{\pi^2}{N_C} r^2 \alpha_s(\mu^2) xg(x,\mu^2) T(b) . \tag{5}$$

The parameters of the gluon density are determined from the fit to the total inclusive DIS cross-section, as shown in Fig. 6 [3]. The transverse profile was determined from the exclusive diffractive J/Ψ cross-sections shown in the same figure. The opacity function Ω determined in this way has predictive properties; it allows to describe other measured reactions, e.g. charm structure function or elastic diffractive J/Ψ production shown in Fig.7.

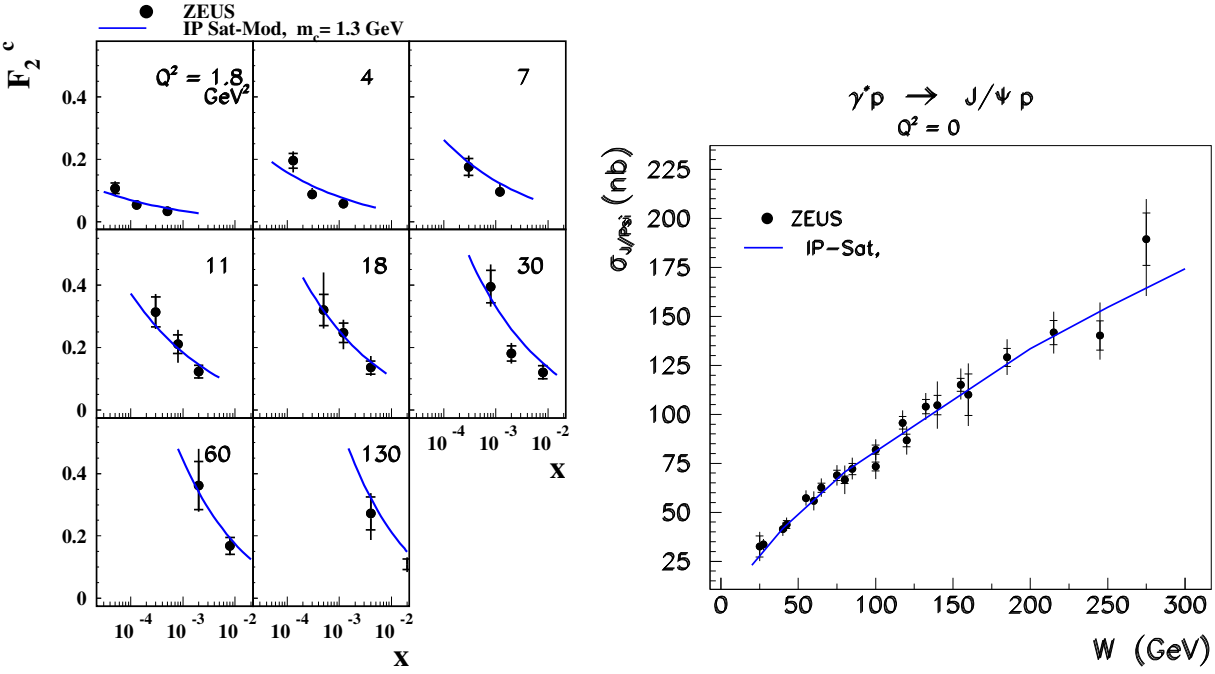

Fig. 7: LHS: Charm structure function, F_2^c. RHS: Total elastic J/Ψ cross-section. The solid line shows the reswult of the IP saturation model.

For a small value of Ω the dipole cross-section, Eq (4), is equal to Ω and therefore proportional to the gluon density. This allows to identify the opacity with the single Pomeron exchange amplitude of Fig. 1. The multi-Pomeron amplitude is determined from the expansion:

$$\frac{d\sigma_{qq}}{d^2b} = 2\left(1-\exp(-\frac{\Omega}{2})\right) = 2\sum_{m=1}^{\infty}(-1)^{m-1}\left(\frac{\Omega}{2}\right)^m \frac{1}{m!} \tag{6}$$

as

$$F^{(m)} = \left(\frac{\Omega}{2}\right)^m \frac{1}{m!}, \tag{7}$$

since the dipole cross-section can be expressed as a sum of multi-Pomeron amplitudes [12] in the following way:

$$\frac{d\sigma_{qq}}{d^2b} = 2\sum_{m=1}^{\infty}(-1)^{m-1}F^{(m)}\ . \tag{8}$$

The cross-section for k cut Pomerons is then obtained from the AGK rules, eq. 2, and from the multi-Pomeron amplitude, Eq. (7), as:

$$\frac{d\sigma_k}{d^2b} = \sum_{m=k}^{\infty}(-1)^{m-k}\,2^m\,\frac{m!}{k!(m-k)!}\left(\frac{\Omega}{2}\right)^m\frac{1}{m!} = \frac{\Omega^k}{k!}\sum_{m=k}^{\infty}(-1)^{m-k}\,\frac{\Omega^{m-k}}{(m-k)!} \tag{9}$$

which leads to a simple expression:

$$\frac{d\sigma_k}{d^2b} = \frac{\Omega^k}{k!}\exp(-\Omega)\ . \tag{10}$$

The diffractive cross-section is given by the difference between the total and the sum over all cut cross-sections:

$$\frac{d\sigma_{diff}}{d^2b} = \frac{d\sigma_{tot}}{d^2b} - \sum_{k=1}^{\infty}\frac{d\sigma_k}{d^2b} = 2\left(1-\exp\left(-\frac{\Omega}{2}\right)\right) - (1-\exp(-\Omega)) = \left(1-\exp\left(-\frac{\Omega}{2}\right)\right)^2\ . \tag{11}$$

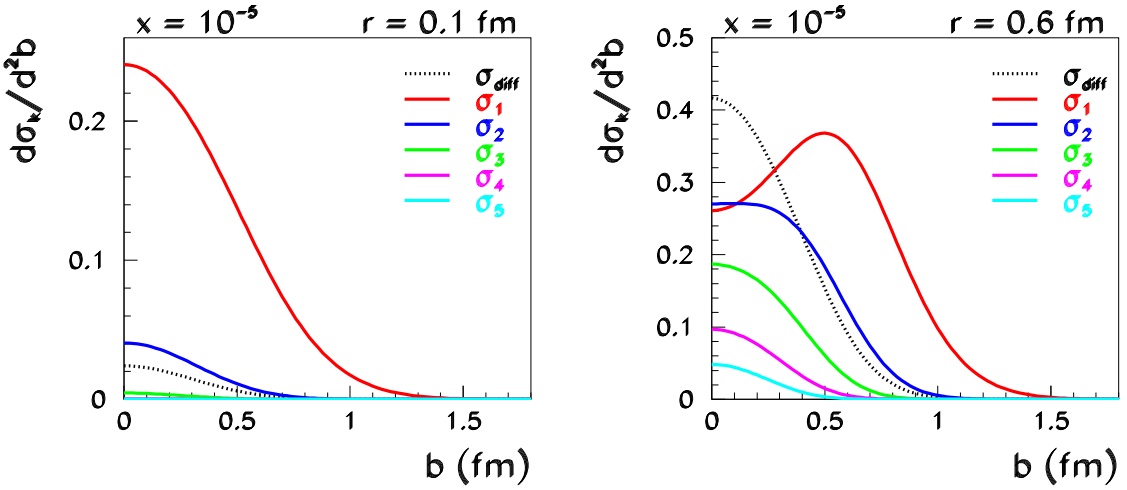

Fig. 8: Examples of b dependence of various cut dipole and diffractive cross-sections.

The cut cross-sections determined in the dipole model analysis of HERA data have several interesting properties shown in Fig. 8: for small dipoles ($r = 0.1$ fm) the opacity Ω is also small, so the single cut cross-section, σ_1, dominates. This leads to particle production emerging only from the one-cut pomeron, which should correspond, in the context of e.g. the LUND model, to a fragmentation of only one string. For larger dipoles ($r = 0.6$ fm) the dipole cross-section starts to be damped in the middle of the proton (at $b \approx 0$) by saturation effects. Therefore, the single cut cross-section is suppressed in the middle while the multiple cut cross-sections, σ_2, σ_3, etc, become substantial and increasingly concentrated in the proton center. These, fairly straight-forward properties of dipoles indicate that in the central scattering events the multiple scattering probability will be enhanced, which may lead at the LHC to substantial effects in a surrounding event multiplicity.

The contribution to F_2 from the k-cut Pomeron exchanges are computed in the analogous way to F_2:

$$F_2^k = \frac{Q^2}{4\pi^2\alpha_{em}}\int d^2r\int\frac{dz}{4\pi}\psi^*\psi\int d^2b\frac{d\sigma_k}{d^2b}. \tag{12}$$

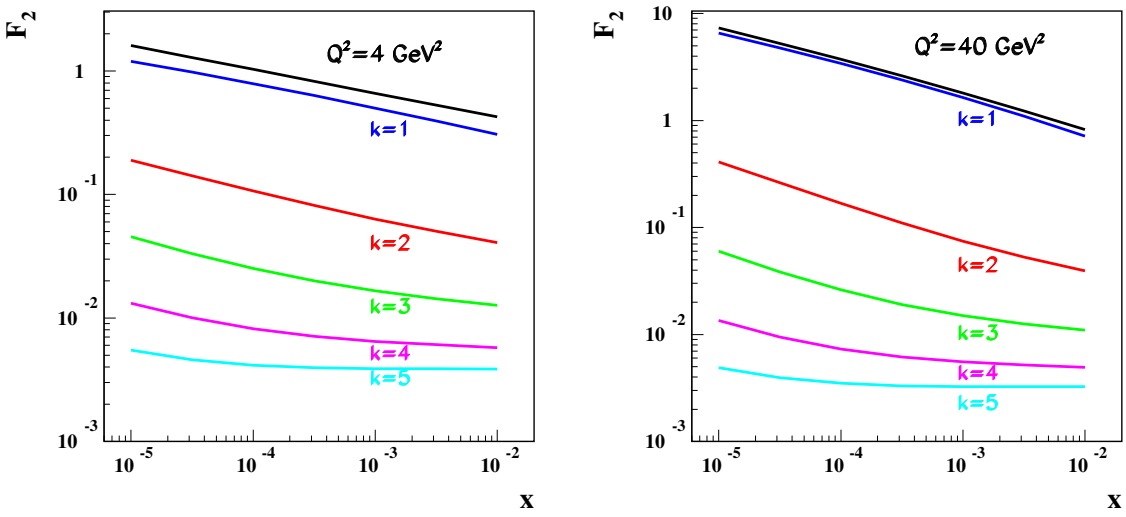

Fig. 9: F_2 and the contributions of k-cut Pomeron processes, F_2^k.

These contributions are shown, together with F_2, as a function of x for two representative Q^2 values in Fig. 9. One finds that multiple interaction contributions, i.e. $k \geq 2$, in the perturbative region, at $Q^2 = 4$ GeV^2, are substantial. In the typical HERA range of $x \approx 10^{-3} - 10^{-4}$, the $k = 2$ contribution is around 10% of F_2 and the contributions of higher cuts are also non-negligible. For example, the contribution of the 5-cut Pomeron exchanges is still around 0.5%, which means that at HERA, many thousand events may come from this type of process. Figure 10 shows the fraction of the multpile interaction processes,

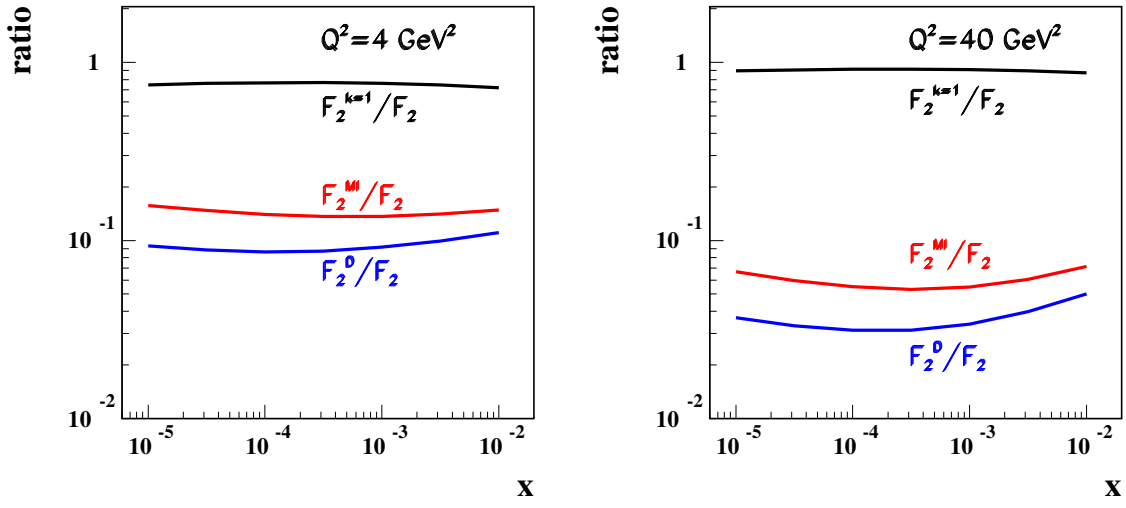

Fig. 10: Fractions of single (k=1), multiple interaction (MI) and diffraction (D) in DIS

$F_2^{MI} = F_2^{k=2} + F_2^{k=3} + F_2^{k=4} + F_2^{k=5}$ in F_2, at the same Q^2 values. At $Q^2 = 4$ GeV^2 the fraction of multiple scattering events is around 14% and at $Q^2 = 40$ GeV^2 around 6%, in the HERA x region, which indicates that the decrease of multiple scattering with increasing Q^2 is only logarithmic. The fraction of diffractive processes, shown for comparison, is of the same order, and drops also logarithmically with Q^2. The logarithmic drop of the diffractive contribution expected in the dipole model is confirmed by the data [6].

The dipole model provides a straight-forward extrapolation to the region of low Q^2, which is partly perturbative and partly non-perturbative. Figure 11 shows the contribution to F_2 of k-cut Pomeron processes and the fractions of multiple interactions and diffractive processes at $Q^2 = 0.4$ GeV^2.

Note also that, as a byproduct of this investigation, the ratio of diffractive and inclusive cross-sections, F_2^D/F_2 is found to be almost independent of x, in agreement with the data and also other dipole model predictions [6, 13, 14]. The absolute amount of diffractive effects is underestimated, since the evaluation of diffraction through AGK rules is oversimplified. It is well known [14], that a proper evaluation of diffraction should also take into account the $q\bar{q}g$ contribution which is missing in the simple AGK schema.

In conclusion, we find that the impact parameter dependent dipole saturation model [3] reproduces well the main properties of the data and leads to the prediction that multiple interaction effects at HERA should be of the order of diffractive effects, which are known to be substantial. The multiple interaction effects should decrease slowly (logarithmically) with increasing Q^2, similarly to the diffractive contribution.

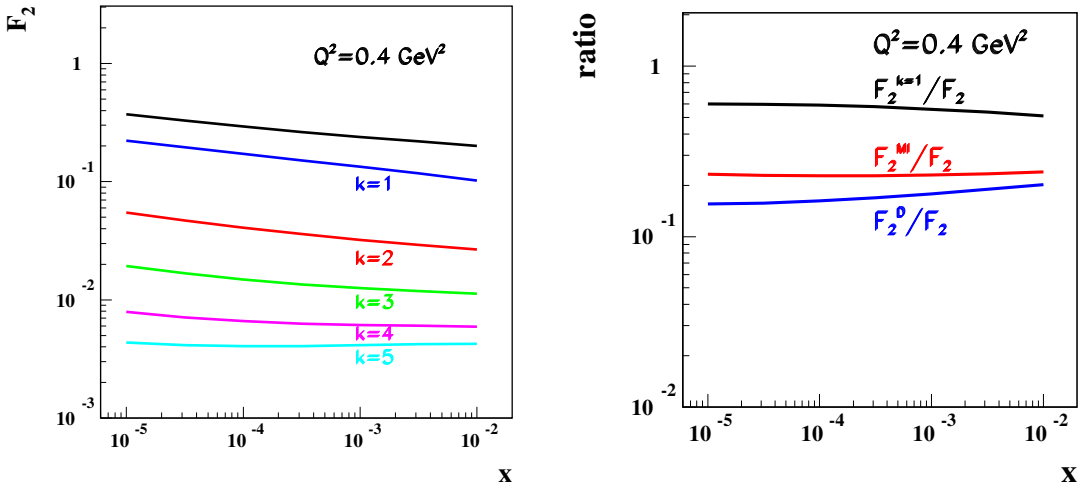

Fig. 11: Left: F_2 and the contributions of k-cut Pomeron processes. Right: Fractions of single (k=1), multiple interaction (MI) and diffraction (D) in DIS at $Q^2 = 0.4$ GeV^2.

4 Acknowledgements

I would like to thank Jochen Bartels for many illuminating discussions about physics of the multi-ladder QCD diagrams.

References

[1] G. Wolf, International Europhysics Conference on HEP (2001).
[2] Abramovski, Gribov, Kancheli, Sov. J. Nucl. Phys. **18**, 308 (1974).
[3] H. Kowalski and D. Teaney, Phys. Rev. D **68**, 114005 (2003).
[4] ZEUS Collaboration, S. Chekanov et al., Nucl. Phys. B **672**, 3 (2003).
[5] ZEUS Collaboration, S. Chekanov et al., Phys. Letters B **545**, 244 (2002).
[6] ZEUS Collaboration, S. Chekanov et al., Nucl. Phys. B **713**, 3 (2005).
[7] A. Levy, Nucl. Phys. B (Proc. Suppl) **146**, 92 (2005).
[8] J. Bartels and M. Ryskin, Z. Phys. **C 76**, 241 (1997).
[9] J. Bartels, M. Salvadore, and G.P. Vacca, Eur. Phys. J. C **42**, 53 (2005).
[10] N.N. Nikolaev and B.G. Zakharov, Z. Phys. C **49**, 607 (1991).
[11] A.H. Mueller, Nucl. Phys. B **415**, 373 (1994).
[12] A.H. Mueller and G.P. Salam, Nucl. Phys. B **475**, 293 (1996).
[13] K. Golec-Biernat and M. Wuesthoff, Phys. Rev. D **60**, 014023 (1999).
[14] J. Bartels, K. Golec-Biernat and H. Kowalski, Phys. Rev. D **66**, 014001 (2002).

From HERA to LHC through the Color Glass Condensate

Raju Venugopalan
Physics Department
Brookhaven National Laboratory
Upton, NY 11973, USA.

Abstract
A classical effective field theory, the Color Glass Condensate (CGC), provides a unified treatment of high parton density effects in both DIS and hadron-hadron collisions at very high energies. The validity and limitations of $k_\perp$ factorization can be studied in this effective theory. Multi-parton correlations in the effective theory are described by universal dipole and multipole operators. The evolution of these operators with energy provides a sensitive test of multi-parton dynamics in QCD at high energies.

1 Introduction

In the Bjorken limit of QCD, $Q^2 \to \infty$, $s \to \infty$, $x_{\rm Bj} \approx Q^2/s = \text{fixed}$, we have a powerful framework to compute a large number of processes to high accuracy. Underlying this machinery is the Operator Product Expansion (OPE), where cross-sections are identified as a convolution of short distance "coefficient functions" which are process dependent and long distance parton distribution functions which are universal. The evolution of the parton distribution functions with x and Q^2 is described by splitting functions, which determine the probability of "parent" partons to split into a pair of "daughter" partons. Both coefficient functions and splitting functions for DIS inclusive cross-sections are now available to Next-Next-Leading-Order (NNLO) accuracy [1].

While this is a tremendous achievement, the contribution of high Q^2 processes to the total cross-section is very small. The bulk of the cross-section can perhaps be better understood in the Regge asymptotic limit: $x_{\rm Bj} \to 0$, $s \to \infty$, $Q^2 = \text{fixed}$. The BFKL renormalization group equation [3] describes the leading $\alpha_S \ln(1/x)$ behavior of gluon distributions in this limit. The solutions of the BFKL equation predict that gluon distributions grow very rapidly with decreasing x. In the Regge asymptotics, since the transverse size of the partons is fixed, this growth of distributions will lead to the overlapping of partons in the transverse plane of the hadron. In this regime, contributions that were power suppressed in the BFKL scheme become important. These are recombination and screening effects which slow down the growth of gluon distributions leading ultimately to a saturation of these distributions [4, 5]. Such effects must appear at small x because the occupation number [1] of partons in QCD be at most of order $1/\alpha_S$.

Thus qualitatively, the competition between Bremsstrahlung and recombination/screening effects becomes of the same order when

$$\frac{1}{2\,(N_c^2-1)}\,\frac{x\,G(x,Q^2)}{\pi R^2 Q^2} \approx \frac{1}{\alpha_S(Q^2)}\,, \tag{1}$$

where R is the radius of the target. This relation is solved self-consistently when $Q \equiv Q_s(x)$. The scale $Q_s(x)$ is termed the saturation scale and it grows as one goes to smaller values of x. When $Q^2 \leq Q_s^2$, higher twist effects are important; at sufficiently small x, $Q_s^2 \gg \Lambda^2_{\rm QCD}$, which makes feasible a weak coupling analysis of these effects. At HERA, reasonable fits of small x inclusive and diffractive data

[1] This corresponds to the number of partons per unit transverse area, per unit transverse momentum, per unit rapidity, in light cone gauge. This condition has its gauge invariant counterpart in the requirement that the field strength squared not exceed $1/\alpha_S$.

for $x \leq 10^{-2}$ are obtained in saturation models with $Q_s^2(x) \approx Q_0^2\,(x_0/x)^\lambda$, with $Q_0^2 = 1$ GeV^2 and $x_0 = 3 \cdot 10^{-4}$. Detailed estimates suggest that the saturation scale for gluons is $Q_s(x) \approx 1.4$ GeV at $x \approx 10^{-4}$ [7]. The applicability of weak coupling techniques at these scales is dubious. Nevertheless, they cannot be ruled out since the effective scale at which the coupling runs can be larger than the estimate. Leading twist evolution of "shadowed" distributions at the saturation scale can extend out to significantly large values of x. A hint of this possibility is suggested by the fact that geometrical scaling-the dependence of cross-sections on the dimensionless ratio Q^2/Q_s^2 alone-extends out to $Q^2 \approx 450$ GeV^2 at HERA [8].

The possibility that weak coupling may apply at high energies is good news. Some of the remarkable regularities in high energy scattering data may be understood in a systematic way. The OPE, for instance, is no longer a good organizing principle since its usefulness is predicated on the twist expansion. In the next section, we will discuss an effective field theory approach which may provide a more efficient organizing principle at high parton densities.

2 The Color Glass Condensate

The physics of high parton densities can be formulated as a classical effective theory [6] because there is a Born-Oppenheimer separation between large x and small x modes [9] which are respectively the slow and fast modes in the effective theory. Large x partons are static sources of color charge for the dynamical wee (small x) parton fields. The generating functional of wee partons has the form

$$\mathcal{Z}[j] = \int [d\rho]\, W_{\Lambda^+}[\rho] \left\{ \frac{\int^{\Lambda^+} [dA]\delta(A^+) e^{iS[A,\rho]-j\cdot A}}{\int^{\Lambda^+} [dA]\delta(A^+) e^{iS[A,\rho]}} \right\} \tag{2}$$

where the wee parton action has the form

$$S[A,\rho] = \frac{-1}{4} \int d^4x\, F_{\mu\nu}^2 + \frac{i}{N_c} \int d^2x_\perp dx^- \delta(x^-)\, \mathrm{Tr}\left(\rho(x_\perp) U_{-\infty,\infty}[A^-]\right) . \tag{3}$$

In Eq. (2), ρ is a two dimensional classical color charge density and $W[\rho]$ is a weight functional of sources (which sits at momenta $k^+ > \Lambda^+$: note, $x = k^+/P^+_{\rm hadron}$). The sources are coupled to the dynamical wee gluon fields (which in turn sit at $k^+ < \Lambda^+$) via the gauge invariant term which is the second term on the RHS of Eq. (3). Here $U_{-\infty,\infty}$ denotes a path ordered exponential of the gauge field A^- in the x^+ direction. The first term in Eq. (3) is the QCD field strength tensor squared — thus the wee gluons are treated in full generality in this effective theory, which is formulated in the light cone gauge $A^+ = 0$. The source j is an external source — derivatives taken with respect to this source (with the source then put to zero) generate correlation functions in the usual fashion.

The argument for why the sources are classical is subtle and follows from a coarse graining of the effective action. The weight functional for a large nucleus is a Gaussian in the source density [6, 11], with a small correction for SU(N_c) coming from the $N_c - 2$ higher Casimir operators [10]. The variance of the Gaussian, the color charge squared per unit area μ_A^2, proportional to $A^{1/3}$, is a large scale — and is the only scale in the effective action [2]. Thus for $\mu_A^2 \gg \Lambda^2_{\rm QCD}$, $\alpha_S(\mu_A^2) \ll 1$, and one can compute the properties of the theory in Eq. (2) in weak coupling.

The saddle point of the action in Eq. (3) gives the classical distribution of gluons in the nucleus. The Yang-Mills equations can be solved analytically to obtain the classical field of the nucleus as a function of ρ: $A_{\rm cl.}(\rho)$ [6, 11, 12]. One can determine, for Gaussian sources, the occupation number $\phi = dN/\pi R^2/dk_\perp^2 dy$ (the number of partons per unit transverse momentum, per unit rapidity y, where $y = \ln(1/x)$) of wee partons in the classical field of the nucleus. One finds for $k_\perp \gg Q_s^2$, the Weizsäcker-Williams spectrum $\phi \sim Q_s^2/k_\perp^2$; for $k_\perp \leq Q_s$, one obtains a complete resummation to all orders in $k_\perp$,

[2] μ_A^2 is simply related in the classical theory to the saturation scale Q_s^2 via the relation $Q_s^2 = \alpha_S N_c \mu_A^2 \ln(Q_s^2/\Lambda^2_{\rm QCD})$

which gives $\phi \sim \frac{1}{\alpha_S}\ln(Q_s/k_\perp)$. (The behavior at low $k_\perp$ can, more accurately, be represented as $\frac{1}{\alpha_S}\Gamma(0,z)$ where Γ is the incomplete Gamma function and $z = k_\perp^2/Q_s^2$ [13]).

A high energy hadron is a Color Glass Condensate for the following reasons [2]. The 'color' is obvious since the parton degrees of freedom are colored. It is a glass because the sources, static on time scales much larger than time scales characteristic of the system, induce a stochastic (space-time dependent) coupling between the partons under quantum evolution — this is analogous to a spin glass. Finally, the matter is a condensate because the wee partons have large occupation numbers (of order $1/\alpha_S$) and have momenta peaked about Q_s. These properties are enhanced by quantum evolution in x. The classical field retains its structure — while the saturation scale grows: $Q_s(x') > Q_s(x)$ for $x' < x$.

Small fluctuations about the effective action in Eq. (3) give large corrections of order $\alpha_S \ln(1/x)$ (see Ref. [14]). The Gaussian weight functional is thus fragile under quantum evolution of the sources. A Wilsonian renormalization group (RG) approach systematically treats these corrections [15]. In particular, the change of the weight functional $W[\rho]$ with x is described by the JIMWLK- non-linear RG equations [15]. These equations form an infinite hierarchy of ordinary differential equations for the gluon correlators $\langle A_1 A_2 \cdots A_n\rangle_Y$, where $Y = \ln(1/x)$ is the rapidity. The JIMWLK equation for an arbitrary operator $\langle O\rangle$ is

$$\frac{\partial\langle\mathcal{O}[\alpha]\rangle_Y}{\partial Y} = \left\langle \frac{1}{2}\int_{x_\perp,y_\perp} \frac{\delta}{\delta\alpha_Y^a(x_\perp)}\,\chi^{ab}_{x_\perp,y_\perp}[\alpha]\,\frac{\delta}{\delta\alpha_Y^b(y_\perp)}\mathcal{O}[\alpha]\right\rangle_Y , \tag{4}$$

where $\alpha = (\nabla_\perp^2)^{-1}\rho$. Here χ is a non-local object expressed in terms of path ordered (in rapidity) Wilson lines of α [2]. This equation is analogous to a (generalized) functional Fokker-Planck equation, where Y is the "time" and χ is a generalized diffusion coefficient. It illustrates the stochastic properties of operators in the space of gauge fields at high energies. For the gluon density, which is proportional to a two-point function $\langle\alpha^a(x_\perp)\alpha^b(y_\perp)\rangle$, one recovers the BFKL equation in the limit of low parton densities.

3 Dipoles in the CGC

In the limit of large N_c and large A ($\alpha_S^2 A^{1/3} \gg 1$), the JIMWLK hierarchy closes for the two point correlator of Wilson lines because the expectation value of the product of traces of Wilson lines factorizes into the product of the expectation values of the traces:

$$\langle \mathrm{Tr}(V_x V_z^\dagger)\mathrm{Tr}(V_z V_y^\dagger)\rangle \longrightarrow \langle \mathrm{Tr}(V_x V_z^\dagger)\rangle\,\langle \mathrm{Tr}(V_z V_y^\dagger)\rangle\,, \tag{5}$$

where $V_x = \mathcal{P}\exp\left(\int dz^-\alpha^a(z^-,x_\perp)T^a\right)$. Here $\mathcal{P}$ denotes path ordering in x^- and T^a is an adjoint SU(3) generator. In Mueller's dipole picture, the cross-section for a dipole scattering off a target can be expressed in terms of these 2-point dipole operators as [16, 17]

$$\sigma_{q\bar{q}N}(x,r_\perp) = 2\int d^2b\,\mathcal{N}_Y(x,r_\perp,b)\,, \tag{6}$$

where $\mathcal{N}_Y = 1 - \frac{1}{N_c}\langle \mathrm{Tr}(V_x V_y^\dagger)\rangle_Y$, the imaginary part of the forward scattering amplitude. Note that the size of the dipole, $\vec{r}_\perp = \vec{x}_\perp - \vec{y}_\perp$, and the impact parameter, $\vec{b} = (\vec{x}_\perp + \vec{y}_\perp)/2$. The JIMWLK equation for the two point Wilson correlator is identical in the large A, large N_c mean field limit to an equation derived independently by Balitsky and Kovchegov — the Balitsky-Kovchegov equation [18], which has the operator form

$$\frac{\partial\mathcal{N}_Y}{\partial Y} = \frac{\alpha_S N_c}{\pi}\,\mathcal{K}_{\mathrm{BFKL}}\otimes\left\{\mathcal{N}_Y - \mathcal{N}_Y^2\right\}\,. \tag{7}$$

Here $\mathcal{K}_{\mathrm{BFKL}}$ is the well known BFKL kernel. When $\mathcal{N} \ll 1$, the quadratic term is negligible and one has BFKL growth of the number of dipoles; when $\mathcal{N}$ is close to unity, the growth saturates. The approach to

unity can be computed analytically [19]. The B-K equation is the simplest equation including both the Bremsstrahlung responsible for the rapid growth of amplitudes at small x as well as the repulsive many body effects that lead to a saturation of this growth.

A saturation condition which fixes the amplitude at which this change in behavior is significant, say $\mathcal{N} = 1/2$, determines the saturation scale. One obtains $Q_s^2 = Q_0^2 \exp(\lambda Y)$, where $\lambda = c\alpha_S$ with $c \approx 4.8$. The saturation condition affects the overall normalization of this scale but does not affect the power λ. In fixed coupling, the power λ is large and there are large pre-asymptotic corrections to this relation-which die off only slowly as a function of Y. BFKL running coupling effects change the behavior of the saturation scale completely–one goes smoothly at large Y to $Q_s^2 = Q_0^2 \exp(\sqrt{2b_0 c(Y + Y_0)})$ where b_0 is the coefficient of the one-loop QCD β-function. The state of the art computation of Q_s is the work of Triantafyllopoulos, who obtained Q_s by solving NLO-resummed BFKL in the presence of an absorptive boundary (which corresponds to the CGC) [20]. The pre-asymptotic effects are much smaller in this case and the coefficient $\lambda \approx 0.25$ is very close to the value extracted from saturation model fits to the HERA data [21]. Fits of CGC inspired models to the HERA data have been discussed elsewhere [22] and will not be discussed here.

4 Hadronic scattering and $k_\perp$ factorization in the CGC

Collinear factorization is the pQCD mechanism to compute hard scattering. At collider energies, a new window opens up where $\Lambda^2_{\rm QCD} \ll M^2 \ll s$, where M is the invariant mass of the final state. In principle, cross-sections in this window can be computed in the collinear factorization language–however, one needs to sum up large logarithmic corrections in s/M^2. An alternative formalism is that of $k_\perp$-factorization [23, 24], where one has a convolution of $k_\perp$ dependent "un-integrated" gluon distributions from the two hadrons with the hard scattering matrix. In this case, the in-coming partons from the wavefunctions have non-zero $k_\perp$. Levin et al. [25] suggested that at high energies the typical $k_\perp$ is the saturation scale Q_s. The rapidity dependence of the unintegrated distributions is given by the BFKL or BK equations. However, unlike the structure functions, it has not been proven that these unintegrated distributions are universal functions.

At small x, both the collinear factorization and $k_\perp$ factorization limits can be understood in a systematic way in the framework of the Color Glass Condensate. The expectation value of an operator $\mathcal{O}$ can be computed as

$$\langle \mathcal{O} \rangle_Y = \int [d\rho_1]\, [d\rho_2]\, W_{x_1}[\rho_1]\, W_{x_2}[\rho_2]\, \mathcal{O}(\rho_1, \rho_2)\,, \tag{8}$$

where $Y = \ln(1/x_F)$ and $x_F = x_1 - x_2$. Quantum information, to leading logarithms in x, is contained in the source functionals $W_{x_{1(2)}}[\rho_1(\rho_2)]$ of the two hadrons. The operator $\mathcal{O}$ corresponding to the final state is expressed in terms of gauge fields $A^\mu[\rho_1, \rho_2](x)$. Inclusive gluon production in the CGC is computed by solving the Yang-Mills equations $[D_\mu, F^{\mu\nu}]^a = J^{\nu,a}$ for $A^\mu[\rho_1, \rho_2]$, where the current is given by $J^\nu = \rho_1\, \delta(x^-)\delta^{\nu+} + \rho_2\, \delta(x^+)\delta^{\nu-}$ with initial conditions determined by the Yang-Mills fields of the two hadrons before the collision. These are obtained self-consistently by matching the solutions of the Yang-Mills equations on the light cone [26]. Since we have argued in Section 2 that we can *compute* the Yang-Mills fields in the nuclei before the collision, the classical problem is in principle completely solvable. Quantum corrections not enhanced by powers of $\alpha_S \ln(1/x)$ can be computed systematically. Those terms enhanced by powers of $\alpha_S \ln(1/x)$ are absorbed into the weight functionals $W[\rho_{1,2}]$.

Hadronic scattering in the CGC can therefore be studied through a systematic power counting in the density of sources in powers of $\rho_{1,2}/k^2_{\perp;1,2}$. This power counting is more relevant at high energies than whether the incoming projectile is a hadron or a nucleus. In addition, one can study the applicability of collinear and $k_\perp$ factorization at small x in this approach.

The power counting is applicable as well to a proton at small x. The relevant quantity here is Q_s, which, as one may recall, is enhanced both for large A and small x. As long as $k_\perp \gg Q_s \gg \Lambda_{\rm QCD}$,

one can consider the proton or nucleus as being dilute. To lowest order in $\rho_{p1}/k_\perp^2$ and $\rho_{p2}/k_\perp^2$, one can compute inclusive gluon production analytically [26]. At large transverse momenta, $Q_s \ll k_\perp$, the scattering can be expressed in a $k_\perp$-factorized form. The inclusive cross-section is expressed as the product of two unintegrated ($k_\perp$ dependent) distributions times the matrix element for the scattering. The comparison of this result to the collinear pQCD $gg \to gg$ process and the $k_\perp$ factorized $gg \to g$ was performed in Ref. [27]. At this order, the result is equivalent to the pQCD result first derived by Gunion and Bertsch [28]. This result for gluon production is substantially modified, as we shall discuss shortly, by high parton density effects either because the target is a large nucleus or because small values of x are being probed in the hadron (as in forward pp scattering).

$k_\perp$ factorization is a good assumption at large momenta for quark pair-production. This was worked out in the CGC approach by François Gelis and myself [29]. The result for inclusive quark pair production can be expressed in $k_\perp$ factorized form as

$$\frac{d\sigma_1}{dy_p dy_q d^2p_\perp d^2q_\perp} \propto \int \frac{d^2k_{1\perp}}{(2\pi)^2}\frac{d^2k_{2\perp}}{(2\pi)^2}\delta(k_{1\perp}+k_{2\perp}-p_\perp-q_\perp) \times\phi_1(k_{1\perp})\phi_2(k_{2\perp})\frac{\mathrm{Tr}\left(\left|m_{ab}^{-+}(k_1,k_2;q,p)\right|^2\right)}{k_{1\perp}^2 k_{2\perp}^2}\,, \tag{9}$$

where ϕ_1 and ϕ_2 are the unintegrated gluon distributions in the projectile and target respectively (with the gluon distribution defined as $xG(x,Q^2) = \int_0^{Q^2} d(k_\perp^2)\,\phi(x,k_\perp)$).

The matrix element $\mathrm{Tr}\left(\left|m_{ab}^{-+}(k_1,k_2;q,p)\right|^2\right)$ is identical to the result derived in the $k_\perp$–factorization approach [23, 24]. In the limit $|\vec{k_{1\perp}}|, |\vec{k_{2\perp}}| \to 0$, $\mathrm{Tr}\left(\left|m_{ab}^{-+}(k_1,k_2;q,p)\right|^2\right)\Big/(k_{1\perp}^2 k_{2\perp}^2)$ is well defined–after integration over the azimuthal angles in Eq. (9), one obtains the usual matrix element $|\mathcal{M}|^2_{gg\to q\bar{q}}$, recovering the lowest order pQCD collinear factorization result.

4.1 Gluon and quark production in forward pp and pA collisions

Many analytical results are available when one of the hadrons is dilute and the other is dense. This may correspond to either pA collisions or forward pp collisions. One solves the Yang–Mills equations $[D_\mu, F^{\mu\nu}] = J^\nu$ with the light cone sources $J^{\nu,a} = \delta^{\nu+}\,\delta(x^-)\,\rho_p^a(x_\perp) + \delta^{\nu-}\,\delta(x^+)\,\rho_A^a(x_\perp)$, to determine the gluon field produced-to lowest order in the source density of one projectile ($\rho_p/k_\perp^2 \ll 1$)and to all orders ($\rho_A/k_\perp^2 \sim 1$) in the source density of the other. The inclusive gluon production cross-section, in this framework, was first computed by Kovchegov and Mueller [30] and shown to be $k_\perp$ factorizable in Ref. [31, 34]. The "unintegrated" gluon distribution in the dense system however is here replaced by the gluon "dipole" distribution $\mathcal{N}_Y$ we discussed previously. It is no longer a leading twist object but includes all twists enhanced by high parton density effects. The well known "Cronin" effect observed in Deuteron-Gold collisions at RHIC is obtained in this formalism and can be simply understood in terms of the multiple scattering of a parton from the projectile with those in the target. The energy evolution of the dipole distribution is given by the BK equation, leading to a suppression of the Cronin effect at high densities due to the shadowing of nuclear distributions. This prediction appears to be confirmed by the RHIC data. The "dipole" operators extracted from DIS can therefore be used to predict inclusive hadron production in pp and pA collisions. One can similarly compute Drell-Yan and photon production in forward pp and pA collisions [33, 35].

Unlike gluon production, neither quark pair-production nor single quark production is strictly $k_\perp$ factorizable. The pair production cross-section can however still be written in $k_\perp$ factorized form as a product of the unintegrated gluon distribution in the proton times a sum of terms with three unintegrated distributions, $\phi_{g,g}$, $\phi_{q\bar{q},g}$ and $\phi_{q\bar{q},q\bar{q}}$. These are respectively proportional to 2-point (dipole), 3-point and 4-point correlators of the Wilson lines we discussed previously. Again, these operators include all twist contributions. For instance, the distribution $\phi_{q\bar{q},g}$ is the product of fundamental Wilson lines coupled to

a $q\bar{q}$ pair in the amplitude and adjoint Wilson lines coupled to a gluon in the complex conjugate amplitude. For large transverse momenta or large-mass pairs, the 3-point and 4-point distributions collapse to the unintegrated gluon distribution, and we recover the previously discussed $k_\perp$-factorized result for pair production in the dilute/pp-limit. Single quark distributions are straightforwardly obtained and depend only on the 2-point quark and gluon correlators and the 3-point correlators. For Gaussian sources, as in the McLerran-Venugopalan-model, these 2-,3- and 4-point functions can be computed exactly as discussed in Ref. [32].

The situation gets complicated when one enters a regime where both projectiles are dense–as defined in our power counting. $k_\perp$ factorization breaks down decisively and analytical approaches are likely not possible. Nevertheless, numerical techniques have been developed, which allow the computation of final states, at least to leading logs in x [38].

The results for gluon and quark production in forward pp and pA or dA collisions (for a review, see Ref. [37]), coupled with the previous results for inclusive and diffractive [33–36] distributions in DIS, suggest an important new paradigm. *At small x in DIS and hadron colliders, previously interesting observables such as quark and gluon densities are no longer the only observables to capture the relevant physics. Instead, they should be complemented by dipole and multipole correlators of Wilson lines that seem ubiquitous in all high energy processes and are similarly gauge invariant and process independent. The renormalization group running of these operators may be a powerful and sensitive harbinger of new physics.*

References

[1] A. Vogt, S. Moch and J. A. M. Vermaseren, Nucl. Phys. B **691**, 129 (2004); S. A. Larin, P. Nogueira, T. van Ritbergen and J. A. M. Vermaseren, Nucl. Phys. B **492**, 338 (1997).

[2] E. Iancu and R. Venugopalan, hep-ph/0303204, in QGP3, Ed. R. Hwa and X.-N. Wang, World Scientific (2004).

[3] E. A. Kuraev, L. N. Lipatov and V. S. Fadin, Sov. Phys. JETP **45**, 199 (1977) [Zh. Eksp. Teor. Fiz. **72**, 377 (1977)]; I. I. Balitsky and L. N. Lipatov, Sov. J. Nucl. Phys. **28**, 822 (1978) [Yad. Fiz. **28**, 1597 (1978)].

[4] L.V. Gribov, E.M. Levin, M.G. Ryskin, Phys. Rept. **100**, 1 (1983).

[5] A.H. Mueller, J-W. Qiu, Nucl. Phys. **B 268**, 427 (1986).

[6] L. D. McLerran and R. Venugopalan, Phys. Rev. D **49**, 2233 (1994); *ibid.*, 3352, (1994); *ibid.*, **50**, 2225 (1994).

[7] H. Kowalski and D. Teaney, Phys. Rev. D **68**, 114005 (2003).

[8] A. M. Stasto, K. Golec-Biernat and J. Kwiecinski, Phys. Rev. Lett. **86**, 596 (2001).

[9] L. Susskind, Phys. Rev. **165**, 1535, (1968).

[10] S. Jeon and R. Venugopalan, Phys. Rev. D **70**, 105012 (2004).

[11] Yu.V. Kovchegov, Phys. Rev. **D 54**, 5463 (1996); *ibid.*, **55**, 5445 (1997).

[12] J. Jalilian-Marian, A. Kovner, L.D. McLerran, H. Weigert, Phys. Rev. **D 55**, 5414 (1997).

[13] D. Triantafyllopoulos, hep-ph/0502114.

[14] A. Ayala, J. Jalilian-Marian, L.D. McLerran, R. Venugopalan, Phys. Rev. **D 52**, 2935 (1995); *ibid.*, **53**, 458 (1996).

[15] J. Jalilian-Marian, A. Kovner, A. Leonidov, H. Weigert, Phys. Rev. **D 59**, 014014 (1999); E. Iancu, A. Leonidov, L.D. McLerran, Nucl. Phys. **A 692**, 583 (2001).

[16] A. H. Mueller, Nucl. Phys. B **415**, 373 (1994).

[17] N. N. Nikolaev and B. G. Zakharov, Z. Phys. C**49**, (1991) 607.

[18] I. Balitsky, Nucl. Phys. **B 463**, 99 (1996); Yu.V. Kovchegov, Phys. Rev. **D 61**, 074018 (2000).

[19] E.M. Levin, K. Tuchin, Nucl. Phys. **B 573**, 833 (2000).

[20] D. N. Triantafyllopoulos, Nucl. Phys. B **648**, 293 (2003).

[21] K. Golec-Biernat, M. Wüsthoff, Phys. Rev. **D 59**, 014017 (1999).

[22] R. Venugopalan, arXiv:hep-ph/0412396.

[23] S. Catani, M. Ciafaloni, F. Hautmann, Nucl. Phys. B **366**, 135 (1991).

[24] J. C. Collins and R. K. Ellis, Nucl. Phys. B **360**, 3 (1991).

[25] E. M. Levin, M. G. Ryskin, Y. M. Shabelski and A. G. Shuvaev, Sov. J. Nucl. Phys. **53**, 657 (1991).

[26] A. Kovner, L. D. McLerran and H. Weigert, Phys. Rev. D **52**, 3809 (1995); Y. V. Kovchegov and D. H. Rischke, Phys. Rev. C **56**, 1084 (1997).

[27] M. Gyulassy and L. D. McLerran, Phys. Rev. C **56**, 2219 (1997).

[28] J. F. Gunion and G. Bertsch, Phys. Rev. D **25**, 746 (1982).

[29] F. Gelis and R. Venugopalan, Phys. Rev. D **69**, 014019 (2004).

[30] Y. V. Kovchegov and A. H. Mueller, Nucl. Phys. B **529**, 451 (1998).

[31] J. P. Blaizot, F. Gelis and R. Venugopalan, Nucl. Phys. A **743**, 13 (2004).

[32] J. P. Blaizot, F. Gelis and R. Venugopalan, Nucl. Phys. A **743**, 57 (2004); H. Fujii, F. Gelis and R. Venugopalan, hep-ph/0504047.

[33] F. Gelis and J. Jalilian-Marian, Phys. Rev. D **66**, 094014 (2002); Phys. Rev. D **66**, 014021 (2002); A. Dumitru and J. Jalilian-Marian, Phys. Rev. Lett. **89**, 022301 (2002).

[34] Y. V. Kovchegov and K. Tuchin, Phys. Rev. D **65**, 074026 (2002); D. Kharzeev, Yu. Kovchegov, K. Tuchin, Phys. Rev. D **68**, 094013 (2003).

[35] B. Z. Kopeliovich, J. Raufeisen, A. V. Tarasov and M. B. Johnson, Phys. Rev. C **67**, 014903 (2003).

[36] A. Kovner and U. A. Wiedemann, Phys. Rev. D **64**, 114002 (2001).

[37] J. Jalilian-Marian and Y. V. Kovchegov, arXiv:hep-ph/0505052.

[38] A. Krasnitz and R. Venugopalan, Nucl. Phys. B **557**, 237 (1999); Phys. Rev. Lett. **84**, 4309 (2000); A. Krasnitz, Y. Nara and R. Venugopalan, Phys. Rev. Lett. **87**, 192302 (2001); Nucl. Phys. A **717**, 268 (2003); Nucl. Phys. A **727**, 427 (2003); T. Lappi, Phys. Rev. C **67**, 054903 (2003).

Vector Boson Fusion at CMS

N. Amapane[1,a]*, M. Arneodo*[2]*, R. Bellan*[1]*, S.Bolognesi*[1]*, G. Cerminara*[1]*, C. Mariotti*[3]
1) Torino University and INFN Torino, 2) University of Eastern Piedmont, Novara and INFN Torino,
3) INFN Torino, a) now at CERN

Abstract
The processes of boson-boson scattering and of Higgs production in boson-boson fusion hold the key to electroweak symmetry breaking. A preliminary study has been performed using a fast simulation of the CMS detector. The results are encouraging and suggest that, after few years of data taking at LHC, the region above 1 TeV can be explored, which is interesting if the Higgs is not found.

1 Vector Boson Fusion at CMS

1.1 Introduction

The Standard Model predicts that, without the Higgs boson, the scattering amplitude of the *longitudinally polarized vector boson* (V_L) fusion process violates unitarity at about 1-1.5 TeV. The longitudinal polarization of the *V* arises from the *V* getting massive, i.e. when the symmetry breaks spontaneously. The cross section as a function of the V_LV_L invariant mass will show a resonance at M(V_LV_L)=M(H) if the Higgs is there; otherwise, the cross section will deviate from the Standard Model prediction at high values of M(VV). Therefore, *VV* scattering can probe the Electroweak Symmetry Breaking with or without the assumption the Higgs mechanism.

1.2 The Signal Selection

Two channels have been studied using *Pythia* [1] and the *CMS Fast Simulation* [2]:

- $pp \to \mu\mu jjjj$ [3] through the processes:
  - $pp \to V_LV_Ljj \to Z_LZ_Ljj \to \mu\mu jjjj$,
  - $pp \to Z_LW_Ljj \to Z_LW_Ljj \to \mu\mu jjjj$.
- $pp \to \mu\nu jjjj$ [4] through the process:
  - $pp \to V_LV_Ljj \to W_LW_Ljj \to \mu\nu jjjj$.

The study has been done for high Higgs masses: $m_H = 500$ GeV and $m_H = 1000$ GeV, and for the no-Higgs scenario. The latter has been simulated in Pythia by setting $m_H = 10000$ GeV (the Higgs exchange diagram is suppressed by a m_H^2 term in the denominator of the Higgs propagator). The cross sections of the signal processes are shown in Table 1.

Table 1: Signal cross section (in fb) for different Higgs masses.

Processes	$m_H = 500$ GeV	$m_H = 1000$ GeV	$m_H = 10\,000$ GeV
$pp \to Z_LZ_Ljj \to \mu\mu jjjj$	9.1	3.0	1.7
$pp \to Z_LW_Ljj \to \mu\mu jjjj$	0.7	1.0	1.5
$pp \to W_LW_Ljj \to \mu\nu jjjj$	64.4	26.9	19.7

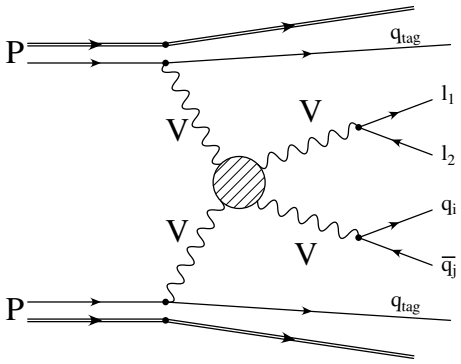

Fig. 1: The signal topology. l_1 and l_2 can be $\mu^{\pm}$ or μ and ν.

The signal has a well defined topology (see Figure 1):

- one μ^+ and one μ^- (or one μ and one ν) in the final state, with high p_T and low η coming from the *Z* (*W*) boson;
- two jets with high p_T and low η, coming from the vector boson decay;
- two energetic jets with high p_T, in the forward-backward regions (large η and $\Delta\eta$).

The aim of the work is to reconstruct the invariant mass of the *VV*-fusion system in both the channels and estimate its resolution. We also attempted a first estimate of the signal to background ratio assuming that the main background processes are:

- $t\bar{t}$ *background*: a six fermion final state, like the signal, but the jets are mainly in the central region; therefore, by requiring two jets at high η and with a large $\Delta\eta$ between them this kind of background can be rejected.
- *VV associated production*: a four fermion final state; it needs however to be kept under control in the case in which one boson decays leptonically since there are several jets from gluon radiation in the final state. The most effective variables to distinguish this background from the signal are the transverse momenta of the jets and of the leptons.
- *V plus one and two hard jets*: it is simple to reject this background because it has a topology not very similar to that of the signal and the additional jets have a very low p_T (since they are generated by the parton shower). However it is fundamental to keep it under control since it has a very large cross section.

The cross section of the background processes are shown in Table 2.

Table 2: Background cross section (in fb).

Background	Cross Section [fb]	**Background**	Cross Section [fb]
$t\bar{t}$, 1 μ	$622 \cdot 10^3$	$t\bar{t}$, 1 μ^- and 1 μ^+	$620 \cdot 10^3$
$ZZ \to \mu^-\mu^+jj$	653	$ZW \to \mu^-\mu^+jj$	663
$WW \to \mu\nu^+jj$	$11 \cdot 10^3$	$W + jj \to \mu\nu jj$	$77 \cdot 10^3$
$Z + jet \to \mu^-\mu^+j$	$13 \cdot 10^6$	$W + j \to \mu\nu j$	$184 \cdot 10^6$

1.3 The Results

A set of cuts has been applied to enhance the signal with respect to the background. A good resolution (estimated using MC info) on the most important observables has been achieved. In particular:

- $Z \to \mu\mu$ invariant mass: $R_z \sim 1.5\%$;
- $V \to jj$ invariant mass, $\mu\mu jjjj$ channel: $R_v \sim 13\%$;
- $V \to jj$ invariant mass, $\mu\nu jjjj$ channel: $R_v \sim 10\%$.

The difference between the two latter resolutions reflects the fact that for the $jjjj\mu\mu$ channel the pile-up has been considered whereas in the $jjjj\mu\nu$ it was not. The resolution on the energy scale of the process ($M_{inv}(VV)$) is:

- 4% for the $pp \to \mu\mu jjjj$ channel;
- 8% for the $pp \to \mu\nu jjjj$ channel.

The difference is due to the worse resolution on the neutrino p_T and p_z reconstruction. The resulting background efficiency is lower than one percent while the signal efficiency reaches 30% for the $jjjj\mu\mu$ channel and 50% for the $jjjj\mu\nu$ channel. A high significance ($S/\sqrt{B}$) has been achieved for an integrated luminosity of $100 fb^{-1}$: for the $\mu\mu jjjj$ samples it is about 8 in the interval $M_{inv}^{VV} \in [0,1]$ TeV for the Higgs mass set to 500 GeV and about 10 for $M_{inv}^{VV} > 1$ TeV for the no-Higgs scenario. Similar values have been obtained for the $\mu\nu jjjj$ channel: a significance of about 5, in the interval $M_{inv}^{VV} \in [0,1]$ TeV, for the Higgs mass set to 500 GeV and about 2.4 in the interval $M_{inv}^{VV} > 1$ TeV for the no-Higgs scenario. In Figs. 2 (no-Higgs scenario) and 3 ($m_H = 500$ GeV) the number of reconstructed events and the selection efficiency as a function of the *VV* invariant mass are shown.

1.4 Future Plans

Further studies are in progress, since for those presented here the Pythia generator was used, which only simulates a subset of the relavant diagrams, and cannot simulate the full set of background processes (notably not the scattering of transversely polarised vector bosons). To better describe the signal (and the background as well) a *Matrix Element Monte Carlo* must be used. *Phase* [5] is the best candidate, since it simulates all processes that lead to a six fermion final state, at order α_{QED}^6. Up to now only the channel $pp \to \mu\nu jjjj$ has been computed; therefore for the the $\mu\mu jjjj$ final state the *MadGraph* [6] event generator was used. This can simulate the $2l4j$ final state through the production (in Narrow Width Approximation) of intermediate vector bosons and their subsequent semileptonic decay.

Moreover it is crucial to redo the analysis, processing the events through the *Full Simulation* [7] of the CMS detector in order to properly take into account the detector resolution.

1.5 Summary

In conclusion, Electroweak Symmetry Breaking can be probed through the fusion of longitudinally polarized vector bosons with the CMS detector at LHC. The signal reconstruction and the background rejection algorithms have been successfully tested with the Fast Simulation. In the near future the study will be repeated with the Full Simulation of the detector and with dedicated generators.

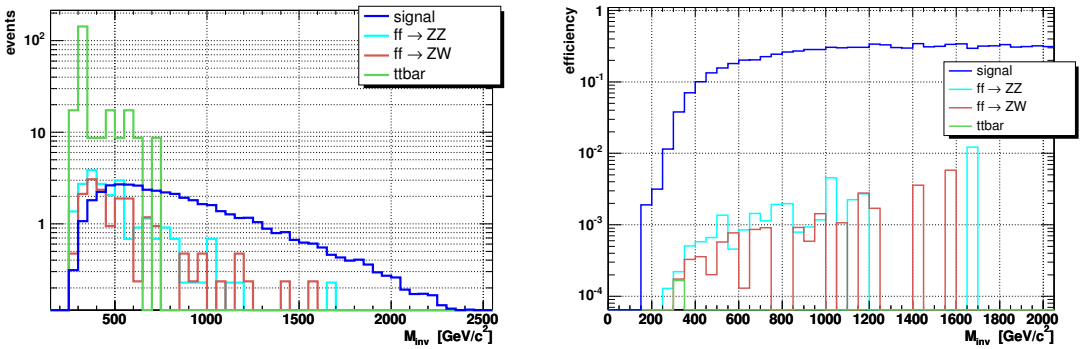

Fig. 2: (Left) Number of reconstructed events as a function of the *VV* invariant mass and (Right) the selection efficiency as a function of the invariant mass of the VV-fusion process; both for the $\mu\mu jjjj$ final state in the no-Higgs scenario and an integrated luminosity of 100 fb^{-1}.

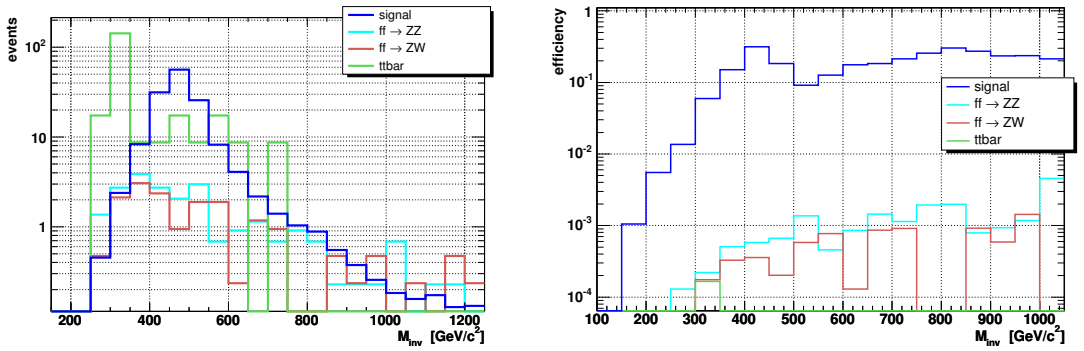

Fig. 3: (Left) Number of reconstructed events as a function of the *VV* invariant mass and (Right) the selection efficiency as a function of the invariant mass of the VV-fusion process; both for the $\mu\mu jjjj$ final state for $m_H = 500$ GeV and an integrated luminosity of 100 fb^{-1}.

References

[1] T. Sjöstrand et al., Comp. Phys. Comm. **135**, 238 (2001).

[2] S. Abdullin, A. Khanov and N. Stepanov, CMS TN/94-180.

[3] R. Bellan, *Observables in VV-fusion at the CMS Experiment*. Thesis, Università degli Studi di Torino, 2004.

[4] G. Cerminara, *A Study of the WW-fusion Process at CMS as a Probe of Symmetry Breaking*. Thesis, Università degli Studi di Torino, 2003.

[5] E. Accomando, A. Ballestrero and E. Maina, hep-ph/0504009.

[6] F. Maltoni and T. Stelzer, hep-ph/0208156.

[7] CMS Software and Computing Group, http://cmsdoc.cern.ch/oscar/;
CMS Software and Computing Group, http://cmsdoc.cern.ch/orca/.